

NASA-CR-194185

7N-34-CR

183177

P-221

Supersonic Turbulent Reacting
Flow Modeling and Calculation

by

Mohammad Farshchi
Nielsen Engineering & Research, Inc.Wolfgang Kollmann and Ebrahim Shirani
University of California, Davis

SBIR 1987 Phase II

April 1991

Prepared for: National Aeronautics & Space Administration
Lewis Research Center
21000 Brookpark Road
Cleveland, OH 44135

NAS3-25633

SBIR - : 01-04-9457

Release Date: 6-20-93

Nielsen Engineering & Research, Inc.
510 Clyde Avenue
Mountain View, CA 94043-2287
Telephone: (415)968-9457 • Facsimile: (415)968-1410

N94-70057

Unclass

0183177

29/34

(NASA-CR-194185) SUPERSONIC
TURBULENT REACTING FLOW MODELING
AND CALCULATION (Nielsen
Engineering and Research) 221 p

TABLE OF CONTENTS

NOMENCLATURE	iii
PROJECT SUMMARY	iv
INTRODUCTION	vi
CHAPTER 1. Governing Equations and Modeling Approaches	1
1.1 Exact Governing Equations	1
1.2 Averaged Governing Equations	3
1.3 Turbulence Closure Models	6
1.3.1 Second Order Modeling	6
1.3.2 Two-Equation Eddy Viscosity Modeling ($k-\epsilon$)	11
1.3.3 Zero-Equation Eddy Viscosity Modeling	16
1.4 Finite Rate Reaction Closure Model	17
1.5 Nondimensionalization	20
1.6 PDF Combustion Closure Model	24
1.6.1 Reaction Mechanism	25
1.6.2 Laminar Flow Reaction Closure	25
1.6.3 Turbulent Flow Reaction Closure	26
1.6.4 Assumed PDF	27
1.6.5 Mean Thermodynamic Variables	31
1.6.6 Mixture Fraction's Mean and Variance	31
CHAPTER 2. Numerical Solutions and Results	35
2.1 RPLUS Program	36
2.1.1 LU Scheme	36
2.1.2 Finite Volume Discretization and Artificial Dissipation	39
2.1.3 Turbulence Models	41
2.1.4 Chemical Reaction Models	42
2.1.5 Boundary and Initial Conditions	44
2.2 Supersonic Free Shear Layers	45
2.2.1 Solution Overshoots and Artificial Numerical Dissipation	47
2.2.2 Mixing Layers with Uniform Species Composition	50
2.2.3 Hydrogen-Air Mixing Layers without Chemical Reaction	55
2.2.4 Hydrogen-Air Mixing Layers with Chemical Reaction	57
2.3 Supersonic Wall-Bounded Shear Layers	59
CHAPTER 3. Joint PDF Analysis of Compressible Flows.....	65
3.1 Prescribed PDF Formalism for Compressible Turbulent Flows with Combustion.....	65
3.1.1 Specification of Order One and Two Components.....	65
3.1.2 Independent Variables.....	66
3.1.3 Statistical Independence in Transformed Scalar Spaces.....	68
3.1.4 Construction of the PDF.....	69
3.1.5 Derivative with respect to the defining moments: Beta-function.....	71

3.1.6 Derivative with respect to the solution variables: Composite PDF.....	73
3.2. Nonreacting Joint PDF Equation	83
3.3 Effects of Discontinuities in Supersonic Flows with Large Fluctuations.....	91
CHAPTER 4. Modeling and Solution of a Transport Equation for a Joint PDF.....	93
4.1 PDF Equation.....	93
4.2 Closure Model for the PDF Equation.....	94
4.2.1 Mixing Model.....	94
4.2.2 Compressibility Effects.....	96
4.3 Prediction of Supersonic Hydrogen Flames.....	98
4.3.1 Thermo-Chemical Properties.....	99
4.3.2 Velocity Field: Second Order Closure.....	100
4.3.3 Scalar Field: PDF Model.....	100
References	102
APPENDIX A. - Two-Dimensional Expansion of the Governing Equations	A-1
A.1 Finite Rate Reaction Model Equations	A-1
A.2 k- ϵ Equations	A-7
A.3 PDF Combustion Model Equations	A-8
Figures.....	

NOMENCLATURE

C_p	specific heat at a constant pressure
D	diffusivity
e	energy per unit mass
e_t	total energy per unit mass
G_i	gravitational acceleration vector
g	joint probability density function
h	enthalpy per unit mass
h_f	enthalpy of formation
p	pressure
s	entropy per unit mass
T	temperature
u	axial velocity
U	velocity vector, $U_i = \tilde{U}_i + U_i'$
v	transverse velocity
W	molar mass
x_i	position vector
Y	mass fraction
δ	Dirac delta function
ϕ	mixture fraction
κ	thermal conductivity
μ	dynamic viscosity
ρ	density
τ_{ij}	shear stress tensor
\dot{T}	volumetric chemical source term
$\langle \rangle$	ensemble average

Superscripts:

$\bar{}$	ensemble average
$\tilde{}$	density-weighted average
\prime	density-weighted fluctuation

PROJECT SUMMARY

The overall objective of this research was to develop turbulence and chemical reaction closure models for compressible reacting flowfields with large velocity and thermo-chemical fluctuations, and to use these closure models in the numerical calculation of several free and wall-bounded supersonic turbulent chemically reacting flows. This work was motivated by the need to develop accurate models for flowfields present in a typical supersonic combustion ramjet (SCRAMJET) engine.

The probability density function (PDF) theory was used in this work to develop a hybrid stochastic model for such flowfields. This modeling technique couples the time-averaged compressible flow equations with a probability density function formulation for the chemical reactions. The advantage of this method is that it treats chemical source terms and the state equations in a turbulent flowfield consistently, and more accurately, than standard approaches. The basic idea behind the above hybrid stochastic model is to solve the time-averaged mass, momentum, and energy conservation equations with standard numerical methods, and obtain the chemical reaction solution from a stochastic model, instead of solving the time-averaged species conservation equations. This method's requirements can be summarized as follows:

- (1) A PDF model for chemical reactions.
- (2) A second order turbulence model for compressible reacting flows.
- (3) A coupling between the mean flowfield and thermo-chemical variables.

To obtain some insight into the coupling between the mean flowfield and the thermodynamic variables, a theoretical study of the joint PDF of velocity components and thermodynamic variables in nonreacting turbulent compressible flows was conducted. This analysis indicated that the principle of the hybrid stochastic model is valid as long as the local effects created by compressibility are included in the turbulent modeling of the velocity field. Next, two different PDF models for chemically reacting flows were developed. The first one was a prescribed PDF model for mixing controlled chemical reactions. This model, along with a two-equation k - ϵ turbulence model, was implemented into a two-dimensional Navier-Stokes solver (RPLUS), and applied to several flowfields. The second PDF model was based on the solution of a transport equation for the joint PDF of a set of scalars representing species composition in a chemically reacting flowfield. This model, along with a second-order Reynolds stress turbulence model, was implemented into a two-dimensional parabolic flow solver and applied to a supersonic round jet. The above work points to the theoretical superiority and numerical feasibility of such comprehensive models for supersonic turbulent reacting flows. However, the results indicate that a robust Navier-Stokes solver with a total variational diminishing technique is required for the numerical solution of the governing transport equations in flowfields with a shock or a contact discontinuity, and the use of artificial numerical dissipation models can lead to serious complications.

The chemical reaction and turbulence models developed in this work can substantially increase the accuracy and versatility of the present computer codes used for the prediction of supersonic turbulent reacting flows. Aircraft engine companies and defense industries will be the main users of the resulting codes as a research and development tool. However, models developed here can be used by researchers and engineers in a variety of other applications such as laser technology.

INTRODUCTION

The modeling of chemically reacting turbulent flows at supersonic speeds has been attempted by many investigators since the late 1950's (Refs. 1 and 2). However, the physical and mathematical complexities of this problem have prevented the development of satisfactory models for the turbulence and combustion mechanisms and their influence on each other in a compressible flowfield.

A widely used approach to the solution of both the subsonic and supersonic problems is to consider the Reynolds averaged conservation equations of total mass, individual species mass, total momentum, and total energy in addition to equations of state relating the thermodynamic quantities for compressible flowfields. Introduction of models for the averaged chemical source terms and models for the turbulence correlation quantities in terms of the mean flow quantities would completely define the set of equations to be solved. The major drawback to this approach for both the subsonic and supersonic cases is the dependence of the chemical source terms on the average thermodynamic quantities. If the local combustion process involves reacting fluid parcels, some of which are at higher than average temperatures and some at lower than average temperatures, the average reaction rate would be biased toward the high-temperature side because of the exponential dependence of chemical reaction rate on temperature. Thus, the average state of reaction in a turbulent flow would be greater than that defined by the average temperature, and a computational model that accounted for only average temperature in the calculation of the chemical reaction rate would predict blowout more readily, i.e., at a higher fuel-air ratio than actually observed (Ref. 3). The higher pressure fluctuations along with lower mean pressure ranges, coupled with the short residency time of the fuel-air mixture in supersonic ramjet engines, make the treatment of the chemistry rate a more crucial factor in the modeling of supersonic combustion.

In recent years there have been many extensive efforts to devise more satisfactory methods for the treatment of the chemical source terms (Ref. 4-8). These methods range from simple phenomenological modeling of turbulent reaction (Ref. 7) to the solution of the exact, unaveraged governing equations (Ref. 8). Phenomenological modeling is accomplished by decoupling the turbulence from the chemistry through consideration of the dominant time scales and classifying the reaction mechanisms into either mixing controlled (diffusion flame) (Ref. 9) or chemistry controlled (premixed flame) (Ref. 10). One of the more promising approaches to the modeling of the chemically reacting turbulent flowfields is the application of the theory of single-point joint Probability Density Function of the velocity components and the thermo-chemical scalar fields (Ref. 11). A transport equation for this joint PDF can be obtained from the partial differential equations which define the conservation laws of the system. This method treats the rate-dependent source terms in the species equation exactly. Such PDF methods are also remarkably successful in alleviating many other modeling difficulties. For example, the effects of convection and the body force are treated without any approximations (Ref. 11). However, there are other terms appearing in the transport equation of the single-point joint PDF that require complicated

models. These non-closed terms include the correlation of variables at different spatial and temporal points and also include terms due to the effects of pressure and molecular transport.

The method of solving a modeled PDF equation was pioneered by the work of Lundgren (Ref. 12), who modeled and solved a transport equation for the joint PDF of velocity in a nonreacting, incompressible field. Dopazo and O'Brien (Ref. 13 and 14) derived, modeled, and solved the transport equations for the joint PDF of a set of scalars representing mass fractions and enthalpy describing the thermochemical state of the fluid. As mentioned before, complicated reactions can be treated exactly with this approach in contrast to conventional turbulence models in which mean reaction rates must be modeled. A major obstacle to the solution of the modeled transport equation of the joint PDF, for both velocity and thermochemical scalars in a compressible flow case, is the problem of obtaining a numerical solution for a realistic problem. This is due to the fact that the single-point joint PDF, for compressible reacting flows, is a function of a large number of independent variables. For a simple reaction, involving only three chemical species in three dimensions, such a general PDF is a function of 11 independent variables (Ref. 15). The numerical solution of the transport equation of such a function is prohibitively time consuming. Therefore, with the present computational powers, a simplified version of the fully joint PDF is desirable.

The complexities of physical phenomena in a turbulent chemically reacting compressible flow suggest that there is no one method of modeling that is superior in all applications. Depending on the nature of the time scales involved in the chemical reaction and the flowfield, an appropriate approach may be to design models that are best suited to the particular physical circumstances under consideration. However, ideally, one is looking for a comprehensive approach that would lead to simpler models in extreme cases. The probability density function (PDF) theory was used in this work to develop a hybrid stochastic model for such flowfields. This modeling technique couples the time-averaged compressible flow equations with a probability density function formulation for the chemical reactions. The advantage of this method is that it treats chemical source terms and the state equations in a turbulent flowfield consistently, and more accurately, than standard approaches. The basic idea behind the above hybrid stochastic model is to solve the time-averaged mass, momentum, and energy conservation equations with standard numerical methods and obtain the chemical reaction solution from a stochastic model, instead of solving the time-averaged species conservation equations. This method's requirements can be summarized as follows:

- (1) A PDF model for chemical reactions.
- (2) A second order turbulence model for compressible reacting flows.
- (3) A coupling between the mean flowfield and thermo-chemical variables.

To obtain some insight into the coupling between the mean flowfield and the thermodynamic variables, a theoretical study of the joint PDF of velocity components and

thermodynamic variables in nonreacting turbulent compressible flows was conducted. This analysis indicated that the principle of the hybrid stochastic model is valid as long as the local effects created by compressibility are included in the turbulent modeling of the velocity field. Next, two different PDF models for chemically reacting flows were developed. The first one was a prescribed PDF model for mixing controlled chemical reactions. This model, along with a two-equation k - ϵ turbulence model, was implemented into a two-dimensional Navier-Stokes solver (RPLUS) and applied to several flowfields. The second PDF model was based on the solution of a transport equation for the joint PDF of a set of scalars representing species composition in a chemically reacting flowfield. This model, along with a second-order Reynolds stress turbulence model, was implemented into a two-dimensional parabolic flow solver and applied to a supersonic round jet.

Chapter One of this report is concerned with the derivation of the density-weighted averaged Navier-Stokes equations for compressible turbulent chemically reacting flows. Several turbulence models and a prescribed PDF combustion model for the above flowfields are also presented in this chapter. Chapter Two discusses the implementation of these models into the RPLUS code and presents the results of the application of the code to several free and wall-bounded supersonic turbulent shear layers with and without chemical reaction. Chapter Three is concerned with the theoretical formalism behind the joint PDF formulation for compressible turbulent flowfields. In Chapter Four, modeling and solution of the transport equation of a joint PDF for a supersonic hydrogen-air flame is considered.

This is the final report for the NASA contract NAS3-25663. Topics related to tasks one and two of the contract are discussed in Chapters One and Two. Chapter Three is concerned with topics related to Tasks Three and Four, and Chapter Four is devoted to discussion of topics related to Task Five of the contract. Several versions of the modified RPLUS code have been delivered to the contract's technical monitor (Mr. Russ Claus) already; however, a final version will also be submitted with this report.

CHAPTER 1. GOVERNING EQUATIONS AND MODELING APPROACHES

In this chapter, the governing transport equations and auxiliary relations of a compressible chemically reacting turbulent flowfield are reviewed briefly. Next the density-averaged form of these equations is discussed. The modeling of the Reynolds stress tensor and other turbulent fluctuation correlations appearing in the averaged equations is discussed in Sections Three and Four. The nondimensionalized form of the averaged governing equation is given in Section Five. In the last section an assumed probability density function combustion closure model is presented, and equations needed by this model are discussed in detail.

1.1 Exact Governing Equations

Consider a mixture of N gaseous species, in which density, species mass fraction, and velocity at a point in space and time are defined by

$$\rho = \sum_{n=1}^N \rho_n \quad (1.1.1)$$

$$Y_n = \rho_n / \rho \quad (1.1.2)$$

$$\underline{U} = \sum_{n=1}^N \underline{U}_n \rho_n / \rho \quad (1.1.3)$$

The conservation laws of mass, species, momentum, and energy are applied to the above mixture. Utilizing the Cartesian tensor notation to express the equations in general three-dimensional form the following equations are obtained:

Mass Conservation:

$$\frac{\partial \rho}{\partial t} + \frac{\partial}{\partial x_j} (\rho U_j) = 0 \quad (1.1.4)$$

Species Conservation:

$$\frac{\partial}{\partial t} (\rho Y_n) + \frac{\partial}{\partial x_j} (\rho U_j Y_n - \rho D_n \frac{\partial Y_n}{\partial x_j}) = \dot{r}_n \quad (1.1.5)$$

$n = 1, 2, \dots, N-1$

Momentum Conservation:

$$\frac{\partial}{\partial t} (\rho U_i) + \frac{\partial}{\partial x_j} (\rho U_j U_i + \delta_{ij} P - \tau_{ij}) = \rho G_i \quad (1.1.6)$$

$$i = 1, 2, 3$$

Energy Conservation:

$$\frac{\partial}{\partial t} (\rho e_t) + \frac{\partial}{\partial x_j} \left\{ \rho U_j e_t + P U_j - \tau_{ij} U_i - \frac{\kappa}{c_p} \left[\frac{\partial h}{\partial x_j} + \sum_{n=1}^N \left(\frac{\rho D_n c_p}{\kappa} - 1 \right) h_n \frac{\partial Y_n}{\partial x_j} \right] \right\} = \rho G_j U_j \quad (1.1.7)$$

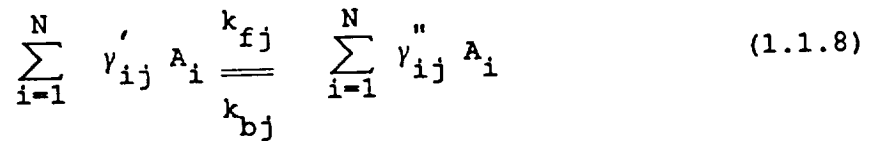
Auxiliary Relations:

$$P = \rho R T \sum_{n=1}^N \frac{Y_n}{W_n}, \quad \tau_{ij} = \mu \left(\frac{\partial U_i}{\partial x_j} + \frac{\partial U_j}{\partial x_i} - \frac{2}{3} \delta_{ij} \frac{\partial U_1}{\partial x_1} \right)$$

$$\sum_{n=1}^N Y_n = 1, \quad e_t = h - \frac{P}{\rho} + \frac{1}{2} U_j^2,$$

$$h_n = h_{f,n}^o + \int_{T_o}^T c_{p,n} dT, \quad h = \sum_{n=1}^N h_n Y_n$$

The chemical source terms depend on the particular chain of reactions taking place. Let a particular chain of reactions be represented by the following symbolic equation



$$j = 1, 2, \dots, J$$

where A_i is the chemical symbol for species i ; γ'_{ij} and γ''_{ij} are the constant stoichiometric coefficients for species i appearing as reactant and product, respectively, in reaction j , where there are J reaction steps decided by the chemical kinetics model chosen. The k 's denote Arrhenius rate constants that depend only on temperature for reactions in ideal gas mixtures. The species source terms are then given by

$$\dot{T}_n = \sum_{j=1}^J \dot{T}_{nj}$$

where

$$\dot{T}_{nj} = (\gamma''_{nj} - \gamma'_{nj}) k_{fj} \prod_{i=1}^N (\rho Y_i)^{\gamma'_{ij}} - (\gamma''_{nj} - \gamma'_{nj}) k_{bj} \prod_{i=1}^N (\rho Y_i)^{\gamma''_{ij}} \quad (1.1.9)$$

$$\text{and } k_{fj} = \beta_j T^{\alpha_j} \exp(-T_{aj}/T)$$

β_j and α_j are Arrhenius constants. T_{aj} is the activation temperature for the j th reaction step (Ref. 16).

1.2 Averaged Governing Equations

The system of equations presented here represents the instantaneous state of the system from an Eulerian point of view. The solution to this set requires a great deal of computing power to accurately resolve all of the important scales of the problem. One way of reducing the scales involved in the problem is the introduction of statistical ensemble averaging, which divides the flowfield into the mean quantities, which are ensemble-averaged, and the fluctuating quantities. The mean quantities are solutions of the averaged governing equations, which contain the correlations of the fluctuating quantities. The modeling of these unknown correlations is called the closure problem and often results in a larger, but more accessible, set of equations whose solution gives the variation of mean and correlated quantities in the flowfield. Density-weighted ensemble averaging is recommended for variable density flowfields (Ref. 5). Except for the density and pressure, which are not density weighted, any other field variable can be represented as

$$\Phi(\underline{x}, t) = \bar{\Phi}(\underline{x}, t) + \Phi''(\underline{x}, t) \quad (1.2.1)$$

$$\text{where } \bar{\Phi}(\underline{x}, t) = \overline{\rho(\underline{x}, t) \Phi(\underline{x}, t)} / \bar{\rho}(\underline{x}, t) \quad (1.2.2)$$

is a density-weighted mean and Φ'' is the fluctuating part. The averaged density $\bar{\rho}(\underline{x}, t)$ is defined by

$$\bar{\rho}(\underline{x}, t) = \lim_{N \rightarrow \infty} \frac{1}{N} \sum_{i=1}^N \rho_i(\underline{x}, t) \quad (1.2.3)$$

where N is the number of experimental repetitions, and the density is then given by $\rho(\underline{x}, t) = \bar{\rho}(\underline{x}, t) + \rho'(\underline{x}, t)$ where $\rho'(\underline{x}, t)$ is the fluctuating part.

In cases of stationary processes, the ergodic assumption allows the use of time averaging instead of ensemble averaging, and mean quantities will become independent of time. Application of the above decomposition to all dependent variables in the governing equations and the subsequent averaging results in the form of the equations given below.

Mass Conservation:

$$\frac{\partial \bar{\rho}}{\partial t} + \frac{\partial}{\partial x_i} (\bar{\rho} \bar{u}_i) = 0 \quad (1.2.4)$$

Species Conservation:

$$\frac{\partial}{\partial t} (\bar{\rho} \bar{Y}_n) + \frac{\partial}{\partial x_i} (\bar{\rho} \bar{u}_i \bar{Y}_n + \bar{\rho} \widetilde{u_i Y_n}) = \frac{\partial}{\partial x_i} (\bar{\rho} \bar{D}_n \frac{\partial \bar{Y}_n}{\partial x_i}) + \bar{\dot{T}}_n \quad (1.2.5)$$

$$n = 1, 2, \dots, N-1$$

Momentum Conservation:

$$\begin{aligned} \frac{\partial}{\partial t} (\bar{\rho} \bar{u}_i) + \frac{\partial}{\partial x_j} (\bar{\rho} \bar{u}_i \bar{u}_j + \bar{\rho} \widetilde{u_i u_j}) = & - \frac{\partial \bar{P}}{\partial x_i} + \bar{\rho} G_i \\ & + \frac{\partial}{\partial x_j} \left[\bar{\rho} \bar{\nu} \left(\frac{\partial \bar{u}_i}{\partial x_j} + \frac{\partial \bar{u}_j}{\partial x_i} - \frac{2}{3} \delta_{ij} \frac{\partial \bar{u}_1}{\partial x_1} \right) \right] \end{aligned} \quad (1.2.6)$$

$$i = 1, 2, 3$$

Energy Conservation:

$$\frac{\partial}{\partial t} (\bar{\rho} \bar{e}_t) + \frac{\partial}{\partial x_j} (\bar{\rho} \bar{U}_j \bar{e}_t + \overline{\rho U_j'' e_t''}) = - \frac{\partial}{\partial x_j} (\bar{P} \bar{U}_j + \overline{P U_j''}) + \bar{\rho} \bar{U}_j G_j \quad (1.2.7)$$

$$+ \frac{\partial}{\partial x_j} (\bar{\tau}_{ij} \bar{U}_i + \overline{\tau_{ij} U_i''}) + \frac{\partial}{\partial x_j} \left(\frac{\bar{k}}{\bar{c}_p} \frac{\partial \bar{h}}{\partial x_j} \right) + \frac{\partial}{\partial x_j} \left[\sum_{n=1}^N \frac{\bar{k}}{\bar{c}_p} (\bar{\rho} \bar{D}_n \bar{c}_p / \bar{k} - 1) \bar{h}_n \frac{\partial \bar{Y}_n}{\partial x_j} \right]$$

with the auxiliary relations:

$$\sum_{n=1}^N \bar{Y}_n = 1 \quad (1.2.8)$$

$$\bar{\rho} \bar{e}_t = \bar{\rho} \bar{h} + \frac{1}{2} \bar{\rho} \bar{U}_i^2 + \frac{1}{2} \bar{\rho} \overline{U_i''^2} - \bar{P} \quad (1.2.9)$$

$$\bar{h}_n = h_{f_n}^o + \frac{1}{\bar{\rho}} \left[\bar{\rho} \int_{T_o}^T c_{p_n}(T) dT \right] \quad (1.2.10)$$

$$\bar{h} = \sum_{n=1}^N (\bar{h}_n \bar{Y}_n + \overline{h_n'' Y_n''}) \quad (1.2.11)$$

$$\bar{P} = R \bar{\rho} \bar{T} \sum_{n=1}^N \left(\frac{\bar{Y}_n}{\bar{W}_n} + \frac{1}{\bar{T}} \frac{\overline{T'' Y_n''}}{\bar{W}_n} \right) \quad (1.2.12)$$

$$\bar{\dot{T}}_n = \sum_{j=1}^J \bar{\dot{T}}_{nj} \quad n = 1, 2, \dots, N \quad (1.2.13)$$

The $\bar{\dot{T}}_{nj}$ are obtained by averaging Equation (1.1.9).

There are two assumptions which are implicit in the above averaged equations. The first is that, in all of the conservation equations, the fluctuations of the molecular diffusivity can be neglected in comparison to the mixing created by velocity fluctuation throughout the turbulent region at high Reynolds numbers. Fluctuating molecular diffusion terms are also negligible in comparison to the mean diffusion effect in near-wall regions, since they approach zero in these regions. The second assumption is that the effect of thermodynamic fluctuations on the molecular properties of the mixture is negligible and molecular properties are evaluated at the mean thermodynamic values. Therefore,

$$\tilde{v} = v(\tilde{T})$$

$$\tilde{D}_n = D_n(\tilde{T})$$

$$\overline{\kappa/c_p} = \tilde{\kappa}/\tilde{c}_p = \kappa(\tilde{T})/c_p(\tilde{T})$$

This assumption is valid for molecular diffusion coefficients at high Reynolds numbers. However, the above approximation for specific heat at constant pressure can be inaccurate at high Mach numbers. Therefore, caution must be exercised in the application of this assumption to the evaluation of species' enthalpy as a temperature integral of the specific heat at constant pressure (see Equation 1.2.7).

1.3 Turbulence Closure Models

Upon examination of the set of averaged governing equations it becomes clear that there are a large number of unknown correlations that need to be modeled before the solution can be attempted. The conservation of momentum requires modeling of the Reynolds stress tensor, i.e., $U_i''U_j''$. Since the behavior of these terms has a major influence on the velocity field, their modeling constitutes the centerpiece of the turbulent flow structure. These terms are extensively studied for incompressible flowfields (Ref. 17). Several approaches to the modeling of Reynolds stresses in compressible flows will be presented in this section. These include second order Reynolds stress modeling, two-equation eddy viscosity k - ϵ modeling, and a zero-equation eddy viscosity modeling approach. The modeling of the other turbulent fluctuation correlation terms explicitly appearing in the averaged governing equations is dependent on the modeling of the Reynolds stresses and will be discussed in a later section.

1.3.1 Second Order Modeling

Reynolds stresses can be viewed as dependent variables and their values can be obtained directly by solving their transport equations. The exact transport equations for the Reynolds stresses can be obtained by multiplying the instantaneous momentum equation with a component of the velocity fluctuation and then taking a density-weighted average of the resulting equation. After some algebra, the following equation is obtained:

$$\begin{aligned}
\frac{\partial}{\partial t} (\bar{\rho} \widetilde{U_i'' U_j''}) + \frac{\partial}{\partial x_1} \left[\underbrace{\bar{\rho} \widetilde{U_1'' U_i'' U_j''}}_{(a)} + \underbrace{\bar{\rho} \widetilde{U_1'' U_i'' U_j''}}_{(b)} \right] = - \left[\underbrace{\bar{\rho} \widetilde{U_1'' U_j''}}_{(c)} \frac{\partial \bar{U}_i}{\partial x_1} + \bar{\rho} \widetilde{U_1'' U_i''} \frac{\partial \bar{U}_j}{\partial x_1} \right] \\
- \left[\underbrace{\overline{U_i'' \frac{\partial \bar{p}}{\partial x_j}} + \overline{U_j'' \frac{\partial \bar{p}}{\partial x_i}}}_{(d)} - \underbrace{\left[\overline{U_i'' \frac{\partial p'}{\partial x_j}} + \overline{U_j'' \frac{\partial p'}{\partial x_i}} \right]}_{(e)} + \frac{\partial}{\partial x_1} \left[\underbrace{\bar{\rho} \widetilde{U_1'' U_i'' U_j''}}_{(f)} \right] - \left[\underbrace{\overline{\tau_{1i} U_j''}}_{(g)} + \overline{\tau_{1j} U_i''} \right]
\end{aligned}
\tag{1.3.1}$$

Term (a) represents the transport of Reynolds stresses due to the mean motion of the flow and does not require any modeling at this level of closure. Term (b) represents the transport of Reynolds stresses due to velocity fluctuations and acts as a diffusive flux for the Reynolds stresses at high Reynolds numbers where the molecular diffusion will be negligible. The most widely used model for this term, suggested by Daly and Harlow (Ref. 18), is given as

$$- \bar{\rho} \widetilde{U_1'' U_i'' U_j''} = c_s' \bar{\rho} \frac{\tilde{q}}{\tilde{\epsilon}} \overline{U_1'' U_m''} \frac{\partial \widetilde{U_i'' U_j''}}{\partial x_m}
\tag{1.3.2}$$

where $\tilde{q} = \frac{1}{2} \overline{U_i'' U_i''}$ is the turbulent kinetic energy and $\tilde{\epsilon}$ is the rate of dissipation of turbulent kinetic energy. Note that the modeled form doesn't have the symmetry properties of the triple velocity correlations.

Term (c) in Equation (1.3.1) represents interaction between the mean and fluctuating motion which leads to exchanges of energy between the mean and the turbulent motion. This term is referred to as the turbulent production term and requires no modeling at this level of closure. Term (d) in Equation (1.3.1) is identically zero for constant density flows but is potentially very important for compressible flows with large pressure gradients, such as a shocked flowfield or a highly accelerated flow. The model suggested by Rubesin (Ref. 19) for $\overline{U_i''}$ is adopted here. This model is given by

$$\overline{U_i''} = \frac{1}{(n-1) c_p \tilde{T}} \tilde{U}_j \widetilde{U_i'' U_j''}
\tag{1.3.3}$$

where n is a polytropic coefficient ($n = 0$ for isobaric processes, $n = 1$ for isothermal processes, $n = c_p/c_v$ for isentropic processes, etc.) and c_p is the specific heat at constant pressure.

Term (e) represents the interaction between the fluctuating pressure gradient and fluctuating velocity field. It can be divided into two terms.

$$\overline{U_i'' \frac{\partial p'}{\partial x_j}} + \overline{U_j'' \frac{\partial p'}{\partial x_i}} = \frac{\partial}{\partial x_1} \left[\delta_{i1} \overline{U_j'' p'} + \delta_{j1} \overline{U_i'' p'} \right] - \overline{p' \left(\frac{\partial U_i''}{\partial x_j} + \frac{\partial U_j''}{\partial x_i} \right)} \quad (1.3.4)$$

The first term is interpreted as spatial transport of Reynolds stresses due to the pressure fluctuations and is lumped with the triple velocity correlations given by Equation (1.3.2). This pressure-induced diffusion term destroys the symmetric character of triple velocity correlations and makes the modeled form more appropriate. The combined term is modeled as

$$- \left[\overline{\rho U_1'' U_i'' U_j''} + \delta_{i1} \overline{U_j'' \rho'} + \delta_{j1} \overline{U_i'' \rho'} \right] = C_s' \bar{\rho} \frac{\tilde{q}}{\tilde{\varepsilon}} \overline{U_1'' U_m''} \frac{\partial \overline{U_i'' U_j''}}{\partial x_m} \quad (1.3.5)$$

The second term transfers energy from one component of the Reynolds stress tensor to another due to collision-like interaction of turbulent eddies. It represents the distribution mechanism between Reynolds stresses. The modeling of this term for chemically reacting flows has been considered in detail by Farshchi (Ref. 20). Neglecting the effect of heat release this model can be given as

$$\begin{aligned} \overline{p' \left(\frac{\partial U_i''}{\partial x_j} + \frac{\partial U_j''}{\partial x_i} \right)} = & -C_1 \bar{\rho} \frac{\tilde{\varepsilon}}{\tilde{q}} \left[\overline{U_i'' U_j''} - \frac{2}{3} \delta_{ij} \tilde{q} \right] - \frac{(C_2 + 8)}{11} \left[\Pi_{ij} - \frac{2}{3} \delta_{ij} \Pi \right] - \\ & \frac{(8C_2 - 2)}{11} \left[\Delta_{ij} - \frac{2}{3} \delta_{ij} \Pi \right] - \frac{(30C_2 - 2)}{55} \bar{\rho} \tilde{q} \left[\frac{\partial U_i''}{\partial x_j} + \frac{\partial U_j''}{\partial x_i} \right] \end{aligned} \quad (1.3.6)$$

$$- \bar{\rho} \frac{\partial \tilde{U}_1}{\partial x_1} \left[\frac{(6C_2 + 4)}{11} \overline{U_1'' U_j''} - \frac{(40C_2 + 12)}{55} \delta_{1j} \tilde{q} \right]$$

where

$$\pi_{ij} = -\bar{\rho} \left[\overline{U_i'' U_1'' \frac{\partial \tilde{U}_j}{\partial x_1}} + \overline{U_j'' U_1'' \frac{\partial \tilde{U}_i}{\partial x_1}} \right], \quad \pi = \frac{1}{2} \pi_{11} \quad \text{and} \quad \Delta_{ij} = -\bar{\rho} \left[\overline{U_i'' U_1'' \frac{\partial \tilde{U}_1}{\partial x_j}} + \overline{U_j'' U_1'' \frac{\partial \tilde{U}_1}{\partial x_i}} \right]$$

Term (f) represents molecular diffusion of Reynolds stresses. At high Reynolds numbers this term is negligible in comparison with the turbulent diffusion term given by Equation (1.3.5). However, near solid walls and in recirculating regions, where the Reynolds number is small, this term must be accounted for. It requires no modeling.

Term (g) is a viscous non-diffusive term which is related to the destruction of Reynolds stresses by viscous action. It represents transfer of turbulent kinetic energy to thermal energy by the viscous action. This interaction can take place only at very small scales of turbulent motion where molecular viscosity has a large role. Since at the small scales turbulent motion is isotropic, an isotropic model is chosen to represent this term, and it only effects the normal components of the Reynolds stress tensor. The total rate of dissipation for a Reynolds stress component is given as

$$\overline{\tau_{1i} \frac{\partial u_j''}{\partial x_1}} + \overline{\tau_{1j} \frac{\partial u_i''}{\partial x_1}} = \frac{2}{3} \tilde{\epsilon} \delta_{ij} \quad (1.3.7)$$

The quantity denoted by $\tilde{\epsilon}$ is the rate of turbulent kinetic energy dissipation by the molecular viscous action. This quantity can be combined with the powers of the turbulent kinetic energy to define the time or length scale of the energy containing turbulent fluctuations. A transport equation for the rate of turbulent kinetic energy dissipation will be developed here to complete this modeling approach.

The modeled Reynolds stress equation is then given by

$$\begin{aligned} \frac{\partial}{\partial t} (\bar{\rho} \overline{u_i'' u_j''}) + \frac{\partial}{\partial x_1} \left[(\bar{\rho} \bar{u}_1 \overline{u_i'' u_j''}) - \left[C'_s \bar{\rho} \frac{\tilde{q}}{\tilde{\epsilon}} \overline{u_1'' u_m''} \frac{\partial \overline{u_i'' u_j''}}{\partial x_m} + \bar{\mu} \frac{\partial \overline{u_i'' u_j''}}{\partial x_1} \right] \right] = \\ - \frac{2}{3} \bar{\rho} \tilde{\epsilon} \delta_{ij} - \left[\bar{\rho} \overline{u_1'' u_j''} \frac{\partial \bar{u}_i}{\partial x_1} + \bar{\rho} \overline{u_1'' u_i''} \frac{\partial \bar{u}_j}{\partial x_1} \right] - \left[\bar{u}_i'' \frac{\partial \bar{P}}{\partial x_j} + \bar{u}_j'' \frac{\partial \bar{P}}{\partial x_i} \right] \\ - C_1 \bar{\rho} \frac{\tilde{\epsilon}}{\tilde{q}} \left[\overline{u_i'' u_j''} - \frac{2}{3} \delta_{ij} \tilde{q} \right] - \frac{(C_2 + 8)}{11} \left[\Pi_{ij} - \frac{2}{3} \delta_{ij} \Pi \right] \\ - \frac{(8C_2 - 2)}{11} \left[\Delta_{ij} - \frac{2}{3} \delta_{ij} \Pi \right] - \frac{(30C_2 - 2)}{55} \bar{\rho} \tilde{q} \left[\frac{\partial \bar{u}_i}{\partial x_j} + \frac{\partial \bar{u}_j}{\partial x_i} \right] \\ - \bar{\rho} \frac{\partial \bar{u}_1}{\partial x_1} \left[\frac{(6C_2 + 4)}{11} \overline{u_i'' u_j''} - \frac{(40C_2 + 12)}{55} \delta_{ij} \tilde{q} \right] \end{aligned} \quad (1.3.8)$$

where $C'_s = 0.25$, $C_1 = 1.5$, $C_2 = 0.4$, and \bar{u}_i'' is given by Equation (1.3.3).

The last unknown remaining in the modelled Reynolds stress transport equation is the rate of turbulent kinetic energy dissipation, $\tilde{\varepsilon}$. An exact transport equation for $\tilde{\varepsilon}$ can be obtained from the Navier-Stokes equations (Ref. 21). A physical interpretation of the individual terms in $\tilde{\varepsilon}$ -equation for incompressible flows has been provided by Tennekes and Lumley (Ref. 22). However, none of the terms in this equation are accessible to measurement, making modeling of this equation very difficult. A well tested $\tilde{\varepsilon}$ -equation for incompressible flow is proposed by Launder et al. (Ref. 23). This equation for variable density flows, in density weighted form, is given as

$$\frac{\partial}{\partial t} (\bar{\rho} \tilde{\varepsilon}) + \frac{\partial}{\partial x_j} [(\bar{\rho} \tilde{U}_j \tilde{\varepsilon}) - \left[\mu \delta_{ij} + c_{\varepsilon} \bar{\rho} \frac{\tilde{q}}{\tilde{\varepsilon}} \overline{U_i'' U_j''} \right] \frac{\partial \tilde{\varepsilon}}{\partial x_i}] = -c_{\varepsilon 1} \bar{\rho} \frac{\tilde{\varepsilon}}{\tilde{q}} \overline{U_i'' U_j''} \frac{\partial \tilde{U}_i}{\partial x_j} \quad (1.3.9)$$

$$-c_{\varepsilon 2} \bar{\rho} \frac{\tilde{\varepsilon}}{\tilde{q}} \tilde{\varepsilon} + c_{\varepsilon 3} \bar{\rho} \tilde{v} \frac{\tilde{q}}{\tilde{\varepsilon}} \overline{U_j'' U_m''} \left[\frac{\partial^2 \tilde{U}_i}{\partial x_j \partial x_1} \right] \left[\frac{\partial^2 \tilde{U}_i}{\partial x_m \partial x_1} \right]$$

An exact transport equation for the dissipation rate of turbulent kinetic energy of compressible flowfields can also be derived (Ref. 24). As expected, such an equation is more complicated than its incompressible counterpart. However, it clearly suggests the contributions of the mean velocity divergence and the mean pressure gradient. The mean velocity divergence term is exact and requires no modeling. It is given as

$$- \frac{2}{3} \bar{\rho} \tilde{\varepsilon} \frac{\partial \tilde{U}_i}{\partial x_i}$$

The mean pressure gradient contribution is modeled as

$$c_{\varepsilon 3} \frac{\tilde{\varepsilon}}{\tilde{q}} \overline{U_i''} \frac{\partial \bar{p}}{\partial x_i}$$

consistent with a similar term in Reynolds stress Equation (1.3.8).

The final modeled transport equation for the rate of dissipation of turbulent kinetic energy in compressible flowfields is given as

$$\begin{aligned}
\frac{\partial}{\partial t} (\bar{\rho} \bar{\varepsilon}) + \frac{\partial}{\partial x_j} [(\bar{\rho} \bar{U}_j \bar{\varepsilon}) - [\bar{\mu} \delta_{ij} + C_{\varepsilon} \bar{\rho} \frac{\tilde{q}}{\bar{\varepsilon}} \overline{U_i'' U_j''}] \frac{\partial \bar{\varepsilon}}{\partial x_i}] &= -C_{\varepsilon 1} \bar{\rho} \frac{\bar{\varepsilon}}{\tilde{q}} \overline{U_i'' U_j''} \frac{\partial \bar{U}_i}{\partial x_j} \\
&- C_{\varepsilon 2} \bar{\rho} \frac{\bar{\varepsilon}}{\tilde{q}} \bar{\varepsilon} + C_{\varepsilon 3} \bar{\rho} \bar{v} \frac{\tilde{q}}{\bar{\varepsilon}} \overline{U_j'' U_m''} \left(\frac{\partial^2 \bar{U}_i}{\partial x_j \partial x_1} \right) \left(\frac{\partial^2 \bar{U}_i}{\partial x_m \partial x_1} \right) \\
&- C_{\varepsilon 4} \frac{\bar{\varepsilon}}{\tilde{q}} \frac{1}{(n-1) C_p \tilde{T}} \overline{U_j'' U_i'' U_j''} \frac{\partial \bar{P}}{\partial x_i} - \frac{2}{3} \bar{\rho} \bar{\varepsilon} \frac{\partial \bar{U}_i}{\partial x_i}
\end{aligned} \tag{1.3.10}$$

with

$$C_{\varepsilon} = 0.2, C_{\varepsilon 1} = 1.28, C_{\varepsilon 2} = 1.8, C_{\varepsilon 3} = 2.0, C_{\varepsilon 4} = 1.0.$$

The system of equations given by Equations (1.3.8) and (1.3.10) establishes a second order model for Reynolds stresses appearing in the mean momentum equations. There are seven equations for three-dimensional equations that must be solved simultaneously with the mean flow variables. Results from application of this model to a round jet hydrogen fuel will be presented in the next chapter.

1.3.2 Two-Equation Eddy Viscosity Modeling (k-ε)

At large Reynolds numbers the molecular diffusive forces are negligible in comparison to the convective forces, and the momentum equation is a balance between the convective terms and the gradient of turbulent shear stresses that appear as source terms. The numerical solution of this form of the momentum equations creates difficulties due to the lack of diagonal dominance of the matrices created by finite differencing of the equations (Ref. 25). This numerical integration difficulty plus the large number of equations that must be solved necessitates development and use of less complex and more numerically stable turbulence closure models. The turbulent eddy viscosity concept is used to define an apparent flow viscosity in terms of the mean flow variables and/or turbulent quantities representing time and length scale of turbulent energy containing motion. Next the Reynolds stresses are related to the gradient of the mean velocity field through the eddy viscosity concept (Ref. 26).

$$-\overline{\rho U_i'' U_j''} = \bar{\rho} \tilde{v}_t \left[\frac{\partial \bar{U}_i}{\partial x_j} + \frac{\partial \bar{U}_j}{\partial x_i} - \frac{2}{3} \delta_{ij} \frac{\partial \bar{U}_1}{\partial x_1} \right] - \frac{2}{3} \delta_{ij} \bar{\rho} \tilde{q} \tag{1.3.11}$$

In the k-ε modeling approach \tilde{v}_t is defined as

$$\tilde{v}_t = C_\mu \frac{\tilde{q}^2}{\tilde{\epsilon}} \quad (1.3.12)$$

where $C_\mu = 0.09$

Transport equations for \tilde{q} and $\tilde{\epsilon}$ are obtained, modeled, and solved to define \tilde{v}_t at every point in the flowfield. The modeling of $\tilde{\epsilon}$ equation was already discussed and a modelled $\tilde{\epsilon}$ equation given by Equation (1.3.10). The Reynolds stresses appearing in Equation (1.3.10) are replaced by their eddy viscosity model given by Equation (1.3.11). To obtain a modeled transport equation for the turbulent kinetic energy, \tilde{q} , one can simply contract the (i,j) indices in Reynolds stress Equation (1.3.8). The resulting equation is given as

$$\frac{\partial}{\partial t} (\bar{\rho} \tilde{q}) + \frac{\partial}{\partial x_j} \left[(\bar{\rho} \tilde{U}_j \tilde{q}) - \left(\bar{\mu} \delta_{ij} + C_s' \bar{\rho} \frac{\tilde{q}}{\tilde{\epsilon}} \widetilde{U_i'' U_j''} \right) \frac{\partial \tilde{q}}{\partial x_i} \right] =$$

$$-\bar{\rho} \tilde{\epsilon} - \bar{\rho} \widetilde{U_i'' U_j''} \frac{\partial \tilde{U}_i}{\partial x_j} - \frac{1}{(n-1) C_p \tilde{T}} \tilde{U}_j \widetilde{U_i'' U_j''} \frac{\partial \bar{P}}{\partial x_i}$$

Equations (1.3.13) and (1.3.10) along with the auxiliary relation for the Reynolds stresses given by Equation (1.3.11) and (1.3.12) constitute a k- ϵ turbulence model.

It is important to note that the above method of derivation of k- ϵ equations is based on the second order turbulence models developed for the Reynolds stress equations and has the advantage that the same constants as for the second order turbulence model can be used here. In addition, the turbulent diffusion coefficients in both k and ϵ equations have a second order tensorial nature, rather than a scalar behavior, and are given by $\bar{\rho} U_i'' U_j'' \tilde{q} / \tilde{\epsilon}$. In a homogeneous turbulent flowfield the eddy viscosity model for Reynolds stresses reduces to $U_i'' U_j'' = \frac{2}{3} \delta_{ij} \tilde{q}$ and the above diffusion coefficient reduces to

$$\frac{2}{3} \bar{\rho} \frac{\tilde{q}}{\tilde{\epsilon}} \delta_{ij} = \frac{2}{3 C_\mu} \bar{\rho} \tilde{v}_t \delta_{ij}$$

which is an isotropic model consistent with models used in traditional two-equation eddy viscosity models.

The k- ϵ model, given by Equations (1.3.9) and (1.3.13), is only valid away from solid walls. To extend the k- ϵ turbulence models to wall-bounded flowfields, many models have been suggested (Refs. 27 and 28). These models are based on the consideration of the behavior of the turbulent kinetic energy and eddy viscosity near a solid wall. A simple

Taylor series expansion of the fluctuating velocity components near a solid wall, $y = 0$, requires that $\tilde{q} \sim y^2$ and $\tilde{v}_t \sim y^3$ (Ref. 17, p. 96). To adjust the behavior of turbulent kinetic energy and its rate of dissipation near a solid wall, sink terms are added to their transport equations. Next the eddy viscosity is modified to include damping effects due to the presence of the solid wall. After detailed examination of several of these models, Jones and Launder Model (Ref. 29) and Chien Model (Ref. 30) were chosen for implementation in the flow solver.

To present the k - ε equations for both these models in a uniform and compact form, the normalized Reynolds stress is denoted by $\phi_{ij} \equiv \overline{U_i' U_j'} / \tilde{q}_1$ which, on using the eddy viscosity concept given by Equation (1.3.11), can be rewritten as

$$\phi_{ij} = -\frac{1}{\tilde{q}} \tilde{v}_t \left[\frac{\partial \tilde{U}_i}{\partial x_j} + \frac{\partial \tilde{U}_j}{\partial x_i} - \frac{2}{3} \delta_{ij} \frac{\partial \tilde{U}_1}{\partial x_1} \right] + \frac{2}{3} \delta_{ij} \quad (1.3.14)$$

Equations (1.3.13) and (1.3.10) for turbulent kinetic energy and its rate of dissipation are rewritten as

$$\frac{\partial}{\partial t} (\bar{\rho} \tilde{q}) + \frac{\partial}{\partial x_j} \left[\bar{\rho} \tilde{U}_j \tilde{q} - \bar{\rho} \left[\tilde{v} \delta_{ij} + \frac{C'_s}{C_\mu} \tilde{v}_t \phi_{ij} \right] \frac{\partial \tilde{q}}{\partial x_i} \right] = -\bar{\rho} \tilde{q} \phi_{ij} \frac{\partial \tilde{U}_i}{\partial x_j} \quad (1.3.15)$$

$$- \bar{\rho} \tilde{\varepsilon} - \frac{1}{(n-1) C_p \tilde{T}} \tilde{U}_j \tilde{q} \phi_{ij} \frac{\partial \bar{P}}{\partial x_i} - \tilde{S}_q$$

and

$$\frac{\partial}{\partial t} (\bar{\rho} \tilde{\varepsilon}) + \frac{\partial}{\partial x_j} \left[\bar{\rho} \tilde{U}_j \tilde{\varepsilon} - \bar{\rho} \left[\tilde{v} \delta_{ij} + \frac{C_\varepsilon}{C_\mu} \tilde{v}_t \phi_{ij} \right] \frac{\partial \tilde{\varepsilon}}{\partial x_i} \right] = -C_{\varepsilon 1} \bar{\rho} \tilde{\varepsilon} \phi_{ij} \frac{\partial \tilde{U}_i}{\partial x_j} \quad (1.3.16)$$

$$-C_{\varepsilon 2} \bar{\rho} \tilde{\varepsilon} \frac{\tilde{\varepsilon}}{\tilde{q}} - C_{\varepsilon 4} \tilde{\varepsilon} \frac{1}{(n-1) C_p \tilde{T}} \tilde{U}_j \phi_{ij} \frac{\partial \bar{P}}{\partial x_i} +$$

$$\frac{C_{\varepsilon 3}}{\tilde{q}} \bar{\rho} \tilde{v}_t \phi_{jm} \left[\frac{\partial^2 \tilde{U}_i}{\partial x_j \partial x_m} \right] \left[\frac{\partial^2 \tilde{U}_i}{\partial x_m \partial x_1} \right] - \frac{2}{3} \bar{\rho} \tilde{\varepsilon} \frac{\partial \tilde{U}_i}{\partial x_i} - \tilde{S}_\varepsilon$$

The value of the constants and the form of the sink terms are given in Table 1.

Model	C_μ	$C_{\epsilon 1}$	$C_{\epsilon 2} f_\epsilon$	$C_{\epsilon 3}$	\tilde{S}_q	\tilde{S}_ϵ
Chien's	$0.09 [1 - \exp(-0.0115y^+)]$	1.28	$1.8 [1.0 - \frac{2}{9} \exp(-Re_t^2/36)]$	0.0	$2\bar{\mu} \frac{\tilde{q}}{y^2}$	$2\bar{\mu} \frac{\tilde{\epsilon}}{y^2} \exp(-y^+/2)$
Jones-Launder	$0.09 \exp[-2.5/(1+0.02Re_t)]$	1.55	$2.0 [1.0 - 0.3 \exp(-Re_t^2)]$	2.0	$2\bar{\mu} \left[\frac{\partial \tilde{q}}{\partial y} \right]^{1/2}$	0

TABLE 1

with $C'_s = 0.25$, $C_\epsilon = 0.2$, and $C_{\epsilon 4} = 1.0$ for both models. The normal distance to a solid surface is denoted by y and $Re_t = \frac{\tilde{q}^2}{\nu \epsilon}$ denotes turbulent Reynolds number.

The turbulence models described here are intended for use in a supersonic reacting flowfield and should accurately reflect compressibility effects present in such flowfields. Except for density-weighted averaging of the governing equation and the mean velocity divergence terms appearing in the Reynolds stresses eddy viscosity equation, (1.3.14), and the dissipation equation, (1.3.16), the above models have no means of accounting for the compressibility and high Mach number effects. The prediction of the behavior of supersonic diffusion flames is particularly sensitive to the rate of turbulent mixing between the fuel and oxidizer streams. At supersonic speeds it has been shown that the convective Mach number of large eddy structures, in the mixing region between the two supersonic streams, substantially influences the rate of spreading of the mixing layer (Ref. 31). Zeman (Ref. 32) has introduced the "dilatation dissipation" as the extra compressibility term in the kinetic energy equation. He used a modeled shock wave structure within the turbulent eddies to obtain the functional form of the compressibility correction. This compressibility term contained two new modeling coefficients, one of them being the kurtosis of the turbulence. Appropriate values of these modeling coefficients were obtained by matching the computational result with the experimental data for the behavior of free shear layers presented in Ref. 31. The Zeman model for total dissipation is given as

$$\tilde{\epsilon}_{\text{tot}} = \tilde{\epsilon}(1 + C_d F(M_t)) \quad (1.3.17)$$

where

$$F(M_t) = \begin{cases} 1 - \exp\left[-\left(\frac{M_t - 0.1}{0.6}\right)^2\right] & \text{if } M_t \geq 0.1, \\ 0 & \text{otherwise} \end{cases} \quad (1.3.18)$$

$$M_t = \frac{\sqrt{2\tilde{q}}}{\tilde{a}} \text{ and } C_d = 0.75 \text{ (}\tilde{a} \text{ is the local speed of sound).}$$

$\tilde{\epsilon}$ is obtained from Equation (1.3.16) and $\tilde{\epsilon}_{\text{tot}}$ used in Equations (1.3.15) and (1.3.12) for the turbulent kinetic energy and eddy viscosity respectively. It is important to note that dilatation dissipation is functionally dependent on the local turbulent Mach number, M_t , and is not explicitly related to the convective Mach number of the large eddy structures in free shear layers. The application of this model to free and wall-bounded shear flows is considered in the next chapter.

1.3.3 Zero-Equation Eddy Viscosity Modeling

The lowest level of turbulence modeling can be achieved by expressing the turbulent eddy viscosity, $\tilde{\nu}_t$, in terms of the local turbulent time and length scales derived from the mean flowfield quantities (Ref. 26). Therefore, there are no turbulent quantities to solve for.

This is the simplest and numerically most stable method of turbulence modeling. However, the development of these models is highly dependent on the insight of the individual modeler, and their application is restricted to the simplest possible flowfields. For more complex flowfields an ad hoc combination of these models without any degree of universality is required. The physical insight used to develop these models makes them very powerful for simple flowfields and impossible to apply to complex ones.

One of the most successful models for wall-bounded shear flows is the Baldwin-Lomax model (Ref. 33), which is extensively used by many researchers. This model was implemented in the original version of the RPLUS code (Ref. 34) and does not require any further explanation. For free shear layers a simple Prandtl mixing length model is used. The Reynolds stresses are related to the mean velocity gradients according to Equation (3.11), and the turbulent eddy viscosity is given as

$$\tilde{\nu}_t = C_m \Delta \tilde{U} \delta \quad (1.3.19)$$

C_m is set to 0.01 for plane mixing layers and plane jets, and $\Delta \tilde{U}$ is the maximum velocity difference across the layer. For mixing layers δ is defined as the distance between points where the velocity differs from the free stream velocity by 5 percent of the maximum velocity difference across the layer. For symmetrical flows (jets, wakes), δ is double the distance from the symmetry axis to the point at which the velocity differs from the free stream velocity by 50% of the maximum velocity difference across the layer.

Zero-equation models were used in this work as a baseline model to evaluate the two-equation model performance for several flowfields. Some of these results will be discussed in the next chapter.

1.4 Finite Rate Reaction Closure Model

Given a model for Reynolds stresses, $\overline{\rho U_i'' U_j''}$, the modeling of the other turbulent fluctuation correlations appearing in the averaged governing equations (1.2.4 to 1.2.13) can be discussed along similar lines. Considering the mean total energy equation, (1.2.7), the first term to be modeled is the turbulent total energy flux term, $\overline{\rho U_j'' e_t''}$. Using the definition of total energy this term can be expanded as

$$\overline{\rho U_j'' e_t''} = \overline{\rho U_j'' h''} + \overline{\rho U_i'' U_i'' U_j''} + \frac{1}{2} \overline{\rho U_i''^2 U_j''} - \overline{P U_j''} \quad (1.4.1)$$

To model the first term on the right-hand side of the above equation one can assume (Ref. 17) that turbulent enthalpy fluctuations are caused by velocity field fluctuations and are dependent on the gradient of the mean enthalpy, such that

$$h'' = -U_i'' \frac{\partial \tilde{h}}{\partial x_i} \quad (1.4.2)$$

therefore

$$\overline{U_j'' h''} = \overline{U_j'' U_i''} \frac{\partial \tilde{h}}{\partial x_i} \quad (1.4.3)$$

The coefficient that changes this proportionality to an equality should have the dimensions of the turbulent time scale. Assuming that the turbulent time scale of the scalar fluctuations is directly proportional to the turbulent time scale of the velocity fluctuation, $\tilde{q}/\tilde{\epsilon}$, the above relation can be written as

$$\overline{\rho U_j'' h''} = -C_h \bar{\rho} \frac{\tilde{q}}{\tilde{\epsilon}} \overline{U_j'' U_i''} \frac{\partial \tilde{h}}{\partial x_i} \quad (1.4.4)$$

with $C_h = 0.36$. At the second-order Reynolds stress closure model level this equation represents a complete closure for the turbulent enthalpy flux term. However, if turbulent eddy viscosity models are used for Reynolds stresses, then Equations (1.3.11) and (1.3.12) and the definition of normalized Reynolds stresses can be used to represent the above equation as

$$\overline{\rho U_j'' h''} = -\sigma_h^{-1} \bar{\rho} \tilde{v}_t \phi_{ij} \frac{\partial \tilde{h}}{\partial x_i} \quad (1.4.5)$$

where $\sigma_h = C_\mu / C_h$. It is important to note that a simpler, but less general, model of this term can be presented as

$$\overline{\rho U_j'' h''} = -Pr_t^{-1} \bar{\rho} \tilde{v}_t \delta_{ij} \frac{\partial \tilde{h}}{\partial x_i} \quad (1.4.6)$$

which is an isotropic subset of the above model where $\phi_{ij} = \delta_{ij}$ and $\sigma_h = Pr_t$ is usually set equal to 0.7. This model is usually used in zero-equation turbulence models.

The second term on the right-hand side of Equation (1.4.1) does not require any modeling and is provided by one of the turbulence models discussed in Section 3. The modeling of the triple velocity fluctuation correlations appearing as the third term on the right-hand side of Equation (1.4.1) was already discussed and is given by Equation (1.3.2) which can be rewritten as

$$\frac{1}{2} \bar{\rho} \overline{U_i''^2 U_j''} = -\frac{C'_s}{C_\mu} \bar{\rho} \tilde{v}_t \phi_{ij} \frac{\partial \tilde{q}}{\partial x_i} \quad (1.4.7)$$

The last term on the right-hand side of Equation (1.4.1) cancels with another term, due to the pressure-velocity fluctuations correlation, on the right-hand side of the mean total energy equation, (1.2.7).

The next term to be modeled in the mean total energy equation, (1.2.7), is $\partial/\partial x_j(\overline{\tau_{ij}}\overline{U_i''})$. This is the total work done by viscous forces on the turbulent velocity fluctuations, and at high Reynolds numbers it is several orders of magnitude smaller than the viscous work done on the mean velocity field, $\partial/\partial x_j(\overline{\tau_{ij}}\overline{U_i})$. Therefore, it is neglected.

The species conservation equations, (1.2.5), contain the most difficult correlations to be modeled. Besides the fluctuation flux term, $\overline{U_i''Y_n''}$, which is modeled by relating it to the n^{th} species' mean mass fraction gradient, there are a number of correlations created by the nonlinear species source terms. These correlations are of the form $\overline{Y_\alpha''Y_\beta''}$, $\overline{T''Y_n''}$, $\overline{T''^2}$, ..., etc. There are few experimental determinations of these correlations which provide insight into their modeling. Equations (1.2.11) and (1.2.12) for the mixture enthalpy and the ideal gas relation also require determination of $\overline{h_n''Y_n''}$ and $\overline{T''Y_n''}$, respectively. The modeling approach taken here is to model the species turbulent flux term, $\overline{U_i''Y_n''}$, in a manner similar to the modeling of the turbulent enthalpy flux given by Equation (1.4.5). Therefore

$$\overline{\rho U_i''Y_n''} = -\sigma_y^{-1} \overline{\rho} \tilde{v}_t \delta_{ij} \frac{\partial \tilde{Y}_n}{\partial x_j} \quad (1.4.8)$$

where $\sigma_y = C_\mu/C_y$ and $C_y = 0.36$. An isotropic version of this model can also be obtained and is given by

$$\overline{\rho U_i''Y_n''} = -Sc_t^{-1} \overline{\rho} \tilde{v}_t \delta_{ij} \frac{\partial \tilde{Y}_n}{\partial x_j} \quad (1.4.9)$$

where $Sc_t = \sigma_y = 0.7$.

All other correlations in the species source terms, thermodynamic state equation, and other auxiliary relations are ignored and only mean thermo-chemical values are used in the calculation. This "laminar like" treatment of the thermo-chemistry aspect of the problem drastically reduces the complexity of the problem and in effect reduces all scales affecting the chemical reaction mechanisms to those decided by mean values. With such simplification one can consider a complex set of chemical kinetics relations, with many intermediate species and multiple reaction steps (Ref. 34). However, the exponential form of the chemical source terms makes them very sensitive to the effect of the neglected correlations. The modeling of the complete set of governing equation (1.2.4 to 1.2.13) for multi-species turbulent compressible reacting flowfields with finite rate kinetics chemistry is now completed. These equations can be solved for premixed flames as well as for diffusion flames depending on the specified initial and boundary conditions.

1.5 Nondimensionalization

Coordinate axes and all the flow variables in the modeled governing equations can be non-dimensionalized with free stream flow properties and geometrical dimensions. Such nondimensionalization is not required for the numerical solution of the equations; however, it introduces well known nondimensionalized parameters, such as Reynolds number, into the equations making it easier to compare geometrically similar flowfields. At least two thermodynamic properties of the free stream are needed to nondimensionalize the flow variables. Density and temperature are used here.

If the free stream flow variables at the inflow region are designated by ∞ subscript and the characteristic geometrical length scale of the problem is given by L , then the coordinate axes are nondimensionalized by L and time is nondimensionalized by L/a_∞ . The nondimensionalized flow variables are given as:

$$\rho = \frac{\bar{\rho}}{\rho_\infty}, \quad U_i = \frac{\tilde{U}_i}{a_\infty}, \quad P = \frac{\bar{P}}{\rho_\infty a_\infty^2}, \quad T = \frac{\bar{T}}{T_\infty}, \quad e_t = \frac{\tilde{e}_t}{a_\infty^2}, \quad h = \frac{\tilde{h}}{a_\infty^2}, \quad Y_n = \tilde{Y}_n$$

$$c_p = \frac{\tilde{c}_p}{\gamma_\infty R_\infty}, \quad c_v = \frac{\tilde{c}_v}{\gamma_\infty R_\infty}, \quad \mu = \frac{\bar{\mu}}{\mu_\infty}, \quad D_n = \frac{\tilde{D}_n}{D_\infty}, \quad \kappa = \frac{\kappa}{\kappa_\infty}, \quad R = \frac{R \sum_{n=1}^N \tilde{Y}_n}{\gamma_\infty R_\infty}$$

$$\dot{T}_n = \frac{L}{\rho_\infty a_\infty} \dot{\tilde{T}}_n, \quad v_t = \frac{v_t}{\mu_\infty / \rho_\infty}, \quad q = \frac{\tilde{q}}{a_\infty^2}, \quad \varepsilon = \frac{\tilde{\varepsilon}}{\left(\frac{\mu_\infty}{\rho_\infty}\right) \left(\frac{a_\infty}{1}\right)^2}, \quad \text{and} \quad \left[\widetilde{U''_i U''_j}\right]_N = \frac{\widetilde{U''_i U''_j}}{a_\infty^2}$$

where

$$a_\infty^2 = \gamma_\infty R_\infty T_\infty, \quad R_\infty = R \sum_{n=1}^N (c_p \tilde{Y}_n)_\infty, \quad c_{p_\infty} = R \sum_{n=1}^N (c_p \tilde{Y}_n)_\infty, \\ c_{v_\infty} = c_{p_\infty} - R_\infty, \quad \gamma_\infty = c_{p_\infty} / c_{v_\infty}, \quad D_\infty = L a_\infty$$

μ_∞ and κ_∞ are molecular viscosity and conductivity evaluated at free stream temperature and density.

Introducing;

$$Re_{\infty} = \frac{\rho_{\infty} La_{\infty}}{\mu_{\infty}}, \quad Sc_{\infty} = \frac{\mu_{\infty}}{\rho_{\infty} D_{\infty}}, \quad Pr_{\infty} = \frac{\mu_{\infty}}{\kappa_{\infty} c p_{\infty}}, \quad \text{and} \quad Le_{\infty} = \frac{\kappa_{\infty}/c p_{\infty}}{\rho_{\infty} D_{\infty}},$$

(here $Re_{\infty} Sc_{\infty} = 1$ since $D_{\infty} = La_{\infty}$).

The complete modeled and nondimensionalized system of equations is given as

Mass Conservation:

$$\frac{\partial \rho}{\partial t} + \frac{\partial}{\partial x_j} (\rho U_j) = 0 \quad (1.5.1)$$

Species Conservation:

$$\frac{\partial}{\partial t} (\rho Y_n) + \frac{\partial}{\partial x_j} \left[\rho U_j Y_n - (Sc_{\infty} Re_{\infty})^{-1} \rho (D_n \delta_{ij} + v_t SC_{\infty} \sigma_y^{-1} \phi_{ij}) \frac{\partial Y_n}{\partial x_i} \right] = \dot{T}_n \quad (1.5.2)$$

$n = 1, 2, \dots, N-1$

Momentum Conservation:

$$\frac{\partial}{\partial t} (\rho U_i) + \frac{\partial}{\partial x_j} [\rho U_j U_i + \delta_{ij} P - (\tau_{ij} + \tau_{t_{ij}})] = \rho G_j \quad (1.5.3)$$

$i = 1, 2, 3$

Energy Conservation:

$$\begin{aligned} \frac{\partial}{\partial t} (\rho e_t) + \frac{\partial}{\partial x_j} [\rho U_j e_t + U_j P - U_i (\tau_{ij} + \tau_{t_{ij}}) - \\ (Pr_{\infty} Re_{\infty})^{-1} \frac{1}{(\gamma_{\infty} - 1)} \left(\kappa \delta_{ij} + c_p (\gamma_{\infty} - 1) Pr_{\infty} \rho v_t \sigma_h^{-1} \phi_{ij} \right) \frac{\partial T}{\partial x_i} \\ - Re_{\infty} \left[\rho v \delta_{ij} + \rho v_t \sigma_k^{-1} \phi_{ij} \right] \frac{\partial q}{\partial x_i} + \\ \sum_{n=1}^N \left[\rho D_n \delta_{ij} + Re_{\infty}^{-1} \rho v_t \sigma_h^{-1} \phi_{ij} \right] h_n \frac{\partial Y_n}{\partial x_i}] = \rho U_j G_j \end{aligned} \quad (1.5.4)$$

with the auxiliary relations

$$\sum_{n=1}^N Y_n = 1 \quad (1.5.5)$$

$$\rho e_t = \rho h + \frac{1}{2} \rho U_i^2 + \rho q - p \quad (1.5.6)$$

$$h_n = h_{fn}^{\circ} + \int_{T_0}^T c_{p_n}(T) dt \quad (1.5.7)$$

$$h = \sum_{n=1}^N h_n Y_n \quad (1.5.8)$$

$$P = \rho RT \quad (1.5.9)$$

$$\tau_{ij} = Re_{\infty}^{-1} \rho v \left(\frac{\partial U_i}{\partial x_j} + \frac{\partial U_j}{\partial x_i} - \frac{2}{3} \delta_{ij} \frac{\partial U_1}{\partial x_1} \right) \quad (1.5.10)$$

$$\tau_{t_{ij}} = -\rho \left[\widetilde{U_i'' U_j''} \right]_N \quad (1.5.11)$$

$$\delta_{ij} = - \frac{\tau_{t_{ij}}}{\rho q} \quad (1.5.12)$$

For turbulent eddy viscosity type turbulence models the nondimensionalized shear stresses are given as

$$-\rho \left[\widetilde{U_i'' U_j''} \right]_N = Re_{\infty}^{-1} \rho v_t \left(\frac{\partial U_i}{\partial x_j} + \frac{\partial U_j}{\partial x_i} - \frac{2}{3} \delta_{ij} \frac{\partial U_1}{\partial x_1} \right) - \frac{2}{3} \delta_{ij} \rho q \quad (1.5.13)$$

where

$$v_t = \text{Re}_\infty^2 C_\mu \frac{q^2}{\varepsilon} \quad (\text{for } k-\varepsilon \text{ model}) \quad (1.5.14)$$

or

$$v_t = \text{Re}_\infty c_m \Delta U \delta \quad (\text{for Prandtl-Mixing Layer Model}) \quad (1.5.15)$$

The set of Equations (1.5.1) to (1.5.12) is independent of the level of turbulence closure model used for Reynolds stresses and can be solved with the second-order Reynolds stress model, the two-equation $k-\varepsilon$ model, or the zero-equation mixing layer model discussed in Section 3. This general form of the mean conservation equations allows development of a numerical solver for the mean flowfield which is independent of the turbulence model used. The second-order Reynolds stress model provides nondimensionalized turbulent stresses, required in Equation (1.5.11), directly. The eddy viscosity turbulence models use Equations (1.5.13) and (1.5.14) or (1.5.15) to provide the Reynolds stresses. If a zero-equation model is used, then the turbulent kinetic energy should either be related to the dominant turbulent shear stress algebraically or its appearance be ignored in all of the preceding equations, with $\delta_{ij} = \delta_{ij}$.

The normalized $k-\varepsilon$ equations are given by

$$\frac{\partial}{\partial t}(\rho q) + \frac{\partial}{\partial x_j} \left[\rho U_j q - \text{Re}_\infty^{-1} \rho \left(v \delta_{ij} + \sigma_k^{-1} v_t \delta_{ij} \right) \frac{\partial q}{\partial x_i} \right] = -\text{Re}_\infty^{-1} \rho \varepsilon \quad (1.5.16)$$

$$- \rho q \delta_{ij} \frac{\partial U_i}{\partial x_j} - \frac{1}{(n-1) c_p T} \tilde{U}_j q \delta_{ij} \frac{\partial P}{\partial x_i} - \text{Re}_\infty^{-1} S_q$$

$$\frac{\partial}{\partial t}(\rho \varepsilon) + \frac{\partial}{\partial x_j} \left[\rho U_j \varepsilon - \text{Re}_\infty^{-1} \rho \left(v \delta_{ij} + \sigma_\varepsilon^{-1} v_t \delta_{ij} \right) \frac{\partial \varepsilon}{\partial x_i} \right] = -C_{\varepsilon 1} \rho \varepsilon \delta_{ij} \frac{\partial U_i}{\partial x_j}$$

$$- \text{Re}_\infty^{-1} C_{\varepsilon 2} f_\varepsilon \rho \frac{\varepsilon}{q} - C_{\varepsilon 4} \frac{1}{(n-1) c_p T} U_j \delta_{ij} \frac{\partial P}{\partial x_i} + \quad (1.5.17)$$

$$\text{Re}_\infty^{-1} \frac{C_{\varepsilon 3}}{C_\mu} \rho v v_t \delta_{jm} \left[\frac{\partial U_i}{\partial x_j \partial x_1} \right] \left[\frac{\partial U_i}{\partial x_m \partial x_1} \right] - \frac{2}{3} \rho \varepsilon \frac{\partial U_i}{\partial x_i} - \text{Re}_\infty^{-1} S_\varepsilon$$

The nondimensionalized form of the near wall functions, given in Table 1, remain unchanged when the nondimensionalized quantities are used. The turbulent Reynolds number is given by $Re_t = Re_\omega^2 q^2 / (\nu \epsilon)$.

The complete set of constants associated with the k- ϵ turbulence model are given by $\sigma_y = C_\mu / C_y$, $\sigma_h = C_\mu / C_h$, $\sigma_k = C_\mu / C'_s$, $\sigma_\epsilon = C_\mu / C_\epsilon$, with $C_\mu = 0.9$, $C_y = C_h = .36$, $C'_s = .25$, $C_\epsilon = .2$, and those give in Table 1.

The complete two-dimensional expansion of the mean conservation equations and k- ϵ equations and their respective flux Jacobians are presented in Appendix A.

1.6 PDF Combustion Closure Model

The complexities of physical phenomena in a turbulent chemically reacting compressible flow suggest that there is no one method of modeling superior in all applications. Depending on the nature of the time scales involved in the chemical reaction and the flowfield, an appropriate approach may be to design models that are best suited to the particular physical circumstances under consideration. However, ideally one is looking for a comprehensive approach that would lead to simpler models in extreme cases. A hybrid stochastic modeling technique is introduced here as a general approach for the modeling of such problems. This modeling technique couples the time-averaged compressible flow equations with a probability density function formulation for the chemical reactions. The advantage of this method is that it treats chemical source terms and the state equations in a turbulent flowfield consistently, and more accurately, than standard approaches.

The basic idea behind the hybrid stochastic model is to solve the time-averaged mass, momentum, and energy conservation equations with standard numerical methods and obtain the chemical reaction solution from a stochastic model, instead of solving the time-averaged species conservation equations. This method's requirements can be summarized as follows:

- (a) A PDF model for chemical reactions.
- (b) Two-equation or higher order turbulence model for the flowfield.
- (c) A coupling between mean flowfield and thermo-chemical variables.

A general PDF transport equation model will provide a detailed analysis of ignition, flame holding, and blow out and will predict NOX formation (Ref. 11). However, development of an advanced PDF model, which requires a lot of CPU time for the solution of the PDF transport equation, should be based on the insight obtained from simpler PDF models. In this section, an assumed PDF reaction model for supersonic turbulent diffusion

flames will be developed. This model is a special case of the general hybrid stochastic model.

1.6.1 Reaction Mechanism

The assumed PDF reaction model developed here is based on the shifting equilibrium reaction mechanism (Ref. 9). This reaction mechanism requires a very fast rate of chemical reaction, which results in elimination of chemical source terms and the effect of large temperature fluctuations on them. In flow regions where it is known that the rate of reaction is very fast, and mixing controls the reaction process, this model along with an adequate turbulence model can accurately predict the flowfield. The mixing process and the transport of all species are represented in terms of the transport of a single conserved scalar. There are several scalar variables which are conserved in a chemical reaction and can be used as a basis for describing the mixing in a nonpremixed reacting flowfield. The mass fraction of a given element is such a variable. A normalized conserved scalar is referred to as the mixture fraction. To obtain a transport equation for the mixture fraction from the species transport equations, the assumption of uniform molecular diffusivity is required (Ref. 9). This assumption is not generally valid, but in turbulent flowfields the mixing done by turbulent eddies is several orders of magnitude larger than molecular mixing. Therefore, one can ignore molecular mixing in this context, to justify this assumption.

1.6.2 Laminar Flow Reaction Closure

Before discussing the role of the PDF model in a turbulent reaction, let us first see how the shifting equilibrium reaction model and the mixture fraction concept help to simplify the solution of a laminar supersonic combustion problem. With the shifting equilibrium model, chemical equilibrium is achieved instantly whenever mixing requires a shift in the composition. This means the reaction takes place instantaneously as soon as reactants come together in stoichiometric proportions at the atomic level. Thus the composition of the mixture at a given point at any particular instant of time is assumed to be the same as if the mixture were isolated and allowed to come to chemical equilibrium. At this local equilibrium the reaction takes place at stoichiometric proportions. Therefore given density, ρ , internal energy, e , mixture fraction, ϕ , and the possible reaction products, one can obtain temperature, pressure, and species mass fractions using a chemical equilibrium calculation code such as STANJAN (Ref. 35) or CEC (Ref. 36).

This reaction model eliminates species conservation equations and reduces the set of transport equations to conservation of mass, momentum, total energy, and mixture fraction. The solution vector of this set in a two-dimensional case is $(\rho, \rho u, \rho v, \rho e, \rho \phi)$. Given this solution vector, pressure, temperature, and species mass fractions can be obtained from a chemical equilibrium calculation. Since the chemical equilibrium calculation has to be repeated at every point in space and time, it can be very expensive. However, chemical equilibrium calculations need only be done once to create tables representing pressure,

temperature, and species mass fractions in terms of density, internal energy, and the mixture fraction, i.e.,

$$P = P(\rho, e, \phi) \quad (1.6.1a)$$

$$T = T(\rho, e, \phi) \quad (1.6.1b)$$

$$Y_i = Y_i(\rho, e, \phi) \quad (1.6.1c)$$

These tables can be used during the flowfield calculation to look up thermodynamic properties. The above functional relationships depend on the specifics of a physical problem and the maximum and the minimum values that density and internal energy attain. To illustrate the form of these multi-dimensional functions, an equilibrium reaction of pure hydrogen at 300° K with air at 1200° K is considered. Figures 1.1 through 1.3 show variations of pressure, temperature, and hydrogen mass fraction with respect to normalized values of mixture fraction and internal energy at a normalized density of one half. Density and internal energy are normalized by their maximum and minimum values.

1.6.3 Turbulent Flow Reaction Closure

The density-weighted averaged form of the transport equations governing the behavior of variable density turbulent flows is used to obtain the averaged solution vector $(\bar{\rho}, \bar{\rho}u, \bar{\rho}v, \bar{\rho}e, \bar{\rho}\phi)$. This averaged solution vector can no longer be directly related to the thermodynamic results obtained from the chemical equilibrium calculations because Equations (1.6.1a) to (1.6.1c) are instantaneous, rather than averaged, relations between pressure, temperature, and species mass fractions and density, internal energy, and mixture fraction. Thus, to obtain the mean values of pressure, temperature, and species mass fractions a closure model is required to relate the statistical averages of these thermodynamic quantities to the statistical mean values of density, internal energy, and mixture fraction through the chemical equilibrium relations.

Introduction of the joint PDF of the density, internal energy, and mixture fraction can bridge the gap between the instantaneous values of these three quantities and the mean values of the other thermodynamic quantities which depend on them. Let $g(\rho, e, \phi)$ denote the joint PDF of density, internal energy, and mixture fraction. Then (Ref. 39)

$$\bar{p} = \int_0^1 \int_0^\infty \int_0^\infty p(\rho, e, \phi) g(\rho, e, \phi) d\rho de d\phi \quad (1.6.2a)$$

$$\bar{T} = \frac{1}{\bar{\rho}} \int_0^1 \int_0^\infty \int_0^\infty \rho T(\rho, e, \phi) g(\rho, e, \phi) d\rho de d\phi \quad (1.6.2b)$$

$$\bar{Y}_i = \frac{1}{\bar{\rho}} \int_0^1 \int_0^\infty \int_0^\infty \rho Y_i(\rho, e, \phi) g(\rho, e, \phi) d\rho de d\phi \quad (1.6.2c)$$

The general form of the joint PDF depends not only on flow conditions but also on chemical reactions and heat release and varies from point to point in the flowfield. Theoretically, one can obtain this function from extensive experimental measurements or from direct solution of its transport equation (Ref. 11 & 37). However, both these methods are quite complicated and expensive in terms of manpower and computer time. Direct solution of the joint PDF's transport equation will be discussed in detail in Chapter 4. Here an attempt is made to represent the joint PDF in terms of known functions of the mean values of its three variables and the variance of the mixture fraction.

1.6.4 Assumed PDF

The simplest method of developing an assumed form of a joint PDF of three random variables is to use separation of variables, which is equivalent to statistical independence, and represent the joint PDF in terms of the product of three independent functions. However, in a reacting flow ρ , e , and ϕ are not independent, and it is essential to have a simple form of the joint PDF that retains the coupling between these variables. Therefore, the assumed form of the joint PDF should provide for possible single point correlations between its variables. This means that the assumed joint PDF can not be represented in terms of three independent functions of the primitive variables ρ , e , and ϕ (Ref. 38). To maintain the coupling between the variations of the random variables in the assumed joint PDF, this function will be expressed in terms of three functions of new primitive variables. Each of the new variables will be related to the original random variables. Therefore, the joint PDF can be represented as

$$g(\rho, e, \phi) = f_1(\rho^*) f_2(e^*) f_3(\phi^*) \quad (1.6.3)$$

At the present time the goal is to come up with the simplest model that satisfies the above objectives and is consistent with the models used for subsonic diffusion flames. In subsonic cases the above joint PDF reduces to a single variable PDF for the mixture fraction (Ref. 9). A clipped Gaussian distribution or a Beta function has been found to adequately represent the form of the mixture fraction's PDF in subsonic diffusion flames (Ref. 15). This

requires that ϕ^* be chosen to be identical to ϕ . Also, the domain of the joint PDF must be examined for the feasibility of using a clipped Gaussian or Beta function distribution to represent $f_3(\phi)$. Figure 1.4 represents an example of the domain of the joint PDF of density and mixture fraction. Internal energy has been set to a particular value, since four dimensional geometry can not be presented on a graph. It is noted that the mixture fraction always varies from zero, at pure oxidizer, to one, at pure fuel. However, density ranges from a minimum value, $\rho_1(\phi)$, to a maximum value, $\rho_2(\phi)$, for a given value of the mixture fraction if a given range of pressures is to be covered. The joint PDF is only defined in this domain. In this figure it is also noted that if an arbitrary path along a fixed value of density is chosen, the PDF is not defined for the full range of values of the mixture fraction. Known functions such as clipped Gaussian or the Beta function are not suitable for the representation of such forms of the mixture fraction PDF. However, there are other possible paths along which the mixture fraction PDFs are defined for the whole range of the mixture fraction values, as shown in Figure 1.5. To obtain a domain in which the mixture fraction's PDF is defined for the full range of the mixture fraction values at any given value of density, a normalized value of density given by

$$\rho^* = \frac{\rho - \rho_1(\phi)}{\rho_2(\phi) - \rho_1(\phi)} \quad (1.6.4)$$

is chosen. Figure 1.6 represents such a domain. Similar normalization of the internal energy results in transformation of the original joint PDF to the function $g(\rho^*, e^*, \phi)$ with the domain

$$\{(\rho^*, e^*, \phi): 0 \leq \rho^* \leq 1, 0 \leq e^* \leq 1, 0 \leq \phi \leq 1\} \quad (1.6.5)$$

where

$$e^* = \frac{e - e_1(\phi)}{e_2(\phi) - e_1(\phi)} \quad (1.6.6)$$

The new normalized variables are now also dependent on the mixture fraction. Thus, separation of the joint PDF into three functions of these variables maintains the coupling of the original variables.

Next, it is assumed that the dependence of the joint PDF on the normalized density and internal energy can be approximated, to the first order, by Dirac delta functions centered at the mean of these variables. This approximation is motivated by the fact that the only known moments related to these random variables are the means of the density and internal energy provided from solution of the mean flowfield. The Dirac delta function is the only appropriate choice for the representation of a random variable whose only known moment is its mean value (Ref. 39). The joint PDF can now be approximated by the following form:

$$g(\rho^*, e^*, \phi) = \delta(\rho^* - \langle \rho^* \rangle) \delta(e^* - \langle e^* \rangle) f_3(\phi) \quad (1.6.7)$$

The function f_3 must be chosen such that

$$\int_0^1 \int_{e_1}^{e_2} \int_{\rho_1}^{\rho_2} g(\rho, e, \phi) d\rho de d\phi = 1 \quad (1.6.8)$$

It is also suggested that the mixture fraction PDF, $f_3(\phi)$, be given in terms of a new function, $\tilde{f}(\phi)$, such that

$$\tilde{\phi} = \frac{\langle \rho \phi \rangle}{\langle \rho \rangle} = \int_0^1 \phi \tilde{f}(\phi) d\phi \quad (1.6.9)$$

where $\langle \rangle$ are used interchangeably with overbars to denote ensemble average value. This condition is not required and is only used to simplify manipulations and integrations required for the determination of density-weighted quantities. The final form of the joint PDF is given as

$$g^*(\rho^*, e^*, \phi) = \frac{\delta(\rho^* - \langle \rho^* \rangle)}{[\rho_2(\phi) - \rho_1(\phi)]} \frac{\delta(e^* - \langle e^* \rangle)}{[e_2(\phi) - e_1(\phi)]} \quad (1.6.10)$$

$$\frac{\langle \rho \rangle}{\langle \rho^* \rangle [\rho_2(\phi) - \rho_1(\phi)] + \rho_1(\phi)} \tilde{f}(\phi)$$

The only remaining task is to choose an appropriate form for the PDF of the mixture fraction, $\tilde{f}(\phi)$. Both clipped Gaussian and Beta functions can be used. Here the Beta function form is chosen based on the ease of its application. This function is given as

$$\tilde{f}(\phi) = \frac{\phi^{a-1} (1 - \phi)^{b-1}}{\int_0^1 \phi^{a-1} (1 - \phi)^{b-1} d\phi} \quad (1.6.11)$$

with

$$a = \bar{\phi} \left[\frac{\bar{\phi}(1 - \bar{\phi})}{\overline{\phi'^2}} - 1 \right] , \quad (1.6.11a)$$

$$b = (1 - \bar{\phi}) \left[\frac{\bar{\phi}(1 - \bar{\phi})}{\overline{\phi'^2}} - 1 \right] \quad (1.6.11b)$$

where $\overline{\phi'^2}$ is the variance of the mixture fraction.

The Beta function takes a variety of shapes depending on the value of the exponents a and b , which are dependent on the mean and the variance of the mixture fraction. Given $\bar{\phi}$ and $\overline{\phi'^2}$, exponents of the Beta function require that the assumed PDF matches at least the mean and the variance of the real PDF exactly.

The above assumed PDF requires the knowledge of the variance of the mixture fraction. An equation governing the transport of the mixture fraction variance is used to obtain its value in the flowfield. This equation will be discussed in more detail in the next section.

Utilizing the above assumed joint PDF, the mean density and density-weighted mean internal energy are given as

$$\langle \rho \rangle^{-1} = \int_0^1 \frac{\bar{f}(\phi)}{\langle \rho^* \rangle (\rho_2 - \rho_1) + \rho_1} d\phi \quad (1.6.12)$$

$$\bar{e} = \frac{\langle \rho e \rangle}{\langle \rho \rangle} = \int_0^1 [\langle e^* \rangle (e_2 - e_1) + e_1] \bar{f}(\phi) d\phi \quad (1.6.13)$$

which reduces to

$$\bar{e} = \langle e^* \rangle [\bar{e}_2 - \bar{e}_1] + \bar{e}_1 \quad (1.6.13a)$$

where

$$\bar{e}_i(\phi) = \int_0^1 e_i(\phi) \bar{f}(\phi) d\phi \quad i=1,2 \quad (1.6.13b)$$

If $\psi(\rho, e, \phi)$ denotes any thermodynamic quantity, its density-weighted and unweighted mean values are given as

$$\bar{\psi} = \int_0^1 \psi(\langle \rho^* \rangle, \langle e^* \rangle, \phi) \tilde{f}(\phi) d\phi \quad (1.6.14)$$

and

$$\bar{\psi} = \int_0^1 \psi(\langle \rho^* \rangle, \langle e^* \rangle, \phi) \frac{\langle \rho \rangle}{\langle \rho^* \rangle (\rho_2 - \rho_1) + \rho_1} \tilde{f}(\phi) d\phi \quad (1.6.15)$$

1.6.5 Mean Thermodynamic Variables

At this point let us briefly review the procedures for obtaining the required mean values of a thermodynamic variable from the above assumed PDF model:

Step 1. The values of $\bar{\rho}$, \tilde{e} , $\tilde{\phi}$, and $\widetilde{\phi'^2}$ are directly obtained from the mean flowfield solution, i.e., $(\bar{\rho}, \bar{\rho}u, \bar{\rho}v, \bar{\rho}e, \bar{\rho}\phi, \bar{\rho}\phi'^2)$.

Step 2. Given $\tilde{\phi}$ and ϕ'^2 , the mixture fraction PDF, $\tilde{f}(\phi)$, is calculated.

Step 3. Given $\bar{\rho}$ and \tilde{e} and using the thermodynamic tables obtained from chemical equilibrium calculations, $\langle e^* \rangle$ and $\langle \rho^* \rangle$ are obtained from Equations (1.6.12) and (1.6.13).

Step 4. Thermodynamic tables are interpolated to determine the desired quantity at $\langle \rho^* \rangle$ and $\langle e^* \rangle$, i.e. $\psi(\langle \rho^* \rangle, \langle e^* \rangle, \phi)$.

Step 5. Given the above information, Equation (1.6.14) or (1.6.15) is used to obtain the desired mean of the thermodynamic variable.

1.6.6 Mixture Fraction's Mean and Variance

A transport equation for the mixture fraction can be obtained from the species transport equations (Ref. 9). The density-averaged form of this equation is given as

$$\frac{\partial}{\partial t} (\bar{\rho} \tilde{\phi}) + \frac{\partial}{\partial x_j} \left[\bar{\rho} \tilde{u}_j \tilde{\phi} + \bar{\rho} \widetilde{u_j \phi} \right] = \frac{\partial}{\partial x_j} \left[\bar{\rho} \tilde{D} \frac{\partial \tilde{\phi}}{\partial x_j} \right] \quad (1.6.16)$$

Consistent with the turbulence modeling approach used in previous sections, it is assumed that mixture fraction fluctuations are caused by the turbulent velocity field fluctuations and are proportional to the gradient of the mean mixture fraction. Assuming that the characteristic time of the turbulent mixing of scalar quantities is that of the turbulent velocity field, the following model can be presented for the mixture fraction turbulent flux term

$$\overline{\rho U_i'' \phi''} = -\sigma_\phi^{-1} \bar{\rho} \tilde{v}_t \delta_{ij} \frac{\partial \tilde{\phi}}{\partial x_j} \quad (1.6.17)$$

The modeled nondimensionalized mixture fraction transport equation is then given as

$$\frac{\partial}{\partial t}(\rho \tilde{\phi}) + \frac{\partial}{\partial x_j} \left[\rho U_j \tilde{\phi} - (Sc_\infty Re_\infty)^{-1} \rho (D_n \delta_{ij} + v_t Sc_\infty \sigma_y^{-1} \delta_{ij}) \frac{\partial \tilde{\phi}}{\partial x_i} \right] = 0 \quad (1.6.18)$$

where $\sigma_\phi = C_\mu / C_\phi$, $C_\phi = 0.36$, and D is some average uniform molecular diffusivity in the flowfield.

An exact transport equation for the mixture fraction variance can be simply obtained from the instantaneous mixture fraction and is given by

$$\begin{aligned} \frac{\partial}{\partial t}(\overline{\rho \phi''^2}) + \frac{\partial}{\partial x_j} \left[\overline{\rho U_j \phi''^2} + \overline{\rho U_j'' \phi''^2} \right] = & -2\bar{\rho} \overline{U_j'' \phi''} \frac{\partial \tilde{\phi}}{\partial x_j} \\ & - 2\rho D \frac{\partial \phi''}{\partial x_i} \frac{\partial \phi''}{\partial x_i} + \frac{\partial}{\partial x_i} \left[\overline{\rho D \phi''^2} \right] \end{aligned} \quad (1.6.19)$$

There are three terms in this equation that require modeling. A gradient transport model has already been given for the mixture fraction turbulent flux, $\overline{U_i'' \phi''}$, by Equation (1.6.17). Recognizing the diffusive nature of the triple product correlation term, $\overline{U_i'' \phi''^2}$, a similar model can be developed for this term by relating it to the gradient of the mixture fraction variance (Ref. 40). This model is given by

$$\overline{\rho U_i'' \phi''^2} = -\sigma_\phi^{-1} \bar{\rho} \tilde{v}_t \delta_{ij} \frac{\partial \overline{\phi''^2}}{\partial x_j} \quad (1.6.20)$$

The last term to be modeled is the second term on the right-hand side of Equation (1.6.19). This term is positive definite and is caused by the molecular diffusive action of the fluid. The negative sign in front of this term ensures that it only acts as a sink term. At high Reynolds numbers the molecular effects are only significant at very small scales of the

motion, and this term can be interpreted as the rate of dissipation of the turbulent scalar fluctuations. A transport equation can be derived for this quantity by manipulating the instantaneous mixture fraction equation (Ref. 40). However, the modeling of this equation for chemically reacting flows is rather complex because of lack of insight into the individual terms of such equations (Ref. 41). Here a simpler approach is used to relate this term to the rate of dissipation of the turbulent kinetic energy.

Denoting the rate of dissipation of mixture fraction fluctuations by $\tilde{\varepsilon}_\phi$, a turbulent scalar field time scale can be defined as

$$t_\phi = \overline{\phi''^2} / \tilde{\varepsilon}_\phi = \overline{\phi''^2} / \left(\rho D \frac{\partial \phi''}{\partial x_i} \frac{\partial \phi''}{\partial x_i} \right) \quad (1.6.21)$$

The turbulent velocity field time scale (Ref. 17) is given by

$$t_t = \tilde{q} / \tilde{\varepsilon} \quad (1.6.22)$$

If the scalar fluctuations are caused by velocity field turbulent fluctuations, then the turbulent scalar field time scale can be directly related to the turbulent velocity field time scale, i.e.,

$$t_t = \frac{1}{2} C_g t_\phi \quad (1.6.23)$$

Experiments (Ref. 42) show that the constant C_g can vary between 0.6 to 2.4 depending on the flowfield. Here value of unity is assigned to C_g . A model for the dissipation rate of the mixture fraction fluctuations can now be given as

$$\overline{\rho D \frac{\partial \phi''}{\partial x_i} \frac{\partial \phi''}{\partial x_i}} = \frac{1}{2} C_g \frac{\tilde{\varepsilon}}{\tilde{q}} \overline{\phi''^2} \quad (1.6.24)$$

Substituting the modeled terms in Equation (1.6.19) and nondimensionalizing it, the following equation is obtained for the mixture fraction variance transport equation

$$\begin{aligned} \frac{\partial}{\partial t} (\rho \overline{\phi''^2}) + \frac{\partial}{\partial x_j} [\rho U_j \overline{\phi''^2} - (Sc_\infty Re_\infty)^{-1} \rho (D \delta_{ij} + \nu_t Sc_\infty \sigma_\phi^{-1} \delta_{ij}) \frac{\partial \overline{\phi''^2}}{\partial x_i}] = \\ + 2 Re_\infty^{-1} \sigma_\phi^{-1} \rho \nu_t \delta_{ij} \frac{\partial \tilde{\phi}}{\partial x_i} \frac{\partial \tilde{\phi}}{\partial x_j} - Re_\infty^{-1} C_g \rho \frac{\tilde{\varepsilon}}{\tilde{q}} \overline{\phi''^2} \end{aligned} \quad (1.6.25)$$

where $\sigma_\phi = C_\mu / C_\phi$, $C_\phi = 0.36$, and $C_g = 1.0$.

Equations (1.6.18) and (1.6.25) provide distribution of the mean and the variance of the mixture fraction throughout the flowfield and are solved along with conservation equations for the mass, momentum, and total energy to provide necessary information to determine all mean thermodynamic variables and chemical reaction products from the PDF combustion model. Complete expansion of the governing equations for the PDF model in two dimensions and their flux Jacobians are given in Appendix A. The dependence of the mean pressure on the mean value and the variance of the mixture fraction are also discussed in Appendix A in relation to the determination of the flux Jacobians.

This concludes the discussion of the governing equations and modeling approaches used in this work. Two methods for the calculation of compressible chemically reacting turbulent flows were presented. The first method is based on the solution of the mass-averaged Navier-Stokes equations along with chemical species transport equations with appropriate chemical reaction source terms. The second method is based on the solution of the mass-averaged Navier-Stokes equations along with mixture fraction's mean and variance equations and a PDF model for the determination of the mean thermodynamic variable and chemical reaction products. A comprehensive discussion of turbulence modeling for turbulent correlation terms appearing in the governing equations was given. Turbulence models considered included a second-order Reynolds stress model, a two-equation eddy viscosity model, and a zero-equation eddy viscosity model. In the next chapter, application of the above models to several geometrically different flowfields will be considered.

CHAPTER 2. NUMERICAL SOLUTIONS AND RESULTS

The major objectives of tasks one and two of this contract were to develop an assumed PDF chemical reaction model along with an appropriate turbulence model for compressible, turbulent diffusion flames. Diffusion flames are created when a stream of fuel is injected into a stream of oxidizer at a different temperature and allowed to mix and react. Accordingly, there are very large gradients in the values of all flow and thermodynamic variables at the surfaces where the two streams meet. Physically the turbulent mixing and molecular transport properties are responsible for smoothing of these very sharp flow gradients and mixing the two streams to a stoichiometric level where chemical reaction can take place.

This class of flames is distinguished from premixed flames by their fast rate of reaction, i.e., the reaction between the fuel and oxidizer takes place as soon as they are mixed, at the molecular level, to a stoichiometric proportion. Reaction of hydrogen fuel with a hot air stream is an example of such diffusion flames. On the contrary, in premixed flames, the rate of chemical reaction is so low that the flowfield has ample time to completely mix before chemical reaction takes place and the flowfield is relatively homogeneous. This means that in premixed flames the chemical kinetic rates control the reaction and in diffusion flames it is the rate of turbulent mixing that is the deciding factor for the level of chemical reaction.

To be able to predict the behavior of diffusion flame flowfields, an accurate turbulence model along with an accurate numerical scheme, which can resolve regions of very sharp gradients, are required. It was stated in the contract that the PDF reaction model and the turbulence models developed here, under tasks one and two, should be implemented in the RPLUS computer program. Therefore, the choice of numerical flow solver was limited to the RPLUS code. The version of RPLUS code, which was supplied by the NASA Lewis' Computational Fluid Dynamics Branch, was a research code at its early developmental stages. The code was designed for the solution of uniform flow of a premixed mixture of hydrogen and air that ignited as it passed through an inclined shock created by a ten degree ramp.

It is the conclusion of the present work that the solution algorithm in the original RPLUS code was not adequate for the solution of diffusion flame flowfields. Therefore, besides the necessary changes to include a PDF combustion model and turbulence models into the code, there was a major effort to enable the code to accurately solve for flowfields with large velocity and scalar gradients in the direction normal to the direction of the mean flow. The results given in this chapter are organized in a format which highlights the difficulties encountered in application of this computer program to a variety of free and wall-bounded shear flows and remedies provided for specific cases. The sequence of case studies begins with the least complex case of shear layers and advances to cases with more complexities introduced by large temperature gradients, species gradients, and chemical reactions. Converged solutions are compared with appropriate experimental results.

Before presenting the results of the case studies, the original RPLUS code and its characteristics will be discussed. A summary of major modifications to the original code will be given and the necessity of each modification will be briefly discussed. Some of the modifications, related to the turbulence modeling and the PDF combustion model, will be discussed in more detail later.

It must be pointed out that modifications and improvements to the RPLUS code were done in such a way that the original capabilities and characteristics of the code were preserved. Specification of appropriate input parameters causes activation of turbulence models, combustion models, and geometrical options which were not available in the original version of the code. Even though this is a very time consuming method of code development, it provides a self-consistent flow solver which can easily be used for a variety of flowfields.

2.1 RPLUS Program

The original RPLUS Computer Program (Ref. 34) employed the fully time implicit, finite volume, lower-upper, symmetric, successive overrelaxation (LU-SSOR) scheme of Jameson and Yoon (Ref. 43) to solve the coupled two-dimensional Navier-Stokes and species transport equations. Most numerical techniques used to solve the set of equations governing chemical reacting flows employ time implicit schemes and require the inversion of bounded block matrices and become exceedingly expensive when the chemical system involves a large number of species. The LU-SSOR scheme has the advantage that it requires only scalar diagonal inversion for the flow equations (continuity, momentum, and energy equations) and diagonal block inversion for the species equations. The scalar inversion of the flow equations and the block inversion of species equations are decoupled and take place in two separate steps. The LU-SSOR scheme has the advantage of a fast convergence rate while requiring an operational count similar to that of an explicit scheme and hence is particularly attractive for reacting flows with large chemical systems. A brief explanation of this method and its advantages are given below.

2.1.1 LU Scheme

The derivation of the LU scheme will be presented for the Euler equations. The final formulation for the Navier-Stokes equations will be given at the end of the derivation. Consider the equation

$$\frac{\partial Q}{\partial t} + \frac{\partial F}{\partial x} + \frac{\partial G}{\partial y} = S \quad (2.1.1)$$

A prototype implicit scheme can be formulated as

$$\delta Q = -\beta \Delta t \{D_x F(Q^{n+1}) + D_y G(Q^{n+1}) - S^{n+1}\} - (1 - \beta) \Delta t \{D_x F(Q^n) + D_y G(Q^n) - S^n\} \quad (2.1.2)$$

where $\delta Q = Q^{n+1} - Q^n$, and D_x and D_y are difference operators that approximate $\frac{\partial}{\partial x}$ and $\frac{\partial}{\partial y}$, and β is a positive number between 0 and 1. Letting the Jacobian matrices be represented by

$$\hat{A} = \frac{\partial F}{\partial Q}, \quad \hat{B} = \frac{\partial G}{\partial Q}, \quad \text{and} \quad H = \frac{\partial S}{\partial Q}$$

the scheme can be linearized by setting

$$F(Q^{n+1}) = F(Q^n) + \hat{A} \delta Q + O(\|\delta Q\|^2)$$

$$G(Q^{n+1}) = G(Q^n) + \hat{B} \delta Q + O(\|\delta Q\|^2)$$

$$S(Q^{n+1}) = S(Q^n) + H \delta Q + O(\|\delta Q\|^2)$$

and dropping terms of second or higher order. This yields

$$[I + \beta \Delta t (D_x \hat{A} + D_y \hat{B} - H)] \delta Q + \Delta t R = 0 \quad (2.1.3)$$

where

$$R = D_x F(Q^n) + D_y G(Q^n) - S^n$$

Transforming from the Cartesian coordinate system (x, y) to generalized curvilinear coordinate system (ξ, η) the above equation can be written as

$$[I + \beta \Delta t (D_\xi A + D_\eta B - H)] \delta Q + \Delta t R = 0 \quad (2.1.4)$$

where

$$A = \xi_x \hat{A} + \xi_y \hat{B} \quad B = \eta_x \hat{A} + \eta_y \hat{B}$$

and ξ_x, ξ_y, η_x , and η_y are transformation matrices. Next the Jacobian matrices A and B are given as

$$A = A^+ + A^- \quad \text{and} \quad B = B^+ + B^-$$

where

$$A^+ = \frac{1}{2}(A + v_A I), \quad A^- = \frac{1}{2}(A - v_A I)$$

$$B^+ = \frac{1}{2}(B + v_B I), \quad B^- = \frac{1}{2}(B - v_B I)$$

$$v_A = \kappa \max(|\lambda_A|), \quad v_B = \kappa \max(|\lambda_B|)$$

λ_A and λ_B are eigenvalues of Jacobian matrices A and B, and κ is a constant greater than or equal to one. Equation (2.1.4) can be written as

$$[I + \beta \Delta t (v_A + v_B)I] \delta Q + \beta \Delta t [D_\xi[(A^+ + A^-)\delta Q] + D_\eta[(B^+ + B^-)\delta Q] - (A^+ - A^- + B^+ - B^- + H) \delta Q] = -\Delta t R \quad (2.1.5)$$

Upwind differencing is used based on the sign of the Jacobian matrix, that is,

$$D_\xi[(A^+ + A^-)\delta Q] = D_\xi^-(A^+\delta Q) + D_\xi^+(A^-\delta Q) \quad (2.1.6)$$

$$D_\eta[(B^+ + B^-)\delta Q] = D_\eta^-(B^+\delta Q) + D_\eta^+(B^-\delta Q) \quad (2.1.7)$$

Let

$$\psi^- \delta Q = D_\xi^-(A^+\delta Q) + D_\eta^-(B^+\delta Q) - A^+\delta Q - B^+\delta Q - H \delta Q$$

$$\psi^+ \delta Q = D_\xi^+(A^-\delta Q) + D_\eta^+(B^-\delta Q) + A^-\delta Q + B^-\delta Q$$

$$\alpha = 1 + \beta \Delta t (v_A + v_B)$$

Then Equation (2.1.5) can be written as

$$[I + \frac{\beta}{\alpha} \Delta t (\psi^- + \psi^+)] \delta Q = -\frac{\Delta t}{\alpha} R \quad (2.1.8)$$

This equation can be factorized to

$$[(I + \frac{\beta}{\alpha} \Delta t \psi^-) (I + \frac{\beta}{\alpha} \Delta t \psi^+)] \delta Q = -\frac{\Delta t}{\alpha} R \quad (2.1.9)$$

Equation (2.1.9) is in LU factorized form and can be solved as

$$[(I + \frac{\beta}{\alpha} \Delta t \psi^-)] \delta Q^* = -\frac{\Delta t}{\alpha} R \quad (2.1.10a)$$

$$[(I + \frac{\beta}{\alpha} \Delta t \psi^+)] \delta Q^* = \delta Q^* \quad (2.1.10b)$$

At each level of solution either upwind or downwind operations are performed.

For the Navier-Stokes equations, F and G on the right-hand side of the Equation (2.1.9) can be replaced by $F - F_v$ and $G - G_v$, when F_v and G_v stand for viscous fluxes. For fully implicit formulation, $\beta = 1$, at the limit of large Δt , Equation (2.1.9) can be reduced to the following form:

$$[DIAG_{i,j} - A_{i-1,j}^+ - B_{i,j-1}^+][(v_A + v_B)I + A_{i+1,j}^- + B_{i,j+1}^-] \delta Q = -(v_A + v_B) R \quad (2.1.11)$$

where $\text{DIAG}_{i,j} = [(v_A + v_B)I - H]_{i,j}$ are $(K + 3) \times (K + 3)$ blocks in the diagonal of the matrix operator. (There are $K-1$ species and 4 Navier-Stokes equations.)

It is important to note that for nonreacting flows ($S=0$ and $H=0$, in Equation (2.1.11)) the present numerical model eliminates the need for banded block matrix inversions without using the diagonalization procedure. In fact, with forward (for the first operator in Equation (2.1.11)) and backward (for the second operator) sweeps in the diagonal directions (indices i,j increasing or decreasing simultaneously), only scalar diagonal inversions are needed to solve Equation (2.1.11) for nonreacting flow problems. For reacting flows due to the presence of the source Jacobian H , the first operator on the left-hand side of Equation (2.1.11) now requires block diagonal inversions. However, since in the present formulation the flow equations (continuity, momentum, and energy equations) have no source terms, the first four rows of the diagonal block (DIAG) of this operator have nonzero terms only in the diagonal. As a result, the first operator of Equation (2.1.11) can be inverted in essentially two separated steps: the scalar diagonal inversion for the flow equation and the block diagonal inversion for the species equations.

2.1.2 Finite Volume Discretization and Artificial Dissipation

Approximating the integral form of the governing equations, a finite-volume space discretization has been developed for the right-hand side of the Equation (2.1.11). The use of a finite-volume method for space discretization allows one to handle arbitrary geometries and help avoid problems with metric singularities that are usually associated with finite-difference methods. The scheme reduces to a central-difference scheme on a Cartesian grid and is second-order accurate in space, provided the mesh is smooth enough.

It is important to point out here that the experience gained by the use of several different kinds of grids suggests that the RPLUS code is very sensitive to grid spacing and the gradual stretching of the grid cells. The stretching must be such that the change in the sides of adjacent cells in each direction would not be more than ten percent. This may be due to the space discretization method used for the viscous flux terms on the right-hand side of Equation (2.1.11). This method is not exactly consistent with the finite-volume approach for nonuniform meshes. Investigation of this problem was outside the scope of this work and, due to time limitations, it was not pursued.

Using a central difference scheme for calculating flows with discontinuities or very sharp gradients typically produces flowfield oscillations in the neighborhood of discontinuity. To suppress the tendency for decoupling between odd and even points and to prevent nonphysical overshoots near regions of very sharp gradient, artificial dissipation models are added to the differenced equations. The original RPLUS code employed a nonlinear mixed explicit second and fourth order dissipation model with isotropic coefficients. To illustrate this dissipation model the numerical balance of the inviscid flux of each cell is written as

$$(F_{i+1/2,j} - F_{i-1/2,j} + G_{i,j+1/2} - G_{i,j-1/2}) - (d_{i+1/2,j} - d_{i-1/2,j} + d_{i,j+1/2} - d_{i,j-1/2}) \quad (2.1.12)$$

where d is the dissipation flux. For the sake of simplicity $d_{i+1/2,j}$ is denoted by $d_{i+1/2}$, then

$$d_{i+1/2} = \varepsilon_{i+1/2}^{(2)} (Q_{i+1} - Q_{i-1}) - \varepsilon_{i+1/2}^{(4)} (Q_{i+2} - 3Q_{i-1} + 3Q_i - Q_{i-1}) \quad (2.1.13)$$

The third order terms are due to fourth order differences and provide for high frequency background noise damping. The first order terms are due to second order differences and are only used near shock waves activated by a pressure jump sensor defined by

$$T_i = \frac{|P_{i+1} - 2P_i + P_{i-1}|}{|P_{i+1} + 2P_i + P_{i-1}|} \quad (2.1.14)$$

where P is the pressure. The coefficient of the first order terms is proportional to the pressure jump sensor through the following relation

$$\varepsilon_{i+1/2}^{(2)} = \kappa_2 \frac{1}{2} [r(A)_{i+1/2} + r(B)_{i+1/2}] \max(T_{i+2}, T_{i+1}, T_i, T_{i-1}) \quad (2.1.15)$$

where $r(A)$ and $r(B)$ are the spectral radii of Jacobian matrices. The coefficient of the third order terms is switched off by the pressure sensor and is given as

$$\varepsilon_{i+1/2}^{(4)} = \max \left[0, \kappa_4 \frac{1}{2} [r(A)_{i+1/2} + r(B)_{i+1/2}] - \varepsilon_{i+1/2}^{(2)} \right] \quad (2.1.16)$$

In the η direction the index i is replaced with j in Equations (2.1.13) to (2.1.16).

The use of spectral radii of both Jacobian matrices A and B in the scaling factors results in an isotropic smoothing. This means that even if the spectral radius of the A Jacobian matrix is small, the artificial dissipation in the ξ direction may be large due to a large value of the spectral radius of the B Jacobian matrix. In order to reduce the amount of unwanted dissipation, especially in the direction normal to the body surfaces inside boundary layers, an anisotropic dissipation model was added to the present version of RPLUS code. This model has the same structure as the original model, discussed above, except for the scaling factor. In the ξ direction Equations (2.1.15) and (2.1.16) are replaced by

$$\varepsilon_{i+1/2}^{(2)} = \kappa_2 r(A)_{i+1/2} \max(T_{i+2}, T_{i+1}, T_i, T_{i-1}) \quad (2.1.17)$$

$$\varepsilon_{i+1/2}^{(4)} = \max(0, \kappa_4 r(A)_{i+1/2} - \varepsilon_{i+1/2}^{(2)}) \quad (2.1.18)$$

In the η direction, the index i is replaced with j and the spectral radius of the B Jacobian matrix, $r(B)$, is used. This directional artificial dissipation model produced better results than the original model, as shown in the next section. However, it was still incapable of providing an overshoot free solution for nonreacting supersonic mixing layers with large

temperature gradient. This made the use of a total variation diminishing (TVD) scheme imperative.

A survey of the literature indicates that even though TVD schemes are well developed for single species nonreacting flowfields, the development for multi-species reacting flows with large source terms is still a topic of ongoing research (Ref. 45, 46, and 47). Therefore, it was decided that since the LU-SSOR scheme decouples the solution of the Navier-Stokes equations (continuity, momentum, and energy) from the solution of the rest of the scalar (species) equations, it is possible to use a TVD scheme for the first four components of the solution vector, i.e. ρ , ρu , ρv , and ρe_t , and use a directional second and fourth order artificial dissipation model for the scalar (species) equations as discussed above. The flux difference split dissipation model, which is based on the concept of Roe's characteristic-based scheme, is used here (Ref. 45). This model creates characteristic fields corresponding to different wave speeds. The dissipation flux is then given as

$$d_{i+1/2} = \frac{1}{2} T_{i+1/2} |\Lambda_{i+1/2}| T_{i+1/2}^{-1} (Q_{i+1} - Q_i) \quad (2.1.19)$$

where T and T^{-1} are similarity transformation matrices and Λ is a diagonal matrix whose elements are eigenvalues of the flux Jacobian matrix A . In the η direction j replaces i and corresponding transformation and eigenvector matrices for the matrix B are used.

The present version of the RPLUS code provides the option of using either a TVD model or a directional explicit second and fourth order dissipation model for treatment of overshoots in profiles of ρ , ρu , ρv , and ρe_t . The scalar equations, which are the species equations for the finite rate chemistry closure model and the mean and the variance of the mixture fraction for the PDF closure model, are still treated with a directional second and fourth order dissipation model. The solutions of k and ϵ equations are also treated with a directional second and fourth order dissipation model. The use of the second and fourth order dissipation model for the scalar equations and the k - ϵ equations is the biggest obstacle in obtaining converged and physical solutions for the diffusion flame reacting mixing layer and ramp flows with large ramp angles.

2.1.3 Turbulence Models

The algebraic eddy viscosity turbulence model of Baldwin-Lomax (Ref. 33) with constant turbulent Prandtl and Schmidt numbers ($Pr_t = Sc_t = 0.9$) was used to account for turbulence in wall-bounded flows in the original version of the RPLUS code. This is a zero-equation turbulence model and only captures the increase of flow diffusivities due to turbulent mixing. Therefore, except for the modified diffusion coefficients, the governing equations were identical to their laminar counterpart. On the other hand, the Baldwin-Lomax model was developed for wall-bounded flows and is not applicable to free shear layers, such as mixing layers, jets, and wakes. Therefore, a zero-equation Prandtl mixing model (see Chapter 1) was added to the RPLUS code to broaden its range of applicability to different flow regimes at the zero-equation level of turbulence modeling. Implementation of

this model did not require any change in the structure of the code. A subroutine was added to provide turbulent eddy viscosity for free shear layers. Depending on the number of solid boundaries at the top and bottom of the domain of solution (zero, one, or two), an appropriate subroutine is called to provide the turbulent eddy viscosity.

The implementation of the k - ϵ model into the RPLUS code involved several major changes. The first step was to solve for the transport equations of the k and ϵ . These equations are coupled together and are solved independent of the mean flow equations at each solution iteration. After the solution of the mean flow variables a call is made to the master k - ϵ subroutine which provides turbulent Reynolds stresses, kinetic energy, eddy viscosity, and time scale for use in the mean flow equations at the next iteration. To solve the k and ϵ transport equations, the implicit, finite volume LU-SSOR scheme was used. However, for the sake of clarity, subroutines exclusive to the k - ϵ equations were developed for this purpose.

The second step was to include the appearance of the turbulent kinetic energy, Reynolds stresses, and nonisentropic turbulent eddy viscosity into the mean flow governing equations. It can be seen from the mean turbulent flow equations presented in section five of chapter one and in Appendix A.1, that the state equation, inviscid and viscous flux vectors and their Jacobians are all effected by these turbulent quantities. Therefore, the turbulence effects are fully felt by all the flow and thermodynamic mean variables. All these changes are fully implemented in the present version of the RPLUS code. Unlike zero-equation models, k - ϵ model is a universal model and can be applied to any flowfield with or without solid boundaries, provided appropriate boundary conditions are used. Near wall correction terms for k and ϵ equations are automatically set to zero for free shear layers with no solid walls.

2.1.4 Chemical Reaction Models

The original RPLUS computer program was equipped with a nine-species, eighteen-step chemistry model for hydrogen-air reactions (Ref. 48). The species included H_2 , O_2 , OH , H_2O , H , O , HO_2 , H_2O_2 , and N_2 . The molecular properties, such as specific heat, thermal conductivity, and viscosity of each species were determined by fourth order polynomials of temperature. The specific heat of the gas mixture was obtained by mass concentration weighting of each species. The thermal conductivity and viscosity of the mixture were calculated using Wilke's mixing rule (Ref. 49). The binary mass diffusivity between two species was obtained using the Chapman-Enskog theory in conjunction with the Lennard-Jones Intermolecular Potential Functions (Ref. 49). The diffusion of a species in the gas mixture was approximated by Fick's Law (Ref. 50), treating each species and its surrounding gas as a binary gas mixture. All these features are preserved in the present version of the RPLUS code.

The sum of mass fractions of all species at any point in time and space should add up to unity. This equality reduces the number of species equations to be solved by one.

Therefore, a nine species finite rate chemistry model requires the solution of only eight species transport equations. This brings the total number of equations to be solved, in a two-dimensional geometry, to twelve. The original RPLUS code automatically solved for twelve transport equations regardless of number of species actually present in the mixture and the presence of any chemical reaction. After the determination of the twelve component solution vector, the code proceeded to calculate the mixtures' mean temperature, pressure, speed of sound, and species' enthalpy and molecular properties.

The assumed PDF combustion model requires the solution of transport equations of the mean and variance of the mixture fraction, in addition to the mean flow equations (continuity, momentum, and energy). Hence, it requires the solution of only six transport equations in a two-dimensional geometry. After the determination of the six-component solution vector, the present version of the RPLUS code proceeds to calculate the reaction's mean species mass fraction, temperature, pressure, and density, by integrating the Beta function PDF, over appropriate equilibrium reaction thermodynamic tables, for each of the above thermodynamic variables. As a consistency check, the mean density is recalculated from the table integration method and compared with the mean density given by the solution vector. These two values of the mean density, obtained from different approaches, must be equal within a small error tolerance. If this consistency check is not verified the calculation stops with an error message.

The determination of the mean thermodynamic variables, after the solution vector determination for a given chemical reaction model, is properly channeled to an appropriate set of subroutines depending on the chemical reaction model used. A number of new subroutines were added to the program to deal with determination of the mean thermochemical variables in the PDF reaction model case. These subroutines are independent of the originally existing subroutines and are only called upon if the PDF combustion model is chosen by specification of an appropriate parameter in the input file. Therefore, except for the use of the main solver subroutines with a reduced solution vector size, there is not much overlap between the solution procedures for the two chemical reaction models.

The main solver subroutines in the RPLUS code have been modified such that it is now capable of solving:

- (a) Four Navier-Stokes equations in the case of uniform species composition, nonreacting flowfields.
- (b) Four Navier-Stokes equations plus mixture fraction mean and variance equations in the case of PDF model hydrogen/air diffusion flame.
- (c) Four Navier-Stokes equations plus eight species equations in the case of nonreacting flows with nonuniform species composition, or diffusion or premixed reaction between hydrogen and air.

These modifications were implemented by changing the solution vector size and modifying the calculation logic of the inviscid and viscous fluxes and their Jacobians. Care was taken in implementing these changes to avoid degrading the code's vectorization properties by not introducing any IF statement in any of the main solvers' DO loops.

2.1.5 Boundary and Initial Conditions

The original RPLUS code was designed for single feed premixed flows with uniform velocity, temperature, pressure, and chemical composition across the inflow plane. There was no provision for parallel injection of any kind of fluid into the flowfield. Solid boundaries were used at the top and the bottom of the flowfield. The uniform inflow velocity profile combined with the no slip boundary condition on solid boundaries created leading edge shocks at the top and bottom of the inflow region. Even though these conditions were all valid, they were not appropriate for free and wall-bounded diffusion flame cases under consideration.

In order to accommodate a variety of flow conditions the RPLUS program was changed to allow for the following conditions:

- (a) Two parallel streams with different properties at the inflow boundary. In this case Mach number, temperature, static pressure, and species mass fraction of each stream is read in from the input file. Pressures at two streams are usually matched. The inflow species composition at each stream can be made up of one or a combination of the following species; oxygen, nitrogen, hydrogen, and/or water. There is a symmetry plane at the bottom boundary and freestream boundary conditions at the top boundary. Both inflow and outflow streams are completely supersonic. To reduce sharp discontinuities at inflow regions between the two incoming streams an error function smoothing can be used for the streamwise component of the velocity, temperature, and species mass fractions. Smoothed values along with uniform static pressure are used to determine density and total internal energy. This smoothing corresponds to consideration of a mixing layer downstream of its splitter plate.
- (b) Same as the above case except each stream is assumed to be on one side of a splitter plate. The inflow streamwise velocity profiles on each side of the splitter plate are calculated using the $1/7$ power law, given the supersonic boundary layer thickness on each side of the splitter plate. Next, temperature, density, and total internal energy are calculated assuming constant static pressure and total enthalpy. This inflow specification corresponds to consideration of boundary layers just upstream of the splitter plate tip.

In both above cases, turbulent kinetic energy and its dissipation rate at the inflow plane are calculated using the eddy viscosity concept, the streamwise velocity inflow profile, and a multiple of the molecular viscosity.

- (c) Uniform species composition with supersonic boundary layer profile for velocity on an adiabatic wall at the bottom boundary. Here the flow Reynolds number at the inflow plane is used to obtain the velocity profile. Assumption of constant static pressure and total enthalpy provides temperature, density, and total internal energy. Turbulent kinetic energy and its dissipation rate at the inflow plane are obtained using the law of the wall for compressible boundary layers.
- (d) Combination of cases (a) and (c) for wall jets.
- (e) The original uniform premixed inflow profiles. For uniform premixed cases specification of the equivalence ratio with a value greater than 10^{-5} overrides species compositions' input values. Species mass fractions are then calculated in the program and set uniformly across the inflow region.
- (f) For diffusion flame cases with the PDF formulation, the mean mixture fraction is set to one at the fuel inflow and zero at the oxidizer inflow. The mixture fraction variance is set to zero at the inflow.

In general, inflow streams are always supersonic; therefore, upstream boundary conditions are provided by specifying the velocity, temperature, static pressure, and species mass fractions as discussed above. At the supersonic outflow boundary, the dependent variables are extrapolated from the interior. However, for wall-bounded flows, the static pressure at the outflow boundary is specified for grid points inside the wall boundary layers where the flow is subsonic. Along solid walls, no slip boundary conditions are specified and the wall is assumed to be adiabatic. The normal derivatives of pressure and species mass fractions are also assumed to be zero. Along a plane of symmetry, the normal derivatives of all the dependent variables are zero, except for the v component of velocity, which is set to zero. The turbulent kinetic energy and normal derivatives of its rate of dissipation are set to zero along solid boundaries. In all cases, the flowfield variables are initialized to their inflow values.

2.2 Supersonic Free Shear Layers

This section is devoted to two-dimensional, supersonic free shear layers with large streamwise velocity, temperature, and species gradients at the inflow plane. The gases used are air, with 24.1% oxygen mass and 75.9% nitrogen mass, in the temperature range of 300°K to 1200°K, and different mixtures of hydrogen and nitrogen in the temperature range of 300°K to 450°K. Considering the mixing layer geometry shown in Figure 2.1, one can generally define the velocity ratio, r , between the two streams as the freestream velocity

of the slower moving stream divided by the freestream velocity of the faster moving stream. The density ratio, s , is defined as the freestream density of the slower moving stream divided by the freestream density of the faster moving stream. Mixing layer convective Mach numbers with respect to each stream are defined as (Ref. 31)

$$M_{c1} = \frac{u_1 - u_c}{a_1} \quad (2.2.1a)$$

and

$$M_{c2} = \frac{u_c - u_2}{a_2} \quad (2.2.1b)$$

where u_1 and a_1 are freestream velocity and speed of sound propagation in the faster moving stream. Similarly u_2 and a_2 are freestream velocity and speed of sound in the slower moving stream. u_c is the speed of convection of the large structure eddies in the mixing layer and is defined as

$$\frac{u_c}{u_1} = \frac{1 + rs^{1/2}}{1 + s^{1/2}} \quad (2.2.2)$$

with $r = u_2/u_1$ and $s = \rho_2/\rho_1$. If the ratio of specific heats in the two streams are equal, i.e., $\gamma_1 = \gamma_2$, then

$$M_{c1} = M_{c2} = M_c \quad (2.2.2)$$

and

$$u_c = \frac{a_2 u_1 + a_1 u_2}{a_1 + a_2} \quad (2.2.4)$$

In all cases considered, the inflow velocities are all supersonic and static pressure is matched between the two incoming streams and set to $1.013 \times 10^5 \text{ Nt/m}^2$. Depending on the velocity and temperature ratios and the convective Mach number between the two layers the incoming mixing layer may remain a mixing layer in the solution domain, or it may develop into a two-dimensional jet or wake. The flow exits the outflow boundary with supersonic speed. Therefore, all dependent variables at this plane are extrapolated from the interior points. The symmetry boundary condition is used at the bottom boundary, and nonreflecting boundary conditions are used at the top boundary. The numerical grid used for most of these flows is an 80×55 clustered grid, with clustering around the splitter plate

location in the normal direction and near the inflow plane in the longitudinal direction (Figure 2.2). The domain dimensions are normalized to a height of 1.0 and length of 4.2 with the height of the inner stream channel set to 0.1

2.2.1 Solution Overshoots and Artificial Numerical Dissipation

To show the overshoots, caused by the use of the isotropic second and fourth order artificial dissipation model used in the original RPLUS code, the simplest possible mixing layers are considered here. In the first case, a mixing layer between two airstreams is considered. The top layer's Mach number is 1.86 at the freestream temperature of 450°K. The bottom layer's Mach number is 1.46 at the freestream temperature of 450°K. Since the two streams are at the same temperature and static pressure, they have the same density and speed of sound propagation. Therefore,

$$s = \frac{\rho_2}{\rho_1} = 1, \quad r = \frac{u_2}{u_1} = \frac{M_2}{M_1} = 0.785, \quad \text{and} \quad M_c = \frac{M_1 - M_2}{2} = 0.2$$

Three different calculations were performed, and in each case, three thousand iterations were made on a CRAY Y-MP computer. In the first calculation, the isotropic artificial dissipation model, which was used in the original version of the RPLUS code, was used. The dissipation coefficients used for this case were those recommended by the original RPLUS code, i.e., $\kappa_2 = \frac{4}{2}$ and $\kappa_4 = \frac{4}{64}$ (see Equations (2.1.15) and (2.1.16)). In the second calculation, the directional artificial dissipation model was used with the same dissipation coefficients as above. In the third case, the TVD scheme was used.

To highlight the effect of the artificial dissipation models and eliminate any other sources of instability and numerical overshoots, no turbulence model was used, but instead, the molecular viscosity of the streams was increased by a factor of one hundred. The convergence history and the CPU time for all three cases are shown in Figure 2.3. All three cases have similar convergence curves and are fully converged. The profiles of the streamwise velocity components, u , along the normal direction, y , at several downstream stations are displayed in Figures 2.4a, 2.4b, and 2.4c. There are large overshoots and undershoots associated with the artificial dissipation models, as can be seen in Figures 2.4a and 2.4b. These overshoots are present at every downstream location and do not go away as one moves away from the inflow plane. Instead they have a wave-like behavior as they move downstream. the isotropic model creates much larger overshoots and slightly more spreading of the mixing layer. The TVD scheme not only provides an overshoot-free solution, it also creates the least amount of numerical diffusion as can be seen by visual inspection of the level of spreading of the mixing layer in these three cases. The only drawback of the TVD scheme is the almost doubling of the computational time required for the calculation of the flowfield, as noted in Figure 2.3. This is a small price to pay for an accurate solution.

There was a suspicion that the reduction of the very large gradient of the streamwise velocity component at the inflow plane may help reduce the large overshoots observed in cases where second and fourth order artificial dissipation models were being used. To test this idea an error function was used to smooth the streamwise velocity component and reduce its gradient at the inflow plane. The solution obtained for the mixing layer with a smoothed inflow velocity and utilizing an isotropic artificial dissipation model is presented in Figure 2.4d. The overshoots are still present in a major portion of the solution field and the inflow smoothing has just helped to reduce the overshoots occurring near the inflow plane. The solution convergence history is very similar to the previous cases shown in Figure 2.3 and is not shown here.

Having established the presence of the overshoots in the absence of any turbulence models, it was important to observe the effect of different turbulence models on the flow solution and the related solution overshoots. Therefore, the elevated molecular viscosity was reduced to its actual value and a Prandtl mixing turbulence model, given by Equation (1.3.19), was used in the calculation of the same mixing layer with all three methods of numerical dissipation. The Prandtl mixing turbulence model used here was slightly modified to suit the unsmoothed inflow streamwise velocity profile in the following three test calculations. The mixing layer thickness, δ , used in this turbulence model, was redefined as the distance between points where the streamwise velocity differs from the freestream velocity by one percent (instead of five percent) of the maximum velocity difference across the layer. This modification provides a slightly larger turbulent viscosity and creates a more rapid spreading of the mixing layer. Since the following three test cases are only used to show the effect of the artificial numerical dissipation schemes and not the accuracy of this turbulence model, the above modification is unimportant. In latter applications of the Prandtl mixing turbulence model, the original definition of δ , given in Section 1.3.3, is always used.

Figures 2.5a, 2.5b, and 2.5c show the streamwise velocity profiles obtained from these calculations. These results display the same trend as before, with the isotropic artificial dissipation model creating the largest overshoots and the TVD scheme producing no observable overshoots. The use of the Prandtl mixing turbulence model has two notable effects, the first one is the disappearance of the wave-like behavior of the overshoots. Therefore, the overshoot magnitude is decreasing as one moves toward the outflow plane region, such that there is very little overshoot at downstream stations near the outflow plane. The second effect is the lack of solution convergence for cases which do not use the TVD scheme. Figure 2.6a shows the convergence history of L_2 density residual for the isotropic artificial dissipation model. Large residual oscillations appear after 1,500 iterations. The convergence history of the directional artificial dissipation model is also oscillatory and very similar to the above case; large residual oscillations appear after about 1,500 iterations. The TVD scheme produces a properly convergent solution as shown by Figure 2.6b.

Based on these results, the TVD scheme was chosen over the second and fourth order artificial dissipation models for the rest of the calculations. However, since the TVD scheme is only applied to the continuity, momentum, and energy equations a second and fourth order artificial dissipation model still needs to be used for the scalar transport equations. Therefore, there was an effort to develop methods which would minimize the level of overshoots caused by the second and fourth order smoothing model. The usual method of achieving this goal is by a simple trial and error method of changing the model coefficients for each specific case under consideration. However, there are some observations that apply to most cases considered. The fourth order dissipation model is responsible for damping the high frequency noise, produced by the numerical solution, at points away from the regions of steep flow variable gradients. Large choices of its constant result in a rapid solution convergence. On the other hand, the magnitude of this constant is directly related to the magnitude of the solution overshoots. These observations point to the reduction of the fourth order model constant and increase of the second order model role. Unlike the static pressure jump across a shock wave, the static pressures across the contact surface of two mixing layers are matched and there is not a physical pressure jump to activate the second order dissipation model across a mixing layer. To increase the role of second order dissipation terms several models were tested. These smoothing techniques included:

- (a) Use of total pressure as well as static pressure to activate the second order smoothing terms. This model was not appropriate for more complex flowfields where both shock waves and mixing layers coexisted in the solution domain. It also created too much diffusion for simple mixing layer cases.
- (b) Starting the numerical solution with a very small amount of the fourth order dissipation term and a small amount of the second order dissipation term throughout the flowfield and independent of the pressure jump condition, then slowly reducing the amount of the second order dissipation terms to zero as the number of iterations increase. This method made the solution blow up in most cases for which it was used.
- (c) Replacing the fourth order dissipation term by a second order term whose coefficient is a function of the fourth order derivative of the local variables. Therefore, the second order dissipation term would damp out the high frequency numerical noise at points away from the regions with steep flow variable gradients. This method resulted in slowly converging or nonconverging solutions with unexpectedly large diffusion in some regions of the flowfield.

Due to lack of success in developing a more accurate and generally valid numerical dissipation model for the scalar transport equations, it was decided to use the traditional directional second and fourth order dissipation model with the smallest possible coefficient of the fourth order term that provided a convergent numerical solution.

2.2.2 Mixing Layers with Uniform Species Composition

In this section, calculation results for turbulent supersonic free shear layers with uniform species composition are presented. The TVD scheme is used for the solution of the Navier-Stokes equations, and the directional second and fourth order artificial dissipation model is used for the solution of the $k-\epsilon$ transport equations. The objective is a close examination of the prediction capabilities of the $k-\epsilon$ and the Prandtl mixing turbulence models and comparison of their results with experimental data. The effects of streamwise velocity ratio, $r = u_2/u_1$, density ratio, $s = \rho_2/\rho_1$, and convective Mach numbers on the spreading rate of supersonic mixing layers are considered. Predictions of Reynolds stresses by the $k-\epsilon$ turbulence model are compared with the experimental results.

The application of the $k-\epsilon$ turbulence model to the supersonic mixing layer discussed earlier, i.e., $s = 1$, $r = 0.785$, and $M_c = 0.2$, produces a fully converged solution with no nonphysical solution overshoots. Figure 2.7 shows the convergence history of this case. The 80×55 clustered grid, shown in Figure 2.2, was used. The physical domain of solution has the height of $H = 10$ cm. and length of $L = 42$ cm. The splitter plate is located at the height of $h = 1$ cm. The coordinate axes are normalized with the height H . The calculation was performed on the NAS CRAY Y-MP computer and took about 0.4 CPU seconds per iteration. The same flowfield calculation using the Prandtl mixing turbulence model, which does not require solution of any transport equations for the turbulence model, takes about 0.3 CPU seconds per iteration (see Figure 2.6b). The $k-\epsilon$ model constants are those given in Table 1, when the contributions due to the solid wall effects are set to zero. Due to the small magnitude of the convective Mach number, M_{c1} , the Zeman's extra compressibility term was not used with the $k-\epsilon$ model.

The k and ϵ inflow profile was based on the inflow profile of the normalized mean streamwise velocity which was smoothed using an error function. The variation of the normalized mean streamwise velocity in the two-dimensional solution domain is shown in Figure 2.8a. The velocity components are normalized with freestream speed of sound propagation in the top stream. Figure 2.8b presents the profile of the streamwise velocity along the normal direction, y , at several downstream locations. In Figure 2.8c, normalized mean streamwise velocity is plotted as a function of the similarity variable $\eta = (y - y_c)/\delta$, where y is the local cross-stream coordinate and y_c is the cross-stream coordinate location where $u = 0.5(u_1 - u_2) + u_2$, and δ is the mixing layer thickness as defined in Section 1.3.3.

For mixing layers the vorticity thickness is defined by

$$\delta_\omega = \frac{|u_1 - u_2|}{(\partial u / \partial y)_{\max}} \quad (2.2.5)$$

where $(\partial u / \partial y)_{\max}$ is the maximum slope taken in the linear region of the mixing layer. Figure 2.9 shows that the calculated vorticity thickness $\delta_\omega(x)$ increases linearly after an initial development phase. The spreading rate of a mixing layer can be given in terms of the rate of change of the vorticity thickness, $\delta_\omega(x)$, with respect to the longitudinal direction, x . Based on experimental results of Brown and Roshko (Ref. 51) this spreading rate is a function of several flow parameters and can be expressed as (Ref. 31)

$$\delta'_\omega = \frac{d\delta_\omega}{dx} = f(r, s, \frac{\gamma_2}{\gamma_1}, M_{c1}) \quad (2.2.6)$$

Since the specific heat ratio, γ , usually changes from 1.4 to 1.7, the effect of γ_2/γ_1 is assumed negligible in comparison to the other parameters. For incompressible mixing layers, M_{c1} is zero and the above functional relationship reduces to

$$\delta'_{\omega,0} = f(r, s) \quad (2.2.7)$$

Papamoschou and Roshko (Ref. 31) have used experimental data to develop the following equation

$$\delta'_{\omega,0} = 0.085 \frac{(1-r)(1+s^{1/2})}{1+rs^{1/2}} \quad (2.2.8)$$

The mixing layer under consideration has $r = 0.785$ and $s = 1$, therefore, the above equation results in $\delta'_{\omega,0} = 0.0205$. The numerical solution of the flow equations, using a $k-\epsilon$ turbulence model, results in $\delta'_\omega = 0.0208$, which is only one percent larger than the above experimental value obtained from Equation (2.2.8). The absence of the convective Mach number effect is expected in this case, since according to Bogdanoff (Ref. 52) these effects are negligible for $M_{c1} \leq 0.35$.

To gain some quantitative insight into the predictive capabilities of the $k-\epsilon$ turbulence model used in the calculation of the above mixing layer, the turbulent eddy viscosity and Reynolds stresses predicted by this model can be examined. Figure 2.10 presents the distribution of the nondimensionalized turbulent eddy viscosity in the solution domain. The predicted turbulent eddy viscosity has reached a value almost 500 times larger than the freestream molecular viscosity within the mixing layer, and smoothly approaches zero outside the mixing layer.

At the $k-\epsilon$ turbulence modeling level, the Reynolds stresses can be obtained from Equation (1.3.11). Square roots of the normal Reynolds stresses, u'^2 and v'^2 , are normalized by the velocity difference across the mixing layer and are referred to as streamwise and lateral turbulent intensities respectively. Similarly, the Reynolds stress, $u'v'$ is normalized by the square of the velocity difference. The ratio of this normalized Reynolds stress by the product of turbulent intensities is referred to as the turbulence correlation coefficient. All

these quantities, obtained from the calculation of the above mixing layer, can be compared with the recent experimental results of Goebel et. al (Ref. 53). The experimental results are for the case of $r = 0.79$, $s = 0.76$, and $M_c = 0.2$, which is very close to the case studied here. The comparisons are made at the downstream location of $x = 400$ mm. The comparison of the calculated similarity profile of the normalized streamwise velocity with the experimental data is shown in Figure 2.11a. Figure 2.11b displays the comparison of the calculated and experimental values of the Reynolds stress. Although the calculated result captures the general shape of the Reynolds stress, it is consistently smaller than the experimental values by about 25% in the middle of the mixing layer. This difference reduces near the mixing layer edges. The comparison of the streamwise and lateral turbulent intensities is shown in Figures 2.11c and 2.11d, respectively.

The $k-\epsilon$ turbulence model predicts almost identical lateral and streamwise turbulent intensities, whereas physically these two components are quite different. The experiment shows that the maximum value of the streamwise turbulent intensity is almost 42% larger than the maximum value of the lateral turbulent intensity. Similar behavior is also reported by Samimy and Elliot (Ref. 54) for a variety of mixing layers. It is interesting to note that in spite of such considerable differences between the calculated and experimentally obtained values of the individual components of the Reynolds stress tensor, the mean streamwise velocity profile (see Figure 2.11a), and the spreading rate of the mixing layer are so well predicted. Comparison of the predicted and experimentally obtained values of the turbulence correlation coefficient $(\overline{u''v''})/(\overline{u''^2})^{1/2}(\overline{v''^2})^{1/2}$, is presented in Figure 2.12. This quantity represents the general structure of the turbulence in the mixing layer. Figure 2.12 indicates that the $k-\epsilon$ turbulence model does a relatively good job in predicting the behavior of the general turbulence structure, even though it is not very successful in predicting the behavior of the individual components of the Reynolds stress tensor. This is the reason behind the relative success of the $k-\epsilon$ model in predicting the global features of this flowfield.

To examine the effects of freestream densities on the prediction capability of the $k-\epsilon$ model a supersonic mixing layer between two air streams with the following characteristics was considered:

$$M_1 = 1.86, \quad T_1 = 1100^\circ\text{K}, \quad P_1 = 1.013 \times 10^5 \text{ Nt/m}^2$$

and

$$M_2 = 1.46, \quad T_2 = 450^\circ\text{K}, \quad P_2 = 1.013 \times 10^5 \text{ Nt/m}^2$$

The speed of air in the top and bottom streams is 648.77 m/s and 423.56 m/s, respectively. Therefore, $r = 0.51$, $s = 2.44$, and, according to Equations (2.2.1) and (2.2.2), $M_{c1} = 0.55$. Figure 2.13 shows the convergence history of this case. As shown by this figure the solution residual drops by almost five orders of magnitude in 4000 iterations and the solution is considered fully converged. However, it does not drop as low as the residual of

the uniform density case, Figure 2.7. The same grid as in the previous cases was used for this case. An error function was used to smooth the inflow temperature and streamwise velocity component profiles. Figures 2.14 a, b, c, d, and e show the calculated profiles of the nondimensionalized temperature, streamwise velocity, turbulent eddy viscosity, turbulent kinetic energy, and turbulent kinetic energy dissipation rate, with respect to the crossflow direction, at several downstream stations.

The convective Mach number for this case is large enough to cause considerable compressibility effects. However, the k- ϵ turbulence model used for the calculation of this case does not include the Zeman's extra compressibility term in the turbulent kinetic energy equation discussed in Section 1.3.2. This exclusion was made to study the density effects on the basic k- ϵ turbulence model and to assess the performance of other compressibility terms in the k and ϵ transport equations. Figure 2.15 displays the linear increase of the calculated vorticity thickness $\delta_\omega(x)$ in the downstream direction, at the rate of $\delta'_\omega = 0.0545$. The experimental spreading rate for an incompressible mixing layer with $s = 2.44$ and $r = 0.51$ is obtained from Equation (2.2.8). This relation results in $\delta'_{\omega,0} = 0.0585$ for the present case. The experimental ratio of a compressible spreading rate to its incompressible counterpart, at the same r and s , can be obtained from Figure 17, page 473 of Reference 31. This figure shows that for $M_{c1} = 0.55$, $\delta'_\omega / \delta'_{\omega,0} = 0.77$. Therefore, the compressible spreading rate for $r = 0.51$, $s = 2.44$, $M_{c1} = 0.55$, and with $\delta'_{\omega,0} = 0.0585$ is found to be $\delta'_\omega = .045$. The spreading rate predicted by the k- ϵ model is 22% larger than the expected experimental value. If the compressibility effects are ignored, then the predicted spreading rate is 6% smaller than the incompressible spreading rate, $\delta'_{\omega,0}$. On the other hand, if the density ratios, s , is set to one in Equation (2.2.8), then

$$\delta'_{\omega,0} = 0.17 \frac{1 - r}{1 + r} \quad (2.2.9)$$

and for $r = 0.51$, $\delta'_{\omega,0} = .0552$ which is very close to the predicted spreading rate. This result clearly indicates that numerical solution of the mixing layer with the k- ϵ turbulence model, without Zeman's correction, can only account for the spreading rate caused by the freestream's velocity ratio r . Furthermore, the freestreams' density ratio effects as well as the supersonic compressibility effects are not captured. However, it must be noted, in this case, that the density ratio contribution is about 6% and almost negligible. For a range of moderate density ratios ($0.5 \leq s \leq 3.0$) with velocity ratios close to one ($0.5 \leq r \leq 1.0$), the k- ϵ turbulence model has difficulty accounting for the small contributions of the density ratio, as can be seen from Figure 2.16. However, for very small and large density ratios, the k- ϵ model crudely follows the experimental trend.

To examine the predictive capabilities of the Prandtl mixing turbulence model and the basic k- ϵ turbulence model, without Zeman's dissipation correction, for supersonic mixing layers with convective Mach numbers between 0.2 and 1.5, a series of calculations were performed. In all these cases the top and bottom stream temperatures were set to 450°K, so that $s = 1$ and the speed of sound would be the same in both streams. The convective Mach

number was varied by changing the stream's Mach numbers at the inflow plane. Static pressure was kept uniform across the two streams. All of the supersonic mixing layer calculations were fully converged and resulted in self similar streamwise velocity profiles (Figure 2.17). The vorticity thickness growth rate results indicated that both of these turbulence models are incapable of predicting the compressibility effects on supersonic mixing layers. For both models, the mixing layer spreading rate was only a function of the streamwise velocity ratio, r . In fact, the $k-\epsilon$ model's predictions very closely followed the incompressible mixing layer's spreading rate, given by Equation (2.2.8), as can be seen in Figure 2.18. Moderate changes in the value of compressibility-related constants in the $k-\epsilon$ turbulence model, i.e., n , $c_{\epsilon 3}$, and $c_{\epsilon 4}$, did not result in any favorable outcome. The Prandtl mixing turbulence model predicted slightly less spreading at higher convective Mach number, but it is not clear if this behavior is due to a favorable response to the convective Mach number increase or an incorrect prediction of spreading rate at smaller velocity ratios. Nevertheless, the reduction in spreading rates at high convective Mach numbers was too small to be of any significance.

Next, Zeman's dilatation dissipation model, as given by Equations (1.3.17) and (1.3.18), was added to the $k-\epsilon$ turbulence model and used to calculate the same set of uniform density supersonic mixing layer cases. The vorticity thickness growth rates obtained from these calculations were normalized by the incompressible vorticity thickness growth rates obtained from Equation (2.2.8) at the same streamwise velocity ratios and with $s = 1$. The results are compared to the experimental data of Bogdanoff (Ref. 52) in Figure 2.19. From this figure it can be seen that Zeman's correction produces a considerable and sudden drop in the vorticity growth rate for convective Mach numbers larger than 0.2, while the experimental results indicate a slow, gradual reduction for convective Mach numbers less than 0.5. Also, the rate of reduction of the growth rate is much faster than the experimental results and the growth rate levels off at a much lower value than that suggested by the experimental results. Figure 2.20 shows the calculated and experimentally (Ref. 55) obtained maximum values of the Reynolds stress as a function of the convective Mach number. Here the calculations, using the Zeman dilatation dissipation model, predict smaller and more rapidly reducing maximum Reynolds stress for increasing convective Mach numbers. This trend is consistent with the large vorticity growth rate reduction discussed above, since as the Reynolds stress reduces, so does the mixing layer growth rate. Therefore, it can be concluded that even though Zeman's correction model produces the general trends, it fails to compare favorably with the experimental results. The application of this model to wall jets and other wall-bounded flows results in solution blow-ups or nonphysical turbulent quantities predictions. This leads to the conclusion that this model is, at best, restricted to free mixing layers, for which it was designed, and is not universal enough to be used in complex flowfields.

2.2.3 Hydrogen-Air Mixing Layers without Chemical Reaction

In this section, mixing layers between a supersonic stream of hydrogen fuel at moderate temperature and a supersonic stream of high temperature air are considered. Physically, such streams go through a chemical reaction process after the turbulent and molecular mixing processes bring the mixture to a stoichiometric proportion. However, the intention of this section is to explore the accuracy of the numerical solver and the turbulence models when applied to turbulent supersonic mixing layers with nonuniform species composition. Therefore, the chemical reaction process is artificially switched off by setting all chemical source terms, in the species transport equations, equal to zero. The numerical solver must now solve for several species mass fraction transport equations in addition to the Navier-Stokes equations and k and ϵ transport equations for the turbulence model. As discussed in Section 2.1.2, the flow solver in the present version of the RPLUS code uses a TVD scheme for the integration of the Navier-Stokes equations and a central differencing method, plus a directional second and fourth order artificial numerical dissipation model for the integration of the species equations and the k - ϵ turbulence model transport equations. The 80×55 clustered grid shown in Figure 2.2 is used here.

The top stream of the supersonic mixing layer considered here was air at Mach number of 1.86, temperature of 1100°K , and pressure of $1.013 \times 10^5 \text{ Nt/m}^2$. The bottom stream was pure hydrogen fuel at Mach number of 1.46, temperature of 450°K , and pressure of $1.013 \times 10^5 \text{ Nt/m}^2$. At these inflow conditions, the air stream's speed of sound propagation was 648.77 m/s with a specific heat ratio of 1.33. The fuel stream's speed of sound was 1612.77 m/s with specific heat ratio of 1.4. This resulted in freestream velocity ratios of $r = u_{\text{air}}/u_{\text{fuel}} = 0.51$ and density ratio of $s = \rho_{\text{air}}/\rho_{\text{fuel}} = 5.86$. Using Equations (2.2.1a), (2.2.1b), and (2.2.2), the convective Mach numbers of the large structure eddies with respect to the two streams can be obtained and are given as $M_{\text{cfuel}} = 0.504$ and $M_{\text{cair}} = 0.517$. The slight difference here is due to the difference between freestream specific heat ratios. Except for the nonuniform species compositions, the controlling parameters for the above mixing layer, i.e., s , r , M_{c1} , and M_{c2} are not very different than the previously studied case of air streams with large temperature difference (see Figures 2.13 through 2.15). Since that case was predicted with a relative degree of success, it was expected that reasonable results could be obtained for the present case. However, contrary to expectation, the solution for the nonuniform species composition case presents several major problems and inaccuracies. The cause of these inaccuracies can be directly traced to the effect of the second and fourth order artificial dissipation model used for the species transport equations, and the creation of large overshoots in the cross-stream profiles of the species mass fractions. Such overshoots result in distorted temperature and pressure profiles. Before presenting the solution of the above flowfield, using a k - ϵ turbulence model, it should be noted that the application of the Prandtl mixing turbulence model, with a turbulent Schmidt number of 0.7, results in a solution with an oscillatory residual. The only way to get rid of the residual oscillations is to increase the turbulence model coefficient, C_m (see Eq. (1.3.19)), by at least 60% to the value of 0.0162. This reinforces the previous observation (see Section 2.2.1 and Figure 2.6a) that the Prandtl mixing turbulence model results in a nonconverging solution

when used with the second and fourth order artificial dissipation model for the solution of any averaged transport equation.

Figure 2.21 presents the convergence history of the solution of the above air/hydrogen mixing layer with a $k-\epsilon$ turbulence model. The density residual drops by about two orders of magnitude after about 1600 iterations and decreases very slowly afterwards. In Figure 2.22a oxygen mass fraction variations in the whole solution domain are shown, indicating overshoots on the air stream side throughout the flowfield. To provide a closer look, the oxygen mass fraction profiles at several downstream locations are shown in Figure 2.22b. It can be clearly seen that there are large overshoots of more than 10% of the maximum allowable level of oxygen mass fraction in the airstream side. The levels of overshoots and undershoots are directly related to the magnitude of the fourth order artificial dissipation coefficients. Due to the absence of any supersonic shock in this flowfield, the second order artificial dissipation term does not play any role here, and its coefficient, κ_2 , in Equation (2.1.17) is set to zero. The presence of the fourth order artificial dissipation term is essential to maintain stability and dissipate high frequency noise in the inviscid portion of the flowfield, outside the turbulent mixing layer. However, it must be much smaller than the physical viscous terms in the mixing layer region. This appears to be the case for most of the flowfield except at the edges of the mixing layer, where the physical viscous terms tend to become very small and the fourth order artificial dissipation terms can become locally large and create the overshoots and undershoots in the profiles of the flow variables being solved for. To minimize this problem, the coefficient of the fourth order artificial dissipation term, κ_4 , in Equation (2.1.18), must be chosen large enough to be effective in the inviscid region and small enough to cause minimum overshoots at the mixing layer edges. Trial and error experimentations indicated that the value of $\kappa_4 = 1/128$ is needed to dissipate high frequency numerical noise in the inviscid region of the flowfield. Unfortunately, this value is not small enough to prevent the occurrence of overshoots at the mixing layer edges. Hence, distorted species mass fraction profiles are obtained, which in turn result in distorted temperature profiles as shown by Figure 2.22c.

The effect of the smoothing of the temperature and species mass fractions at the inflow plane was examined by use of an error function to provide smoothed profiles at the inflow plane. However, this could not prevent the occurrence of the overshoots and merely shifted the location of the maximum overshoots as shown in Figures 2.23a and 2.23b. The basic $k-\epsilon$ turbulence model without any modifications of the model constants was used for these cases. The Zeman's extra compressibility term could not be used with these cases. This model produced such small turbulent diffusivities for species mass fraction equations, with $Sc_t = 0.7$, that the solution blew up. This reconfirms the previous conclusion about the lack of universality of this model for complex supersonic flowfields.

2.2.4 Hydrogen-Air Mixing Layers with Chemical Reaction

In the previous chapter it was shown that the present version of the RPLUS code is incapable of producing an accurate solution for mixing layers between supersonic streams of high temperature air and moderate temperature hydrogen fuel. It was argued that the fourth order artificial dissipation model, needed for the solution of species transport equations, causes nonphysical overshoots in the cross-stream profiles of the species mass fractions. This problem, in a more accurate form, is also present in the chemically reacting cases. In this section the PDF combustion closure model and the finite rate reaction model are considered for the calculation of chemical reactions between an air stream at 1100°K and a hydrogen-nitrogen fuel stream at 450°K.

The top stream of the supersonic reacting mixing layer considered here was air at Mach number of 1.86 and pressure of $1.013 \times 10^5 \text{ Nt/m}^2$. The bottom stream was a mixture of 48.2% hydrogen and 51.8% nitrogen at Mach number of 1.46 and pressure of $1.013 \times 10^5 \text{ Nt/m}^2$. At these inflow conditions the air stream's speed of sound was 648.8 m/s with specific heat ratio of 1.33. The fuel stream's speed of sound was 1162 m/s with specific heat ratio of 1.4. This resulted in freestream velocity ratio of $r = u_{\text{air}}/u_{\text{fuel}} = 0.71$ and density ratio of $s = \rho_{\text{air}}/\rho_{\text{fuel}} = 3.0$. The convective Mach numbers of the large structure eddies with respect to the two streams are given as $M_{\text{cfuel}} = .268$ and $M_{\text{cair}} = .273$. The slight difference is due to the difference between freestream specific heat ratios and one can assume $M_{\text{cfuel}} = M_{\text{cair}} = 0.27$.

To compare the performances of the finite rate reaction model and the PDF reaction model, they were both applied to the flowfield described above. The $k-\epsilon$ turbulence model without any modifications to its modeling constants was used for all calculations presented here. Figures 2.24a and 2.24b show the convergence history of the flowfield's solution for the finite rate reaction model and the PDF reaction model respectively. In neither case does the solution result in a low level of residual after 3,000 iterations. Smoothing of the solution variables at the inflow plane, the use of the Prandtl mixing turbulence model, or the increase of the fourth order artificial dissipation coefficient did not produce a converged solution with a low level of residual for any of the reaction models. In fact, some of these changes caused the solution to blow up. The finite rate reaction model residual curve initially displays large amplitude oscillations. However, after 2500 iterations, declining high frequency oscillations with small amplitude set in. On the other hand, the PDF reaction model residual curve displays low amplitude oscillations with the amplitudes declining as the number of iterations increase. However, the magnitude of the residual increases steadily and appears to level off, after 2700 iterations, to an unacceptable value. Therefore, the residual curves for both reaction models indicate severe problems with the solution of the flowfield.

Since there are no shock waves in the flowfield, there is not sharp local jump in the pressure values and the second order artificial dissipation model is not activated. To get rid of the high frequency numerical noise in the far field solution, the minimum value required

for the fourth order artificial dissipation coefficient, κ_4 , is $1/128$ for the PDF reaction model and $1/32$ for the finite rate reaction model. In the PDF formulation artificial dissipation is used for the solution of the mixture fraction's mean and variance transport equations. In the finite rate reaction formulation, the artificial dissipation is required for the solution of the species transport equations. The fact that κ_4 needed for the finite rate reaction formulation is four times larger than what is needed for the PDF formulation may be due to the exponential source terms appearing in the species transport equations.

Unfortunately, the fourth order artificial dissipation causes large overshoots in the cross-stream profiles of the air and fuel species mass fraction, producing nonphysical behaviors. Figure 2.25a shows the oxygen mass fraction's cross-stream profiles at the inflow plane and at $x = 350$ mm downstream of the inflow plane predicted by the finite rate reaction model. The overshoot in the magnitude of the oxygen mass fraction, at this location, is about 30% larger than the maximum value allowable. Even though the oxygen mass fraction behavior is completely incorrect, the water mass fraction and the mean temperature profiles (see Figures 2.25b and 2.25c) are relatively trouble free, except for their sharp approach to the freestream air values at $0.23 \leq y/H \leq 0.25$. However, the velocity components and pressure field are strongly affected by these nonphysical behaviors and a useless solution is provided. The effect of the fourth order artificial dissipation model on the PDF reaction model is to create overshoots in the mean mixture fraction cross-stream profiles. Here again the predicted water mass fractions and mean temperature profiles appear to follow the expected trends. Figure 2.26a shows the nondimensionalized mean temperature cross-stream profiles at the inflow plane and at the downstream location $x = 350$ mm. The value and the cross-stream location of the maximum temperature achieved in the reaction, as predicted by the PDF reaction model, are slightly lower than those predicted by the finite rate reaction model and the trends are very similar. However, the maximum value of the water mass fraction predicted by the finite rate reaction model is about 50% larger than that predicted by the PDF reaction model as can be seen by comparison of Figures 2.25b and 2.26b. Since none of the reaction models produced a completely accurate and converging solution, no attempt was made to compare the mean temperature and the reaction product's mass fraction with experimental results.

A close look at the mean temperature and water mass fraction profiles predicted by the PDF reaction model reveals that, unlike the finite rate reaction model predictions, the approach to the freestream air values is very smooth. However, the approach to the freestream fuel values is quite bumpy. The cause of this bumpiness goes to the heart of the problem created by the fourth order artificial dissipation model. As explained earlier in Sections 1.6.4 and 2.1.4 the PDF reaction model obtains the mean value of thermodynamic quantities and species mass fractions in the flowfield by constructing the probability density function of the scalar mixture fraction and integrating this function over appropriate thermochemical domains obtained from chemical equilibrium reaction calculations. The construction of the mixture fractions' probability density function is based on the mean and the variance of the mixture fraction obtained from their transport equations. Since the central differencing scheme is used for the spatial integration of these transport equations,

the fourth order artificial dissipation model is added to get rid of high frequency numerical noise created at the far field. Therefore, the overshoots created by the fourth order artificial dissipation in the mean mixture fraction cross-stream profiles affects the calculated value of all of the thermochemical quantities. The values of the mean mixture fraction are bounded by one in the pure fuel stream and zero in the pure oxidizer stream. Therefore, in the case presented here, the mean mixture fraction, $\tilde{\phi}$, is one in the hydrogen-nitrogen stream and zero in the air stream. Since values larger than one and smaller than zero are not allowed, these limits must be enforced if there are any over- or undershoots in the solution of the mean mixture fraction. In the RPLUS code a transport equation is solved for the quantity $\bar{\rho}\tilde{\phi}$. Figure 2.26c presents the cross-stream profiles of the $\bar{\rho}\tilde{\phi}$ at the inflow plane and two downstream planes. The overshoots observed here result in similar overshoots in the profile of the mean mixture fraction, $\tilde{\phi}$. The truncated cross-stream profiles of the mean mixture fraction are presented in Figure 2.26d. The processes of eliminating mean mixture fraction overshoots, near the inflow plane, result in the creation of exaggerated oscillations in its downstream profiles. These oscillations are then reflected in the prediction of the cross-stream profiles of the thermodynamic quantities and species mass fractions, as can be seen in Figure 2.26a and 2.26b.

The results presented in this section indicate that, regardless of the chemical reaction model used, the present version of the RPLUS code is incapable of providing an accurate solution for any type of parallel fuel injection diffusion flame. This conclusion is consistent with the results presented in previous sections. The detailed consideration of a series of mixing layer calculations presented in this chapter strongly points to the method of spatial integration of the scalar transport equation in the RPLUS program as the main source of this problem. This problem can be removed by the use of an upwind integration scheme.

It is clearly impossible to assess the accuracy of the supersonic PDF reaction model on the basis of the results obtained from the present version of the RPLUS program because of inherent inaccuracies of the RPLUS program. However, the comparison of the PDF reaction model results with those of the finite rate reaction model, and the presence of consistent solution trends, indicate that the supersonic PDF reaction model presented here should be pursued further after improving the numerical integration scheme of the RPLUS program.

2.3 Supersonic Wall-Bounded Shear Layers

The prediction capabilities of the present version of the RPLUS program for wall-bounded supersonic shear flows are examined in this section. Supersonic turbulent flows over a flat plate with zero axial pressure gradient and compression ramps are investigated. The range of freestream Mach numbers considered was from one to seven and the Reynolds number, based on the length of the streamwise direction, ranged from 3.8×10^6 to 1.2×10^7 . In all cases air at 318°K with real gas properties was used as the working fluid. No slip, adiabatic wall conditions were assumed for all solid surfaces. Detailed discussion of inflow, outflow, wall, and far field boundary conditions used in the calculations can be found in Section 2.1.5. As explained in the previous chapter the present version of the RPLUS code is

equipped with Jones-Launder (Ref. 29) and the Chien (Ref. 30) versions of the low Reynolds number $k-\epsilon$ turbulence model, in addition to the Baldwin-Lomax (Ref. 33) zero-equation turbulence model. Jones-Launder and Chien turbulence models were developed for incompressible wall-bounded flowfields with moderate temperature and density variations across the flowfield. Chien's model uses the normal distance from a solid wall to account for the near wall effects. On the other hand the Jones-Launder model's low Reynolds number correction terms are not explicitly functions of the normal distance from a solid surface and are more attractive for complex flowfields where solid surfaces at different angles to the mean flow direction and regions of separated and recirculating flowfields are present. In this model, the low Reynolds number effects are accounted for through the use of a local turbulent Reynolds number (see Table 1 in Section 1.3.2). This method of accounting for the near wall effects appears to cause large inaccuracies in the prediction of high Mach number supersonic flows over an adiabatic flat plate. In these cases, the density variation becomes very large across the boundary layer, with a very large gradient near the wall. The local turbulent Reynolds number used by the Jones-Launder model is affected by these density variations, whereas the Chien's model is not greatly influenced. Due to this inadequacy of the Jones-Launder model, this model's results are not discussed any further and the results presented are those of Chien's model. The use of the Zeman dilatation dissipation term for wall-bounded flows results in negative values of turbulent kinetic energy close to the wall and cannot be used in its original form, for these flowfields.

The use of a low Reynolds number $k-\epsilon$ turbulence model makes it possible to integrate the turbulence model's transport equations all the way to the wall and avoids the use of turbulent wall functions (Ref. 17). However, a very fine grid spacing is required to capture the large gradients of turbulent quantities in the near wall region. Letting τ_w , ρ_w , and μ_w denote shear stress, density and dynamic molecular viscosity at the wall, the friction velocity can be defined as $u^* = (\tau_w / \rho_w)^{1/2}$. Using this friction velocity, the normal distance from the wall can be normalized as $y^+ = y \rho_w u^* / \mu_w$. This quantity represents a highly stretched normal distance from the wall such that for a turbulent boundary layer the laminar sublayer is at about $y^+ \leq 7$, inertia region is at $7 \leq y^+ \leq 30$, and the outer edge of the boundary layer is typically at $y^+ \sim 1000$. To properly resolve the near wall region, a layer of nodes at the distance $y^+ < 1$ is needed. Therefore, a stretched mesh is used to reduce the number of grid points used in a calculation. It has been observed that the RPLUS code does not perform well when the stretching between two adjacent cells is more than ten percent. Therefore, for a given freestream Mach number and Reynolds number at the inflow plane, a smoothly varying stretched grid is generated with the first node layers away from the wall at $y^+ < 1$. Figures 2.27a and 2.27b show the grid for a flat plate supersonic flow with $M_\infty = 3.0$ and $Re_\infty = 2.5 \times 10^6$. The height of the domain is $H = 0.02$ m and its length is $L = 0.10$ m. Coordinate axes are normalized by the height of the domain. To check the solutions' grid dependence, the number of grid points were increased by a factor of two. In all flat plate cases considered here, the doubling of the grid points caused the calculated skin friction to change by less than one percent and solutions were considered grid independent.

Figure 2.28 shows the convergence history of the solution of a turbulent supersonic flow over a flat plate with inflow freestream Mach number, $M_\infty = 3$ and Reynolds number, $Re_\infty = 2.5 \times 10^6$. Chien's low Reynolds number $k-\epsilon$ turbulence model is used for this calculation. The density residual drops by three orders of magnitude after 3500 iterations and it gradually decreases, indicating a converged solution. The turbulent kinetic energy residual curve and kinetic energy dissipation residual curve follow a similar pattern as the density residual curve. The comparison of the calculated mean streamwise velocity profile with the experimental results of Laderman (Ref. 56) and Robinson et al (Ref. 57) is shown in Figure 2.29. This figure indicates that the calculated results compare well with the experimental data. The second Crocco-Busemann (Ref. 58) relation between static temperature and streamwise velocity for an ideal gas compressible boundary layer on an adiabatic flat plate with zero pressure-gradient is given as

$$T = - \frac{Pr}{2c_p} u^2 + T_w$$

where Pr is the Prandtl number and c_p is the specific heat at constant pressure. Figure 2.30 shows the calculated variation of the mean static temperature with respect to mean streamwise velocity across the boundary layer. The theoretically expected variation of temperature with respect to the streamwise velocity obtained from the second Crocco-Busemann relation is also shown in this figure. The comparison indicates a good agreement between the calculated results and the theoretical relationship, especially as one approaches the wall. The deviation of the predicted results from the Crocco-Busemann relation is caused by the fact that the recovery factor, defined as

$$r = 2c_p(T_w - T_\infty)/u_\infty^2$$

is assumed equal to the Prandtl number in the Crocco-Busemann relation. The predicted recovery factor is 0.85, which is 13% larger than the value of the Prandtl number, $Pr = 0.75$. The experimental results of Laderman (Ref. 56) indicate that the recovery factor for the above case is about 0.907, which is 6% larger than the predicted value, and 21% larger than the value of the Prandtl number. Other experiments (Ref. 58) also indicate that the recovery factor is approximately equal to $(pr)^{1/3}$. Therefore, the predicted result is closer to the experimental results.

u^+ represents the mean streamwise velocity normalized with the friction velocity. The u^+ profile versus y^+ for $M_\infty = 3$ boundary layer is given in Figure 2.31. The incompressible boundary layer velocity profile given by $u^+ = y^+$ for $y^+ < 10$, and $u^+ = 2.5 \ln y^+ + 5.5$ for $y^+ > 10$ is also shown in the same figure. Experiments (Ref. 19) indicate that in the wake region of the turbulent boundary layer the supersonic u^+ values fall below the incompressible values at the same y^+ location. However, the difference displayed in Figure 2.31 is much larger than the expected drop. This behavior can be explained by examination of the calculated skin friction values, defined as

$$C_f = \frac{\tau_w}{\frac{1}{2} \rho_\infty u_\infty^2}$$

Figure 2.32 presents the calculated skin friction values for a range of freestream Mach numbers at the location where $Re_x \sim 10^7$. The calculated value at $M_\infty = 3$ is about ten percent larger than the experimental value (Ref. 56). Such a small difference can not produce the observed behavior in the u^+ profile. However, comparison of the calculated supersonic skin frictions normalized with the incompressible skin friction with the theoretical formula proposed by Van Driest (Ref. 59) (see Figure 2.32b) indicates that there are large differences between the calculated and theoretical normalized skin frictions. The differences reduce substantially as the Mach number increases. However, at $M_\infty = 3$ there is about 25 percent difference between the predicted and theoretical results. Recalling that $u^+ = u/u^*$, where u^* is the friction velocity, one can see that the large value of the predicted ratio of compressible skin friction to incompressible skin friction, results in the small values of the u^+ observed in Figure 2.31.

For the case of $M_\infty = 3.0$ the predicted total shear stress is normalized by the wall shear stress, and its distribution across the boundary layer is compared with the experimental results of Laderman and Demetriades (Ref. 60) in Figure 2.33a. As can be seen in this figure, the predicted magnitude and cross-stream variation of this quantity are in good agreement with the experimental results. In Figure 2.33b the $M_\infty = 5$ shear stress distribution and the Sandborn (Ref. 61) best estimate curves are also shown. The predicted shear stresses at $M_\infty = 3$ are slightly below the Sandborn curves, whereas the values for $M_\infty = 5$ are consistently larger and closer to the Sandborn best estimate curves.

Next, to evaluate the accuracy of the $k-\epsilon$ turbulence model used in the calculation, the predicted turbulent quantities are compared with the available experimental results. Figures 2.34a and 2.34b show the streamwise and transverse velocity fluctuations for $M_\infty = 3$ case. Velocity fluctuations are defined as

$$u' = (\overline{u'^2})^{1/2} \quad \text{and} \quad v' = (\overline{v'^2})^{1/2}$$

The predicted results are compared with the experimental results of Laderman and Demetriades (Ref. 60) and Robinson et al (Ref. 57). Clearly, the most important shortcoming of the $k-\epsilon$ turbulence model is the isotropic nature of this model. The model predicts very similar values and distributions for the streamwise and transverse velocity fluctuations in the boundary layer. The predicted locations of peak values of these quantities are very close to the experimental values; however, the magnitude of the peak values are underestimated by about 25 percent. The transverse velocity fluctuations are in good agreement with the hotwire measurements across the turbulent boundary layer except close to the wall region. On the other hand, the streamwise velocity fluctuations are overpredicted by about ten percent across the boundary layer, except close to the wall, where they are underpredicted by 25 percent. The experimental results (Ref. 60) indicate that the streamwise velocity fluctuations rapidly decrease with increasing freestream Mach numbers. The streamwise

velocity fluctuation is normalized with the friction velocity, and variations of its values at the point $y/\delta = 0.5$, in the turbulent boundary layer, are compared with experimental values in Figure 2.35a (δ denotes the boundary layer thickness). This figure indicates that the present calculations correctly predict the expected decrease of streamwise velocity fluctuation with increasing Mach numbers. The only problem is that a similar behavior is predicted for the transverse velocity fluctuations, whereas the experiments show that the transverse velocity fluctuations are independent of the freestream Mach numbers. Therefore, the increasing freestream Mach number results in a highly anisotropic flow, characterized by transverse velocity fluctuations being much larger than the streamwise velocity fluctuations. The $k-\epsilon$ turbulence model in its present form is incapable of predicting such anisotropic behavior.

The Reynolds stress correlation coefficient is defined as

$$R_{uv} = \frac{\overline{-u''v''}}{(\overline{u''^2})^{1/2} (\overline{v''^2})^{1/2}}$$

The predicted correlation coefficients at $y/\delta = 0.5$ are equal to 0.3 for all Mach numbers considered. As shown in Figure 2.35b, the above predicted value is very close to the experimental results of Yantal and Lee (Ref. 65) at Mach 3. However, based on a large pool of experimental results, Laderman and Demetriades (Ref. 60) have decided that the value of the Reynolds stress correlation coefficient at $y/\delta = 0.5$ is independent of both Mach number and wall temperature and is approximately 0.5. This experimental value is about 65 percent larger than the predicted value of the correlation coefficient; however, from the point of view of turbulence modeling it is important that the calculations correctly predict the independence of this quantity from Mach number changes.

Figure 2.36a shows the maximum values of the turbulent kinetic energy, normalized by the friction velocity, at the downstream location where $Re_x \sim 10^7$ as a function of Mach number. This figure indicates that the maximum turbulent kinetic energy decreases with increasing freestream Mach number; however, the rate of decrease of this quantity reduces considerably for freestream Mach numbers larger than five. Figure 2.36b shows the normalized transverse location of the maximum turbulent kinetic energy in the boundary layer. It is interesting to note that both the maximum value of the turbulent kinetic energy and its transverse location decrease with the freestream Mach number. The available experimental results were not sufficient to substantiate this trend.

Based on the examination of the predicted results provided by the present version of the RPLUS code with a low Reynolds number $k-\epsilon$ turbulence model, it can be concluded that, except for inherent shortcomings of the $k-\epsilon$ turbulence model, the calculated results compare favorably with available experimental data for supersonic flows over a flat plate.

The application of the present version of the RPLUS code with the Chien's $k-\epsilon$ turbulence model to 8, 10, and 20 degree compression ramps was not satisfactory. At small ramp angles erroneous solutions were obtained and at large ramp angles the solution blew up. To understand the basic reason behind these problems, the solution of a Mach 2.87 flow over an adiabatic eight-degree ramp is considered. A 121×101 stretched grid with the first transverse node layers at $y^+ < 1$ (see Figure 2.37) was used. The height of the domain was $H = .12$ m and its length was $L = .48$ m. Coordinate axes were normalized with the height of the domain. Figure 2.38 shows the convergence history of the solution. The density residual drops by two orders of magnitude after 2700 iterations and is gradually decreasing, indicating a converged solution. Figure 2.39 shows the comparison of the predicted surface static pressure distribution with the experimental data of Settles et al (Ref. 67). This figure indicates that the pressure profile across the shock is well captured. However, the comparison of the predicted skin friction with the experimental results (see Figure 2.40) indicates that the skin friction is greatly overpredicted. The incorrect behaviors of the turbulent kinetic energy and the turbulent kinetic energy dissipation rate in the flowfield cause such erroneous results. The reason for this behavior in the solution of the $k-\epsilon$ equation is the large levels of second and fourth order numerical dissipation coefficients required to obtain the above converged solution. In the calculation of flat plate cases discussed earlier the second order and the fourth order artificial dissipation coefficients, κ_2 and κ_4 , were set to zero and the $1/128$ respectively. For the 8 degree ramp case minimum coefficients required to obtain a solution were $\kappa_2 = 15$ and $\kappa_4 = 1/16$. Subsequently, these large numerical dissipation terms completely distorted the solution of the $k-\epsilon$ equations, resulting in the wrong skin friction coefficient and other flow quantities. The same difficulty was present for the ten and twenty degree ramp cases. A survey of the current literature on the application of higher order turbulence models to flowfields with shock waves indicates that a numerical scheme with a robust numerical dissipation, such as MacCormack's scheme (Ref. 68) or a TVD scheme (Ref. 46), is needed in the $k-\epsilon$ solver to have a well behaved solution for the turbulent quantities. Here, as in the case of chemically reacting mixing layers, it is clear that the lack of a TVD scheme for the solution of the turbulence model's transport equations is the main cause of the failure of the present version of the RPLUS code in the case of relatively complex flowfields. It is recommended that a general TVD scheme be developed and incorporated into the RPLUS code before any further improvement of the turbulence and combustion models.

CHAPTER 3. JOINT PDF ANALYSIS OF COMPRESSIBLE FLOWS.

The objective of this chapter is the study of various formulations of pdf equations for compressible turbulent flows and the analysis of their structural properties. The results to be reported here are the analysis of a prescribed pdf formalism suitable for reacting compressible flows, theoretical study of the joint pdf of nonreacting compressible flows, and the study of random discontinuities in compressible flows and their effect on pdf methods.

3.1 Prescribed pdf formalism for compressible turbulent flows with combustion.

Compressible turbulent flows with combustion reactions that are assumed infinitely fast can be described locally by three thermodynamic variables. There are several equivalent possibilities for the choice of these variables and in the present case the set (ζ, u, ρ) will be considered, where ζ denotes mixture fraction, u the specific internal energy and ρ the density. This particular set is appropriate for implementation in a general solver (RPLUS) for compressible flows. The calculation of the mean thermodynamic state requires then the pdf $f(\zeta, u, \rho; \underline{x}, t)$ of the three scalar variables and the expectation of any local function Φ of the scalars follows from

$$\langle \Phi \rangle(\underline{x}, t) = \int d\zeta \int du \int d\rho \Phi(\zeta, u, \rho) f(\zeta, u, \rho; \underline{x}, t) \quad (3.1.1).$$

The integration is carried out over the set S_3 of all realizable states called scalar space. There two methods for the determination of the pdf and in the present case only the explicit construction of the pdf in the form of a functional relation to selected moments of order one and two will be discussed. The construction of the pdf depends crucially on the geometry of the scalar space S_3 spanned by the set of all realizable values for the scalar variables. For mixture fraction, internal energy and density it follows that S_3 is given by

$$S_3 = \{(\zeta, u, \rho) : 0 \leq \zeta \leq 1, u_o(\zeta) \leq u \leq u_1(\zeta), \rho_o(\zeta) \leq \rho \leq \rho_1(\zeta)\} \quad (3.1.2)$$

where $u_o(\zeta), \rho_o(\zeta)$ and $u_1(\zeta), \rho_1(\zeta)$ are extremal values for the internal energy and density depending on mixture fraction which can be estimated from an expected pressure variation in the flow field. If such estimates cannot be established, internal energy should vary in an interval given by realizable states (which depends on mixture fraction) and density in $[0, \infty)$. The scalar space is of sufficiently simple structure to allow construction of the pdf. Several possibilities will be considered.

3.1.1 Specification of order one and two moments.

The method of constructing the pdf consists of two steps: First mappings are used to transform each scalar to an image variable with the range $(-\infty, \infty)$. Then a three-dimensional Gaussian pdf for the image variables is constructed which requires exactly all moments of order one and two. However, nonlinear mappings imply that first and second order moments

of the image variables depend possibly on a larger set of moments or all moments of the original variables, which defeats the purpose of constructing the pdf from first and second order moments only. However, the geometry of the scalar space contains information on possible correlations, which may prove valuable for the construction of the pdf. This will be exploited in chapter 4 in the context of the zero Mach-number limit.

3.1.2 Independent variables.

The scalar space is assumed to be a cube. This case serves as an example only and will be shown to be unacceptable for reacting flows, but quite realistic for the nonreacting case. All moments of order one and all variances are specified and the variables are assumed independent. It follows that the pdf is then the product of the single scalar pdfs

$$f(\zeta, u, \rho) = f_\zeta(\zeta)f_u(u)f_\rho(\rho) \quad (3.1.3)$$

The most important quantity to be calculated from the pdf is the mean pressure $\langle p \rangle$, which enters the averaged balance equations for momentum and energy thus modifying the flow field according to the heat released by the combustion reactions. The functional relation of the pdfs f_i to the respective moments is set up as follows. Mixture fraction varies in the unit interval and for this reason the beta-function B is chosen as realizable pdf.

$$B(\zeta; \underline{x}, t) = \frac{1}{N} \zeta^{\alpha-1} (1 - \zeta)^{\beta-1} \quad (3.1.4)$$

where the exponents α and β depend on mean and variance of mixture fraction and N denotes the normalizing denominator defined by

$$N \equiv \int_0^1 d\zeta \zeta^{\alpha-1} (1 - \zeta)^{\beta-1} \quad (3.1.5)$$

The exponents can be expressed in terms of the mean and variance

$$\alpha = \tilde{\zeta} \left(\frac{\tilde{\zeta}(1 - \tilde{\zeta})}{\widetilde{\zeta'^2}} - 1 \right) \quad (3.1.6)$$

$$\beta = (1 - \tilde{\zeta}) \left(\frac{\tilde{\zeta}(1 - \tilde{\zeta})}{\widetilde{\zeta'^2}} - 1 \right) \quad (3.1.7)$$

where the tilde indicates Favre-averaging. The denominator can be evaluated using the Gamma-function.

$$N = \frac{\Gamma(\alpha)\Gamma(\beta)}{\Gamma(\alpha + \beta)} \quad (3.1.8)$$

It remains to set up the modelled transport equations for the mean $\tilde{\zeta}$ and the variance $\widetilde{\zeta'^2}$. It follows from the instantaneous balance for mixture fraction

$$\rho \left(\frac{\partial}{\partial t} + v_\alpha \frac{\partial}{\partial x_\alpha} \right) \zeta = \frac{\partial}{\partial x_\alpha} \left(\rho \Gamma \frac{\partial \zeta}{\partial x_\alpha} \right) \quad (3.1.9)$$

that mean and variance are governed by

$$\langle \rho \rangle \left(\frac{\partial}{\partial t} + \tilde{v}_\alpha \frac{\partial}{\partial x_\alpha} \right) \tilde{\zeta} = \frac{\partial}{\partial x_\alpha} \left\{ \left(\langle \rho \rangle \Gamma + \frac{\mu_t}{\sigma_\zeta} \right) \frac{\partial \tilde{\zeta}}{\partial x_\alpha} \right\} \quad (3.1.10)$$

where μ_t denotes the turbulent viscosity and

$$\langle \rho \rangle \left(\frac{\partial}{\partial t} + \tilde{v}_\alpha \frac{\partial}{\partial x_\alpha} \right) \tilde{\zeta}''^2 = \frac{\partial}{\partial x_\alpha} \left\{ \left(\langle \rho \rangle \Gamma + \frac{\mu_t}{\sigma_{\zeta^2}} \right) \frac{\partial \tilde{\zeta}''^2}{\partial x_\alpha} \right\} + 2 \frac{\mu_t}{\sigma_\zeta} \frac{\partial \tilde{\zeta}}{\partial x_\alpha} \frac{\partial \tilde{\zeta}}{\partial x_\alpha} - 2 \langle \rho \rangle \tilde{\epsilon}_\zeta \quad (3.1.11)$$

where $\tilde{\epsilon}_\zeta$ denotes the scalar dissipation rate. This completes the construction of the pdf for mixture fraction. Since the scalar space is a cube, both internal energy and density vary in domains with bounds independent of the scalars. Therefore, normalized variables can be defined which are statistically independent. First and second order moments must be specified for density and internal energy if pdfs such as the beta-function are employed. Density will be considered next. Mass balance appears in Favre-averaged form as

$$\frac{\partial \langle \rho \rangle}{\partial t} + \frac{\partial}{\partial x_\alpha} (\langle \rho \rangle \tilde{v}_\alpha) = 0 \quad (3.1.12)$$

and the variance $\langle \rho'^2 \rangle$ is governed by

$$\left(\frac{\partial}{\partial t} + \tilde{v}_\alpha \frac{\partial}{\partial x_\alpha} \right) \langle \rho'^2 \rangle = - \frac{\partial}{\partial x_\alpha} \langle \rho'^2 v''_\alpha \rangle - 2 \langle \rho'^2 \rangle \frac{\partial \tilde{v}_\alpha}{\partial x_\alpha} - 2 \langle \rho' v''_\alpha \rangle \frac{\partial \langle \rho \rangle}{\partial x_\alpha} - \langle \rho'^2 \rangle \frac{\partial v''_\alpha}{\partial x_\alpha} - 2 \langle \rho \rangle \langle \rho' \frac{\partial v''_\alpha}{\partial x_\alpha} \rangle \quad (3.1.13)$$

Closure models are required for turbulent diffusion and three of the four source/sink terms in (3.1.13). It is worth noting that none of the source terms is clearly destructive or productive in contrast to the variance of mixture fraction for instance. The first (and closed) source term

$$Q_1 \equiv -2 \langle \rho'^2 \rangle \frac{\partial \tilde{v}_\alpha}{\partial x_\alpha}$$

is apparently productive for compression in the mean and destructive for expansion. The second term

$$Q_2 \equiv -2 \langle \rho' v''_\alpha \rangle \frac{\partial \langle \rho \rangle}{\partial x_\alpha}$$

is clearly productive if the gradient-flux model holds as in crossflow direction of boundary-layer flows, but is destructive in longitudinal direction as measurements in turbulent diffusion flames have shown (see Ref.41). The third term

$$Q_3 \equiv - \langle \rho'^2 \rangle \frac{\partial v''_\alpha}{\partial x_\alpha}$$

is also productive for fluctuating compression and destructive for expansion like Q_1 . The last term

$$Q_4 \equiv -2 \langle \rho \rangle \langle \rho' \frac{\partial v''_\alpha}{\partial x_\alpha} \rangle$$

is difficult to estimate. There are two obvious possibilities: ρ' and the fluctuating divergence of velocity are weakly correlated or strongly correlated. Q_4 can be neglected in the first case. In the second case of strong correlation it is likely that compression (negative divergence) implies positive density fluctuation and expansion negative ρ' . Hence is Q_4 in essence a production term in this case. However, no estimate for its magnitude can be offered at present. The particular case of density weighted pdfs requires also the third moment as will be shown later. The transport equation for the third moment can be derived in same manner as for the variance. The result appears in the form

$$\left(\frac{\partial}{\partial t} + \bar{v}_\alpha \frac{\partial}{\partial x_\alpha}\right) \langle \rho'^3 \rangle = -\frac{\partial}{\partial x_\alpha} \langle \rho'^3 v''_\alpha \rangle - 3 \langle \rho'^3 \rangle \frac{\partial \bar{v}_\alpha}{\partial x_\alpha} - 3 \langle \rho'^2 v''_\alpha \rangle \frac{\partial \langle \rho \rangle}{\partial x_\alpha} - 2 \langle \rho'^3 \rangle \frac{\partial v''_\alpha}{\partial x_\alpha} - 3 \langle \rho \rangle \langle \rho'^2 \rangle \frac{\partial v''_\alpha}{\partial x_\alpha} \quad (3.1.14)$$

There are four source/sink terms describing the interaction of the turbulence with the mean rate of strain and the mean density gradient, and the interaction of the fluctuating density with the fluctuations of the rate of volume expansion. It will be shown in chapter 4 that the prediction of the pdf with nonzero density fluctuations due to compressibility effects requires the third moment.

3.1.3 Statistical independence in transformed scalar spaces.

All moments of order one and all variances are specified and the variables are assumed independent. Furthermore, the case that the variances for certain functions of internal energy and density are set to zero, is also considered. The trivial case is obtained if the mappings are identities. If the variances for density and internal energy are zero, it follows that the expectation of any local function Φ of the scalars is given by

$$\langle \Phi \rangle(\underline{x}, t) = \langle \rho \rangle \int_0^1 d\zeta \frac{\Phi(\zeta, \bar{u}, \langle \rho \rangle)}{\rho} f(\zeta; \underline{x}, t).$$

where \hat{f} denotes the unweighted pdf. This restricted definition of the pdf

$$f(\zeta, u, \rho) = f_\zeta(\zeta; \underline{x}, t) \delta(u - \bar{u}) \delta(\rho - \langle \rho \rangle) \quad (3.1.15)$$

is applicable if the scalar space is a cube. It should be noted, however, that the scalar space cannot be a cube if one of the scalars is enthalpy or internal energy and chemical reactions take place, because the enthalpies of formation for reactants and products are different and extension of the scalar space to a cube can lead to unphysical states (negative absolute temperatures).

The mean pressure plays a central role in the solution procedure RPLUS and it is of prime importance to calculate the derivatives of $\langle p \rangle$ with respect to the other dependent variables. Let the mean pressure be given by

$$\langle p \rangle = \langle \rho \rangle \int_0^1 d\zeta \int_{u_0(\zeta)}^{u_1(\zeta)} du \int_{\rho_0(\zeta)}^{\rho_1(\zeta)} d\rho \frac{p(\zeta, u, \rho)}{\rho} f(\zeta, u, \rho; \bar{\zeta}, \bar{\zeta}''^2, \bar{u}, \bar{u}''^2, \langle \rho \rangle, \langle \rho'^2 \rangle, \langle \rho'^3 \rangle) \quad (3.1.16)$$

where $p(\zeta, u, \rho)$ is the local thermodynamic relation of the pressure to the scalars and the integration is carried out over the scalar domain. The essence of the prescribed pdf formalism is the assumption of the local dependence of the pdf on the selected set of moments $\tilde{\zeta}, \tilde{\zeta}''^2, \tilde{u}, \tilde{u}''^2, \langle \rho \rangle, \langle \rho'^2 \rangle$, which are called defining variables. Since this functional relation is known, it follows that the derivatives of the mean pressure or the expectation of any other function of the scalars with respect to the variables in this set can be established. For instance, the derivative of $\langle p \rangle$ with respect to $\tilde{\zeta}$ is given by

$$\frac{\partial \langle p \rangle}{\partial \tilde{\zeta}} = \langle \rho \rangle \int_0^1 d\zeta \int_{u_0(\zeta)}^{u_1(\zeta)} du \int_{\rho_0(\zeta)}^{\rho_1(\zeta)} d\rho \frac{p(\zeta, u, \rho)}{\rho} \frac{\partial f}{\partial \tilde{\zeta}} \quad (3.1.17)$$

and the derivative of the pdf can be calculated explicitly.

3.1.4 Construction of the pdf.

The density-weighted pdf for mixture fraction, internal energy and density will be constructed in the form of a product of functions given by

$$f(\zeta, u, \rho) = f_\zeta(\zeta) f_u^*(u^*(\zeta, u, \rho)) f_\rho^*(\rho^*(\zeta, u, \rho)) \quad (3.1.18)$$

and the variables u^* and ρ^* are functions of ζ, u, ρ such that $f_u^* = \delta(u^* - \langle u^* \rangle)$ and $f_\rho^* = \delta(\rho^* - \langle \rho^* \rangle)$ implies the properties of a turbulent flame at zero Mach-number. It follows from the fact that the zero Mach-number flame burns (in first order approximation) at constant pressure that the mean value $\langle u^* \rangle$ must be a function of $\zeta, \langle p \rangle$ and the mean value $\langle \rho^* \rangle$ a function of $\zeta, \langle p \rangle, u^*$. Constructing the pdf f as product of beta functions for all three independent variables implies then that the variances for u^* and ρ^* are measures for the effect of compressibility on the flow. The coupling with the mean pressure makes the relations very complex and iterative procedures would be required for the calculation of the moments of u^* and ρ^* in terms of the moments of u and ρ . Hence, an approximation in the form

$$u^*(\zeta, u) \equiv \frac{u - u_0(\zeta)}{u_1(\zeta) - u_0(\zeta)} \quad (3.1.19)$$

and

$$\rho^*(\zeta, \rho) \equiv \frac{\rho - \rho_0(\zeta)}{\rho_1(\zeta) - \rho_0(\zeta)} \quad (3.1.20)$$

will be considered, where u_1, u_0, ρ_1 and ρ_0 are the bounds for internal energy and density at a given value for the mixture fraction. If u^* and ρ^* are kept at fixed values, thermodynamic relations $\phi(\zeta)$ are produced (by interpolation in the three-dimensional table), which will not agree with the zero Mach-number limit, where enthalpy is a linear function of mixture fraction and the pressure is constant. However, the choice of the bounds $u_1(\zeta)$, etc. allows the approximation of this limit if the shape of the accessible domain corresponds to constant pressure surfaces. The pdf f constructed with the density-weighted moments (except density) is regarded as density-weighted pdf. It follows that the unweighted pdf is given by

$$\hat{f}(\zeta, u, \rho) = \frac{\langle \rho \rangle}{\rho} f(\zeta, u, \rho) \quad (3.1.21)$$

The construction of f according to (3.1.18) is based on selected moments. The moments of mixture fraction ζ are given by

$$\tilde{\zeta}^n = \int_0^1 d\zeta \int_0^1 du^* \int_0^1 d\rho^* \zeta^n [u_1(\zeta) - u_0(\zeta)] [\rho_1(\zeta) - \rho_0(\zeta)] f(\zeta, u^*, \rho^*)$$

and it is clear that choosing the beta function for f_ζ in (3.1.18) violates normalisation. Hence, the modified beta function

$$f_\zeta(\zeta) = \frac{B(\zeta; \alpha, \beta)}{[u_1(\zeta) - u_0(\zeta)] [\rho_1(\zeta) - \rho_0(\zeta)]} \quad (3.1.22)$$

is the correct choice and it follows that the marginal pdf for mixture fraction is indeed the beta function and the exponents α and β are determined by the moments $\tilde{\zeta}$ and $\tilde{\zeta}''^2$ according to (3.1.6) and (3.1.7). It remains to establish the moments of u^* and ρ^* in terms of the moments of u and ρ . Noting that

$$\begin{aligned} & \int_0^1 d\zeta \int_{u_0(\zeta)}^{u_1(\zeta)} du \int_{\rho_0(\zeta)}^{\rho_1(\zeta)} d\rho u f(\zeta, u, \rho) = \\ & \int_0^1 d\zeta \int_0^1 du^* \int_0^1 d\rho^* [u_0(\zeta) + u^*(u_1(\zeta) - u_0(\zeta))] B(\zeta; \alpha, \beta) f_u^*(u^*) f_\rho^*(\rho^*) \end{aligned}$$

holds, we get

$$\langle u^* \rangle = \frac{\tilde{u} - \tilde{u}_0}{\tilde{u}_1 - \tilde{u}_0} \quad (3.1.23)$$

where $\langle u^* \rangle$ is the mean value required for the construction of f_u^* . The variance of u follows in the same manner as

$$\langle u^{*2} \rangle = \frac{\widetilde{u''^2} - \widetilde{u_0''^2} - (u_1'' - u_0'')^2 \langle u^* \rangle^2 - 2(\widetilde{u_0'' u_1''} - \widetilde{u_0''^2}) \langle u^* \rangle}{(\tilde{u}_1 - \tilde{u}_0)^2 + (u_1'' - u_0'')^2}$$

or in semi-implicit form

$$\langle u^{*2} \rangle = \frac{\widetilde{u''^2} + \tilde{u}^2 - \tilde{u}_0^2 - 2\langle u^* \rangle (\widetilde{u_0 u_1} - \tilde{u}_0^2)}{(\tilde{u}_1 - \tilde{u}_0)^2} - \langle u^* \rangle^2 \quad (3.1.24)$$

The relations for the moments of density are somewhat different because f is density weighted. It follows that

$$\frac{\langle \rho'^2 \rangle}{\langle \rho \rangle} + \langle \rho \rangle = \tilde{\rho}_0 + \langle \rho^* \rangle (\tilde{\rho}_1 - \tilde{\rho}_0) \quad (3.1.25)$$

and

$$\frac{\langle \rho'^3 \rangle}{\langle \rho \rangle} + 3\langle \rho'^2 \rangle + \langle \rho \rangle^2 = \tilde{\rho}_0^2 + 2\langle \rho^* \rangle (\widetilde{\rho_0 \rho_1} - \tilde{\rho}_0^2) + \langle \rho^* \rangle^2 (\tilde{\rho}_1 - \tilde{\rho}_0)^2 + \langle \rho^{*2} \rangle (\tilde{\rho}_1 - \tilde{\rho}_0)^2 \quad (3.1.26)$$

hold. It is worth noting that the first three moments of ρ are required to determine the first two moments of ρ^* . Two possible forms for the pdf f will be considered

$$f(\zeta, u, \rho) = \frac{B(\zeta)B(u^*(\zeta, u))B(\rho^*(\zeta, \rho))}{[u_1(\zeta) - u_0(\zeta)][\rho_1(\zeta) - \rho_0(\zeta)]} \quad (3.1.27)$$

and

$$f(\zeta, u, \rho) = \frac{B(\zeta)\delta(u^*(\zeta, u) - \langle u^* \rangle)\delta(\rho^*(\zeta, \rho) - \langle \rho^* \rangle)}{[u_1(\zeta) - u_0(\zeta)][\rho_1(\zeta) - \rho_0(\zeta)]} \quad (3.1.28)$$

where the second form corresponds to the zero Mach-number limit if the scalar space is chosen appropriately. It is important for the calculation of the derivatives to note the dependence of the various defining moments on the solution variables $(\tilde{\zeta}, \tilde{\zeta}''^2, \tilde{u}, \tilde{u}''^2, \langle \rho \rangle, \langle \rho'^2 \rangle, \langle \rho'^3 \rangle)$ which are not identical with the defining moments. First we note that

$$B(\zeta) = B(\zeta; \tilde{\zeta}, \tilde{\zeta}''^2)$$

holds. Likewise we get for internal energy

$$B(u^*) = B(u^*; \langle u^* \rangle, \langle u^{*'}^2 \rangle)$$

but the defining moments are not solution variables. The equations (3.1.23) and (3.1.24) show that

$$\langle u^* \rangle = F(\tilde{u}, \tilde{\zeta}, \tilde{\zeta}''^2)$$

and

$$\langle u^{*'}^2 \rangle = F(\tilde{u}, \tilde{u}''^2, \tilde{\zeta}, \tilde{\zeta}''^2)$$

hold, because \tilde{u}_1 etc. depend on $\tilde{\zeta}$ and $\tilde{\zeta}''^2$ via $B(\zeta)$. Turning to density we get

$$B(\rho^*) = B(\rho^*; \langle \rho^* \rangle, \langle \rho^{*'}^2 \rangle)$$

but the defining moments are not solution variables. The equations (3.1.25) and (3.1.26) show that

$$\langle \rho^* \rangle = F(\langle \rho \rangle, \langle \rho'^2 \rangle, \tilde{\zeta}, \tilde{\zeta}''^2)$$

and

$$\langle \rho^{*'}^2 \rangle = F(\langle \rho \rangle, \langle \rho'^2 \rangle, \langle \rho'^3 \rangle, \tilde{\zeta}, \tilde{\zeta}''^2)$$

hold, because $\tilde{\rho}_1$ etc. depend on $\tilde{\zeta}$ and $\tilde{\zeta}''^2$ via $B(\zeta)$.

3.1.5 Derivatives with respect to the defining moments: Beta -function.

The derivatives of a beta function with respect to the defining moments can be evaluated using properties of the Γ -function and implicit differentiation. Let f_ζ be the beta-function (3.1.4). It follows that

$$\frac{\partial f}{\partial \tilde{\zeta}} = f \left\{ \frac{\partial \alpha}{\partial \tilde{\zeta}} \log(\zeta) + \frac{\partial \beta}{\partial \tilde{\zeta}} \log(1 - \zeta) - \frac{\partial \log(N)}{\partial \tilde{\zeta}} \right\}$$

holds. Note that the integrand is modified by the logarithms which put more weight to the values of $p(\zeta, u, \rho)$ at the end points of the range of ζ . It follows, however, that this derivative becomes singular if the pdf is not bounded at these end points. The derivative of N appears as combination of Gamma-functions

$$\frac{\partial \log(N)}{\partial \tilde{\zeta}} = \frac{\partial \log(\Gamma(\alpha))}{\partial \tilde{\zeta}} + \frac{\partial \log(\Gamma(\beta))}{\partial \tilde{\zeta}} - \frac{\partial \log(\Gamma(\alpha + \beta))}{\partial \tilde{\zeta}}$$

which can be expressed in terms of the Ψ -function using the definition

$$\Psi(x) \equiv \frac{d}{dx} \log(\Gamma(x)) \quad (3.1.29)$$

The Ψ -function can be calculated according to the infinite product

$$\exp(\Psi(x)) = x \prod_{s=0}^{\infty} \left(1 + \frac{1}{x+s}\right) \exp\left(-\frac{1}{x+s}\right)$$

which is valid for $x > 0$. It can be recast as

$$\Psi(x) = -\frac{1}{x} + \log(1+x) + \log\left(\prod_{s=1}^{\infty} \left(1 + \frac{1}{x+s}\right) \exp\left(-\frac{1}{x+s}\right)\right) \quad (3.1.30)$$

There are efficient and accurate algorithms in standard software packages (such as IMSL) available for the calculation of Ψ . It follows that the derivative of N can be given as

$$\frac{\partial \log(N)}{\partial \tilde{\zeta}} = \frac{\partial \alpha}{\partial \tilde{\zeta}} \Psi(\alpha) + \frac{\partial \beta}{\partial \tilde{\zeta}} \Psi(\beta) - \left(\frac{\partial \alpha}{\partial \tilde{\zeta}} + \frac{\partial \beta}{\partial \tilde{\zeta}}\right) \Psi(\alpha + \beta)$$

and the derivative of the pdf is finally established in the form

$$\frac{\partial f}{\partial \tilde{\zeta}} = f \left\{ \frac{\partial \alpha}{\partial \tilde{\zeta}} [\log(\zeta) - \Psi(\alpha) + \Psi(\alpha + \beta)] + \frac{\partial \beta}{\partial \tilde{\zeta}} [\log(1 - \zeta) - \Psi(\beta) + \Psi(\alpha + \beta)] \right\} \quad (3.1.31)$$

The derivatives of the exponents α and β can be calculated which leads to

$$\frac{\partial \alpha}{\partial \tilde{\zeta}} = \frac{\tilde{\zeta}(2 - 3\tilde{\zeta})}{\tilde{\zeta}^{\prime\prime 2}} - 1 \quad (3.1.32)$$

and

$$\frac{\partial \beta}{\partial \tilde{\zeta}} = \frac{(1 - \tilde{\zeta})(1 - 3\tilde{\zeta})}{\tilde{\zeta}^{\prime\prime 2}} + 1 \quad (3.1.33)$$

The calculation of the derivative of the expectation of a function $\phi(\zeta)$ with respect to the mean mixture fraction is thus established. The result can be given in the form

$$\frac{\partial \langle \phi \rangle}{\partial \tilde{\zeta}} = \langle \phi \rangle \left\{ [\Psi(\alpha + \beta) - \Psi(\alpha)] \frac{\partial \alpha}{\partial \tilde{\zeta}} + [\Psi(\alpha + \beta) - \Psi(\beta)] \frac{\partial \beta}{\partial \tilde{\zeta}} \right\}$$

$$+\frac{\partial\alpha}{\partial\tilde{\zeta}}\langle\phi(\zeta)\log(\zeta)\rangle+\frac{\partial\beta}{\partial\tilde{\zeta}}\langle\phi(\zeta)\log(1-\zeta)\rangle \quad (3.1.34)$$

The derivative with respect to the variance follows in analog manner

$$\begin{aligned} \frac{\partial\langle\phi\rangle}{\partial\widetilde{\zeta''^2}} &= \langle\phi\rangle\{[\Psi(\alpha+\beta)-\Psi(\alpha)]\frac{\partial\alpha}{\partial\widetilde{\zeta''^2}}+[\Psi(\alpha+\beta)-\Psi(\beta)]\frac{\partial\beta}{\partial\widetilde{\zeta''^2}}\} \\ &+\frac{\partial\alpha}{\partial\widetilde{\zeta''^2}}\langle\phi(\zeta)\log(\zeta)\rangle+\frac{\partial\beta}{\partial\widetilde{\zeta''^2}}\langle\phi(\zeta)\log(1-\zeta)\rangle \end{aligned} \quad (3.1.35)$$

where

$$\frac{\partial\alpha}{\partial\widetilde{\zeta''^2}}=-\frac{\tilde{\zeta}^2(1-\tilde{\zeta})}{\widetilde{\zeta''^2}^2} \quad (3.1.36)$$

and

$$\frac{\partial\beta}{\partial\widetilde{\zeta''^2}}=-\frac{\tilde{\zeta}(1-\tilde{\zeta})^2}{\widetilde{\zeta''^2}^2} \quad (3.1.37)$$

Note, that the angular brackets are defined as

$$\langle\phi\rangle\equiv\int_0^1d\zeta B(\zeta;\tilde{\zeta},\widetilde{\zeta''^2})\phi(\zeta)$$

The beta function $B(\zeta;\tilde{\zeta},\widetilde{\zeta''^2})$ is regarded as density-weighted pdf and it follows that $\langle\phi\rangle=\tilde{\phi}$ holds. Furthermore are derivatives with respect to variables which are products with the mean density determined according to implicit differentiation. For instance, let

$$z\equiv\langle\rho\rangle\tilde{\zeta}$$

then holds

$$\frac{\partial}{\partial z}=\frac{1}{\langle\rho\rangle}\frac{\partial}{\partial\tilde{\zeta}}$$

It is clear from the previous considerations that spatial or temporal derivatives of the expectation of the function $\phi(\zeta)$ can be expressed in terms of derivatives of the moments entering the functional relation defining the pdf f . It follows that the gradient of $\langle\phi\rangle$ can be expressed as follows

$$\frac{\partial\langle\phi\rangle}{\partial x_\alpha}=\sum_{i=1}^n\int\int\int d\zeta du d\rho\phi(\zeta,u,\rho)\frac{\partial f}{\partial\phi_i}\frac{\partial\phi_i}{\partial x_\alpha} \quad (3.1.38)$$

where the set of moments defining the pdf is denoted by $\{\phi_i, i=1, n\}$. If the pdf f is the product of beta-functions the derivatives appear in the form (3.1.21).

3.1.6 Derivatives with respect to the solution variables: Composite pdf.

The calculation of the derivatives of the expectation of a function of the probabilistic scalars with respect to the solution variables is now straightforward. Consider the mean pressure, which is given by

$$\langle p \rangle = \langle \rho \rangle \int_0^1 d\zeta \int_0^1 du^* \int_0^1 d\rho^* \frac{p(\zeta, u^*, \rho^*)}{\rho_0 + \rho^*(\rho_1 - \rho_0)}$$

$$B(\zeta; \tilde{\zeta}, \tilde{\zeta}''^2) f_u^*(u^*; \langle u^* \rangle, \langle u^{*''2} \rangle) f_\rho^*(\rho^*; \langle \rho^* \rangle, \langle \rho^{*''2} \rangle) \quad (3.1.39)$$

where the defining moments for f_u^* and f_ρ^* depend in turn on $\tilde{\zeta}$ and $\tilde{\zeta}''^2$. There are six defining moments and seven solution variables. The calculation of quantities such as the Jacobian matrix requires the derivatives of expectations such as (3.1.39) with respect to all solution variables. This will be carried out in detail.

Derivative with respect to $\eta = \tilde{\zeta}$ and $\eta = \tilde{\zeta}''^2$.

The solution variables $\eta = \tilde{\zeta}$ and $\eta = \tilde{\zeta}''^2$ are also defining moments for the beta - function $B(\zeta)$. It follows from (3.1.39) that the derivative of the mean pressure with respect to η consists of three contributions

$$\frac{\partial \langle p \rangle}{\partial \eta} = \langle \rho \rangle \int_0^1 d\zeta \int_0^1 du^* \int_0^1 d\rho^* \frac{p(\zeta, u^*, \rho^*)}{\rho_0 + \rho^*(\rho_1 - \rho_0)} \left\{ \frac{\partial B}{\partial \eta} f_u^* f_\rho^* + B \frac{\partial f_u^*}{\partial \eta} f_\rho^* + B f_u^* \frac{\partial f_\rho^*}{\partial \eta} \right\}$$

The first part can be evaluated at once using (3.1.31) and (3.1.34) leading to

$$\begin{aligned} \frac{\partial \langle p \rangle}{\partial \eta} &= \langle \rho \rangle \left\langle \frac{p}{\rho} \right\rangle \{ [\Psi(\alpha + \beta) - \Psi(\alpha)] \frac{\partial \alpha}{\partial \eta} + [\Psi(\alpha + \beta) - \Psi(\beta)] \frac{\partial \beta}{\partial \eta} \} \\ &+ \langle \rho \rangle \left\{ \frac{\partial \alpha}{\partial \eta} \left\langle \frac{p}{\rho} \log(\zeta) \right\rangle + \frac{\partial \beta}{\partial \eta} \left\langle \frac{p}{\rho} \log(1 - \zeta) \right\rangle \right\} \\ &+ \langle \rho \rangle \int_0^1 d\zeta \int_0^1 du^* \int_0^1 d\rho^* \frac{p(\zeta, u^*, \rho^*)}{\rho_0 + \rho^*(\rho_1 - \rho_0)} \left\{ B \frac{\partial f_u^*}{\partial \eta} f_\rho^* + B f_u^* \frac{\partial f_\rho^*}{\partial \eta} \right\} \end{aligned} \quad (3.1.40)$$

The second and third parts represent the statistical dependence of internal energy and density on mixture fraction. Implicit differentiation leads to

$$\frac{\partial f_u^*}{\partial \eta} = \frac{\partial f_u^*}{\partial \langle u^* \rangle} \frac{\partial \langle u^* \rangle}{\partial \eta} + \frac{\partial f_u^*}{\partial \langle u^{*''2} \rangle} \frac{\partial \langle u^{*''2} \rangle}{\partial \eta} \quad (3.1.41)$$

and

$$\frac{\partial f_\rho^*}{\partial \eta} = \frac{\partial f_\rho^*}{\partial \langle \rho^* \rangle} \frac{\partial \langle \rho^* \rangle}{\partial \eta} + \frac{\partial f_\rho^*}{\partial \langle \rho^{*''2} \rangle} \frac{\partial \langle \rho^{*''2} \rangle}{\partial \eta} \quad (3.1.42)$$

The coefficients can be calculated explicitly using (3.1.23) - (3.1.26).

Derivative $\partial\langle u^* \rangle / \partial\eta$

The derivative of $\langle u^* \rangle$ with respect to η will be considered first. It follows from (3.1.23) that

$$\frac{\partial\langle u^* \rangle}{\partial\eta} = -\frac{1 - \langle u^* \rangle}{\tilde{u}_1 - \tilde{u}_0} \frac{\partial\tilde{u}_0}{\partial\eta} - \frac{\langle u^* \rangle}{\tilde{u}_1 - \tilde{u}_0} \frac{\partial\tilde{u}_1}{\partial\eta} \quad (3.1.43)$$

holds, which contains the derivatives of u_1 and u_0 with respect to η . Recalling that \tilde{u}_1 etc. are integrals involving $B(\zeta; \tilde{\zeta}, \tilde{\zeta}''^2)$, we obtain

$$\frac{\partial\tilde{u}_i}{\partial\eta} = \int_0^1 d\zeta u_i(\zeta) \frac{\partial B}{\partial\eta}, \quad i = 0, 1 \quad (3.1.44)$$

The derivative of the beta-function with respect to the defining moment η was established in the previous chapter. It follows from (3.1.31) and (3.1.34) that

$$\begin{aligned} \frac{\partial\tilde{u}_i}{\partial\eta} &= \tilde{u}_i \left\{ [\Psi(\alpha + \beta) - \Psi(\alpha)] \frac{\partial\alpha}{\partial\eta} + [\Psi(\alpha + \beta) - \Psi(\beta)] \frac{\partial\beta}{\partial\eta} \right\} \\ &+ \frac{\partial\alpha}{\partial\eta} \langle u_i(\zeta) \log(\zeta) \rangle + \frac{\partial\beta}{\partial\eta} \langle u_i(\zeta) \log(1 - \zeta) \rangle, \quad i = 0, 1 \end{aligned} \quad (3.1.45)$$

holds. The derivatives of the exponents α and β of the beta function are given by (3.1.32) and (3.1.33) or (3.1.36) and (3.1.37). Combining (3.1.45) and (3.1.43) leads to

$$\begin{aligned} \frac{\partial\langle u^* \rangle}{\partial\eta} &= -\frac{\tilde{u}}{\tilde{u}_1 - \tilde{u}_0} \left\{ [\Psi(\alpha + \beta) - \Psi(\alpha)] \frac{\partial\alpha}{\partial\eta} + [\Psi(\alpha + \beta) - \Psi(\beta)] \frac{\partial\beta}{\partial\eta} \right\} \\ &- \frac{1 - \langle u^* \rangle}{\tilde{u}_1 - \tilde{u}_0} \left\{ \frac{\partial\alpha}{\partial\eta} \langle u_0(\zeta) \log(\zeta) \rangle + \frac{\partial\beta}{\partial\eta} \langle u_0(\zeta) \log(1 - \zeta) \rangle \right\} \\ &- \frac{\langle u^* \rangle}{\tilde{u}_1 - \tilde{u}_0} \left\{ \frac{\partial\alpha}{\partial\eta} \langle u_1(\zeta) \log(\zeta) \rangle + \frac{\partial\beta}{\partial\eta} \langle u_1(\zeta) \log(1 - \zeta) \rangle \right\} \end{aligned} \quad (3.1.46)$$

which completes the calculation of the derivative.

$\partial\langle u^{*2} \rangle / \partial\eta$

The derivative of $\langle u^{*2} \rangle$ with respect to the defining moment η of the beta function will be considered next. It follows from the semi-implicit equation (3.1.24) that

$$\begin{aligned} \frac{\partial\langle u^{*2} \rangle}{\partial\eta} &= -2\langle u^* \rangle \frac{\partial\langle u^* \rangle}{\partial\eta} - \frac{1}{(\widetilde{u_1 - u_0})^2} \{ \langle u^{*2} \rangle + \langle u^* \rangle^2 \} \frac{\partial}{\partial\eta} (\widetilde{u_1 - u_0})^2 \\ &- \frac{1}{(\widetilde{u_1 - u_0})^2} \left\{ \frac{\partial\widetilde{u_0^2}}{\partial\eta} + 2(\widetilde{u_0 u_1} - \widetilde{u_0^2}) \frac{\partial\langle u^* \rangle}{\partial\eta} + 2\langle u^* \rangle \left(\frac{\partial\widetilde{u_0 u_1}}{\partial\eta} - \frac{\partial\widetilde{u_0^2}}{\partial\eta} \right) \right\} \end{aligned} \quad (3.1.47)$$

holds, which contains the derivatives of density-weighted expectations of various functions of ζ with respect to η . Recalling that u_1 etc. are functions of ζ only, it follows from (3.1.35) that

$$\begin{aligned} \frac{\partial \widetilde{u_1^2}}{\partial \eta} &= \widetilde{u_1^2} \left\{ [\Psi(\alpha + \beta) - \Psi(\alpha)] \frac{\partial \alpha}{\partial \eta} + [\Psi(\alpha + \beta) - \Psi(\beta)] \frac{\partial \beta}{\partial \eta} \right\} \\ &\quad + \frac{\partial \alpha}{\partial \eta} \langle u_1^2(\zeta) \log(\zeta) \rangle + \frac{\partial \beta}{\partial \eta} \langle u_1^2(\zeta) \log(1 - \zeta) \rangle \end{aligned} \quad (3.1.48)$$

holds. The derivatives of the exponents α and β of the beta function are given by (3.1.32) and (3.1.33). Collecting all the derivatives we get

$$\begin{aligned} \frac{\partial \langle u^{*2} \rangle}{\partial \eta} &= 2 \left\{ \langle u^* \rangle + \frac{\widetilde{u_0 u_1} - \widetilde{u_0^2}}{(u_1 - u_0)^2} \right\} \left(\frac{\widetilde{u}}{\widetilde{u_1} - \widetilde{u_0}} \left\{ [\Psi(\alpha + \beta) - \Psi(\alpha)] \frac{\partial \alpha}{\partial \eta} + [\Psi(\alpha + \beta) - \Psi(\beta)] \frac{\partial \beta}{\partial \eta} \right\} \right. \\ &\quad + \frac{1 - \langle u^* \rangle}{\widetilde{u_1} - \widetilde{u_0}} \left\{ \frac{\partial \alpha}{\partial \eta} \langle u_0(\zeta) \log(\zeta) \rangle + \frac{\partial \beta}{\partial \eta} \langle u_0(\zeta) \log(1 - \zeta) \rangle \right\} \\ &\quad \left. + \frac{\langle u^* \rangle}{\widetilde{u_1} - \widetilde{u_0}} \left\{ \frac{\partial \alpha}{\partial \eta} \langle u_1(\zeta) \log(\zeta) \rangle + \frac{\partial \beta}{\partial \eta} \langle u_1(\zeta) \log(1 - \zeta) \rangle \right\} \right) \\ &\quad - \frac{\langle u^* \rangle + \langle u^{*2} \rangle - \langle u^* \rangle (1 - \langle u^* \rangle)}{(u_1 - u_0)^2} \left(\widetilde{u_1^2} \left\{ [\Psi(\alpha + \beta) - \Psi(\alpha)] \frac{\partial \alpha}{\partial \eta} + [\Psi(\alpha + \beta) - \Psi(\beta)] \frac{\partial \beta}{\partial \eta} \right\} \right. \\ &\quad \left. + \frac{\partial \alpha}{\partial \eta} \langle u_1^2(\zeta) \log(\zeta) \rangle + \frac{\partial \beta}{\partial \eta} \langle u_1^2(\zeta) \log(1 - \zeta) \rangle \right) \\ &\quad - 2 \frac{\langle u^* \rangle (1 - \langle u^* \rangle) - \langle u^{*2} \rangle}{(u_1 - u_0)^2} \left(\widetilde{u_0 u_1} \left\{ [\Psi(\alpha + \beta) - \Psi(\alpha)] \frac{\partial \alpha}{\partial \eta} + [\Psi(\alpha + \beta) - \Psi(\beta)] \frac{\partial \beta}{\partial \eta} \right\} \right. \\ &\quad \left. + \frac{\partial \alpha}{\partial \eta} \langle u_0(\zeta) u_1(\zeta) \log(\zeta) \rangle + \frac{\partial \beta}{\partial \eta} \langle u_0(\zeta) u_1(\zeta) \log(1 - \zeta) \rangle \right) \\ &\quad - \frac{1 - \langle u^* \rangle + \langle u^{*2} \rangle - \langle u^* \rangle (1 - \langle u^* \rangle)}{(u_1 - u_0)^2} \left(\widetilde{u_0^2} \left\{ [\Psi(\alpha + \beta) - \Psi(\alpha)] \frac{\partial \alpha}{\partial \eta} + [\Psi(\alpha + \beta) - \Psi(\beta)] \frac{\partial \beta}{\partial \eta} \right\} \right. \\ &\quad \left. + \frac{\partial \alpha}{\partial \eta} \langle u_0^2(\zeta) \log(\zeta) \rangle + \frac{\partial \beta}{\partial \eta} \langle u_0^2(\zeta) \log(1 - \zeta) \rangle \right) \end{aligned} \quad (3.1.49)$$

completing the derivative of the variance $\langle u^{*2} \rangle$ with respect to $\eta = \tilde{\zeta}$ or $\eta = \tilde{\zeta}^{1/2}$.

Derivative $\partial \langle \rho^* \rangle / \partial \eta$

The derivative of the defining moment $\langle \rho^* \rangle$ with respect to the solution variable η is completely analogous to the derivative of \tilde{u} . It follows from (3.1.25) and (3.1.43) that

$$\frac{\partial \langle \rho^* \rangle}{\partial \eta} = - \frac{1 - \langle \rho^* \rangle}{\tilde{\rho}_1 - \tilde{\rho}_0} \frac{\partial \tilde{\rho}_0}{\partial \eta} - \frac{\langle \rho^* \rangle}{\tilde{\rho}_1 - \tilde{\rho}_0} \frac{\partial \tilde{\rho}_1}{\partial \eta} \quad (3.1.50)$$

holds and using (3.1.46) we get

$$\begin{aligned}
\frac{\partial \langle \rho^* \rangle}{\partial \eta} = & -\frac{\langle \rho \rangle + \frac{\langle \rho'^2 \rangle}{\langle \rho \rangle}}{\tilde{\rho}_1 - \tilde{\rho}_0} \{ [\Psi(\alpha + \beta) - \Psi(\alpha)] \frac{\partial \alpha}{\partial \eta} + [\Psi(\alpha + \beta) - \Psi(\beta)] \frac{\partial \beta}{\partial \eta} \} \\
& - \frac{1 - \langle \rho^* \rangle}{\tilde{\rho}_1 - \tilde{\rho}_0} \left\{ \frac{\partial \alpha}{\partial \eta} \langle \rho_0(\zeta) \log(\zeta) \rangle + \frac{\partial \beta}{\partial \eta} \langle \rho_0(\zeta) \log(1 - \zeta) \rangle \right\} \\
& - \frac{\langle \rho^* \rangle}{\tilde{u}_1 - \tilde{u}_0} \left\{ \frac{\partial \alpha}{\partial \eta} \langle \rho_1(\zeta) \log(\zeta) \rangle + \frac{\partial \beta}{\partial \eta} \langle \rho_1(\zeta) \log(1 - \zeta) \rangle \right\}
\end{aligned} \tag{3.1.51}$$

which completes the calculation of the derivative.

Derivative $\partial \langle \rho^{*2} \rangle / \partial \eta$

The derivative of the density variance $\langle \rho'^2 \rangle$ with respect to η is completely analogous to the derivative of the variance $\langle u'^2 \rangle$. It follows from (3.1.26) and (3.1.47) that

$$\begin{aligned}
\frac{\partial \langle \rho^{*2} \rangle}{\partial \eta} = & -2 \left\{ \langle \rho^* \rangle + \frac{\widetilde{\rho_0 \rho_1} - \tilde{\rho}_0^2}{(\rho_1 - \rho_0)^2} \right\} \frac{\partial \langle \rho^* \rangle}{\partial \eta} - \frac{\langle \rho^* \rangle + \langle \rho^{*2} \rangle - \langle \rho^* \rangle (1 - \langle \rho^* \rangle)}{(\rho_1 - \rho_0)^2} \frac{\partial \tilde{\rho}_1^2}{\partial \eta} \\
& - 2 \frac{\langle \rho^* \rangle (1 - \langle \rho^* \rangle) - \langle \rho^{*2} \rangle}{(\rho_1 - \rho_0)^2} \frac{\partial \widetilde{\rho_0 \rho_1}}{\partial \eta} - \frac{1 - \langle \rho^* \rangle + \langle \rho^{*2} \rangle - \langle \rho^* \rangle (1 - \langle \rho^* \rangle)}{(\rho_1 - \rho_0)^2} \frac{\partial \tilde{\rho}_0^2}{\partial \eta}
\end{aligned} \tag{3.1.52}$$

holds and using (3.1.49) we get

$$\begin{aligned}
\frac{\partial \langle \rho^{*2} \rangle}{\partial \eta} = & 2 \left\{ \langle \rho^* \rangle + \frac{\widetilde{\rho_0 \rho_1} - \tilde{\rho}_0^2}{(\rho_1 - \rho_0)^2} \right\} \left(\frac{\langle \rho \rangle + \frac{\langle \rho'^2 \rangle}{\langle \rho \rangle}}{\tilde{\rho}_1 - \tilde{\rho}_0} \{ [\Psi(\alpha + \beta) - \Psi(\alpha)] \frac{\partial \alpha}{\partial \eta} + [\Psi(\alpha + \beta) - \Psi(\beta)] \frac{\partial \beta}{\partial \eta} \} \right. \\
& + \frac{1 - \langle \rho^* \rangle}{\tilde{\rho}_1 - \tilde{\rho}_0} \left\{ \frac{\partial \alpha}{\partial \eta} \langle \rho_0(\zeta) \log(\zeta) \rangle + \frac{\partial \beta}{\partial \eta} \langle \rho_0(\zeta) \log(1 - \zeta) \rangle \right\} \\
& \left. + \frac{\langle \rho^* \rangle}{\tilde{\rho}_1 - \tilde{\rho}_0} \left\{ \frac{\partial \alpha}{\partial \eta} \langle \rho_1(\zeta) \log(\zeta) \rangle + \frac{\partial \beta}{\partial \eta} \langle \rho_1(\zeta) \log(1 - \zeta) \rangle \right\} \right) \\
& - \frac{\langle \rho^* \rangle + \langle \rho^{*2} \rangle - \langle \rho^* \rangle (1 - \langle \rho^* \rangle)}{(\rho_1 - \rho_0)^2} \left(\tilde{\rho}_1^2 \{ [\Psi(\alpha + \beta) - \Psi(\alpha)] \frac{\partial \alpha}{\partial \eta} + [\Psi(\alpha + \beta) - \Psi(\beta)] \frac{\partial \beta}{\partial \eta} \} \right. \\
& \left. + \frac{\partial \alpha}{\partial \eta} \langle \rho_1^2(\zeta) \log(\zeta) \rangle + \frac{\partial \beta}{\partial \eta} \langle \rho_1^2(\zeta) \log(1 - \zeta) \rangle \right) \\
& - 2 \frac{\langle \rho^* \rangle (1 - \langle \rho^* \rangle) - \langle \rho^{*2} \rangle}{(\rho_1 - \rho_0)^2} \left(\widetilde{\rho_0 \rho_1} \{ [\Psi(\alpha + \beta) - \Psi(\alpha)] \frac{\partial \alpha}{\partial \eta} + [\Psi(\alpha + \beta) - \Psi(\beta)] \frac{\partial \beta}{\partial \eta} \} \right. \\
& \left. + \frac{\partial \alpha}{\partial \eta} \langle \rho_0(\zeta) u_1(\zeta) \log(\zeta) \rangle + \frac{\partial \beta}{\partial \eta} \langle \rho_0(\zeta) u_1(\zeta) \log(1 - \zeta) \rangle \right)
\end{aligned}$$

$$\begin{aligned}
& - \frac{1 - \langle \rho^* \rangle + \langle \rho^{*12} \rangle - \langle \rho^* \rangle (1 - \langle \rho^* \rangle)}{(\rho_1 - \rho_0)^2} \left(\tilde{\rho}_0^2 \{ [\Psi(\alpha + \beta) - \Psi(\alpha)] \frac{\partial \alpha}{\partial \eta} + [\Psi(\alpha + \beta) - \Psi(\beta)] \frac{\partial \beta}{\partial \eta} \} \right. \\
& \quad \left. + \frac{\partial \alpha}{\partial \eta} \langle \rho_0^2(\zeta) \log(\zeta) \rangle + \frac{\partial \beta}{\partial \eta} \langle \rho_0^2(\zeta) \log(1 - \zeta) \rangle \right) \quad (3.1.53)
\end{aligned}$$

completing the derivative of the variance $\langle \rho^{*12} \rangle$ with respect to $\eta = \tilde{\zeta}$ or $\eta = \tilde{\zeta}^{12}$.

Derivatives $\partial \langle p \rangle / \partial \tilde{\zeta}$ and $\partial \langle p \rangle / \partial \tilde{\zeta}^{12}$ for the product of beta-functions.

The derivative of the mean pressure with respect to η can be assembled using (3.1.40) and the form (3.1.27) for the pdfs f_u^* and f_ρ^* . The result can be given in the form

$$\begin{aligned}
\frac{\partial \langle p \rangle}{\partial \eta} &= \langle \rho \rangle \left\langle \frac{p}{\rho} \right\rangle \{ [\Psi(\alpha_\zeta + \beta_\zeta) - \Psi(\alpha_\zeta)] \frac{\partial \alpha_\zeta}{\partial \eta} + [\Psi(\alpha_\zeta + \beta_\zeta) - \Psi(\beta_\zeta)] \frac{\partial \beta_\zeta}{\partial \eta} \} \\
&\quad + \langle \rho \rangle \left\{ \frac{\partial \alpha_\zeta}{\partial \eta} \left\langle \frac{p}{\rho} \log(\zeta) \right\rangle + \frac{\partial \beta_\zeta}{\partial \eta} \left\langle \frac{p}{\rho} \log(1 - \zeta) \right\rangle \right\} \\
&\quad + \langle \rho \rangle \frac{\partial \langle u^* \rangle}{\partial \eta} \left(\left\langle \frac{p}{\rho} \right\rangle \{ [\Psi(\alpha_u + \beta_u) - \Psi(\alpha_u)] \frac{\partial \alpha_u}{\partial \langle u^* \rangle} + [\Psi(\alpha_u + \beta_u) - \Psi(\beta_u)] \frac{\partial \beta_u}{\partial \langle u^* \rangle} \} \right. \\
&\quad \left. + \frac{\partial \alpha_u}{\partial \langle u^* \rangle} \left\langle \frac{p}{\rho} \log(u^*) \right\rangle + \frac{\partial \beta_u}{\partial \langle u^* \rangle} \left\langle \frac{p}{\rho} \log(1 - u^*) \right\rangle \right) \\
&\quad + \langle \rho \rangle \frac{\partial \langle u^{*12} \rangle}{\partial \eta} \left(\left\langle \frac{p}{\rho} \right\rangle \{ [\Psi(\alpha_u + \beta_u) - \Psi(\alpha_u)] \frac{\partial \alpha_u}{\partial \langle u^{*12} \rangle} + [\Psi(\alpha_u + \beta_u) - \Psi(\beta_u)] \frac{\partial \beta_u}{\partial \langle u^{*12} \rangle} \} \right. \\
&\quad \left. + \frac{\partial \alpha_u}{\partial \langle u^{*12} \rangle} \left\langle \frac{p}{\rho} \log(u^*) \right\rangle + \frac{\partial \beta_u}{\partial \langle u^{*12} \rangle} \left\langle \frac{p}{\rho} \log(1 - u^*) \right\rangle \right) \\
&\quad + \langle \rho \rangle \frac{\partial \langle \rho^* \rangle}{\partial \eta} \left(\left\langle \frac{p}{\rho} \right\rangle \{ [\Psi(\alpha_\rho + \beta_\rho) - \Psi(\alpha_\rho)] \frac{\partial \alpha_\rho}{\partial \langle \rho^* \rangle} + [\Psi(\alpha_\rho + \beta_\rho) - \Psi(\beta_\rho)] \frac{\partial \beta_\rho}{\partial \langle \rho^* \rangle} \} \right. \\
&\quad \left. + \frac{\partial \alpha_\rho}{\partial \langle \rho^* \rangle} \left\langle \frac{p}{\rho} \log(\rho^*) \right\rangle + \frac{\partial \beta_\rho}{\partial \langle \rho^* \rangle} \left\langle \frac{p}{\rho} \log(1 - \rho^*) \right\rangle \right) \\
&\quad + \langle \rho \rangle \frac{\partial \langle \rho^{*12} \rangle}{\partial \eta} \left(\left\langle \frac{p}{\rho} \right\rangle \{ [\Psi(\alpha_\rho + \beta_\rho) - \Psi(\alpha_\rho)] \frac{\partial \alpha_\rho}{\partial \langle \rho^{*12} \rangle} + [\Psi(\alpha_\rho + \beta_\rho) - \Psi(\beta_\rho)] \frac{\partial \beta_\rho}{\partial \langle \rho^{*12} \rangle} \} \right. \\
&\quad \left. + \frac{\partial \alpha_\rho}{\partial \langle \rho^{*12} \rangle} \left\langle \frac{p}{\rho} \log(\rho^*) \right\rangle + \frac{\partial \beta_\rho}{\partial \langle \rho^{*12} \rangle} \left\langle \frac{p}{\rho} \log(1 - \rho^*) \right\rangle \right) \quad (3.1.54)
\end{aligned}$$

The derivatives of the defining moments with respect to the solution variables are given by (3.1.46), (3.1.49), (3.1.51), and (3.1.53) and the derivatives of the exponents α and β with respect to mean values are given by (3.1.32) and (3.1.33) and the derivatives with respect to the variances are given by (3.1.36) and (3.1.37). This completes the calculation of the derivative of the mean pressure with respect to $\eta = \tilde{\zeta}$ or $\eta = \tilde{\zeta}''^2$.

Derivative with respect to $\eta = \tilde{u}$ and $\eta = \tilde{u}''^2$.

The solution variables $\eta = \tilde{u}$ and $\eta = \tilde{u}''^2$ are not defining moments for the beta-function $B(u^*)$. They are related to the defining moments $\langle u^* \rangle$ and $\langle u^{*2} \rangle$ by (3.1.23) and (3.1.24). Implicit differentiation of (3.1.39) leads to

$$\frac{\partial \langle p \rangle}{\partial \eta} = \langle \rho \rangle \int_0^1 d\zeta \int_0^1 du^* \int_0^1 d\rho^* \frac{p(\zeta, u^*, \rho^*)}{\rho_0 + \rho^*(\rho_1 - \rho_0)} B \frac{\partial f_u^*}{\partial \eta} f_\rho^*$$

since only f_u^* depends on η via (3.1.23) or (3.1.24). Further implicit differentiation of f_u^* leads to

$$\frac{\partial f_u^*}{\partial \eta} = \frac{\partial f_u^*}{\partial \langle u^* \rangle} \frac{\partial \langle u^* \rangle}{\partial \eta} + \frac{\partial f_u^*}{\partial \langle u^{*2} \rangle} \frac{\partial \langle u^{*2} \rangle}{\partial \eta}$$

The coefficients can be calculated explicitly using (3.1.23) and (3.1.24). We consider first $\eta = \tilde{u}$ and obtain using (3.1.23)

$$\frac{\partial \langle u^* \rangle}{\partial \tilde{u}} = \frac{1}{\tilde{u}_1 - \tilde{u}_0} \quad (3.1.56)$$

and using (3.1.24)

$$\frac{\partial \tilde{u}''^2}{\partial \tilde{u}} = 2\tilde{u} \left(\frac{1}{(\tilde{u}_1 - \tilde{u}_0)^2} - \frac{1}{(\tilde{u}_1 - \tilde{u}_0)^2} \right) - \frac{2}{\tilde{u}_1 - \tilde{u}_0} \left(\frac{\tilde{u}_0 \tilde{u}_1 - \tilde{u}_0^2}{(\tilde{u}_1 - \tilde{u}_0)^2} - \frac{\tilde{u}_0}{\tilde{u}_1 - \tilde{u}_0} \right) \quad (3.1.57)$$

The derivative of the pressure gradient follows now from (3.1.54) as

$$\begin{aligned} \frac{\partial \langle p \rangle}{\partial \tilde{u}} &= \langle \rho \rangle \frac{\partial \langle u^* \rangle}{\partial \tilde{u}} \left(\left\langle \frac{p}{\rho} \right\rangle \{ [\Psi(\alpha_u + \beta_u) - \Psi(\alpha_u)] \frac{\partial \alpha_u}{\partial \langle u^* \rangle} + [\Psi(\alpha_u + \beta_u) - \Psi(\beta_u)] \frac{\partial \beta_u}{\partial \langle u^* \rangle} \} \right. \\ &\quad \left. + \frac{\partial \alpha_u}{\partial \langle u^* \rangle} \left\langle \frac{p}{\rho} \log(u^*) \right\rangle + \frac{\partial \beta_u}{\partial \langle u^* \rangle} \left\langle \frac{p}{\rho} \log(1 - u^*) \right\rangle \right) \\ &+ \langle \rho \rangle \frac{\partial \langle u^{*2} \rangle}{\partial \tilde{u}} \left(\left\langle \frac{p}{\rho} \right\rangle \{ [\Psi(\alpha_u + \beta_u) - \Psi(\alpha_u)] \frac{\partial \alpha_u}{\partial \langle u^{*2} \rangle} + [\Psi(\alpha_u + \beta_u) - \Psi(\beta_u)] \frac{\partial \beta_u}{\partial \langle u^{*2} \rangle} \} \right. \\ &\quad \left. + \frac{\partial \alpha_u}{\partial \langle u^{*2} \rangle} \left\langle \frac{p}{\rho} \log(u^*) \right\rangle + \frac{\partial \beta_u}{\partial \langle u^{*2} \rangle} \left\langle \frac{p}{\rho} \log(1 - u^*) \right\rangle \right) \end{aligned} \quad (3.1.58)$$

and the coefficients are given by (3.1.56) and (3.1.57). We consider next $\eta = \widetilde{u'^2}$ and obtain using (3.1.23)

$$\frac{\partial \langle u^* \rangle}{\partial \widetilde{\zeta'^2}} = 0$$

and using (3.1.24)

$$\frac{\partial \langle u'^2 \rangle}{\partial \widetilde{\zeta'^2}} = \frac{1}{(u_1 - u_0)^2} \quad (3.1.59)$$

The derivative of the pressure gradient follows now from (3.1.54) as

$$\begin{aligned} \frac{\partial \langle p \rangle}{\partial \widetilde{u'^2}} = \frac{\langle \rho \rangle}{(u_1 - u_0)^2} & \left(\left\langle \frac{p}{\rho} \right\rangle \{ [\Psi(\alpha_u + \beta_u) - \Psi(\alpha_u)] \frac{\partial \alpha_u}{\partial \langle u'^2 \rangle} + [\Psi(\alpha_u + \beta_u) - \Psi(\beta_u)] \frac{\partial \beta_u}{\partial \langle u'^2 \rangle} \} \right. \\ & \left. + \frac{\partial \alpha_u}{\partial \langle u'^2 \rangle} \left\langle \frac{p}{\rho} \log(u^*) \right\rangle + \frac{\partial \beta_u}{\partial \langle u'^2 \rangle} \left\langle \frac{p}{\rho} \log(1 - u^*) \right\rangle \right) \end{aligned} \quad (3.1.60)$$

and the derivatives of the exponents α and β are given by (3.1.36) and (3.1.37).

Derivatives with respect to $\eta = \langle \rho \rangle$, $\langle \rho'^2 \rangle$ and $\eta = \langle \rho'^3 \rangle$.

The solution variables $\eta = \langle \rho \rangle$, $\langle \rho'^2 \rangle$ and $\eta = \langle \rho'^3 \rangle$ are not defining moments for the beta - function $B(\rho^*)$. They are related to the defining moments $\langle \rho^* \rangle$ and $\langle \rho'^2 \rangle$ by (3.1.25) and (3.1.26). Implicit differentiation of (3.1.39) for $\eta = \langle \rho \rangle$ leads to

$$\frac{\partial \langle p \rangle}{\partial \eta} = \left\langle \frac{p}{\rho} \right\rangle + \langle \rho \rangle \int_0^1 d\zeta \int_0^1 du^* \int_0^1 d\rho^* \frac{p(\zeta, u^*, \rho^*)}{\rho_0 + \rho^*(\rho_1 - \rho_0)} B(\zeta) f_u^*(u^*) \frac{\partial f_\rho^*}{\partial \eta}$$

and for $\eta \neq \langle \rho \rangle$ to

$$\frac{\partial \langle p \rangle}{\partial \eta} = \langle \rho \rangle \int_0^1 d\zeta \int_0^1 du^* \int_0^1 d\rho^* \frac{p(\zeta, u^*, \rho^*)}{\rho_0 + \rho^*(\rho_1 - \rho_0)} B(\zeta) f_u^*(u^*) \frac{\partial f_\rho^*}{\partial \eta}$$

since only f_ρ^* depends on η via (3.1.25) or (3.1.26). Further implicit differentiation of f_ρ^* leads to

$$\frac{\partial f_\rho^*}{\partial \eta} = \frac{\partial f_\rho^*}{\partial \langle \rho^* \rangle} \frac{\partial \langle \rho^* \rangle}{\partial \eta} + \frac{\partial f_\rho^*}{\partial \langle \rho'^2 \rangle} \frac{\partial \langle \rho'^2 \rangle}{\partial \eta}$$

The coefficients can be calculated explicitly using (3.1.25) and (3.1.26) and obtain using (3.1.25)

$$\frac{\partial \langle \rho^* \rangle}{\partial \langle \rho \rangle} = \frac{1 - \frac{\langle \rho'^2 \rangle}{\langle \rho \rangle^2}}{\tilde{\rho}_1 - \tilde{\rho}_0} \quad (3.1.61)$$

and using (3.1.26)

$$\frac{\partial \langle \rho'^2 \rangle}{\partial \langle \rho \rangle} = \frac{1}{\langle \rho \rangle^2} \frac{2\langle \rho \rangle^3 - \langle \rho'^3 \rangle}{(\rho_1 - \rho_0)^2} - \frac{2}{\langle \rho \rangle^2} \frac{\langle \rho \rangle^2 - \langle \rho'^2 \rangle}{\tilde{\rho}_1 - \tilde{\rho}_0} \left(\frac{\widetilde{\rho_0 \rho_1} - \tilde{\rho}_0^2}{(\rho_1 - \rho_0)^2} + \langle \rho^* \rangle \right) \quad (3.1.62)$$

The derivative of the pressure gradient follows now from (3.1.54) as

$$\begin{aligned}
\frac{\partial \langle p \rangle}{\partial \langle \rho \rangle} &= \langle \frac{p}{\rho} \rangle + \langle \rho \rangle \frac{\partial \langle \rho^* \rangle}{\partial \langle \rho \rangle} \left(\langle \frac{p}{\rho} \rangle \{ [\Psi(\alpha_\rho + \beta_\rho) - \Psi(\alpha_\rho)] \frac{\partial \alpha_\rho}{\partial \langle \rho^* \rangle} + [\Psi(\alpha_\rho + \beta_\rho) - \Psi(\beta_\rho)] \frac{\partial \beta_\rho}{\partial \langle \rho^* \rangle} \} \right. \\
&\quad \left. + \frac{\partial \alpha_\rho}{\partial \langle \rho^* \rangle} \langle \frac{p}{\rho} \log(\rho^*) \rangle + \frac{\partial \beta_\rho}{\partial \langle \rho^* \rangle} \langle \frac{p}{\rho} \log(1 - \rho^*) \rangle \right) \\
&+ \langle \rho \rangle \frac{\partial \langle \rho^{*2} \rangle}{\partial \langle \rho \rangle} \left(\langle \frac{p}{\rho} \rangle \{ [\Psi(\alpha_\rho + \beta_\rho) - \Psi(\alpha_\rho)] \frac{\partial \alpha_\rho}{\partial \langle \rho^{*2} \rangle} + [\Psi(\alpha_\rho + \beta_\rho) - \Psi(\beta_\rho)] \frac{\partial \beta_\rho}{\partial \langle \rho^{*2} \rangle} \} \right. \\
&\quad \left. + \frac{\partial \alpha_\rho}{\partial \langle \rho^{*2} \rangle} \langle \frac{p}{\rho} \log(\rho^*) \rangle + \frac{\partial \beta_\rho}{\partial \langle \rho^{*2} \rangle} \langle \frac{p}{\rho} \log(1 - \rho^*) \rangle \right) \quad (3.1.63)
\end{aligned}$$

and the coefficients are given by (3.1.61) and (3.1.62). We consider next $\eta = \langle \rho'^2 \rangle$ and obtain using (3.1.25)

$$\frac{\partial \langle \rho^* \rangle}{\partial \langle \rho'^2 \rangle} = \frac{1}{\langle \rho \rangle (\tilde{\rho}_1 - \tilde{\rho}_0)} \quad (3.1.64)$$

and using (3.1.26)

$$\frac{\partial \langle \rho^{*2} \rangle}{\partial \langle \rho'^2 \rangle} = \frac{3}{(\rho_1 - \rho_0)^2} - \frac{2}{\langle \rho \rangle (\tilde{\rho}_1 - \tilde{\rho}_0)} \left(\langle \rho^* \rangle + \frac{\widetilde{\rho_0 \rho_1} - \tilde{\rho}_0^2}{(\rho_1 - \rho_0)^2} \right) \quad (3.1.65)$$

The derivative of the pressure gradient follows now from (3.1.63) as

$$\begin{aligned}
\frac{\partial \langle p \rangle}{\partial \langle \rho'^2 \rangle} &= \langle \rho \rangle \frac{\partial \langle \rho^* \rangle}{\partial \langle \rho'^2 \rangle} \left(\langle \frac{p}{\rho} \rangle \{ [\Psi(\alpha_\rho + \beta_\rho) - \Psi(\alpha_\rho)] \frac{\partial \alpha_\rho}{\partial \langle \rho^* \rangle} + [\Psi(\alpha_\rho + \beta_\rho) - \Psi(\beta_\rho)] \frac{\partial \beta_\rho}{\partial \langle \rho^* \rangle} \} \right. \\
&\quad \left. + \frac{\partial \alpha_\rho}{\partial \langle \rho^* \rangle} \langle \frac{p}{\rho} \log(\rho^*) \rangle + \frac{\partial \beta_\rho}{\partial \langle \rho^* \rangle} \langle \frac{p}{\rho} \log(1 - \rho^*) \rangle \right) \\
&+ \langle \rho \rangle \frac{\partial \langle \rho^{*2} \rangle}{\partial \langle \rho'^2 \rangle} \left(\langle \frac{p}{\rho} \rangle \{ [\Psi(\alpha_\rho + \beta_\rho) - \Psi(\alpha_\rho)] \frac{\partial \alpha_\rho}{\partial \langle \rho^{*2} \rangle} + [\Psi(\alpha_\rho + \beta_\rho) - \Psi(\beta_\rho)] \frac{\partial \beta_\rho}{\partial \langle \rho^{*2} \rangle} \} \right. \\
&\quad \left. + \frac{\partial \alpha_\rho}{\partial \langle \rho^{*2} \rangle} \langle \frac{p}{\rho} \log(\rho^*) \rangle + \frac{\partial \beta_\rho}{\partial \langle \rho^{*2} \rangle} \langle \frac{p}{\rho} \log(1 - \rho^*) \rangle \right) \quad (3.1.66)
\end{aligned}$$

and the coefficients are given by (3.1.64) and (3.1.65). The derivatives of the exponents α and β are given by (3.1.36) and (3.1.37).

Finally, $\eta = \langle \rho'^3 \rangle$ is considered. We obtain using (3.1.25)

$$\frac{\partial \langle \rho^* \rangle}{\partial \langle \rho'^3 \rangle} = 0$$

and using (3.1.26)

$$\frac{\partial \langle \rho^{*12} \rangle}{\partial \langle \rho^{13} \rangle} = \frac{1}{\langle \rho \rangle (\rho_1 - \rho_0)^2} \quad (3.1.67)$$

The derivative of the pressure gradient follows now from (3.1.63) as

$$\begin{aligned} \frac{\partial \langle p \rangle}{\partial \langle \rho^{13} \rangle} = & \frac{1}{(\rho_1 - \rho_0)^2} \left(\left\langle \frac{p}{\rho} \right\rangle \{ [\Psi(\alpha_\rho + \beta_\rho) - \Psi(\alpha_\rho)] \frac{\partial \alpha_\rho}{\partial \langle \rho^{*12} \rangle} + [\Psi(\alpha_\rho + \beta_\rho) - \Psi(\beta_\rho)] \frac{\partial \beta_\rho}{\partial \langle \rho^{*12} \rangle} \right\} \\ & + \frac{\partial \alpha_\rho}{\partial \langle \rho^{*12} \rangle} \left\langle \frac{p}{\rho} \log(\rho^*) \right\rangle + \frac{\partial \beta_\rho}{\partial \langle \rho^{*12} \rangle} \left\langle \frac{p}{\rho} \log(1 - \rho^*) \right\rangle \right) \quad (3.1.68) \end{aligned}$$

The derivatives of the exponents α and β are given by (3.1.36) and (3.1.37).

In this section it was shown that pdfs for three scalar variables describing the local thermodynamic state in a compressible reacting flow can be constructed from a selected set of moments of order three or less. Statistical independence was assumed for the image variables in a transformed space, that reduces approximately to the properties of reacting flows at zero Mach-number if two of the image variables are kept at fixed values. All derivatives of expectations of arbitrary functions of the scalars with respect to the moments in physical space used for the construction of the pdf were calculated analytically.

3.2. Nonreacting Joint PDF Equation

In this section the objectives are to analyze the compressible flow equations, to understand the role of pressure and its fluctuations on turbulence dynamics, and to see if this phenomenon is similar or related to that in the incompressible flowfields. To do this, a theoretical joint probability density function formalism is developed for velocity components and thermodynamic variables in nonreacting turbulent compressible flowfields. Utilizing the conservations of mass, momentum, and the second law of thermodynamics and two general state equations, a differential transport equation can be derived for the joint PDF of velocity components, entropy, and pressure. A summary of this derivation and subsequent analysis is given below.

A nonreacting compressible flowfield is governed by a set of equations consisting of the conservation of mass equation (Eq. 1.1.4), the conservation of momentum equation (Eq. 1.1.6), and a transport equation for entropy given as

$$\rho \left[\frac{\partial S}{\partial t} + U_j \frac{\partial S}{\partial x_j} \right] = \frac{1}{T} \tau_{ij} \varepsilon_{ij} + \frac{1}{T^2} \kappa \left[\frac{\partial T}{\partial x_i} \right]^2 + \frac{\partial}{\partial x_i} \left[\frac{1}{T} \kappa \frac{\partial T}{\partial x_i} \right] \quad (3.2.1)$$

where $\varepsilon_{ij} = 1/2(\partial U_i/\partial x_j + \partial U_j/\partial x_i)$ is the strain rate tensor. The general forms of thermodynamic state relations are

$$\rho = \rho(P, S) \quad (3.2.2)$$

$$T = T(P, S) \quad (3.3.3)$$

The specific functional forms of state relations depend on the gas under consideration and are left undefined to keep the analysis general and applicable to ideal as well as real gases. The total changes in density and temperature in terms of thermodynamic variables are given as

$$d\rho = \left[\frac{\partial \rho}{\partial P} \right]_S dP + \left[\frac{\partial \rho}{\partial S} \right]_P dS \quad (3.2.4)$$

$$dT = \left[\frac{\partial T}{\partial P} \right]_S dP + \left[\frac{\partial T}{\partial S} \right]_P dS \quad (3.2.5)$$

The partial derivative $(\partial \rho / \partial P)_S$ is defined as the inverse of the square of the speed of sound propagation in the medium and goes to zero for incompressible flowfields. The other partial derivatives can be related to the well-known thermodynamic coefficients using Maxwell relationships. It should be noted that only three of the thermodynamic partial derivatives are independent and the rest can be expressed in terms of those three.

The knowledge of the velocity, pressure, and entropy fields, $\underline{U}(\underline{x},t)$, $S(\underline{x},t)$ and $P(\underline{x},t)$, at any point in a compressible flowfield completely determines the state of the fluid. In a turbulent field these quantities can be viewed as random fields. The joint probability density function of these random fields at any given point in space and time is denoted by $f(\xi, \eta, \zeta; \underline{x}, t)$ where ξ , η , and ζ are dummy variables denoting the value spaces of velocity, entropy, and pressure respectively. The domain of these value spaces is infinite for all of the random fields. The joint PDF is a nonnegative function of ξ , η , and ζ at any point (\underline{x},t) , and it should satisfy the following property,

$$\int_{-\infty}^{\infty} f(\xi_1, \xi_2, \xi_3, \eta, \zeta) d\xi_1 d\xi_2 d\xi_3 d\eta d\zeta = 1 \quad (3.2.6)$$

Also, since the expectation (ensemble average) of velocity components, pressure, and entropy are finite, the above function should go to zero faster than its arguments go to infinity. In general, if Q is a function of flowfield quantities, i.e., $Q = Q(\underline{U}(\underline{x},t), S(\underline{x},t), P(\underline{x},t))$, then

$$\langle Q(\underline{U}, S, P) \rangle = \int_{-\infty}^{\infty} Q(\xi, \eta, \zeta) f(\xi, \eta, \zeta; \underline{x}, t) d\xi d\eta d\zeta \quad (3.2.7)$$

The expectation of any variable, such as U_i , is given as

$$\langle U_i(\underline{x}, t) \rangle = \int_{-\infty}^{\infty} \xi_i f(\xi_1, \xi_2, \xi_3, \eta, \zeta; \underline{x}, t) d\xi_1 d\xi_2 d\xi_3 d\eta d\zeta \quad (3.2.8)$$

$i = 1, 2, 3$

To obtain a transport equation for the above joint PDF, define a "fine-grained" function

$$g = \delta(S(\underline{x}, t) - s) \delta(P(\underline{x}, t) - p) \prod_{i=1}^3 \delta(U_i(\underline{x}, t) - u_i);$$

then the expectation of this function is given as

$$\langle g(\underline{x}, t) \rangle = \int_{-\infty}^{\infty} \delta(\eta-s) \delta(\zeta-p) \prod_{i=1}^3 \delta(\xi_i - u_i) \quad (3.2.9)$$

$$f(\underline{\xi}, \eta, \zeta; \underline{x}, t) d\underline{\xi} d\eta d\zeta$$

which based on the definition of delta functions is reduced to

$$\langle g \rangle = f(\underline{u}, s, p; \underline{x}, t) \quad (3.2.10)$$

The time and space derivatives of the fine-grained function are obtained using the chain rule

$$\frac{\partial g}{\partial t} = - \frac{\partial g}{\partial u_1} \frac{\partial U_1}{\partial t} - \frac{\partial g}{\partial s} \frac{\partial S}{\partial t} - \frac{\partial g}{\partial p} \frac{\partial P}{\partial t} \quad (3.2.11)$$

$$\frac{\partial g}{\partial x_j} = - \frac{\partial g}{\partial u_1} \frac{\partial U_1}{\partial x_j} - \frac{\partial g}{\partial s} \frac{\partial S}{\partial x_j} - \frac{\partial g}{\partial p} \frac{\partial P}{\partial x_j} \quad (3.2.12)$$

Multiplying both sides of Equation (3.2.12) by U_j and adding it to Equation (3.2.11) the following equation is obtained

$$\frac{Dg}{Dt} = - \left[\frac{\partial g}{\partial u_1} \frac{DU_1}{Dt} + \frac{\partial g}{\partial s} \frac{DS}{Dt} + \frac{\partial g}{\partial p} \frac{DP}{Dt} \right] \quad (3.2.13)$$

where

$$D()/Dt = \frac{\partial ()}{\partial t} + U_j \frac{\partial ()}{\partial x_j}$$

Multiplying the above equation by density, ρ , and the conservation of mass equation by g and adding obtains the following equation

$$\begin{aligned} \frac{\partial}{\partial t} (\rho g) + \frac{\partial}{\partial x_1} (\rho g U_1) &= \frac{\partial g}{\partial u_1} \left(\rho \frac{DU_1}{Dt} \right) \\ &+ \frac{\partial g}{\partial s} \left(\rho \frac{DS}{Dt} \right) + \frac{\partial g}{\partial p} \left(\rho \frac{DP}{Dt} \right) \end{aligned} \quad (3.2.14)$$

The expectation of the above equation is taken to obtain a transport equation for the joint PDF. The expectation of the first term is given as

$$\left\langle \frac{\partial}{\partial t} (\rho g) \right\rangle = \frac{\partial}{\partial t} \int_{-\infty}^{\infty} \rho(\eta, \zeta) \delta(\underline{x} - \underline{u}) \delta(\eta - s) \delta(\zeta - p) \quad (3.2.15)$$

$$f(\underline{x}, \eta, \zeta; \underline{x}, t) d\underline{x} d\eta d\zeta$$

Therefore,

$$\left\langle \frac{\partial}{\partial t} (\rho g) \right\rangle = \frac{\partial}{\partial t} [\rho(s, p) f(\underline{u}, s, p; \underline{x}, t)] = \rho(s, p) \frac{\partial f}{\partial t} \quad (3.2.16)$$

Similarly,

$$\left\langle \frac{\partial}{\partial x_j} (\rho u_j g) \right\rangle = \frac{\partial}{\partial x_j} [\rho(s, p) u_j f(\underline{u}, s, p; \underline{x}, t)] = \rho(s, p) u_j \frac{\partial f}{\partial x_j} \quad (3.2.17)$$

Substituting from Equation (3.2.16) and (3.2.17) for the left-hand terms of expectation of Equation (3.2.14) and utilizing the conservation equations (1.1.6) and (3.2.1) for the total derivatives appearing on the right-hand of Equation (3.2.14), the following transport equation is obtained for the joint PDF, f ,

$$\begin{aligned} \rho(s, p) \frac{\partial f}{\partial t} + \rho(s, p) u_j \frac{\partial f}{\partial x_j} = & \left\langle \frac{\partial g}{\partial u_1} \left(-\frac{\partial p}{\partial x_1} + \frac{\partial \tau_{1j}}{\partial x_j} + \rho G_1 \right) \right\rangle \quad (3.2.18) \\ & + \left\langle \frac{\partial g}{\partial s} \left(\frac{1}{T} \tau_{1j} \varepsilon_{1j} + \frac{\kappa}{T^2} \left(\frac{\partial T}{\partial x_1} \right)^2 + \frac{\partial}{\partial x_1} \left(\kappa \frac{\partial \ln T}{\partial x_1} \right) \right) \right\rangle + \left\langle \frac{\partial g}{\partial p} \left(\rho \frac{Dp}{Dt} \right) \right\rangle \end{aligned}$$

The objective is to obtain a partial differential equation expressing the joint PDF, f , in terms of its arguments u_i , p , and s . Therefore, the right-hand side of Equation (3.2.18) must be expanded to obtain terms in the desirable form. The momentum and entropy transport equations have been used to replace the material derivatives of velocity and entropy. However, the choice of a transport equation for pressure is not very clear. One obvious method is to use the thermodynamic state Equation (3.2.2) to relate pressure to density and entropy. Here the transport equation for enthalpy was used to obtain a transport equation for pressure, i.e.,

$$\frac{Dp}{Dt} = \rho \frac{Dh}{Dt} - \frac{\partial}{\partial x_j} \left(\kappa \frac{\partial T}{\partial x_j} \right) - \tau_{ij} \varepsilon_{ij} \quad (3.2.19)$$

After substitution of this term in the right-hand side of Equation (3.2.18), the expectation of each term on the right-hand side of Equation (3.2.18) should be evaluated. This procedure is straightforward, (Ref. 37), but rather lengthy, and the final equation contains over forty terms on the right-hand side. Since the primary focus of this study is on investigating the role of pressure, the terms containing the effects of viscosity and heat conduction are neglected. This simplification results in the following equation for the variation of the probability density function with respect to velocity, entropy, and pressure at any given point in space and time.

$$\begin{aligned}
 \rho(s, p) \frac{\partial f}{\partial t} + \rho(s, p) u_j \frac{\partial f}{\partial x_j} = & \left\{ -p \frac{\partial^2 f}{\partial x_1 \partial u_1} - \frac{\partial^2}{\partial u_1 \partial u_j} \langle p g \frac{\partial u_j}{\partial x_1} \rangle \right. \\
 & \left. - \frac{\partial^2}{\partial u_1 \partial s} \langle p g \frac{\partial s}{\partial x_1} \rangle - \frac{\partial^2}{\partial u_1 \partial p} \langle p g \frac{\partial p}{\partial x_1} \rangle + G_1 \rho(s, p) \frac{\partial f}{\partial u_1} \right\} \\
 & + \left\{ \left[\rho \left(\frac{\partial h}{\partial p} \right)_s + 2h \left(\frac{\partial \rho}{\partial p} \right)_s \right] \left(\rho \frac{\partial f}{\partial t} + u_j \rho \frac{\partial f}{\partial x_j} \right) + \rho^2 h \left(\frac{\partial^2 f}{\partial p \partial t} + u_j \frac{\partial^2 f}{\partial p \partial x_j} \right) \right. \\
 & \left. + \frac{\partial^2}{\partial p^2} \langle \rho^2 h g \frac{Dp}{Dt} \rangle + \frac{\partial^2}{\partial u_1 \partial p} \langle \rho^2 h g \frac{Du_1}{Dt} \rangle - \frac{\partial}{\partial p} \langle \rho h g \frac{Dp}{Dt} \rangle + \frac{\partial^2}{\partial p \partial s} \langle \rho^2 h g \frac{Ds}{Dt} \rangle \right\} + \text{viscous terms}
 \end{aligned} \tag{3.2.20}$$

The above equation is a linear partial differential equation for the single-point joint PDF, $f(\underline{u}, s, p; \underline{x}, t)$. In three-dimensional physical space, f is a function of nine independent variables, and the above equation represents the changes in this function caused by changes in these nine dimensions. Those terms appearing in ensemble average bracket signs, $\langle \cdot \rangle$, are nonclosed and relate this single-point joint PDF to other multi-point joint PDF's. These terms must be modeled. The first group of terms appearing on the right-hand of the PDF transport equation are due to the momentum transport, and the second group of terms are due to the pressure transport. The entropy transport causes changes in the joint PDF only through molecular diffusion effects and all its contributions are included in the neglected viscous terms. However, entropy gradients (or hot spots) also affect the nature of the joint PDF through changes in pressure and other thermodynamic quantities. This statement is supported by the presence of the nonclosed terms involving the spatial and temporal variation of entropy in the above equation. These nonviscous entropy effects on the joint PDF can be interpreted as the contribution of temperature spottiness in modifying the joint

PDF and hence they effect the acoustic and dynamic nature of the flowfield. To be able to determine the extent of such effects and the effect of other nonclosed terms one must model them in terms of the single-point joint PDF. Such modeling requires information or assumptions regarding the nature of multi-point joint probability density functions (Ref. 11) and their relation to the above function.

The presence of the closed form terms makes it possible to investigate the nature of the above equation, and the effect that these terms have on it. Before investigating the effect of closed form terms it should be noted that the above form of the PDF equation is drastically different from its incompressible counterpart. It is a common practice to use the turbulence models developed for incompressible flowfields in the modeling of turbulent compressible flowfields. Therefore, it is important to discuss the relation of the above equation to its incompressible counterpart.

For an incompressible flowfield the density of a fluid particle stays constant as one follows this fluid particle. This assumption implies that the conservation of mass reduces to

$$\frac{D\rho}{Dt} = 0 \quad (3.2.21)$$

From a thermodynamic point of view this case implies a zero change in the thermodynamic quantities in response to a finite change in pressure. This results in an infinite value of the speed of sound defined by

$$a^2 = \left[\frac{\partial P}{\partial \rho} \right]_s \quad (3.2.22)$$

In other words, the change in pressure does not cause a change of volume and subsequent storage of energy in the internal energy mode. Instead, the only role that the change of pressure plays is in the transportation of the fluid particle such that the conservation of internal energy for an incompressible inviscid nonheat-conducting flowfield reduces to

$$\frac{De}{Dt} = 0 \quad (3.2.23)$$

However, the conservation of kinetic (mechanical) energy shows the role of pressure and is given as

$$\rho \frac{D}{Dt} \left(\frac{1}{2} U_i U_i \right) = \rho G_i U_i - U_i \frac{\partial P}{\partial x_i} \quad (3.2.24)$$

Therefore, there is a decoupling between the momentum equation and the conservation of energy equation. Pressure is now defined as a forcing function which creates a flowfield in which the velocity field satisfies the condition of zero divergence in addition to the

appropriate boundary conditions. This means that given the velocity field satisfying the appropriate boundary conditions, and with zero divergence, the pressure can be determined exactly. Statistically, pressure is no longer a random variable but a function of the velocity field with an exact functional relationship given by the following equation:

$$P(\underline{x}, t) = - \frac{1}{4\pi} \iiint_0 \frac{\rho}{|\underline{x}-\underline{y}|} \frac{\partial u_i}{\partial y_j} \frac{\partial u_j}{\partial y_i} dy_1 dy_2 dy_3 \quad (3.2.25)$$

The PDF is no longer a function of pressure and the role of entropy appears only through viscous terms. The single-point joint PDF transport equation for incompressible flowfields is given by (Ref. 37)

$$\frac{\partial f}{\partial t} + u_j \frac{\partial f}{\partial x_j} = - \left\langle \frac{1}{\rho} \frac{\partial P}{\partial x_i} \frac{\partial g}{\partial u_i} \right\rangle + G_i \frac{\partial f}{\partial u_i} + \text{viscous terms} \quad (3.2.26)$$

The integral dependence of pressure on the velocity field links the single-point PDF to every point in the flowfield instantaneously. In contrast, the compressible PDF transport equation includes closed form terms that display the local effect of pressure on the function f . These terms will be studied next.

Assuming perfect gas behavior and neglecting all nonclosed (multi-point) and gravitation terms, Equation (3.2.20) reduces to

$$\frac{\partial f}{\partial t} + u_i \frac{\partial f}{\partial x_i} = \frac{\gamma p^2}{2h\rho^2} \frac{\partial^2 f}{\partial x_i \partial u_i} - \frac{\gamma p}{2} \left(\frac{\partial^2 f}{\partial p \partial t} + u_i \frac{\partial f}{\partial p \partial x_i} \right) \quad (3.2.27)$$

Since the effects of entropy are only present in neglected nonclosed terms, the above equation can be simplified by considering isentropic processes, i.e.,

$$h = h_r (p/p_r)^{\frac{\gamma-1}{\gamma}} \quad \text{and} \quad \rho = \rho_r (p/p_r)^{\frac{1}{\gamma}}.$$

Utilizing this assumption and integrating the above equation over pressure and entropy space, the following equation is obtained for the probability density function of the velocity field \hat{f}

$$\frac{\partial \hat{f}}{\partial t} + u_i \frac{\partial \hat{f}}{\partial x_i} = \frac{2A_r}{2-\gamma} \frac{\partial^2}{\partial x_i \partial u_i} \int_{-\infty}^{\infty} \int_{-\infty}^{\infty} p^{\frac{\gamma-1}{\gamma}} f(\underline{u}, s, p; \underline{x}, t) dp ds \quad (3.2.28)$$

where

$$\hat{f}(\underline{u}; \underline{x}, t) = \int_{-\infty}^{\infty} \int_{-\infty}^{\infty} f(\underline{u}, s, p; \underline{x}, t) dp ds$$

and

$$A_r = \frac{1}{2} a_r^2 p_r^{\frac{1}{\gamma}} / \rho_r h_r$$

a_r is the referenced speed of sound propagation. This equation can be thought of as the simplest possible counterpart of the incompressible PDF equation, Equation (3.2.26). It indicates a strong local coupling between velocity and pressure fields which is dependent on the speed of sound. However, it is expected that as the speed of sound approaches large values this local coupling reduces, and the multi-point nonclosed terms become the only link between pressure and velocity fields. Therefore, this term is only active at high Mach numbers and acts as a pressure dependent diffusion.

It should be emphasized that Equation (3.2.27) is a closed form linear partial differential equation for the PDF of the velocity, pressure, and entropy fields, and given appropriate boundary conditions, it can be solved for $f(\underline{u}, s, p; \underline{x}, t)$. Therefore, this equation can be investigated to see under what conditions, neglecting the nonclosed terms, there exists a unique solution for this equation. This analysis indicates that the principle of the hybrid stochastic model is valid as long as the local effects created by compressibility are included in the turbulence modeling of the velocity field.

3.3 Effects of discontinuities in supersonic flows with large fluctuations.

The interaction of shocks with turbulence poses a formidable problem of practical importance (Billig and Dugger Ref.69). So far, mostly moment closures (Kollmann, Haminh and Vandromme Ref.70) have been used to predict mean fields in the region of interaction and mean shock properties and location were calculated with shock-capturing techniques. The application of pdf methods to supersonic flows with embedded shocks is a new area. Since shocks are near discontinuities for finite Reynolds/Peclet numbers (and approach genuine discontinuities as Reynolds/Peclet numbers go to infinity), it is natural to ask what the structure of the pdf equation will be in the presence of discontinuities. For the investigation of this question, a single balance equation for a scalar quantity $\Phi(x, t)$ is considered. The equation

$$\frac{\partial \Phi}{\partial t} + \frac{\partial F}{\partial x} - S = 0, \quad \Phi(x, 0) = \Phi_0(x) \quad (3.3.1)$$

where $F(\Phi, x, t)$ is the flux and $S(\Phi, x, t)$ the source term. This equation admits discontinuous solution in its weak form (Majda Ref.71). If the initial condition is chosen randomly from a set of differentiable functions, then the statistical properties of the solution can be described in terms of the pdf $f_1(\varphi; x, t)$.

$$\hat{f} \equiv \delta(\Phi(x, t) - \varphi), \quad f_1 = \langle \hat{f} \rangle$$

If the flux F and the source S are local functions of Φ , and if the solution Φ remains at least once continuously differentiable, then the pdf equation can be obtained in the form

$$\frac{\partial f_1}{\partial t} + \frac{\partial F}{\partial \Phi} \frac{\partial f_1}{\partial x} + \frac{\partial}{\partial \varphi} (S(\varphi) f_1) = \left\langle \frac{\partial^2 F}{\partial \Phi^2} \frac{\partial \Phi}{\partial x} \hat{f} \right\rangle \quad (3.3.2)$$

However, the right hand side is nonzero if the flux F is a nonlinear function of Φ . Its structure is not suited for the analysis of discontinuities and a different method must be used for this case. The theory of stochastic differential equations allows analysis of the scalar Φ taken at a fixed location x . The temporal increment of Φ is then

$$d\Phi = d\Phi_0 + dP + dW \quad (3.3.3)$$

where $d\Phi_0$ is the deterministic and differentiable part of $d\Phi$, dP the increment due to a jump process and dW the increment due to a continuous but not differentiable process. The differential equation (3.3.1) leads to

$$d\Phi = -\frac{\partial F}{\partial x} dt + S dt$$

The source term $S dt$ can now be viewed as the sum

$$S dt = S_0 dt + dW \quad (3.3.4)$$

of the differentiable contribution $S_0 dt$ and a continuous but non-differentiable part dW . The flux term requires a closer look. If $F(\Phi)$ depends on Φ in a nonlinear fashion such that discontinuities form in finite time from smooth initial conditions, then there exist random and discrete time instances when discontinuities cross the fixed location x . Hence, the derivative of the flux is the sum of a singular and a continuous part

$$\frac{\partial F}{\partial x} = \sum_{t_i \leq t} [\Phi]_i \delta(t - t_i) + \left(\frac{\partial F}{\partial x}\right)_c$$

where $[\Phi]_i$ denotes the jump height at time t_i and $(\frac{\partial F}{\partial x})_c$ the continuous part. Hence,

$$dP \equiv \sum_{t_i \leq t} [\Phi]_i dt \delta(t - t_i) \quad (3.3.5)$$

is the increment of a jump process and the increments in the stochastic differential equation are now identified as

$$d\Phi_0 \equiv (S_0 - \left(\frac{\partial F}{\partial x}\right)_c) dt$$

along with (3.3.4) and (3.3.5). The pdf equation for the solution process of (3.3.3) is then given by

$$\frac{\partial f_1}{\partial t} + \frac{\partial}{\partial \varphi} \left\{ \left(S_0 - \left(\frac{\partial F}{\partial x}\right)_c \right) f_1 \right\} = \frac{1}{2} \frac{\partial^2}{\partial \varphi^2} \{ B f_1 \} + \frac{1}{\tau} \left\{ \int d\Phi' f_1(\Phi') T(\Phi' \rightarrow \Phi) - f_1 \right\} \quad (3.3.6)$$

if dW is specialized to a Wiener process. It becomes clear by inspection of this equation that the discontinuities crossing a given location x affect the evolution equation for the pdf in integral form appropriate for jump processes. This integral requires the probability of a jump from Φ' to Φ , denoted by $T(\Phi' \rightarrow \Phi)$, and the time scale τ for the appearance of discontinuities at x . The pdf equation derived from (3.3.3) does not provide this information, because only a single location x is considered and x -derivatives constitute therefore new unknowns.

This example showed that the appearance of shock waves with random location and strength produces an integral contribution to the pdf equation. It can be expected that the time scale and the transition pdf $T(\Phi' \rightarrow \Phi)$ are functionals of the flow variables. The explicit form of this functional relation is unknown at present.

CHAPTER 4. MODELING AND SOLUTION OF A TRANSPORT EQUATION FOR A JOINT PDF.

Task 5 of the contract was devoted to the study of possible formulations of the pdf method for compressible turbulent flows with combustion reactions and the development of closure models for this type of flow. The pdf method can be based on the transport equation for the pdf of thermo-chemical scalars plus variables measuring the rate of relative volume expansion or the material derivative of the pressure. The pdf approach offers the possibility of treating chemical non-equilibrium in rigorous fashion, which is particularly important for high speed flows characterized by high shearing rates and short residence times. The progress achieved in the development of a closure model for the pdf equation and the successful application of this model to supersonic hydrogen flames will be reported in detail.

4.1 Pdf equation.

Turbulent flow at supersonic speed can be modified significantly by compressibility and the interaction with shocks created outside the turbulent flow field and random shocks (called shocklets, Johnson et al. Ref.72) generated in supersonic turbulent shear layers. Pdf methods can be adapted to cope with the effects of compressibility including random discontinuities and combustion. We consider the case of infinitely fast reactions, in which three variables determine the local state: Mixture fraction, pressure and enthalpy. Pressure can vary significantly in supersonic flows and enthalpy is not conserved due to frictional heating in high shear regions. Hence, no further simplification, as in the case of low Mach number subsonic flames, is possible. The single point pdf f_1 is then set up for the velocity \underline{v} , density ρ or a local function of density such as $\log(\rho)$ which will be used below, internal energy u , relative rate of volume expansion D and mixture fraction ξ

$$f_1(\underline{v}, d, u, \zeta, \eta; \underline{x}, t) \equiv \langle \delta(\underline{v} - \underline{v}) \delta(\rho - d) \delta(e - u) \delta(D - \zeta) \delta(\xi - \eta) \rangle \quad (4.1.1)$$

The transport equation for this pdf can be obtained using standard methods and emerges in the form

$$\begin{aligned} d \left(\frac{\partial f_1}{\partial t} + v_\alpha \frac{\partial f_1}{\partial x_\alpha} \right) = & - \frac{\partial}{\partial v_\alpha} \left\{ - \left(\frac{\partial p}{\partial x_\alpha} \right) \hat{f} \right\} + \frac{1}{Re} \left\langle \frac{\partial \tau_{\alpha\beta}}{\partial x_\beta} \hat{f} \right\rangle + B d \langle f_\alpha \hat{f} \rangle \\ & + \frac{\partial}{\partial d} (d^2 \zeta f_1) - \frac{\partial}{\partial u} \left\{ - \frac{\gamma - 1}{c_v} du \zeta f_1 + \gamma(\gamma - 1) \frac{M_0^2}{Re} \langle \Phi \hat{f} \rangle - \frac{\gamma}{Pe} \left\langle \frac{\partial q_\alpha}{\partial x_\alpha} \hat{f} \right\rangle \right\} \\ & - \frac{\partial}{\partial \zeta} \left\{ \frac{1}{Re} \left\langle \frac{\partial}{\partial x_\alpha} \left(\frac{1}{\rho} \frac{\partial \tau_{\alpha\beta}}{\partial x_\beta} \right) \hat{f} \right\rangle - \left\langle \frac{\partial v_\alpha}{\partial x_\beta} \frac{\partial v_\beta}{\partial x_\alpha} \hat{f} \right\rangle + B \left\langle \frac{\partial f_\alpha}{\partial x_\alpha} \hat{f} \right\rangle - \left\langle \frac{\partial}{\partial x_\alpha} \left(\frac{1}{\rho} \frac{\partial p}{\partial x_\alpha} \right) \hat{f} \right\rangle \right\} - \frac{\partial}{\partial \eta} \left\langle \frac{\partial}{\partial x_\alpha} (\rho \Gamma \frac{\partial \zeta}{\partial x_\alpha}) \hat{f} \right\rangle \end{aligned} \quad (4.1.2)$$

Mean thermodynamic properties follow from the pdf f_1 by integration. The mean pressure for instance is given by

$$\langle p \rangle = \int dd \int du \int d\eta p(d, u, \eta) f_1(d, u, \eta)$$

where $p(d, u, \eta)$ denotes the local relation of pressure to density, internal energy and mixture fraction. The calculation of this type of local relation was discussed in the first report.

4.2 Closure model for the pdf equation.

The closure model to be considered refers to the pdf equation resulting from (4.1.2) by integration over velocity space and introduction of the density-weighted pdf \tilde{f}_1 defined by

$$\tilde{f}_1 \equiv \frac{\rho(\varphi_1, \dots, \varphi_l)}{\langle \rho \rangle} f_1(\varphi_1, \dots, \varphi_l; \underline{x}, t) \quad (4.2.1)$$

where $\underline{\varphi}$ corresponds to the scalar variables (ρ, e, D, ζ) and $l = 4$. The integrated pdf transport equation for the set of l thermo-chemical variables follows from (4.1.2) for high Reynolds numbers in the form

$$\begin{aligned} \langle \rho \rangle \left\{ \frac{\partial \tilde{f}_1}{\partial t} + \tilde{v}_\beta \frac{\partial \tilde{f}_1}{\partial x_\beta} - \frac{\partial}{\partial d} (d \zeta \tilde{f}_1) \right\} + \frac{\partial}{\partial u} \left\{ -\langle \rho \rangle \frac{\gamma-1}{c_v} u \zeta \tilde{f}_1 + \gamma(\gamma-1) \frac{M_0^2}{Re} \langle \Phi \tilde{f} \rangle \right\} \\ + \frac{\partial}{\partial \eta} \left\{ -\left\langle \frac{\partial v_\alpha}{\partial x_\beta} \frac{\partial v_\beta}{\partial x_\alpha} \tilde{f} \right\rangle + B \left\langle \frac{\partial f_\alpha}{\partial x_\alpha} \tilde{f} \right\rangle - \left\langle \frac{\partial}{\partial x_\alpha} \left(\frac{1}{\rho} \frac{\partial p}{\partial x_\alpha} \right) \tilde{f} \right\rangle \right\} = -\frac{\partial}{\partial x_\alpha} \left(\langle \rho \rangle \langle v_\alpha'' | \Psi_j = \varphi_j \rangle \tilde{f}_1 \right) \\ - \frac{\partial}{\partial u} \frac{\gamma}{Pe} \left\langle \frac{\partial q_\alpha}{\partial x_\alpha} \tilde{f} \right\rangle - \frac{\partial}{\partial \zeta} \frac{1}{Re} \left\langle \frac{\partial}{\partial x_\alpha} \left(\frac{1}{\rho} \frac{\partial \tau_{\alpha\beta}}{\partial x_\beta} \right) \tilde{f} \right\rangle - \frac{\partial}{\partial \eta} \left\langle \frac{\partial}{\partial x_\alpha} (\rho \Gamma \frac{\partial \zeta}{\partial x_\alpha}) \tilde{f} \right\rangle \end{aligned} \quad (4.2.2)$$

The terms on the right hand side can be shown to contain dominant terms describing turbulent mixing in scalar space which appear in the form

$$\left(\frac{\partial \tilde{f}_1}{\partial t} \right)_{mix} = - \sum_{j=2}^l \sum_{k=2}^l \frac{\partial^2}{\partial \varphi_j \partial \varphi_k} (\langle \epsilon_{jk} | \Psi_j = \varphi_j \rangle \tilde{f}_1) \quad (4.2.3)$$

and the scalar dissipation rates ϵ_{ij} in the conditional expectations are defined by

$$\epsilon_{ij} \equiv \Gamma \frac{\partial \Psi_i}{\partial x_\alpha} \frac{\partial \Psi_j}{\partial x_\alpha} \quad (4.2.4)$$

with equal diffusivities $\Gamma_i = \Gamma_j = \Gamma$. Note that no such term acts in the first scalar direction which corresponds to the variation of density.

4.2.1 Mixing Model.

Any closure model for the mixing process described by (4.2.4) should share as many properties as possible with the exact term. It should preserve normalisation and mean values and decrease variances and covariances. The pdf should remain nonnegative and should not spread outside the domain of allowable states. The pair interaction model for the $l-1$ (note

that one of the scalars does not mix as will be explained in the next chapter) scalar variables is defined by

$$\left(\frac{\partial \tilde{f}_1}{\partial t}\right)_{\text{mix}} = \frac{1}{\tau} \left\{ \int_{\mathfrak{R}} d\underline{\varphi}' \int_{\mathfrak{R}} d\underline{\varphi}'' \tilde{f}_1(\underline{\varphi}') \tilde{f}_1(\underline{\varphi}'') T(\underline{\varphi}', \underline{\varphi}'', \underline{\varphi}) - \tilde{f}_1(\underline{\varphi}) \right\} \quad (4.2.5)$$

It is assumed that all scalars are appropriately normalized such that the scalar space (set of all realizable states) \mathfrak{R} is a subset of an $l-1$ -dimensional cube. It should be noted that \mathfrak{R} may have intricate boundaries as a consequence of realizability conditions. The transition pdf $T(\underline{\varphi}', \underline{\varphi}'', \underline{\varphi})$ must satisfy the requirements

$$T(\underline{\varphi}', \underline{\varphi}'', \underline{\varphi}) = T(\underline{\varphi}', \underline{\varphi}'', \underline{\varphi}' + \underline{\varphi}'' - \underline{\varphi}) \quad (4.2.6)$$

and

$$T(\underline{\varphi}', \underline{\varphi}'', \underline{\varphi}) = 0 \text{ for } \underline{\varphi} \notin N(\underline{\varphi}', \underline{\varphi}'') \quad (4.2.7)$$

The central part of the condition (4.9) is the construction of the neighbourhood $N(\underline{\varphi}', \underline{\varphi}'')$ which is the interval $[\varphi', \varphi'']$ in the single scalar case. N can be at most the cube $C_{l-1} \equiv \{\underline{\varphi} : \varphi_i \in [\varphi'_i, \varphi''_i], i = 2, l\}$ defined by $\underline{\varphi}'$ and $\underline{\varphi}''$ for pairwise interaction. Realizability requires that the mixed states are in \mathfrak{R} , hence

$$N \subseteq C_{l-1} \cap \mathfrak{R} \quad (4.2.8)$$

must hold. Symmetry

$$\underline{\varphi} \in N \Leftrightarrow \underline{\varphi}' + \underline{\varphi}'' - \underline{\varphi} \in N \quad (4.2.9)$$

must be imposed to insure the properties of a mixing model. Furthermore is T pdf with respect to $\underline{\varphi}$

$$\int_{\mathfrak{R}} d\underline{\varphi} T(\underline{\varphi}', \underline{\varphi}'', \underline{\varphi}) = 1 \quad (4.2.10)$$

Conditions (4.2.6)-(4.2.10) do not define the mixing model uniquely but represent a class of models. It is important to realize that the structure of the scalar domain \mathfrak{R} modifies the neighbourhood N unless N is reduced to the line connecting $\underline{\varphi}'$ and $\underline{\varphi}''$. If $\underline{\varphi}'$ and $\underline{\varphi}''$ are close to the boundary of \mathfrak{R} the neighbourhood is essentially the connecting line due to (4.2.8), but if the points are inside \mathfrak{R} and far away from its boundary then may N be the cube C_{l-1} . The transition pdf T is set up as

$$T(\underline{\varphi}', \underline{\varphi}'', \underline{\varphi}) = G(\zeta) H(\underline{\varphi}', \underline{\varphi}'', \underline{\varphi}) \quad (4.2.11)$$

where

$$H(\underline{\varphi}', \underline{\varphi}'', \underline{\varphi}) = \begin{cases} \frac{1}{\mu_{l-1}(N)} & \text{for } \underline{\varphi} \in N(\underline{\varphi}', \underline{\varphi}'') \\ 0 & \text{otherwise} \end{cases} \quad (4.2.12)$$

and $\mu_{l-1}(N)$ is the $l-1$ -dimensional volume of $N(\underline{\varphi}', \underline{\varphi}'')$ and ζ denotes the centered variable

$$\zeta_i \equiv \frac{2}{\mu_{l-1}(N)^{\frac{1}{l-1}}} \left[\varphi_i - \frac{1}{2}(\varphi'_i + \varphi''_i) \right], \quad i = 2, l \quad (4.2.13)$$

It follows that T satisfies

$$\int_N d\zeta G(\zeta) = 2^{l-1} \quad (4.2.14)$$

and

$$G(\zeta) = G(-\zeta) \quad (4.2.15)$$

The present choice for the function $G(\zeta)$ is a constant determined by the condition (4.2.14). This concludes the construction of the mixing model for (4.2.2).

4.2.2 Compressibility Effects.

The closure model representing the effects of compressibility is most conveniently formulated in the Lagrangean frame in the form of stochastic differential equations. The basic laws are written in abbreviated form

$$\frac{d \log \rho}{dt} = -D \quad (4.2.16)$$

$$\frac{dD}{dt} = Q_D \quad (4.2.17)$$

$$\frac{dE}{dt} = Q_E \quad (4.2.18)$$

$$\frac{d\zeta}{dt} = Q_\zeta \quad (4.2.19)$$

where d/dt denotes the material derivative and $D \equiv \nabla \cdot \underline{v}$ the relative rate of volume expansion. The right hand side terms are conveniently set up in the Eulerian frame (or implicit Lagrangean). The basic laws lead to the explicit form of the Q_i given by

$$Q_D \equiv \frac{1}{Re} \frac{\partial}{\partial x_\alpha} \left(\frac{1}{\rho} \frac{\partial \tau_{\alpha\beta}}{\partial x_\beta} \right) - \frac{\partial}{\partial x_\alpha} \left(\frac{1}{\rho} \frac{\partial p}{\partial x_\alpha} \right) - \frac{\partial v_\alpha}{\partial x_\beta} \frac{\partial v_\beta}{\partial x_\alpha} + \frac{\partial q_\alpha}{\partial x_\alpha} \quad (4.2.20)$$

where q_α denotes the energy flux vector,

$$Q_E \equiv -\gamma(\gamma-1)M_a^2(1+p)D + \frac{1}{Re} \gamma(\gamma-1)M_a^2 \Phi - \frac{\gamma}{Re Pr} \frac{\partial q_\alpha}{\partial x_\alpha} \quad (4.2.21)$$

where Φ is the dissipation function,

$$Q_\zeta \equiv \frac{1}{Re Sc} \frac{\partial}{\partial x_\alpha} \left(\rho \Gamma \frac{\partial \zeta}{\partial x_\alpha} \right) \quad (4.2.22)$$

The general form of the closure model for the pdf equation given above (47) (which contains the dynamics of the variables density, internal energy, relative rate of volume expansion and mixture fraction) is set up in terms of the stochastic differential equation

$$dY_i = A_i dt + b_{ij} dW_j + dJ_i \quad (4.2.23)$$

where dW_i is the increment of a normalized random process (such as the Wiener process) and dJ_i is the increment corresponding to a jump process. The closure for the equations (4.2.16) - (4.2.19) will now be discussed in detail.

A. The time rate of change of the relative rate of volume expansion consists of three contributions: The increment due molecular transport which is regarded as mixing, the increment due to the passage of isentropic compression and expansion waves past the material point considered, and the passage of random shock waves past. The first contribution ΔD_{mix} is represented by the mixing model. It can be shown that the viscous term in (4.2.20) implies indeed that D is subject to diffusion. Hence will D participate in the mixing model described in the previous chapter. The second contribution is modelled according to an Ornstein-Uhlenbeck process

$$\Delta D_{is} = \{c_{\rho 1} f(M_a) \frac{\Delta t}{\tau}\}^{\frac{1}{2}} \eta - c_{\rho 2} f(M_a) \frac{\Delta t}{\tau} (D - \langle D \rangle) \quad (4.2.24)$$

where $c_{\rho 1} = 1.0$ and $c_{\rho 2} = 0.5$ are constants and

$$f(M_a) = M_a^2$$

is an empirical function of the local Mach-number. It ensures that the increment of D vanishes as the Mach-number goes to zero. The first part of ΔD is a Wiener process (η is a Gaussian random variable with zero mean and unit variance) representing the random stirring effect of isentropic compression and expansion waves moving past the point considered. The second part is a drift term ensuring the existence of a steady state. Finally τ is the turbulent time scale provided by the second order closure. The model for Q_D follows as

$$Q_D \Delta t \triangleq \Delta D_{mix} + \Delta D_{is} + \Delta D_{sh} \quad (4.2.25)$$

where the last term represents the random occurrence of shocks. This contribution is nearly singular and corresponds to the derivative of a Dirac-pseudofunction in the inviscid limit. There is no model for it at present and random shocks will be taken into account in the mass balance discussed below.

B. Mass balance (4.16) does not require closure and contains only a drift term

$$d \log \rho = -D dt \quad (4.2.26)$$

as long as the relative rate of volume expansion remains sufficiently smooth. The case of random shocks leads to a singularity for D and will be treated as separate contribution to $d \log(\rho)/dt$ in the form of a jump process. If the local Mach-number is greater than unity, shocks may appear with the maximal strength given by the normal shock relation

$$G(M_a) = \begin{cases} \frac{M_a^2 - 1}{1 + \frac{1}{2} M_a^2} & \text{for } M_a \geq 1 \\ 0 & \text{otherwise.} \end{cases} \quad (4.2.27)$$

and the increment dJ_1 for the jump process representing the random shocks is modelled by

$$dJ_1 = G(M_a) \frac{\tilde{\epsilon}}{k} N_s \left(\frac{dt}{\tau} \right) \eta \quad (4.2.28)$$

where $N_s(\phi)$ denotes a nonnegative integer random variable representing the number of shocks arriving at the material point in ϕ dimensionless time units and $0 \leq \eta \leq 1$ is the random variable giving the dimensionless shock strength. The current model for $N_s(\phi)$ is a Poisson process and η is a random variable with uniform distribution. The complete increment for the logarithm of density is given by

$$\Delta \log \rho \doteq -D\Delta t + dJ_1 + \Delta D_{dis} \quad (4.2.29)$$

where the last contribution is due to frictional heating at constant pressure to be discussed below. This contribution is given by

$$\Delta D_{dis} = \rho(\zeta, u + \Delta u, p) - \rho(\zeta, u, p)$$

where Δu is the increment of internal energy due to frictional heating. Finally, note that $\log \rho$ does not participate in the mixing process.

C. The increment for the internal energy consists of several contributions

$$Q_E \Delta t \doteq \Delta u_{mix} + \Delta u_{is} + \{-\gamma(\gamma - 1)M_a^2(1 + p)D + \frac{1}{Re}\gamma(\gamma - 1)M_a^2\Phi\}\Delta t + \Delta u_{sh} \quad (4.2.30)$$

The first part is due to heat conduction and is therefore part of the mixing model applied to internal energy. The second part of the increment is due to the isentropic expansion and compression waves passing the point considered and can be written as

$$\Delta u_{is} = u(\zeta, s, \rho + \Delta \rho) - u(\zeta, s, \rho)$$

where $\Delta \rho = -D\Delta t$ denotes the change of density as a result of the change in the relative rate of volume expansion. The third part contains the pressure work term and the frictional heating contribution. The dissipation function consists of

$$\Phi = \nu \left(\frac{\partial \tilde{u}}{\partial y} \right)^2 + \tilde{\epsilon}$$

for flows of boundary layer type.

The last contribution is due to the random arrival of shocks at the material point considered.

D. The increment for the mixture fraction has only the mixing contribution.

4.3 Prediction of supersonic hydrogen flames.

The closure model developed in the previous chapter was applied to the prediction of supersonic hydrogen flames burning in coflowing stream of air. The flow configuration was a round H_2 jet with a coflowing stream of air at higher temperature than the fuel. The boundary conditions and the nozzle geometry were chosen according to the first test case

of Evans et al. Ref.73: The exit properties of the fuel H_2 are $T_0 = 251^\circ K$, Mach number $M_a = 2.0$ and pressure $p_0 = 0.1 MPa$ and the exit properties of the coflowing air stream are given by $T_e = 1495^\circ K$, Mach number $M_a = 1.9$ and the same pressure as the fuel stream. The geometrical arrangement is shown in fig.1 according to Evans et al. Ref.73. The calculation of the turbulent nonpremixed flame is carried out with the hybrid method developed by Chen and Kollmann Ref.74. The first step in the solution procedure is the calculation of the thermo-chemical properties, which are stored in a table for the later use in the solution of the pdf equation.

4.3.1 Thermo-Chemical Properties.

The thermo-chemical properties of the reacting mixture of H_2 and air are determined from the condition of chemical equilibrium constrained with pressure and internal energy. This assumption is unrealistic for many situations in supersonic flows, but it is the logical first step in the development of prediction models for such flows. The extension to chemical non-equilibrium has been carried out for zero Mach-number flames (see Chen and Kollmann, Ref.74) and, once the questions concerning compressibility effects on the turbulence structure have been sorted out, the results obtained for zero Mach-number flames can be applied to supersonic flows.

The fuel considered in the present prediction was a mixture of hydrogen and nitrogen ($Y_{H_2} = 0.22335$ and $Y_{N_2} = 0.77665$, in order to raise the stoichiometric value of mixture fraction from $\zeta_{st} = 0.0283$ for pure hydrogen fuel to $\zeta_{st} = 0.113$. The pure hydrogen case was also considered but only results for the former case will be discussed. The thermo-chemical properties were calculated with a standard equilibrium code (STANJAN) and a selected set of results are shown in fig.2 to fig.5. The available thermodynamic data started at a temperature of $T = 300^\circ K$ which implies that the fuel temperature could not be reached in the equilibrium code and $T = 301^\circ K$ was used instead. This implies that a significant discrepancy in density and temperature must be expected in the initial region. All the results are plotted for the upper limit of density (fig.2,3,5) or the upper limit of internal energy (fig.4). The boundaries of the thermo-chemical domain were established to be approximately isobaric. The importance of this property for prescribed pdf methods was discussed in chapter 3.1. The temperature as function of mixture fraction ζ and internal energy u in fig.2 shows the expected maximum near the stoichiometric value of ζ . The variation of T with u for constant ζ is essentially due to compression or expansion since composition and density are constant for constant ζ . The pressure $p(\zeta, u)$ in fig.3 shows that the lower boundary is close to an isobaric line but the upper boundary shows a moderate variation of pressure with mixture fraction. The pressure as function of mixture fraction and density in fig.4 (note that density is normalized with the local extremal values $\rho_{min}(\zeta)$, $\rho_{max}(\zeta)$) by

$$\rho^* \equiv \frac{\rho - \rho_{min}}{\rho_{max} - \rho_{min}} \quad (4.3.1)$$

for the purpose of plotting) illustrates the strong influence of the flame front $\zeta = \zeta_{st}$. Finally, fig.5 shows the variation of a radical mass fraction (component OH) with mixture fraction and internal energy at the upper limit for density.

4.3.2 Velocity Field: Second Order Closure.

The statistical properties of the velocity field are determined from the solution of a second order moment closure (see Dibble et al., Ref.41 for details). The mean velocity $\bar{u}(x, r)$ at $x/D = 6.56$ in fig.6 reflects the initial conditions. The comparison of $r\bar{u}(\rho)$ with the experiments of Evans et al. Ref.73 in fig.7 at $x/D = 6.56$ and in fig.8 at $x/D = 26.2$ proves reasonable agreement given the uncertainties in the conditions at the entrance section. The same holds for the comparison of the Pitot pressure with the experiment in fig.9 except near the axis where the calculated pressure is too high. The Reynolds stress components in fig.10 and the dissipation rate in fig.11 at $x/D = 6.56$ are qualitatively correct but no experimental values are available for comparison. The same holds true for the station $x/D = 26.2$ in fig.12 to fig.14. The profiles are fully developed and similar to the incompressible case.

4.3.3 Scalar Field: PDF Model.

The prediction of the pdf $f(\zeta, u, \rho; x, r)$ at two cross sections will be presented in detail. The mean profiles for $x/D = 6.56$ in fig.15 to fig.19 prove that the jet is essentially a circular mixing layer. There exists clearly a core region and the maximal temperature is reached in the high shear region off the symmetry axis. The profiles for auto- and cross-correlations in fig.20 to fig.27 at this station show that mixture fraction and internal energy are negatively correlated (fig.21) and that the correlation of mixture fraction and density (fig.22) is the sign opposite to the correlation of internal energy and density (fig.25) and both change signs with increasing distance from the symmetry axis. The double peaks in the auto-correlations indicate the properties of a mixing layer. The information of the various pdfs is contained in fig.28 to fig.45 for the station $x/D = 6.56$. Two radial stations were selected to show the variation of the pdf as the shear region is traversed. At $r/D = 0.14$ we note that the one-dimensional pdf of mixture fraction (fig.28) and internal energy (fig.29) are quite different which is due to the influence of compressibility. The Ornstein-Uhlenbeck process described in chapter 4.2 as model for the random fluctuations of the relative rate of volume expansion lead to a broadening of the pdf for thermodynamic variables which would be related locally in incompressible flows. This effect leads also to the differences in one-dimensional pdfs. The pdf for density in fig.30 shows the incursion of hot combustion products as long tail at low values of density. The pdf of relative rate of volume expansion D in fig.31 is close to a Gaussian, but the two-dimensional pdf in fig.33 for density and D proves that D is not a Gaussian phenomenon despite the Gaussian appearance of the marginal pdf. The pdf for the thermodynamic variables such as density and internal energy in fig.34 shows the adherence to the equilibrium line with spreading due to compressibility effects.

The results for the station $x/D = 30.14$ in fig.46 to fig.73 documents the development of the flow from a circular mixing layer to a round jet. The mean profiles in fig.46 to fig.48 show the decay of the mixture fraction and the spreading of the jet. The auto- and cross-correlations in fig.49 to fig.56 bring to light the properties of jets in contrast to the initial behaviour as mixing layers. No sign change is observed for the cross-correlations of mixture fraction and internal energy (fig.50) and mixture fraction and density (fig.51). The same holds true for density and internal energy in fig.54. The one-dimensional pdfs in fig.57 to

fig.68 allow the detailed study of the radial development. The most interesting result is the appearance of a double peak in the pdf for internal energy at $r/D = 6.55$ in fig.66. This can be attributed to the intermittent nature of the flow simulated stochastically, where the right peak corresponds to entrained air. A similar property can be seen in the pdf of density at the same station in fig.67. The entrained air appears here as a distinct spike at the high density. The two-dimensional pdfs in fig.69 to fig.73 show less spread around the equilibrium lines which indicates smaller compressibility effects.

It was shown that pdfs for three scalar variables describing the local thermodynamic state in a compressible reacting flow can be determined as solutions of model equation that simulates the effects of convection, turbulent diffusion, chemical reactions and reversible and irreversible compression and expansion processes occurring randomly in a turbulent flow at high speed. The limited amount of experimental information does not allow to draw a final conclusion concerning the accuracy of the calculations, but it is clear that pdf predictions of compressible reacting flows are feasible. There are, however, several problems awaiting solution. In particular the role of the fluctuating pressure containing several different modes (acoustic mode, entropy mode) and the significance of chemical non-equilibrium need to be investigated. Pdf methods are especially well suited for the latter because they allow rigorous treatment of nonlinear and local processes.

References

1. Penner, S. S. and Mullins, B. P.: Explosions, Detonations, Flammability and Ignition. Pergamon Press, 1959.
2. Olfe, D. B. and Zakkay, V., ed.: Supersonic Flow Chemical Processes and Radiative Transfer. Pergamon Press, 1964.
3. Rhodes, R. P., Harsha, P. T., and Peters, C. E.: Turbulent Kinetic Energy Analyses of Hydrogen-Air Diffusion Flames. Acta Astronautica, Vol. 1, 1974.
4. Kollmann, W., ed.: Prediction Methods for Turbulent Flows. Hemisphere, 1980.
5. Libby, P. A. and Williams, F. A., ed.: Turbulent Reacting Flows. Springer-Verlag, 1980.
6. Murthy, S. N. B., ed.: Turbulent Mixing in Nonreacting and Reacting Flows. Plenum Press, 1975.
7. Drummond, J. P., Rogers, R. C., and Evans, J. S.: Combustor Modeling for Scramjet Engines. AGARD CP 275. Presented at AGARD Combustor Modeling, Cologne, Oct. 1979.
8. Drummond, P. J., Hussaini, M. Y., and Zang, T. A.: Spectral Methods For Modeling Supersonic Chemical Flowfields. NASA-CR-172578, 1985.
9. Bilger, R. W.: Turbulent Flows with Nonpremixed Reactants. In Turbulent Reacting Flows, Springer-Verlag, 1980.
10. Bray, S. F.: Turbulent Flows with Premixed Reactants. In Turbulent Reacting Flows, Springer-Verlag, 1980.
11. O'Brien, E. E.: The Probability Density Function Approach to Reacting Turbulent Flows. In Turbulent Reacting Flows, Springer-Verlag, 1980.
12. Lundgren, T. S.: Model Equation for Nonhomogeneous Turbulence. Physics of Fluids, Vol. 12, No. 3, 1969.
13. Dopazo, C. and O'Brien, E. E.: An Approach to the Autoignition of a Turbulent Mixture. Acta Astronautica, Vol. 1, 1974.
14. Dopazo, C. and O'Brien, E. E.: Functional Formulation of Nonisothermal Turbulent Reactive Flows. Physics of Fluids, Vol. 17, 1975.

15. Pope, S. B.: The Statistical Theory of Turbulent Flames. Phils. Trans. Royal Soc. London, A291, 1979.
16. Glassman, I.: Combustion. Academic Press, 1977.
17. Launder, B. E., Reynolds, W. C., and Rodi, W.: Turbulence Models and Their Applications, Vol. 2. Eyrols, 1984.
18. Daly, B. J. and Harlow, F. H.: Transport Equations in Turbulence. Physics of Fluids, Vol. 13, No. 11, 1970.
19. Rubesin, M. W.: A One-Equation Model of Turbulence for Use with Compressible Navier-Stokes Equations. NASA TMX-73128, 1976.
20. Farshchi, M.: Prediction of Heat Release Effects on a Mixing Layer. AIAA Paper 86-0058, 1986.
21. Harlow, F. H. and Nakayama, P. I.: Transport of Turbulence Energy Decay Rate. Los Alamos National Laboratory, University of California Report LA3854, 1968.
22. Tenneks, H. and Lumley, J. L.: A First Course in Turbulence. The MIT Press, 1972.
23. Launder, B. E., Reece, G., and Rodi, W.: Progress in the Development of a Reynolds-Stress Turbulence Closure. Journal of Fluid Mechanics, Vol. 68, Part 3, 1975, p. 537.
24. Haminh, H., Kollmann, W., and Vandromme, D.: Reynolds Stress Model for Compressible Flows. Final Report for Contract NASA NCCR-186, 1983.
25. Vandromme, D. D. and Haminh, H.: Solution of the Compressible Navier-Stokes Equations: Applications to Complex Turbulent Flows. Von Karman Institute Lecture Series in CFD, Belgium, 1983.
26. Rodi, W.: Turbulence Models and Their Application in Hydraulics. International Association for Hydraulic Research, 1980.
27. Nagano, Y. and Hishida, M.: Improved Form of the $k-\epsilon$ Model for Wall Turbulent Shear Flows. ASME J. of Fluids Engineering, Vol. 109, 1987, p. 156.
28. Patel, V. C., Rodi, W., and Scheuerer, G.: Turbulence Models for Near-Wall and Low Reynolds Number Flows: A Review. AIAA Journal, Vol. 23, September 1985, p. 1308.
29. Jones, W. P. and Launder, B. E.: The Prediction of Laminarization with a Two-Equation Model of Turbulence. Int. J. of Heat Mass Transfer, Vol. 15, 1972, p. 301.

30. Chien, K. Y.: Predictions of Channel and Boundary-Layer Flows with a Low Reynolds Number Turbulence Model. AIAA Journal, Vol. 20, January 1982, p. 33.
31. Papamoschou, D. and Roshko, A.: The Compressible Turbulent Shear Layer: An Experimental Study. J. of Fluid Mechanics, Vol. 197, 1988, p. 453.
32. Zeman, O.: Dilatation Dissipation: The Concept and Application in Modeling Compressible Mixing Layers. Physics of Fluids A, Vol. 2, No. 2, 1990, p. 178.
33. Baldwin, B. and Lomax, H.: Thin Layer Approximation and Algebraic Model for Separated Turbulent Flows. AIAA Paper 78-257, 1978.
34. Shuen, J. S. and Yoon, S.: Numerical Study of Chemically Reacting Flows Using an LU Scheme. NASA-TM-180882, also AIAA-88-0436, 1988.
35. Reynolds, W. C.: STANJAN; Interactive Computer programs for Chemical Equilibrium Analysis. Department of Mechanical Engineering, Stanford University, 1981.
36. Gordon, S. and McBride, B. J.: Computer Program for Calculation of Complex Chemical Equilibrium Composition, Rocket Performance, Incident and Reflected Shocks, and Chapman-Jouguet Detonations. NASA SP-273, 1976.
37. Pope, S. B.: Transport Equation for the Joint Probability Density Function of Velocity and Scalars in Turbulent Flow. Physics of Fluids, Vol. 24, No. 4, p. 588, 1981.
38. Lumley, J. L.: Stochastic Tools in Turbulence. Academy Press, 1970.
39. Feller, W.: An Introduction to Probability Theory and Its Applications. Wiley, 1968.
40. Farshchi, M.: Second Order Closure Model for Turbulent Reacting Flows. Ph.D. Thesis, University of California, Davis, 1984.
41. Dibble, R. W., Kollmann, W., Farshchi, M., and Scheffer, R. W.: Second-Order Closure for Turbulent Nonpremixed Flames: Scalar Dissipation and Heat Release Effects. 21st Symposium on Combustion, Combustion Institute, 1986, p. 1329.
42. Warhaft, Z. and Lumley, J. L.: An Experimental Study of the Decay of Temperature Fluctuations in Grid Generated Turbulence. J. of Fluid Mechanics, Vol. 88, 1978, p. 659.
43. Jameson, A. and Yoon, S.: Lower-Upper Implicit Schemes with Multiple Grids for the Euler Equations. AIAA Journal, Vol. 25, No. 7, 1987, p. 229.

44. Jameson, A., Schmidt, W., and Turkel, E.: Numerical Solutions of the Euler Equations by Finite Volume Methods Using Runge-Kutta Time-Stepping Schemes. AIAA Paper 81-1259, 1981.
45. Yee, H. C.: Upwind and Symmetric Shock Capturing Schemes. NASA TM 89464, 1987.
46. Leveque, R. J. and Yee, H. C.: A Study of Numerical Methods for Hyperbolic Conservation Laws with Stiff Source Terms. NASA TM 100075, 1988.
47. Shuen, J. S., Liou, M. S., VanLeer, B.: Inviscid Flux-Splitting Algorithms for Real Gases with Non-Equilibrium Chemistry. Journal of Computational Physics, Vol. 90, No. 2, 1990, p. 371.
48. Westbrook, C. K.: Hydrogen Oxidation Kinetics in Gaseous Detonations. Combustion Science and Technology, Vol. 29, No. 1-2, 1982, p. 67.
49. Reid, R. C., Prausnitz, J. M., and Sherwood, T. K.: The Properties of Gases and Liquids. 3rd Edition, McGraw-Hill Publishing Co., 1977.
50. Williams, F. A.: Combustion Theory, 2nd Edition, Benjamin/Cummings Publishing Co., 1985.
51. Brown, G. L., and Roshko, A.: On Density Effects and Large Structures in Turbulent Mixing Layers. Journal of Fluid Mechanics, Vol. 64, Part 4, 1974, p. 775.
52. Bogdanoff, D. W.: Compressibility Effects in Turbulent Shear Layers. AIAA Journal, Vol. 21, No. 6, 1983, p. 926.
53. Goebel, S. G., Dutton, J. C. Krier, H., and Renie, J. P.: Mean and Turbulence Velocity Measurements of Supersonic Mixing Layers. Experiments in Fluids, Vol. 8, 1990, p. 263.
54. Samimy, M. and Elliot, G. S.: Effects of Compressibility on the Characteristics of Free Shear Layers. AIAA Journal, Vol. 28, No. 3, 1990, p. 439.
55. Elliot, G. S. and Samimy, M.: Compressibility Effects in Free Shear Layers. AIAA Paper No. 90-0705, 1990.
56. Laderman, A. J.: Effect of Wall Temperature on a Supersonic Turbulent Boundary Layer. AIAA Journal, Vol. 16, No. 7, 1978, p. 723.
57. Robinson, S. K., Seegmiller, H. L., and Kussoy, M. I.: Hot-wire and Laser Doppler Anemometer Measurements in a Supersonic Boundary Layer. AIAA Paper 83-1723, 1983.

58. White, F. M.: Viscous Fluid Flow. McGraw-Hill, 1974.
59. Rohsenow, W. M. and Hartnett, J. P.: Handbook of Heat Transfer. McGraw-Hill, 1973, p. 8-156.
60. Laderman, A. J. and Demetriades, A.: Turbulent Shear Stresses in Compressible Boundary Layers. AIAA Journal, Vol. 17, No. 7, 1979, p. 736.
61. Sandborn, V. A.: A Review of Turbulent Measurements in Compressible Flow. NASA TM X-62337, 1974.
62. Klebanoff, P. S.: Characteristics of Turbulence in a Boundary Layer with Zero Pressure Gradient. NACA TR 1247, 1955.
63. Kistler, A. L.: Fluctuation Measurements in a Supersonic Turbulent Boundary Layer. The Physics of Fluids, Vol. 2, No. 3, 1959, p. 290.
64. Owen, F. K., Horstman, C. C., and Kussoy, M. K.: Mean and Fluctuating Flow Measurements of a Fully Developed, Non Adiabatic Hypersonic Boundary Layer. Journal of Fluid Mechanics, Vol. 70, Pt. 2, 1975, p. 393.
65. Yanta, W. J. and Lee, R. E.: Determination of Turbulence Transport Properties with the Laser Doppler Velocimeter and Conventional Time-Averaged Mean Flow Measurements at Mach 3. AIAA Journal, Vol. 14, 1976, p. 725.
66. Mikulla, V. and Horstmann, C. C.: The Measurement of Shear Stress and Total Heat Flux in a Non-Adiabatic Turbulent Hypersonic Boundary Layer. AIAA Paper 75-119, 1975.
67. Settles, G. S., Fitzpatrick, T. J., and Bogdonoff, S. M.: Detailed Study of Attached and Separated Compression Corner Flowfields in High Reynolds Number Supersonic Flow. AIAA Journal, Vol. 17, No. 6, 1979, p. 579.
68. Viegas, J. I., Rubesin, M. W., and Hortsman, C. C.: On the Use of Wall Functions as Boundary Conditions for Two-Dimensional Separated Compressible Flows. AIAA Paper 85-0180, 1985.
69. Billing, F. S. and Dugger, G. L.: The Interaction of Shock Waves and Heat Addition in the Design of Supersonic Combustors. 12th Symposium (Int.) on Combustion, The Combustion Institute, 1969, p. 1125.

70. Kollmann, W., Haminh, H., and Vandromme, D.: The Behavior of Turbulence Anisotropy through Shock Waves and Expansions. 5th Turbulent Shear Flows Conference, Cornell University, 1985.
71. Majda, A.: Compressible Fluid Flow and Systems of Conservation Laws in Several Space Dimensions, Springer Verlag, 1984.
72. Johnson, J. A., Zang, Y., and Johnson, L. E.: Evidence of Reynolds Number Sensitivity in Supersonic Turbulent Shocklets. AIAA Journal, Vol. 26, 1988, p. 502.
73. Evans, J. S., Schexnayder, C. J., and Beach, H. L.: Application of a Two-Dimensional Parabolic Computer Program to Prediction of Turbulent Reacting Flows. NASA-TP-1169, 1978.
74. Chen, J. Y. and Kollmann, W.: Chemical Models for PDF Modeling of Hydrogen Air Non-Premixed Turbulent Flames. To appear in Combustion and Flame, 1991.

APPENDIX A

Two-Dimensional Expansion of the Governing Equations

Two distinct models for the prediction of compressible turbulent chemically reacting flows were given in Chapter 1. Complete governing equations and their expansion in two-dimensional space are presented here for each model. The RPLUS computer program is modified to solve all equations in each set of governing equations simultaneously. Therefore, the vector form of these equations is presented here. Flux Jacobian matrices for each solution vector are also presented. First, finite rate reaction model equations are given. Next, k- ϵ turbulence model equations, and then PDF combustion model equations are given.

A.1 Finite Rate Reaction Model Equations

The transport equations governing the behavior of the turbulent flow of a chemically reacting mixture of N gaseous species were modeled and nondimensionalized in Chapter 1 and are given by Equations (1.5.1) to (1.5.4). These equations can be represented in a compact vector form as

$$\frac{\partial Q}{\partial t} + \frac{\partial (F - F_v)}{\partial x} + \frac{\partial (G - G_v)}{\partial y} = S \quad (A.1.1)$$

Utilizing the k- ϵ turbulence closure model the above vectors can be given by;

$$Q = \begin{bmatrix} \rho \\ \rho u \\ \rho v \\ \rho e_t \\ \rho Y_n \end{bmatrix}$$

$$F = \begin{bmatrix} \rho u \\ \rho u^2 + \rho q + p \\ \rho uv \\ u(\rho e_t + \rho q + p) \\ \rho u Y_n \end{bmatrix}$$

$$G = \begin{bmatrix} \rho v \\ \rho uv \\ \rho v^2 + \rho q + p \\ v(\rho e_t + \rho q + p) \\ \rho v Y_n \end{bmatrix}$$

$$F_v = Re_\infty^{-1} \begin{bmatrix} 0 \\ \tau_{xx} \\ \tau_{xy} \\ u\tau_{xx} + v\tau_{xy} + \theta_{xx} + \theta_{xy} + \chi_{xx} + \chi_{xy} + \Lambda_{xx} + \Lambda_{xy} \\ (\lambda_{xx} + \lambda_{xy})_n \end{bmatrix}$$

$$G_v = Re_\infty^{-1} \begin{bmatrix} 0 \\ \tau_{yx} \\ \tau_{yy} \\ u\tau_{yx} + v\tau_{yy} + \theta_{yx} + \theta_{yy} + \chi_{yx} + \chi_{yy} + \Lambda_{yx} + \Lambda_{yy} \\ (\lambda_{yx} + \lambda_{yy})_n \end{bmatrix} \quad S = \begin{bmatrix} 0 \\ 0 \\ 0 \\ 0 \\ \dot{T}_n \end{bmatrix} \quad n = 1, 2, \dots, n-1$$

where

$$\tau_{xx} = \rho(v + v_t) \left[2 \frac{\partial u}{\partial x} - \frac{2}{3} \left(\frac{\partial u}{\partial x} + \frac{\partial v}{\partial y} \right) \right] \quad (A.1.2a)$$

$$\tau_{xy} = \rho(v + v_t) \left(\frac{\partial u}{\partial y} + \frac{\partial v}{\partial x} \right) \quad (A.1.2b)$$

$$\tau_{yx} = \tau_{xy} \quad (A.1.2c)$$

$$\tau_{yy} = \rho(v + v_t) \left[2 \frac{\partial v}{\partial y} - \frac{2}{3} \left(\frac{\partial u}{\partial x} + \frac{\partial v}{\partial y} \right) \right] \quad (A.1.2d)$$

$$\theta_{xx} = \left[\frac{Pr_{\infty}^{-1}}{(\gamma_{\infty}-1)} \kappa + c_p \rho v_t \sigma_h^{-1} \dot{\phi}_{11} \right] \frac{\partial T}{\partial x} \quad (A.1.3a)$$

$$\theta_{xy} = \left[c_p \rho v_t \sigma_h^{-1} \dot{\phi}_{12} \right] \frac{\partial T}{\partial y} \quad (A.1.3b)$$

$$\theta_{yx} = \left[c_p \rho v_t \sigma_h^{-1} \dot{\phi}_{21} \right] \frac{\partial T}{\partial y} \quad (A.1.3c)$$

$$\theta_{yy} = \left[\frac{Pr_{\infty}^{-1}}{(\gamma_{\infty}-1)} \kappa + c_p \rho v_t \sigma_h^{-1} \dot{\phi}_{22} \right] \frac{\partial T}{\partial y} \quad (A.1.3d)$$

$$\chi_{xx} = \rho \left[v + v_t \sigma_{\kappa}^{-1} \dot{\phi}_{11} \right] \frac{\partial q}{\partial x} \quad (A.1.4a)$$

$$\chi_{xy} = \rho \left[v_t \sigma_{\kappa}^{-1} \dot{\phi}_{12} \right] \frac{\partial q}{\partial y} \quad (A.1.4b)$$

$$\chi_{yx} = \rho \left[v_t \sigma_{\kappa}^{-1} \dot{\phi}_{21} \right] \frac{\partial q}{\partial x} \quad (A.1.4c)$$

$$\chi_{yy} = \rho \left[v + v_t \sigma_{\kappa}^{-1} \dot{\phi}_{22} \right] \frac{\partial q}{\partial y} \quad (A.1.4d)$$

$$\lambda_{xx_n} = \rho \left[\text{Re}_\infty D_n + v_t \sigma_y^{-1} \delta_{11} \right] \frac{\partial Y_n}{\partial x} \quad (\text{A.1.5a})$$

$$\lambda_{xy_n} = \rho \left[v_t \sigma_y^{-1} \delta_{12} \right] \frac{\partial Y_n}{\partial y} \quad (\text{A.1.5b})$$

$$\lambda_{yx_n} = \rho \left[v_t \sigma_y^{-1} \delta_{21} \right] \frac{\partial Y_n}{\partial x} \quad (\text{A.1.5c})$$

$$\lambda_{yy_n} = \rho \left[\text{Re}_\infty D_n + v_t \sigma_y^{-1} \delta_{22} \right] \frac{\partial Y_n}{\partial y} \quad (\text{A.1.5d})$$

$$\Lambda_{xx} = \sum_{n=1}^N \rho \left[\text{Re}_\infty D_n + v_t \sigma_h^{-1} \delta_{11} \right] h_n \frac{\partial Y_n}{\partial x} \quad (\text{A.1.6a})$$

$$\Lambda_{xy} = \sum_{n=1}^N \rho \left[v_t \sigma_h^{-1} \delta_{12} \right] h_n \frac{\partial Y_n}{\partial y} \quad (\text{A.1.6b})$$

$$\Lambda_{yx} = \sum_{n=1}^N \rho \left[v_t \sigma_h^{-1} \delta_{21} \right] h_n \frac{\partial Y_n}{\partial x} \quad (\text{A.1.6c})$$

$$\Lambda_{yy} = \sum_{n=1}^N \rho \left[\text{Re}_\infty D_n + v_t \sigma_h^{-1} \delta_{22} \right] h_n \frac{\partial Y_n}{\partial y} \quad (\text{A.1.6d})$$

$$\delta_{11} = \frac{2}{3} - \text{Re}_\infty^{-1} \frac{1}{q} v_t \left[2 \frac{\partial u}{\partial x} - \frac{2}{3} \left(\frac{\partial u}{\partial x} + \frac{\partial v}{\partial y} \right) \right] \quad (\text{A.1.7a})$$

$$\delta_{12} = -\text{Re}_\infty^{-1} \frac{1}{q} v_t \left[\frac{\partial u}{\partial y} + \frac{\partial v}{\partial x} \right] \quad (\text{A.1.7b})$$

$$\delta_{21} = \delta_{12} \quad (\text{A.1.7c})$$

$$\delta_{22} = \frac{2}{3} - \text{Re}_\infty^{-1} \frac{1}{q} v_t \left[2 \frac{\partial v}{\partial y} - \frac{2}{3} \left(\frac{\partial u}{\partial x} + \frac{\partial v}{\partial y} \right) \right] \quad (\text{A.1.7d})$$

To obtain the Jacobian of the above flux vectors, pressure must be expressed in terms of the elements of the solution vector Q. This relation in two dimensions is given by

$$P = (\hat{\gamma} - 1) \left\{ \rho e_t - \frac{1}{2} \rho (u^2 + v^2) - \rho q - \sum_{n=1}^{N-1} \rho Y_n \left[\left(h_{f_n}^\circ - h_{o_n} \right) - \left(h_{f_N}^\circ - h_{o_N} \right) \right] - \rho \left(h_{f_N}^\circ - h_{o_N} \right) \right\} \quad (\text{A.1.8})$$

where

$$\hat{\gamma} = \frac{\int_0^T \sum_{n=1}^N c_{p_n} Y_n dT}{\int_0^T \sum_{n=1}^N c_{p_n} Y_n dT - RT}, \quad h_{o_n} = \int_0^{T_o} c_{p_n} dT,$$

$h_{f_n}^\circ$ = nth species formation enthalpy and T_o = formation ref. temp.

The Jacobians of the above flux vectors are given as

$$A = \frac{\partial F}{\partial Q} \quad \text{and} \quad B = \frac{\partial G}{\partial Q}$$

Using a transformation to an orthogonal curvilinear coordinate system

$$\xi = \xi(x,y) \quad \text{and} \quad \eta = \eta(x,y)$$

the transformed Jacobians are given as

$$\hat{A} = \xi_x A + \xi_y B \quad \text{and} \quad \hat{B} = \eta_x A + \eta_y B$$

\hat{A} is given by the matrix A.1.1. In this matrix $\Delta \dot{h}_{fn} = (\dot{h}_{fn} - h_{on}) - (\dot{h}_{fN} - h_{oN})$. For \hat{B} replace ξ with η .

MATRIX A.1.1

0	ξ_x	ξ_y	0	0	0	0	---	0
$[(\hat{\gamma}-1)(K-q-(h_{iN}-h_{0N})) - u^2 + q_2^2]\xi_x - (uv)\xi_y$	$u(3-\gamma)\xi_x + v\xi_y$	$-(\hat{\gamma}-1)v\xi_x + u\xi_y$	$(\hat{\gamma}-1)\xi_x$	$-(\hat{\gamma}-1)\Delta h_{i1}\xi_x$	$-(\hat{\gamma}-1)\Delta h_{i2}\xi_x$	$-(\hat{\gamma}-1)\Delta h_{i3}\xi_x$	---	$-(\hat{\gamma}-1)\Delta h_{iN-1}\xi_x$
$[(\hat{\gamma}-1)(K-q-(h_{iN}-h_{0N})) - v^2 + q_3^2]\xi_y - uv\xi_x$	$v\xi_x - (\hat{\gamma}-1)u\xi_y$	$u\xi_x + (3-\hat{\gamma})v\xi_y$	$(\hat{\gamma}-1)\xi_y$	$-(\hat{\gamma}-1)\Delta h_{i1}\xi_y$	$-(\hat{\gamma}-1)\Delta h_{i2}\xi_y$	$-(\hat{\gamma}-1)\Delta h_{i3}\xi_y$	---	$-(\hat{\gamma}-1)\Delta h_{iN-1}\xi_y$
$-(\rho e_t+p)(u\xi_x+v\xi_y) + (\hat{\gamma}-1)[K-q-(h_{iN}-h_{0N})](u\xi_x+v\xi_y)$	$[\frac{1}{\rho}(\rho e_t+p) + q_3^2 - u^2(\hat{\gamma}-1)]\xi_x - uv(\hat{\gamma}-1)\xi_y$	$[\frac{1}{\rho}(\rho e_t+p) + q_2^2 - v^2(\hat{\gamma}-1)]\xi_y - uv(\hat{\gamma}-1)\xi_x$	$\hat{\gamma}(u\xi_x+v\xi_y)$	$(\hat{\gamma}-1)\Delta h_{i1}(-u\xi_x-v\xi_y)$	$(\hat{\gamma}-1)\Delta h_{i2}(-u\xi_x-v\xi_y)$	$(\hat{\gamma}-1)\Delta h_{i3}(-u\xi_x-v\xi_y)$	---	$(\hat{\gamma}-1)\Delta h_{iN-1}(-u\xi_x-v\xi_y)$
$-Y_1(u\xi_x+v\xi_y)$	$Y_1\xi_x$	$Y_1\xi_y$	0	$u\xi_x + v\xi_y$	0	0	---	
$-Y_2(u\xi_x+v\xi_y)$	$Y_2\xi_x$	$Y_2\xi_y$	0	0	$u\xi_x + v\xi_y$	0	---	
					0		---	
$-Y_{N-1}(u\xi_x+v\xi_y)$	$Y_{N-1}\xi_x$	$Y_{N-1}\xi_y$	0	0	0	0	---	$u\xi_x+v\xi_y$

A.2 k-ε Equations

The modeled and nondimensionalized transport equations for the turbulent kinetic energy, q , and the rate of turbulent kinetic energy dissipation, ε , are given by Equations (5.16) and (5.17) in Chapter 1. Using the compact vector notation, the two-dimensional expansion of these equations is given as

$$Q = \begin{bmatrix} \rho q \\ \rho \varepsilon \end{bmatrix}, \quad F = \begin{bmatrix} \rho u q \\ \rho u \varepsilon \end{bmatrix}, \quad G = \begin{bmatrix} \rho v q \\ \rho v \varepsilon \end{bmatrix}$$

$$F_v = \text{Re}_\infty^{-1} \begin{bmatrix} \chi_{xx} + \chi_{xy} \\ \chi_{\varepsilon_{xx}} + \chi_{\varepsilon_{xy}} \end{bmatrix} \quad G_v = \text{Re}_\infty^{-1} \begin{bmatrix} \chi_{yx} + \chi_{yy} \\ \chi_{\varepsilon_{yx}} + \chi_{\varepsilon_{yy}} \end{bmatrix}$$

$$S = \begin{bmatrix} -\rho q \left[\phi_{11} \frac{\partial u}{\partial x} + \phi_{12} \left(\frac{\partial u}{\partial y} + \frac{\partial v}{\partial x} \right) + \phi_{22} \frac{\partial v}{\partial y} \right] - \text{Re}_\infty^{-1} \rho \varepsilon - \\ \frac{q}{(n-1)c_p T} \left[\phi_{11} u \frac{\partial p}{\partial x} + \phi_{12} \left(u \frac{\partial p}{\partial y} + \frac{\partial p}{\partial x} \right) + \phi_{22} v \frac{\partial p}{\partial y} \right] - \text{Re}_\infty^{-1} S_q \\ -c_{\varepsilon 1} \rho \varepsilon \left[\phi_{11} \frac{\partial u}{\partial x} + \phi_{12} \left(\frac{\partial u}{\partial y} + \frac{\partial v}{\partial x} \right) + \phi_{22} \frac{\partial v}{\partial y} \right] - c_{\varepsilon 2} f_\varepsilon \text{Re}_\infty^{-1} \rho \frac{\varepsilon}{q} - \\ c_{\varepsilon 4} \frac{\varepsilon}{(n-1)c_p T} \left[\phi_{11} u \frac{\partial p}{\partial x} + \phi_{12} \left(u \frac{\partial p}{\partial y} + \frac{\partial p}{\partial x} \right) + \phi_{22} v \frac{\partial p}{\partial y} \right] + \\ \text{Re}_\infty^{-1} \frac{c_{\varepsilon 3}}{c_\mu} \rho v v_t \left[\phi_{11} \Psi_{11} + 2\phi_{12} \Psi_{12} + \phi_{22} \Psi_{22} \right] - \frac{2}{3} \rho \varepsilon \left(\frac{\partial u}{\partial x} + \frac{\partial v}{\partial y} \right) - \text{Re}_\infty^{-1} S_\varepsilon \end{bmatrix}$$

where

$$\chi_{\varepsilon_{xx}} = \rho \left[v + v_t \sigma_\varepsilon^{-1} \phi_{11} \right] \frac{\partial \varepsilon}{\partial x} \quad \chi_{\varepsilon_{xy}} = \rho \left[v_t \sigma_\varepsilon^{-1} \phi_{12} \right] \frac{\partial \varepsilon}{\partial y} \quad (\text{A.2.1a,b})$$

$$\chi_{\varepsilon_{yx}} = \rho \left[v_t \sigma_\varepsilon^{-1} \phi_{21} \right] \frac{\partial \varepsilon}{\partial x} \quad \chi_{\varepsilon_{yy}} = \rho \left[v + v_t \sigma_\varepsilon^{-1} \phi_{22} \right] \frac{\partial \varepsilon}{\partial y} \quad (\text{A.2.1c,d})$$

$$\Psi_{11} = \left[\frac{\partial^2 u}{\partial x^2} \right]^2 + \left[\frac{\partial^2 u}{\partial x \partial y} \right]^2 + \left[\frac{\partial^2 v}{\partial x^2} \right]^2 + \left[\frac{\partial^2 v}{\partial x \partial y} \right]^2, \quad (\text{A.2.2a})$$

$$\Psi_{12} = \frac{\partial^2 u}{\partial x^2} \frac{\partial^2 u}{\partial y \partial x} + \frac{\partial^2 u}{\partial x \partial y} \frac{\partial^2 u}{\partial y^2} + \frac{\partial^2 v}{\partial x^2} \frac{\partial^2 v}{\partial y \partial x} + \frac{\partial^2 v}{\partial x \partial y} \frac{\partial^2 v}{\partial y^2}, \quad \Psi_{21} = \Psi_{12} \quad (\text{A.2.2bc})$$

$$\Psi_{22} = \left[\frac{\partial^2 u}{\partial y \partial x} \right]^2 + \left[\frac{\partial^2 u}{\partial y^2} \right]^2 + \left[\frac{\partial^2 v}{\partial y \partial x} \right]^2 + \left[\frac{\partial^2 v}{\partial y^2} \right]^2 \quad (\text{A.2.2d})$$

The Jacobians of the flux vectors are given as

$$A = \frac{\partial F}{\partial Q} = \begin{bmatrix} u & 0 \\ 0 & u \end{bmatrix}, \quad B = \frac{\partial G}{\partial Q} = \begin{bmatrix} v & 0 \\ 0 & v \end{bmatrix}$$

$$\hat{A} = \xi_x A + \xi_y B = \begin{bmatrix} u\xi_x + v\xi_y & 0 \\ 0 & u\xi_x + v\xi_y \end{bmatrix}$$

For \hat{B} replace ξ with η .

A.3 PDF Combustion Model Equations

The transport equations needed to be solved with a PDF model for a turbulent chemical reaction in a compressible mixture of N gaseous species are given by Equations (1.5.1), (1.5.3), (1.5.4), (1.6.18), and (1.6.25). Two-dimensional expansion of these equations in a vector form is given as

$$Q = \begin{bmatrix} \rho \\ \rho u \\ \rho v \\ \rho e_t \\ \rho \tilde{\phi} \\ \rho \tilde{\phi}^2 \end{bmatrix}$$

$$F = \begin{bmatrix} \rho u \\ \rho u^2 + \rho q + p \\ \rho uv \\ u(\rho e_t + \rho q + p) \\ \rho u \tilde{\phi} \\ \rho u \tilde{\phi}^2 \end{bmatrix}$$

$$G = \begin{bmatrix} \rho v \\ \rho vu \\ \rho v^2 + \rho q + p \\ v(\rho e_t + \rho q + p) \\ \rho v \tilde{\phi} \\ \rho v \tilde{\phi}^2 \end{bmatrix}$$

$$F_v = Re_\infty^{-1} \begin{bmatrix} 0 \\ \tau_{xx} \\ \tau_{xy} \\ u\tau_{xx} + v\tau_{xy} + \theta_{xx} + \theta_{xy} + \chi_{xx} + \chi_{xy} + \Lambda_{xx} + \Lambda_{xy} \\ \alpha_{xx} + \alpha_{xy} \\ \beta_{xx} + \beta_{xy} \end{bmatrix}$$

$$G_v = Re_\infty^{-1} \begin{bmatrix} 0 \\ \tau_{yx} \\ \tau_{yy} \\ u\tau_{yx} + v\tau_{yy} + \theta_{yx} + \theta_{yy} + \chi_{yx} + \chi_{yy} + \Lambda_{yx} + \Lambda_{yy} \\ \alpha_{yx} + \alpha_{yy} \\ \beta_{yx} + \beta_{yy} \end{bmatrix}$$

$$S = Re_\infty^{-1} \begin{bmatrix} 0 \\ 0 \\ 0 \\ 0 \\ 0 \\ 2\rho\sigma^{-1}v_t \left[\xi_{11} \left(\frac{\partial \tilde{\phi}}{\partial x} \right)^2 + \xi_{12} \frac{\partial \tilde{\phi}}{\partial x} \frac{\partial \tilde{\phi}}{\partial y} + \xi_{22} \left(\frac{\partial \tilde{\phi}}{\partial y} \right)^2 \right] - \rho C_g \frac{\varepsilon}{q} \tilde{\phi}^2 \end{bmatrix}$$

where

$$\alpha_{xx} = \rho \left[\text{Re}_\infty D + v_t \sigma_\phi^{-1} \xi_{11} \right] \frac{\partial \tilde{\phi}}{\partial x} \quad (\text{A.3.1a})$$

$$\alpha_{xy} = \rho \left[v_t \sigma_\phi^{-1} \xi_{12} \right] \frac{\partial \tilde{\phi}}{\partial y} \quad (\text{A.3.1b})$$

$$\alpha_{yx} = \rho \left[v_t \sigma_\phi^{-1} \xi_{21} \right] \frac{\partial \tilde{\phi}}{\partial x} \quad (\text{A.3.1c})$$

$$\alpha_{yy} = \rho \left[\text{Re}_\infty D + v_t \sigma_\phi^{-1} \xi_{22} \right] \frac{\partial \tilde{\phi}}{\partial y} \quad (\text{A.3.1d})$$

$$\beta_{xx} = \rho \left[\text{Re}_\infty D + v_t \sigma_\phi^{-1} \xi_{11} \right] \frac{\partial \sqrt{\phi'^2}}{\partial x} \quad (\text{A.3.2a})$$

$$\beta_{xy} = \rho \left[v_t \sigma_\phi^{-1} \xi_{12} \right] \frac{\partial \sqrt{\phi'^2}}{\partial y} \quad (\text{A.3.2b})$$

$$\beta_{yx} = \rho \left[v_t \sigma_\phi^{-1} \xi_{21} \right] \frac{\partial \sqrt{\phi'^2}}{\partial x} \quad (\text{A.3.2c})$$

$$\beta_{yy} = \rho \left[\text{Re}_\infty D + v_t \sigma_\phi^{-1} \xi_{22} \right] \frac{\partial \sqrt{\phi'^2}}{\partial y} \quad (\text{A.3.2d})$$

The variations of the mean pressure with respect to the mean and variance of the mixture fraction are required for the solution of the governing equations. Pressure explicitly appears in both of the flux vectors F and G. Therefore, to obtain the Jacobian of these flux vectors, pressure must be given in terms of the elements of the solution vector, which includes $\rho \tilde{\phi}$ and $\rho \sqrt{\phi'^2}$. Pressure equations given in Section A.1 hold in general for a mixture of reacting ideal gases, independent of the method of chemical reaction closure. Therefore, then can be used to obtain variations of pressure with respect to ρ , ρu , ρv , and ρe_t . However, there is no explicit dependence on the mean or the variance of the mixture fraction. Implicitly, species mass fractions are decided from the integration of the PDF which is locally fixed by values of the mean and the variance of the mixture fraction. The use of this implicit relation and chain rules is too cumbersome to find derivatives of pressure with respect to $\rho \tilde{\phi}$ and $\rho \sqrt{\phi'^2}$. A more straightforward approach is to make use of the definition of the mean pressure in the PDF closure model. As pointed out in Section 1.6.4, the mean value of any thermodynamic quantity can be obtained from Equation (1.6.15). For the mean pressure this equation can be rewritten as

$$\bar{P} = \int_0^1 P(\phi) \tilde{f}(\phi) d\phi \quad (\text{A.3.3})$$

where $P(\phi)$ denotes pressure as a function of the mixture fraction. This function is obtained from equilibrium thermodynamic reaction calculations. $\tilde{f}(\phi)$ is an assumed Beta function given by Equation (1.6.11). The local form of the Beta function is fixed by the mean and the variance of the mixture fraction as given by Equations (1.6.11a) and (1.6.11b). Therefore, Equation (A.3.3) can be differentiated with respect to $\tilde{\phi}$ and $\tilde{\phi}^2$. Following the notation introduced in Section 1.6.4, these derivatives can be given by

$$\frac{\partial \bar{P}}{\partial (\rho \tilde{\phi})} = \int_0^1 P(\phi) \left[\frac{\partial \tilde{f}}{\partial a} \frac{\partial a}{\partial (\rho \tilde{\phi})} + \frac{\partial \tilde{f}}{\partial b} \frac{\partial b}{\partial (\rho \tilde{\phi})} \right] d\phi \quad (\text{A.3.4})$$

and

$$\frac{\partial \bar{P}}{\partial (\rho \tilde{\phi}^2)} = \int_0^1 P(\phi) \left[\frac{\partial \tilde{f}}{\partial a} \frac{\partial a}{\partial (\rho \tilde{\phi}^2)} + \frac{\partial \tilde{f}}{\partial b} \frac{\partial b}{\partial (\rho \tilde{\phi}^2)} \right] d\phi \quad (\text{A.3.5})$$

where

$$\frac{\partial \tilde{f}}{\partial a} = \tilde{f}(\phi) \left\{ \ln \phi - \frac{\int_0^1 \phi^{a-1} (1-\phi)^{b-1} \ln \phi d\phi}{\int_0^1 \phi^{a-1} (1-\phi)^{b-1} d\phi} \right\} \quad (\text{A.3.6})$$

For $\partial \tilde{f} / \partial b$ replace $\ln \phi$ by $\ln(1-\phi)$ in the above equation.

$$\frac{\partial a}{\partial (\rho \tilde{\phi})} = \frac{1}{\rho} \left[\frac{2\tilde{\phi} - 3\tilde{\phi}^2}{\tilde{\phi}^2} - 1 \right] \quad (\text{A.3.7})$$

$$\frac{\partial b}{\partial (\rho \tilde{\phi})} = \frac{1}{\rho} \left[\frac{(1-\tilde{\phi})(1-3\tilde{\phi})}{\tilde{\phi}^2} + 1 \right] \quad (\text{A.3.8})$$

$$\frac{\partial a}{\partial (\rho \phi^{n^2})} = - \frac{1}{\rho} \frac{\tilde{\phi}^2 (1 - \tilde{\phi})}{(\phi^{n^2})^2} \quad (\text{A.3.9})$$

$$\frac{\partial b}{\partial (\rho \phi^{n^2})} = - \frac{1}{\rho} \frac{\tilde{\phi} (1 - \tilde{\phi})^2}{(\phi^{n^2})^2} \quad (\text{A.3.10})$$

The Jacobian matrices are denoted by

$$A = \frac{\partial F}{\partial Q} \quad \text{and} \quad B = \frac{\partial G}{\partial Q}$$

In the curvilinear coordinate system $\hat{A} = \xi_x A + \xi_y B$ is given by the matrix A.3.1, where DPQ5 denotes $\partial \bar{p} / \partial (\rho \tilde{\phi})$ and DPQ6 denotes $\partial \bar{p} / \partial (\rho \tilde{\phi}^{n^2})$. For \hat{B} replace ξ with η .

MATRIX A.3.1

0	ξ_x	ξ_y	0	0	0
$[(\hat{\gamma}-1)(K-q(h_{iN}^*h_{oN})) - u^2 + q_3^2]\xi_x - (uv)\xi_y$	$u(3-\hat{\gamma})\xi_x + v\xi_y$	$-(\hat{\gamma}-1)v\xi_x + u\xi_y$	$(\hat{\gamma}-1)\xi_x$	DPQ5 ξ_x	DPQ6 ξ_x
$[(\hat{\gamma}-1)(K-q(h_{iN}^*h_{oN})) - v^2 + q_3^2]\xi_y - uv\xi_x$	$v\xi_x - (\hat{\gamma}-1)u\xi_y$	$u\xi_x + (3-\hat{\gamma})v\xi_y$	$(\hat{\gamma}-1)\xi_y$	DPQ5 ξ_y	DPQ6 ξ_y
$-(\rho c_t + p)(u\xi_x + v\xi_y) + (\hat{\gamma}-1)[K-q(h_{iN}^*h_{oN})] \times (u\xi_x + v\xi_y)$	$[\frac{1}{p}(\rho c_t + p) + q_3^2 - u^2(\hat{\gamma}-1)]\xi_x - uv(\hat{\gamma}-1)\xi_y$	$[\frac{1}{p}(\rho c_t + p) + q_3^2 - v^2(\hat{\gamma}-1)]\xi_y - uv(\hat{\gamma}-1)\xi_x$	$\hat{\gamma}(u\xi_x + v\xi_y)$	DPQ5 $(u\xi_x - v\xi_y)$	DPQ6 $(u\xi_x - v\xi_y)$
$-(u\xi_x + v\xi_y)\bar{\phi}$	$\xi_x\bar{\phi}$	$\xi_y\bar{\phi}$	0	$u\xi_x + v\xi_y$	0
$-(u\xi_x + v\xi_y)\phi'^2$	$\xi_x\phi'^2$	$\xi_y\phi'^2$	0	0	$u\xi_x + v\xi_y$

*K = $\frac{1}{2}(u^2 + v^2)$

$$P = P(\rho, e, \phi)$$

(H₂ - Air)

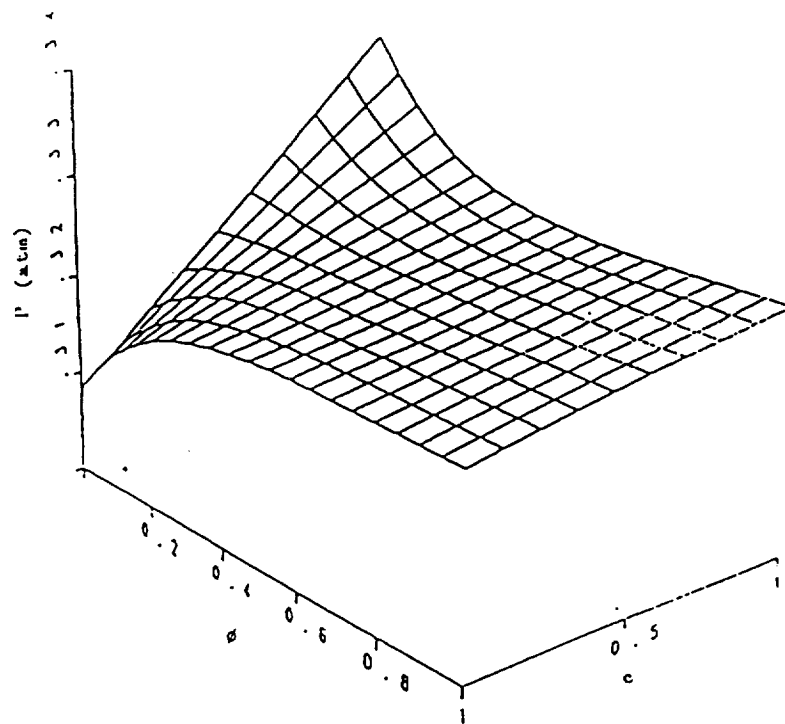


Figure 1.1 - Chemical equilibrium plot for P at fixed density.

$$T = T(\rho, e, \phi)$$

(H₂ - Air)

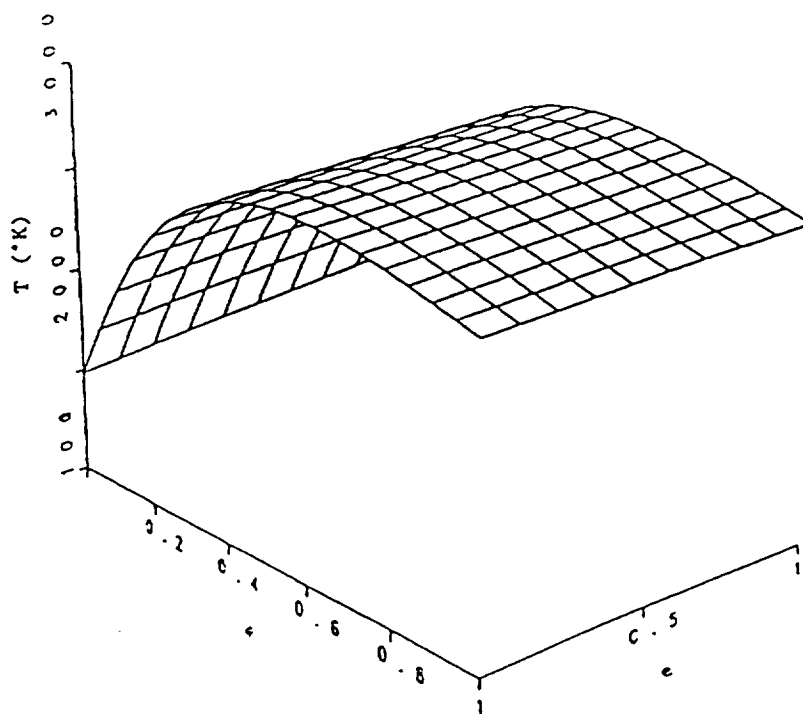


Figure 1.2 - Chemical equilibrium plot for T at fixed density.

$$Y_{H_2} = Y_{H_2}(\rho, e, \phi)$$

(H₂ - Air)

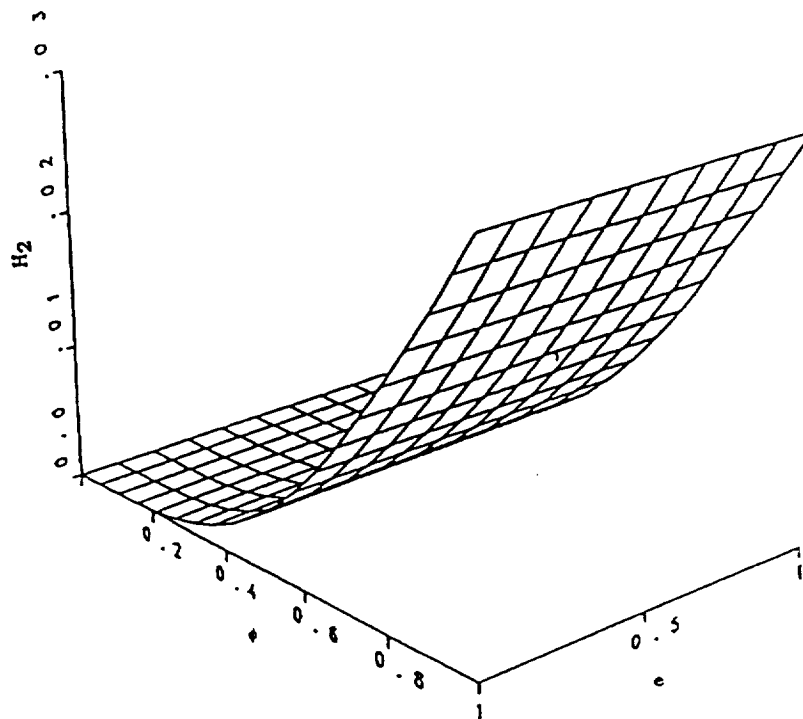


Figure 1.3- Chemical equilibrium plot for Y_{H_2}
at fixed density.

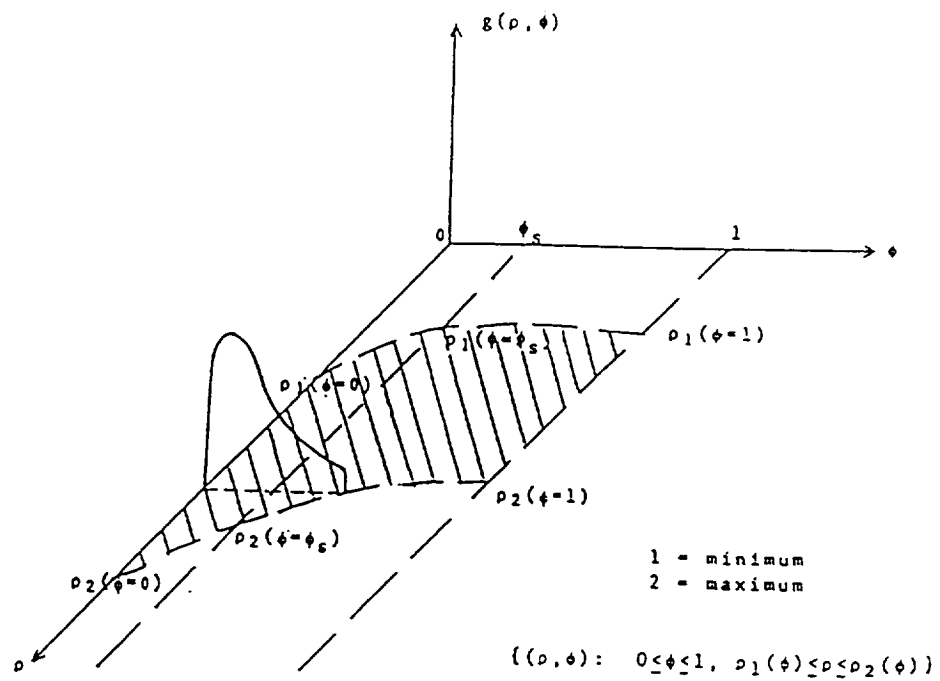


Figure 1.4 -PDF of mixture fraction along $\rho = \text{constant}$.

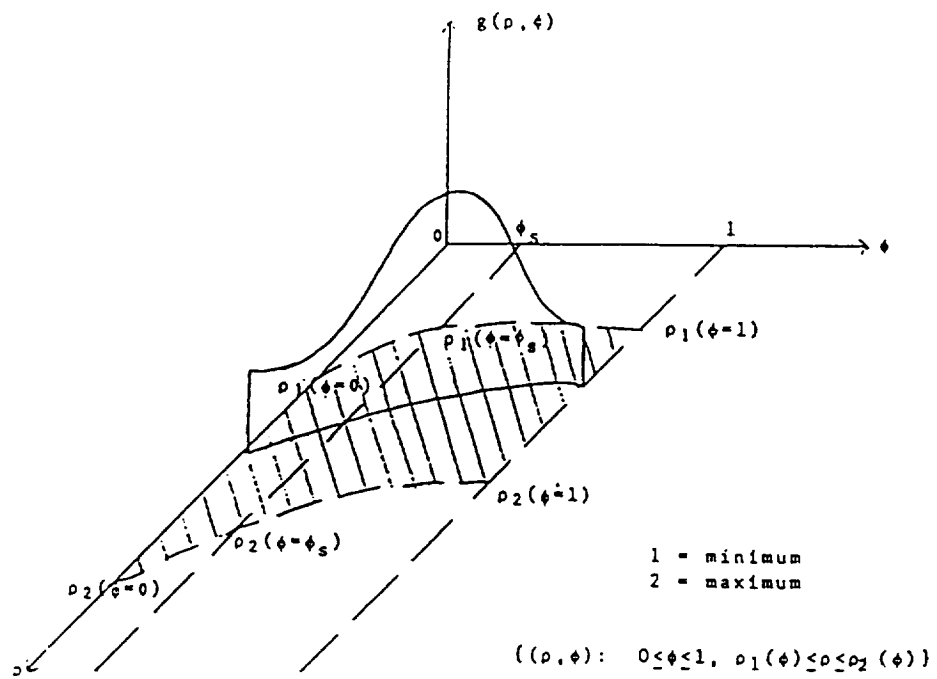


Figure 1.5 - PDF of mixture fraction along $\rho^* = \text{constant}$.

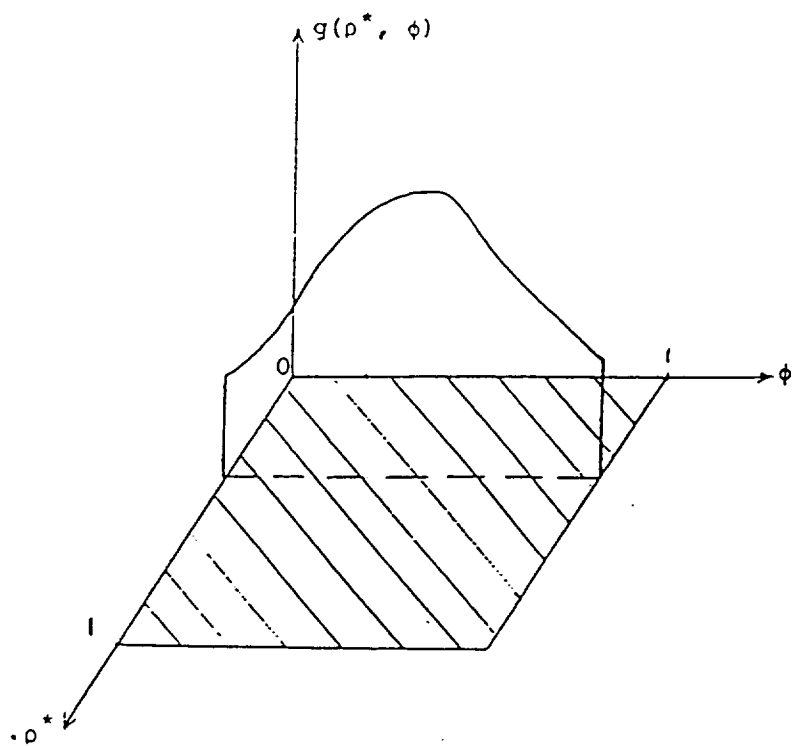


Figure 1.6 - Normalized joint PDF domain.

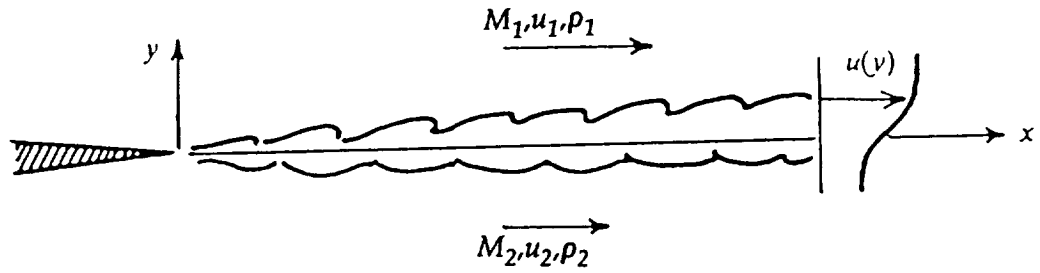


Figure 2.1 - Shear layer geometry.

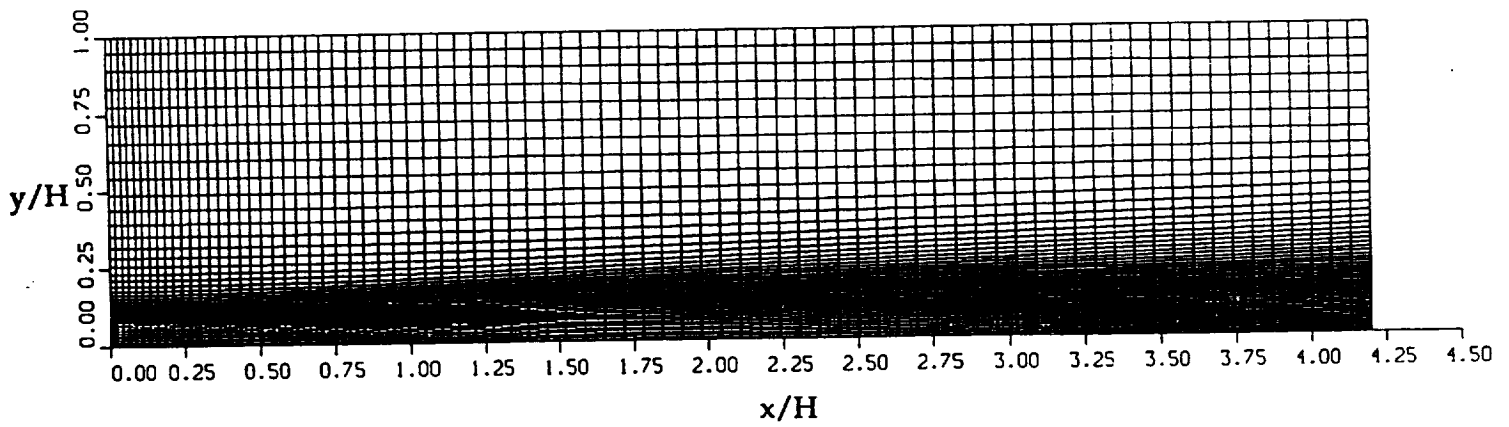


Figure 2.2a - 80 x 55 clustered grid used for mixing layer calculations.

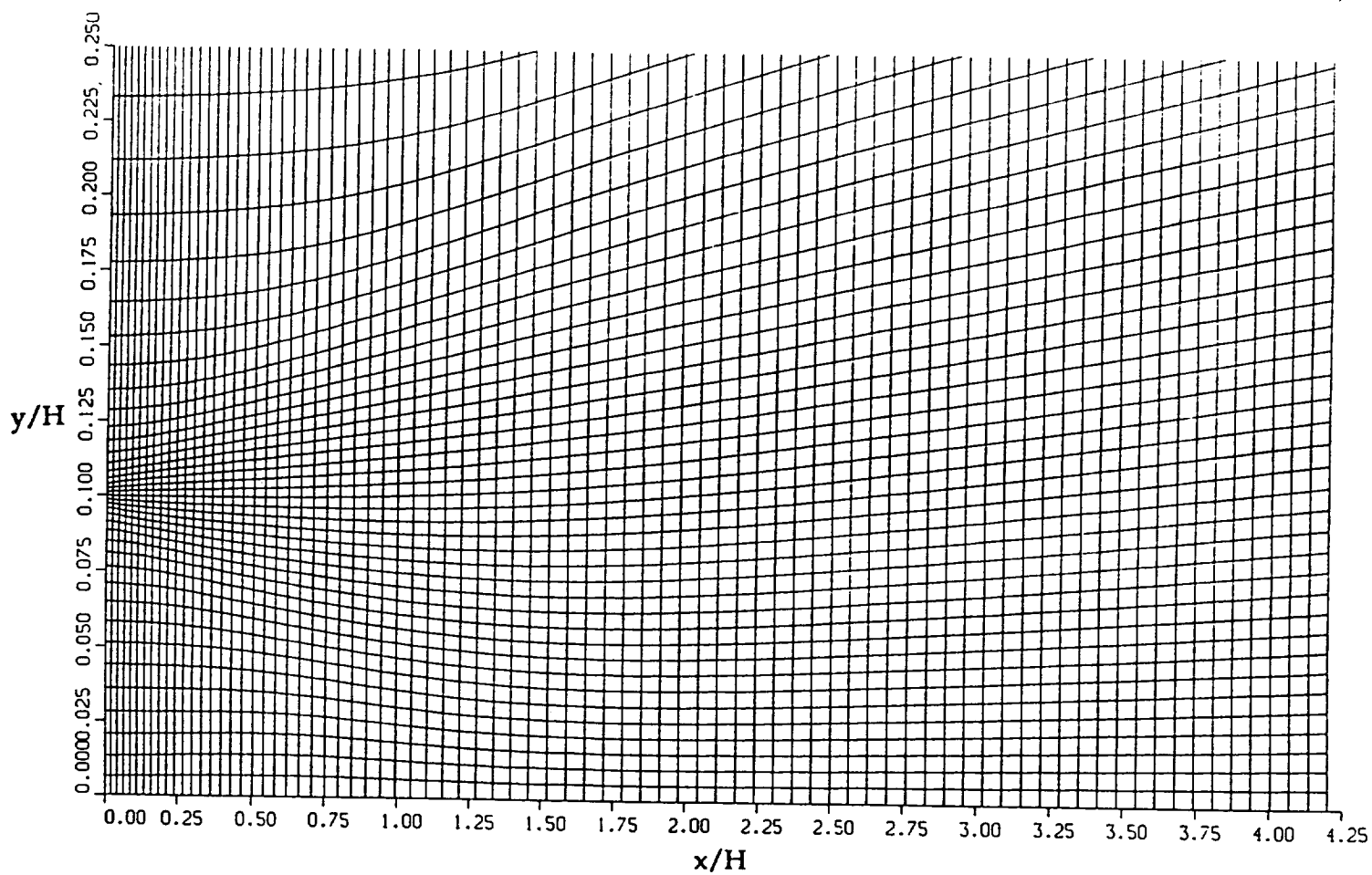


Figure 2.2b - 80 x 55 clustered grid magnified near the splitter plate location.

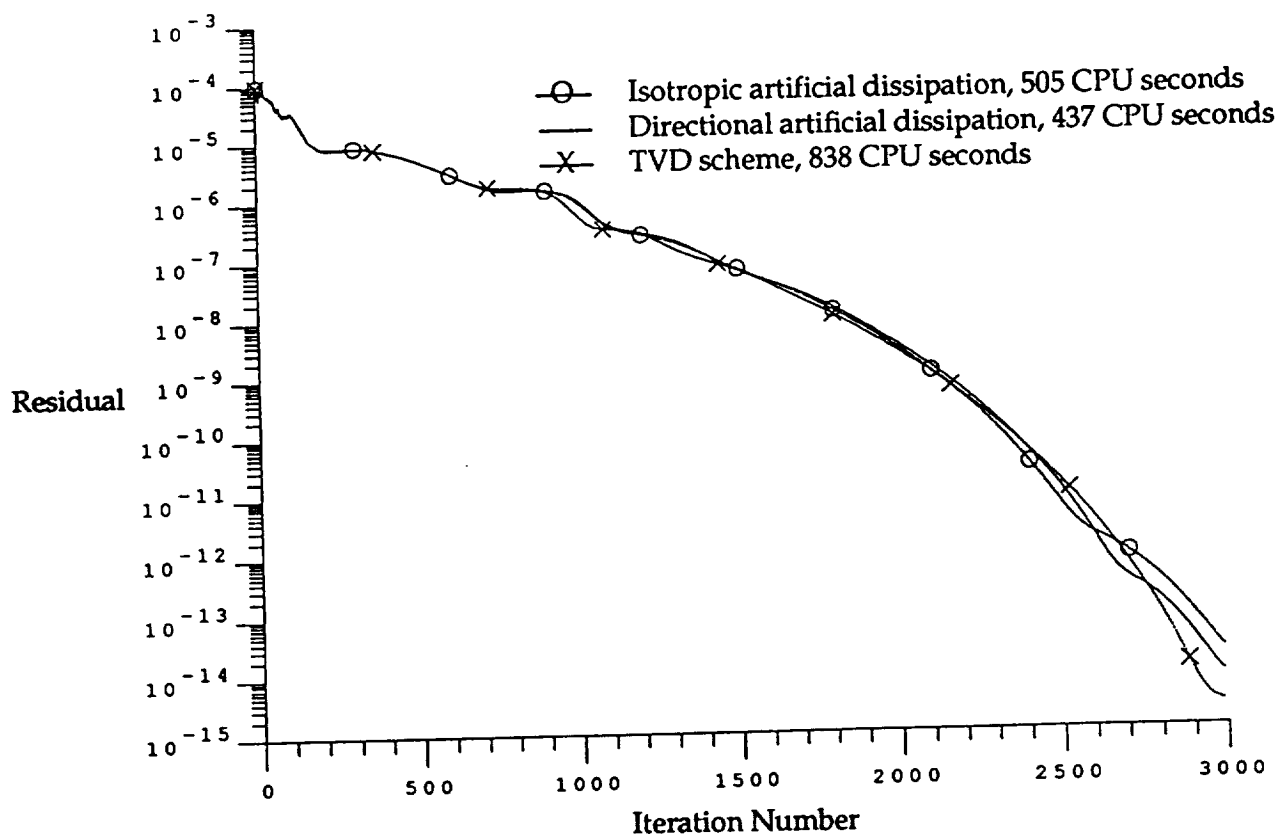


Figure 2.3 - Convergence history of nondimensionalized L_2 density residual.

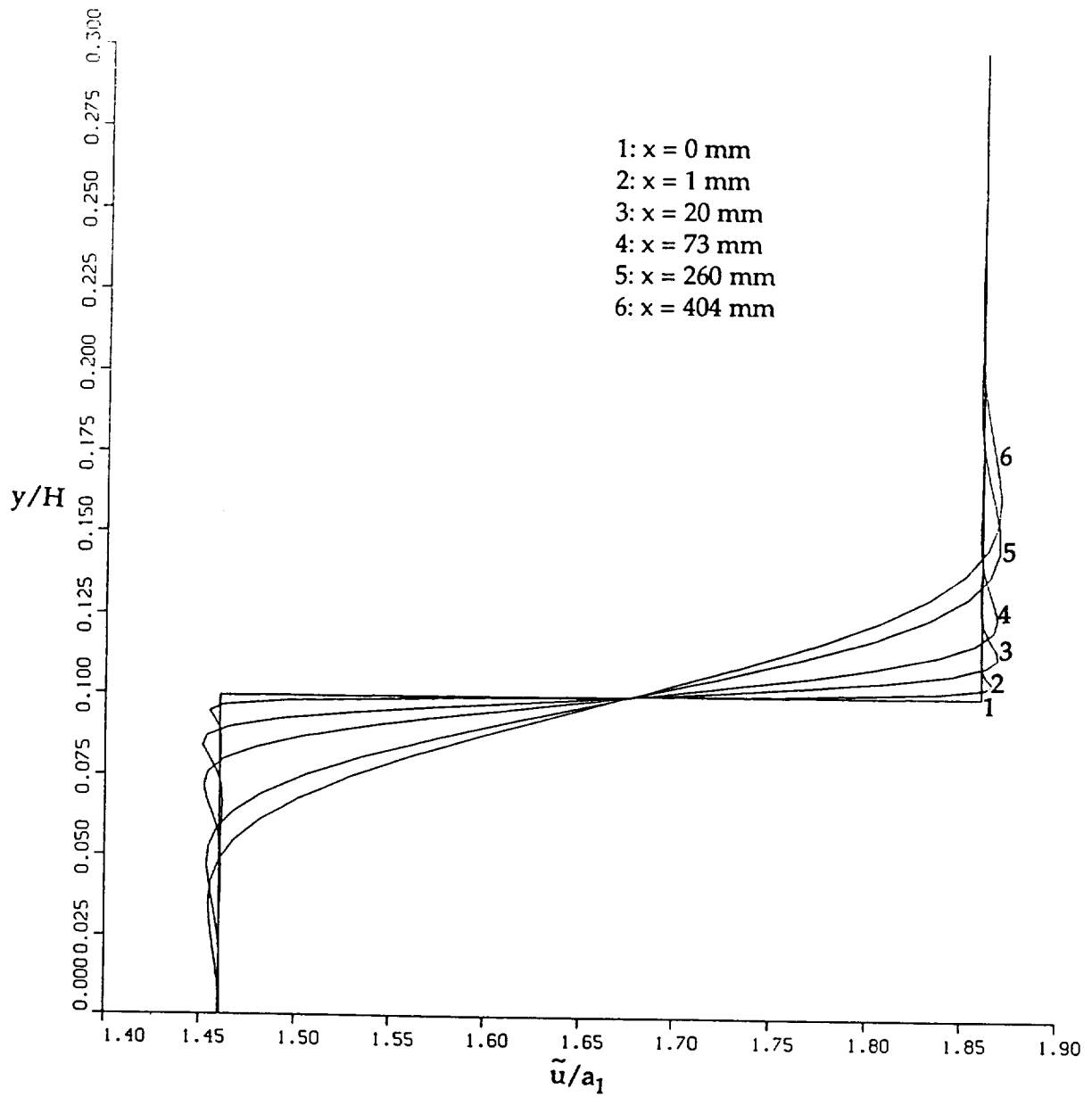


Figure 2.4a - Profiles of streamwise velocity for mixing layer with $s = 1.0$ and $r = 0.785$.
 (Isotropic artificial dissipation applied)

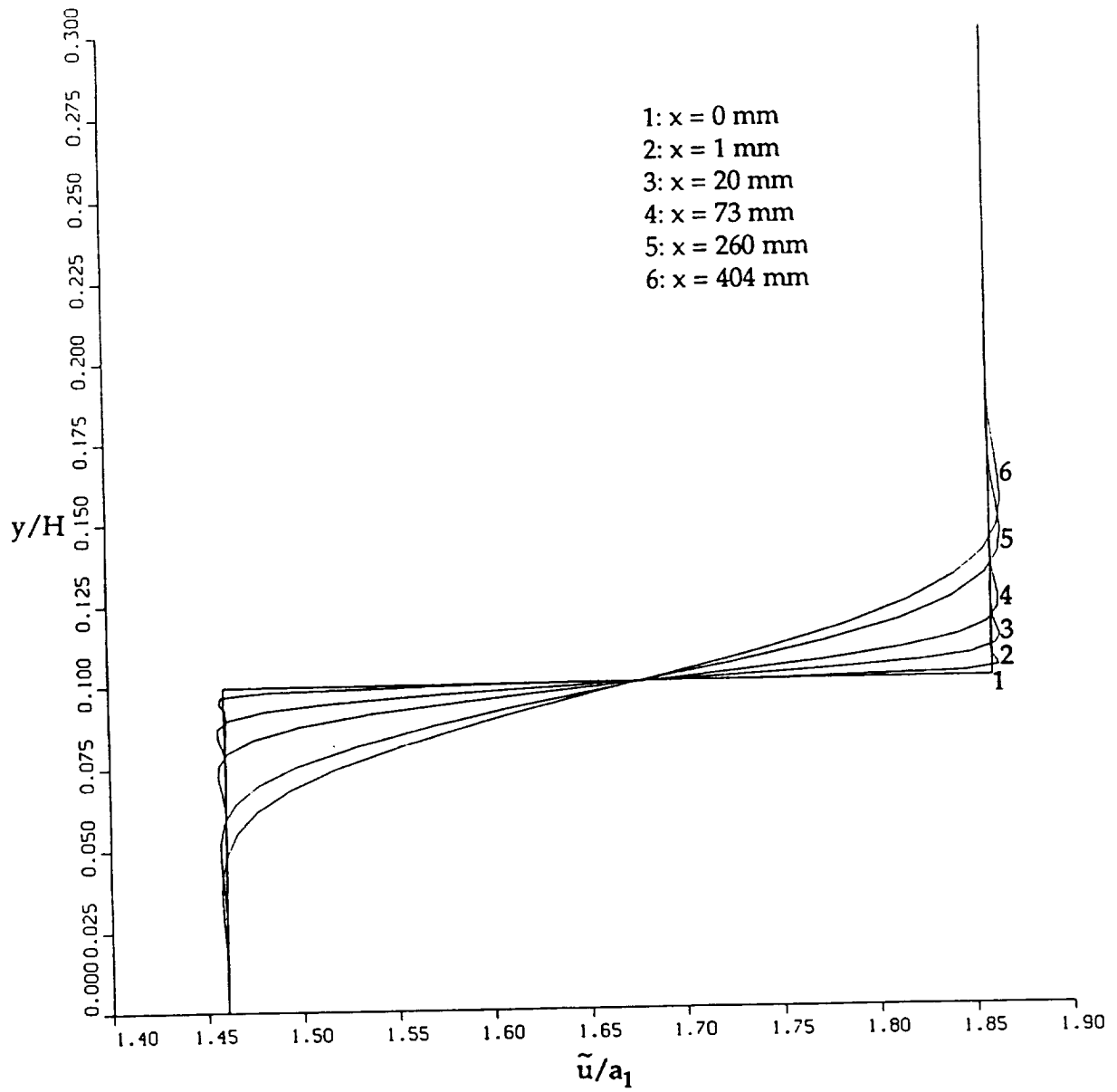


Figure 2.4b - Profiles of streamwise velocity for mixing layer with $s = 1.0$ and $r = 0.785$.
 (Directional artificial dissipation applied)

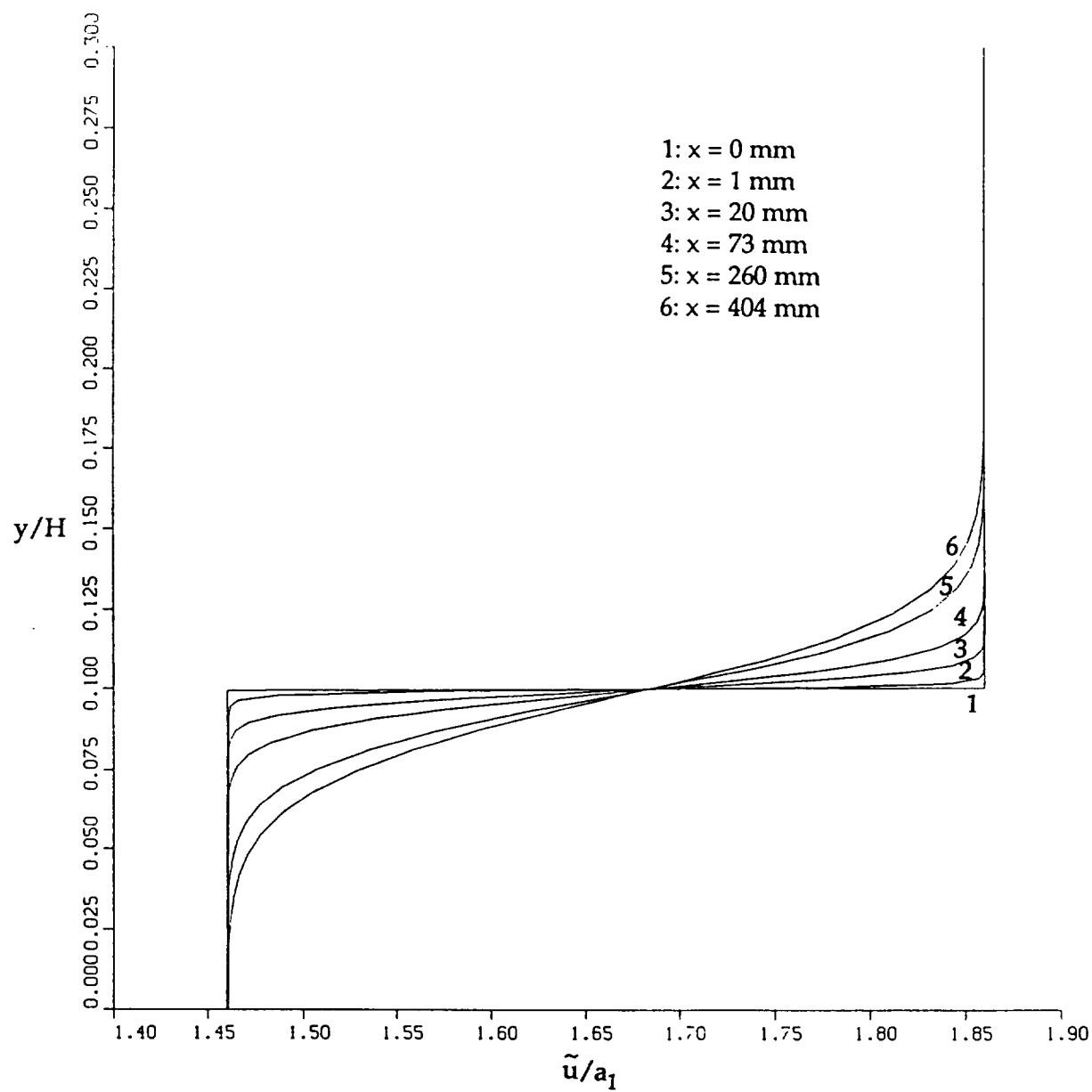


Figure 2.4c - Profiles of streamwise velocity for mixing layer with $s = 1.0$ and $r = 0.785$.
 (TVD scheme applied)

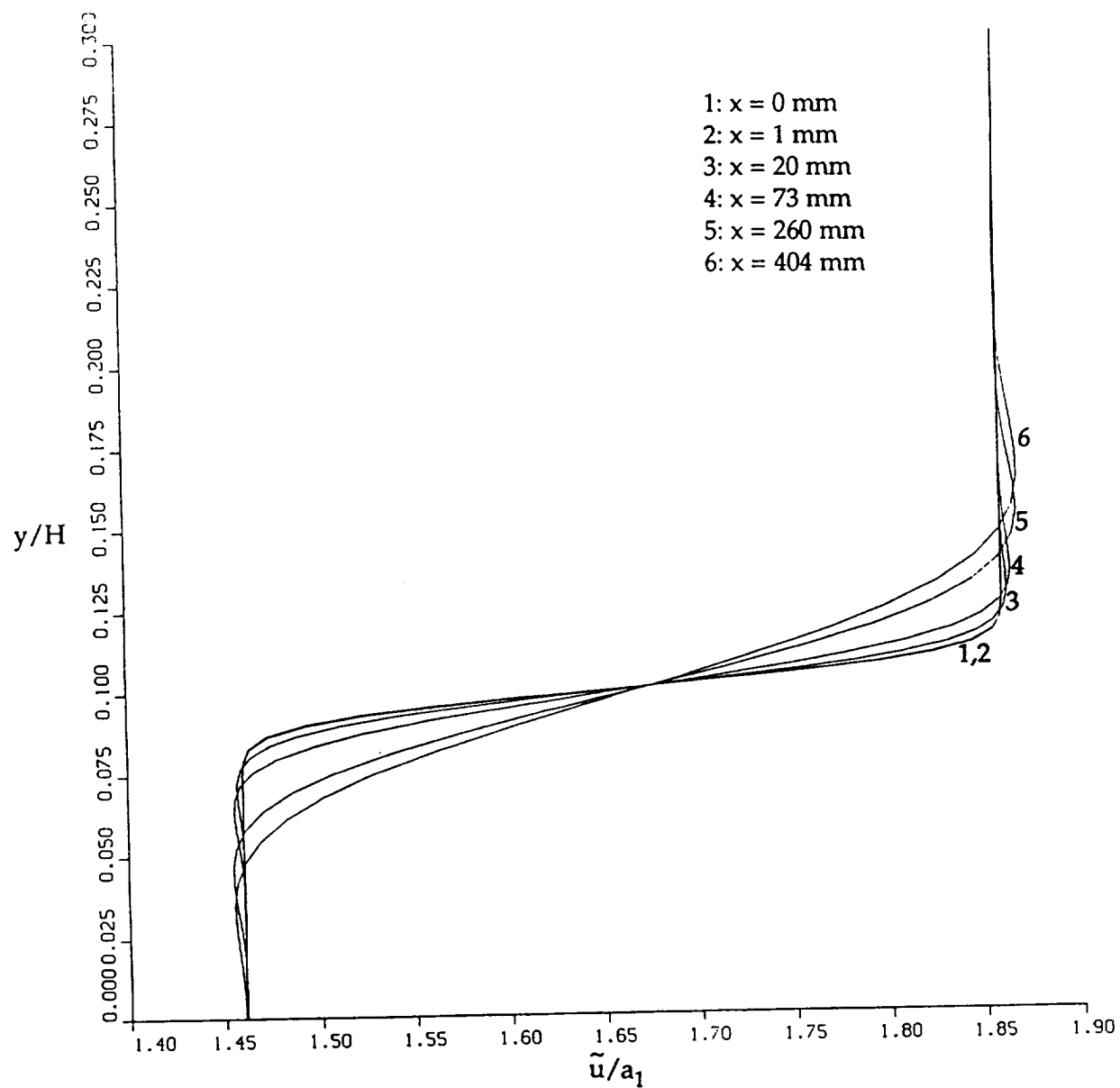


Figure 2.4d - Profiles of streamwise velocity for mixing layer with $s = 1.0$ and $r = 0.785$.
 (Smoothed inflow velocity, isotropic artificial dissipation applied)

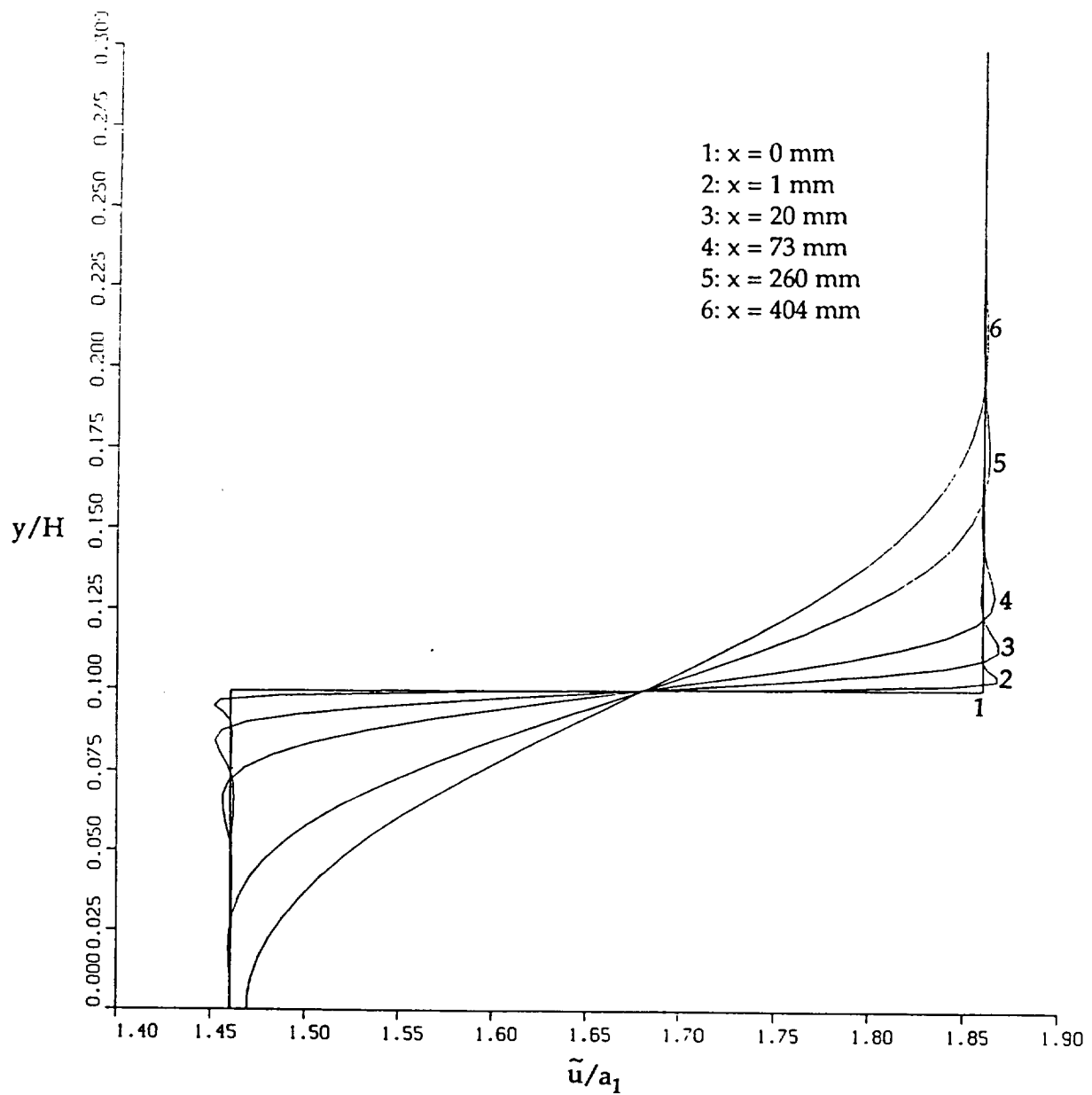
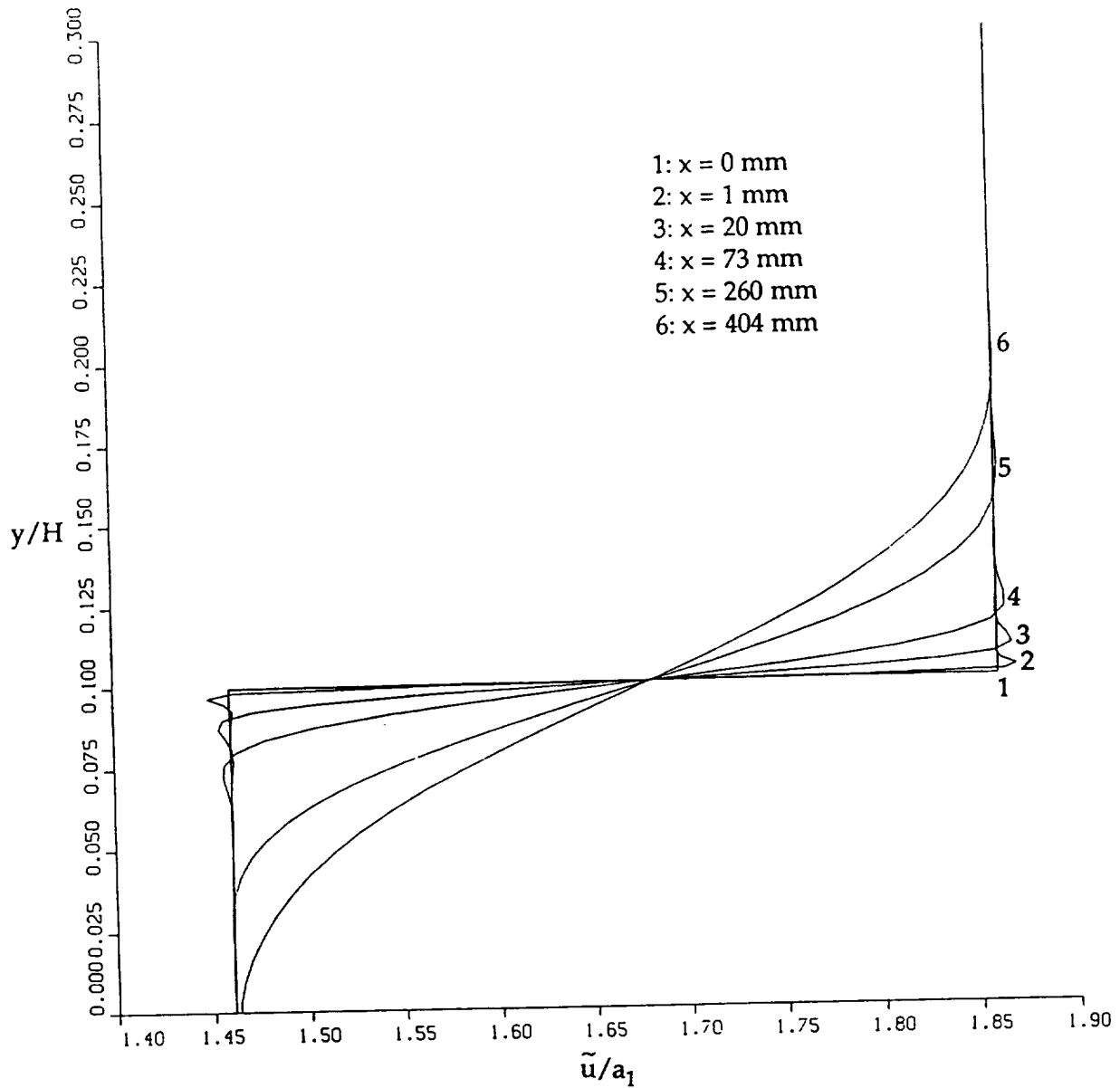


Figure 2.5a - Profiles of streamwise velocity for turbulent mixing layer with $s = 1$ and $r = 0.785$.
 (Isotropic artificial dissipation applied with Prandtl mixing turbulence model)



**Figure 2.5b - Profiles of streamwise velocity for turbulent mixing layer with $s = 1$ and $r = 0.785$.
 (Direction artificial dissipation applied with Prandtl mixing turbulence model)**

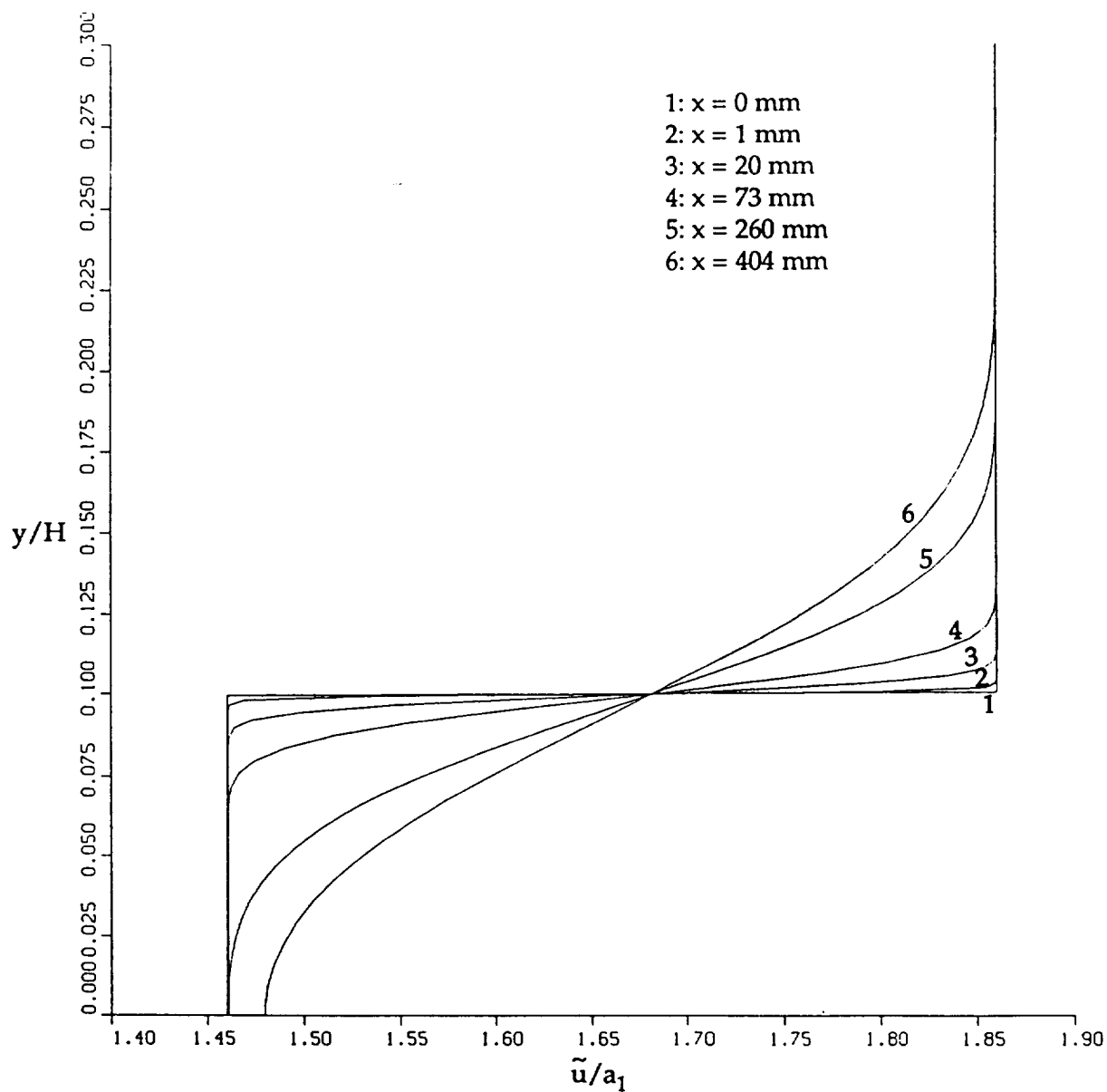


Figure 2.5c - Profiles of streamwise velocity for turbulent mixing layer with $s = 1$ and $r = 0.785$.

(TVD scheme applied with Prandtl mixing turbulence model)

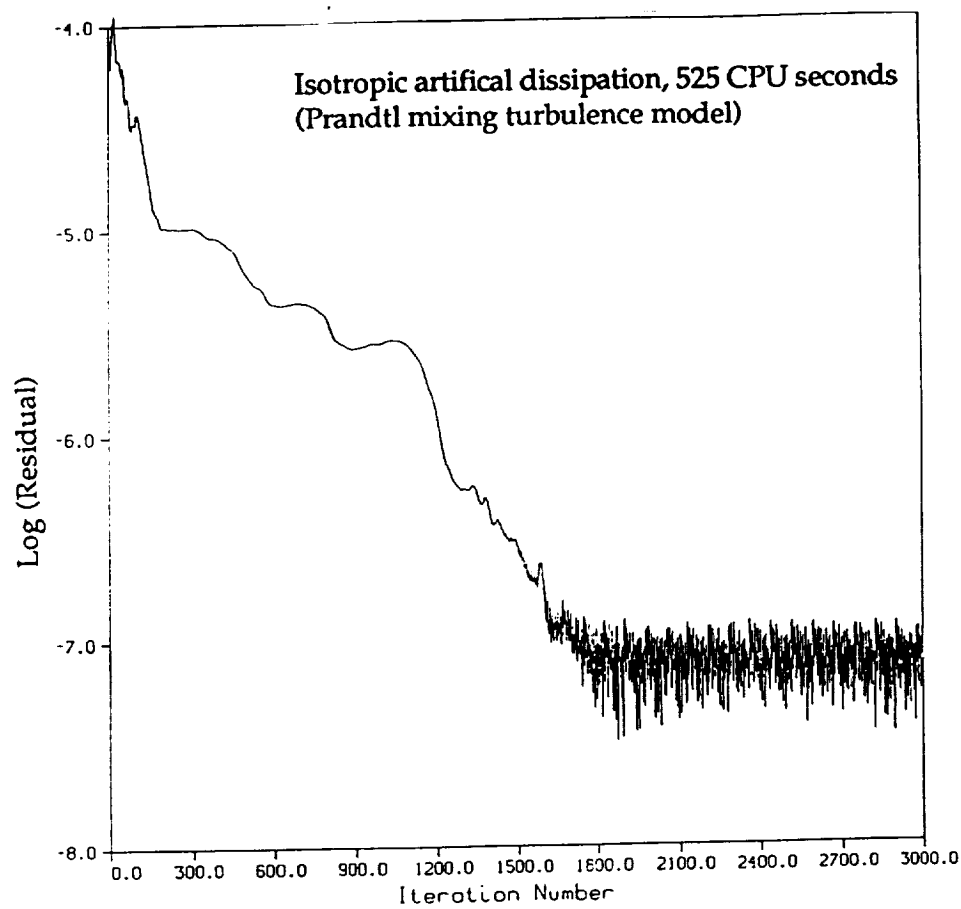


Figure 2.6a - Convergence history of nondimensionalized L_2 density residual.

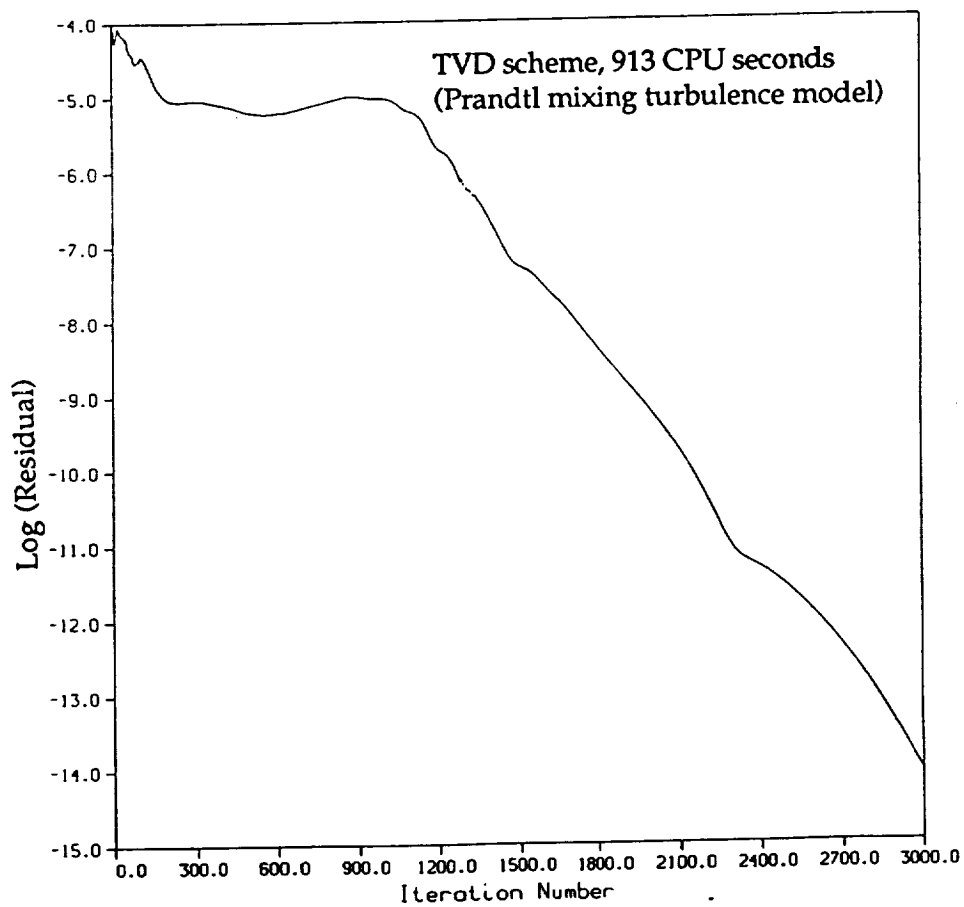


Figure 2.6b - Convergence history of nondimensionalized L_2 density residual.

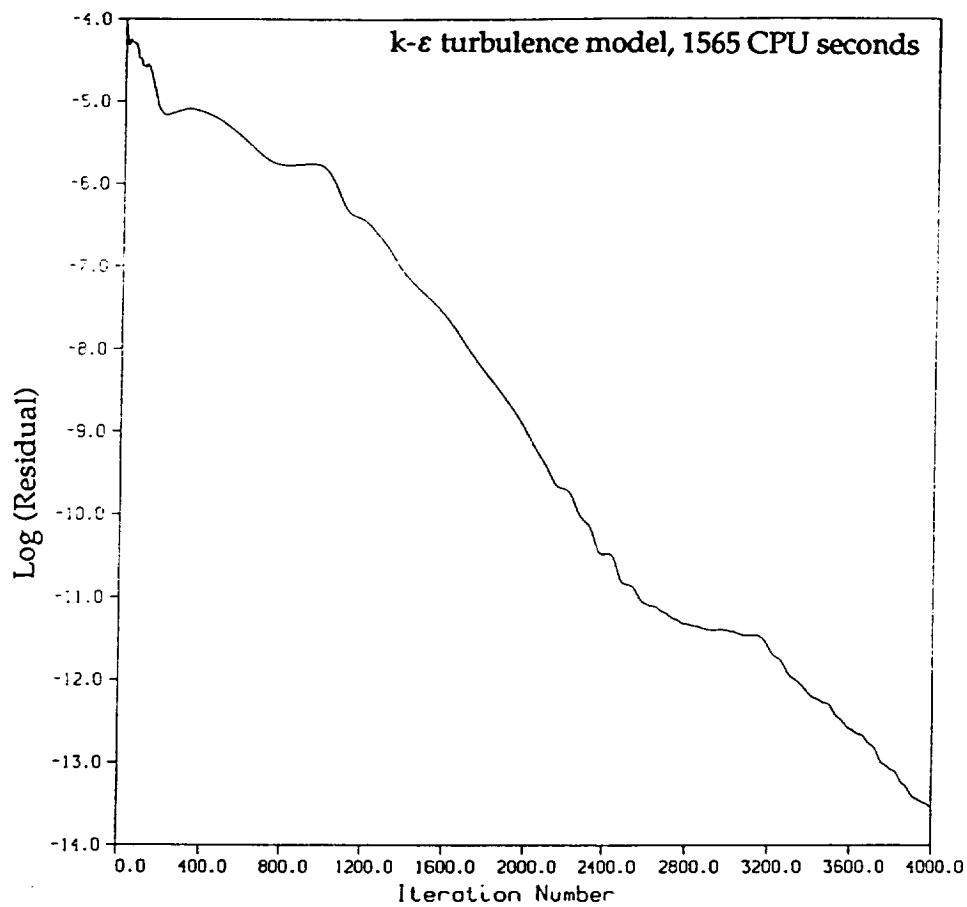


Figure 2.7 - Convergence history of nondimensionalized L_2 density residual ($s = 1$, $r = .785$, and $M_c = .2$).

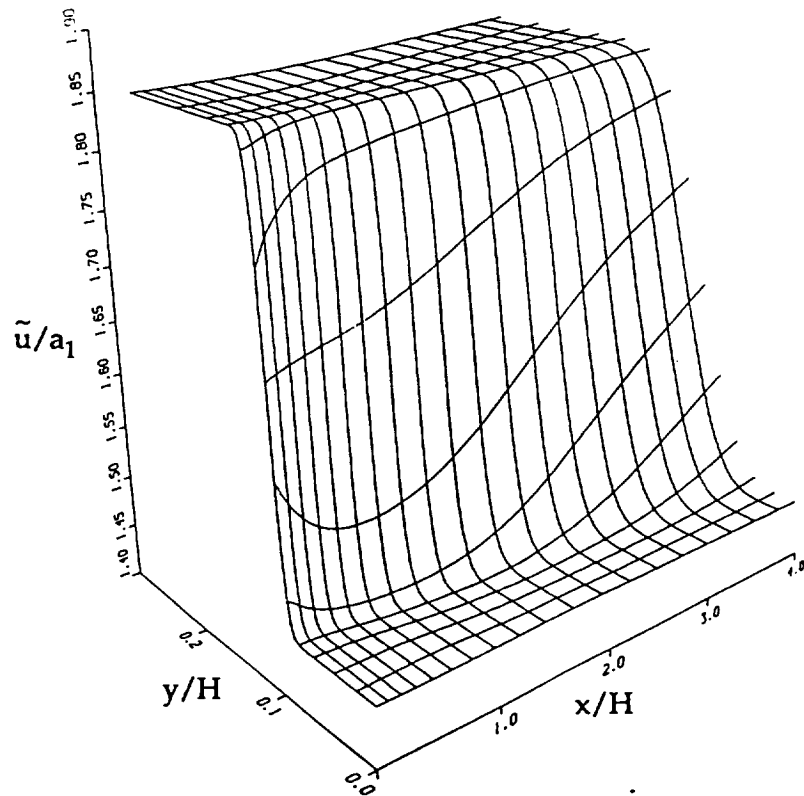


Figure 2.8a - Streamwise velocity variations in the solution domain ($s = 1.0$, $r = 0.785$, $M_c = 0.2$, $k-\epsilon$ turbulence model used).

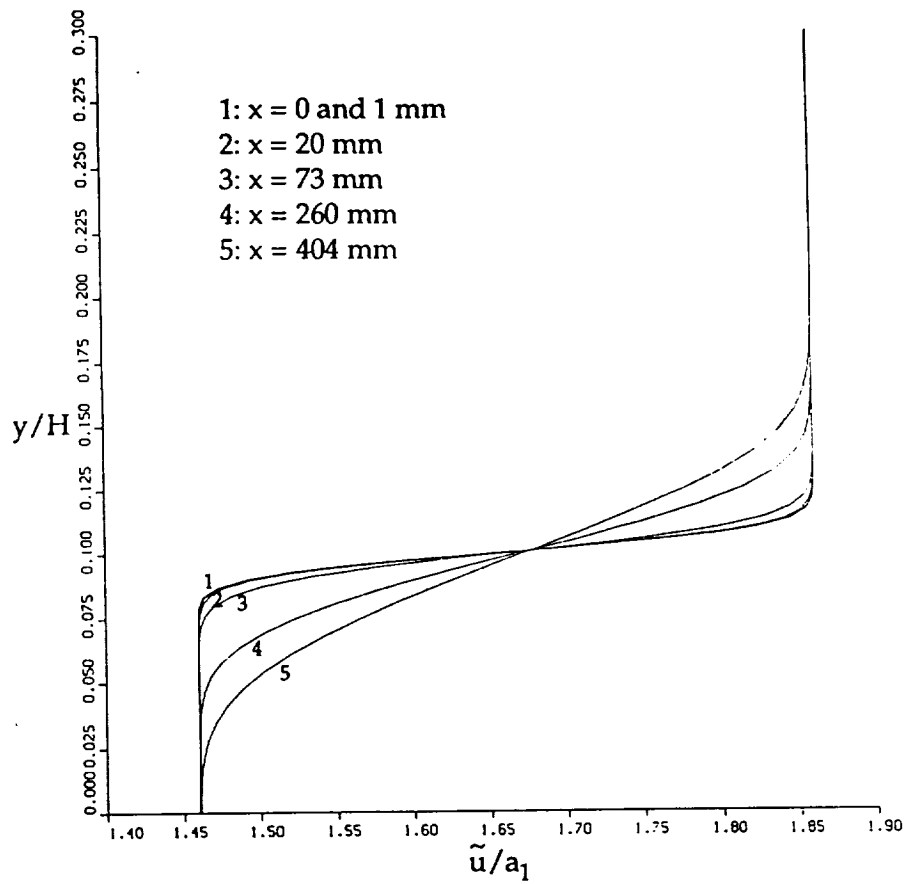


Figure 2.8b - Streamwise velocity profiles at several downstream locations ($s = 1.0$, $r = 0.785$, $M_c = 0.2$, $k-\epsilon$ turbulence model used).

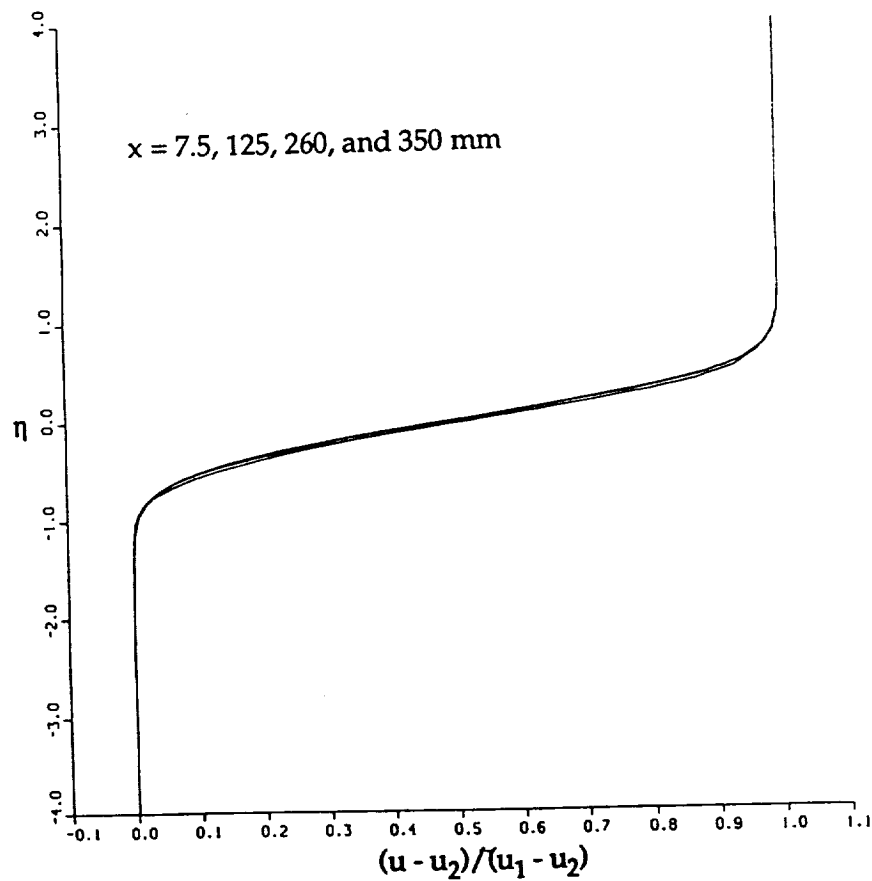


Figure 2.8c - Streamwise velocity profiles with respect to the similarity variable ($s = 1.0$, $r = 0.785$, $M_c = 0.2$, $k-\epsilon$ turbulence model used).

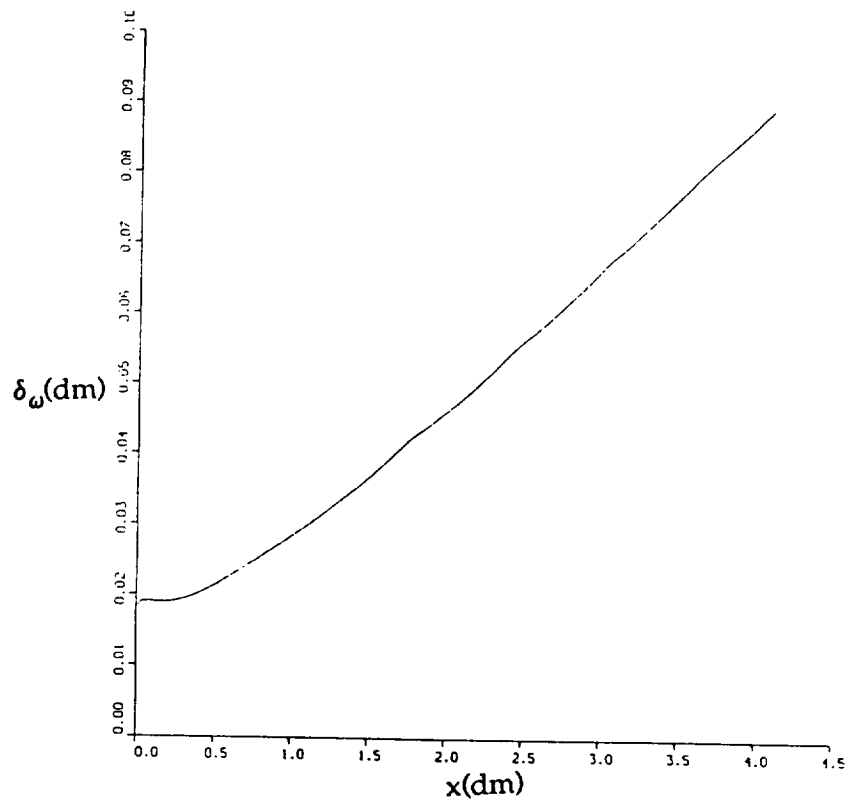


Figure 2.9 - Vorticity thickness growth
($s = 1.0$, $r = 0.785$, $M_c = 0.2$, k - ϵ turbulence model used).

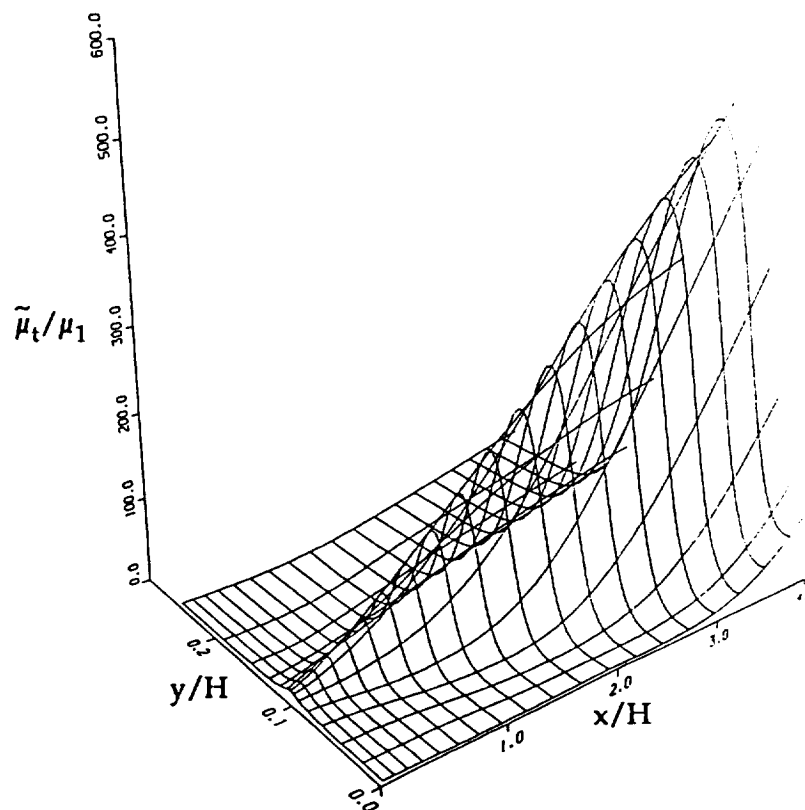


Figure 2.10 - Nondimensionalized turbulent eddy viscosity
($s = 1.0$, $r = 0.785$, $M_c = 0.2$, k - ϵ turbulence model used).

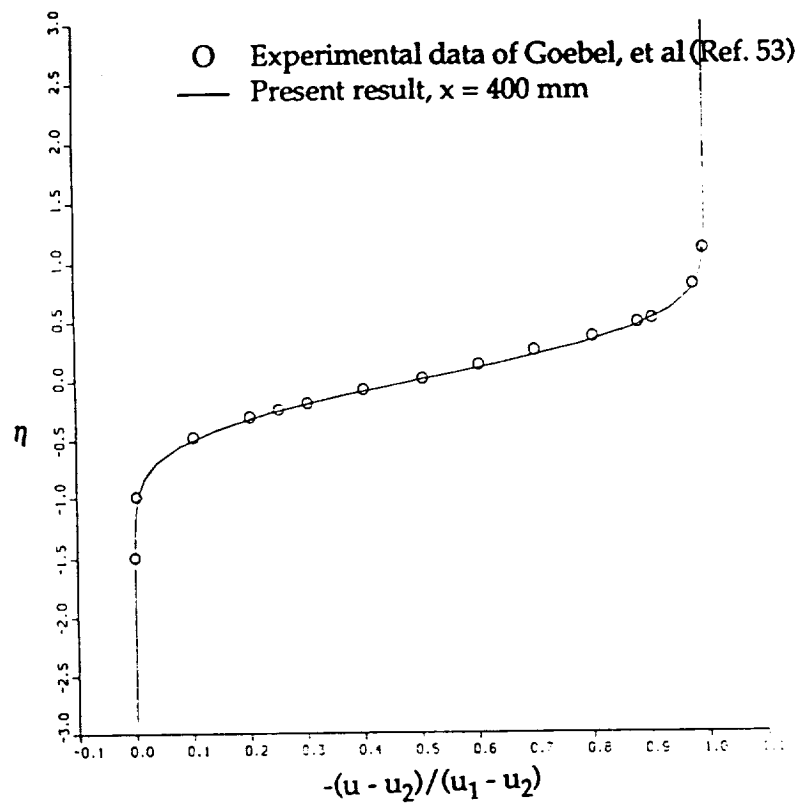


Figure 2.11a - Similarity profile of normalized mean streamwise velocity
 ($s = 1.0$, $r = 0.785$, $M_c = 0.2$, $k-\epsilon$ turbulence model used).

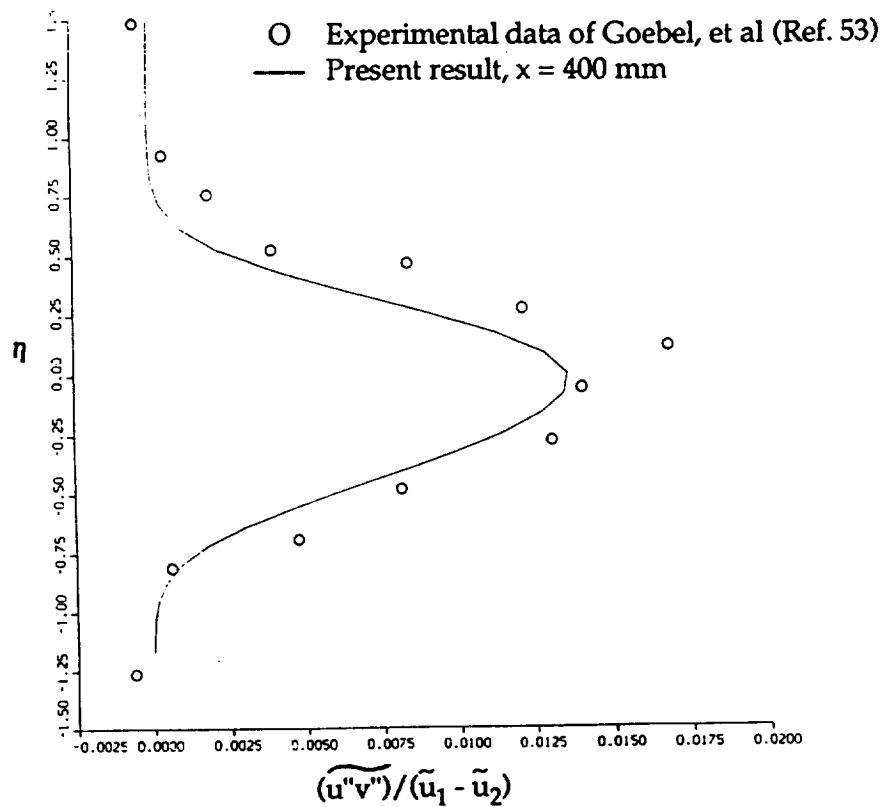


Figure 2.11b - Reynold stress profile at $x = 400$ mm
 ($s = 1.0$, $r = 0.785$, $M_c = 0.2$, $k-\epsilon$ turbulence model used).

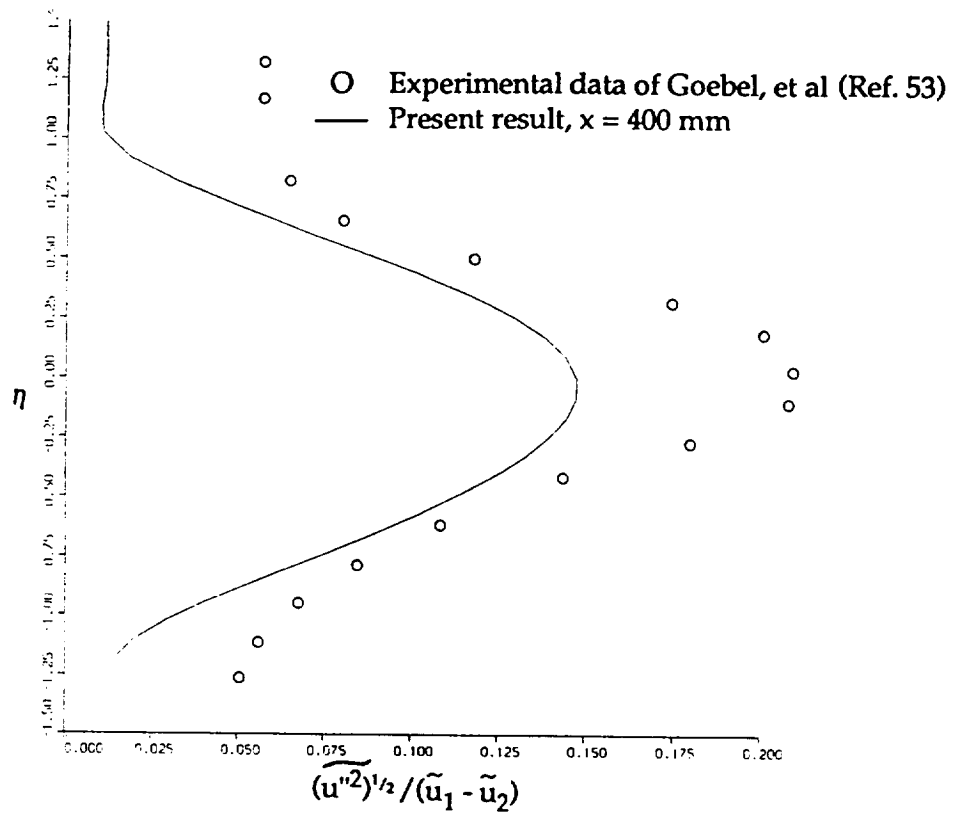


Figure 2.11c - Streamwise turbulent intensity profile at $x = 400$ mm
 ($s = 1.0$, $r = 0.785$, $M_c = 0.2$, $k-\epsilon$ turbulence model used).

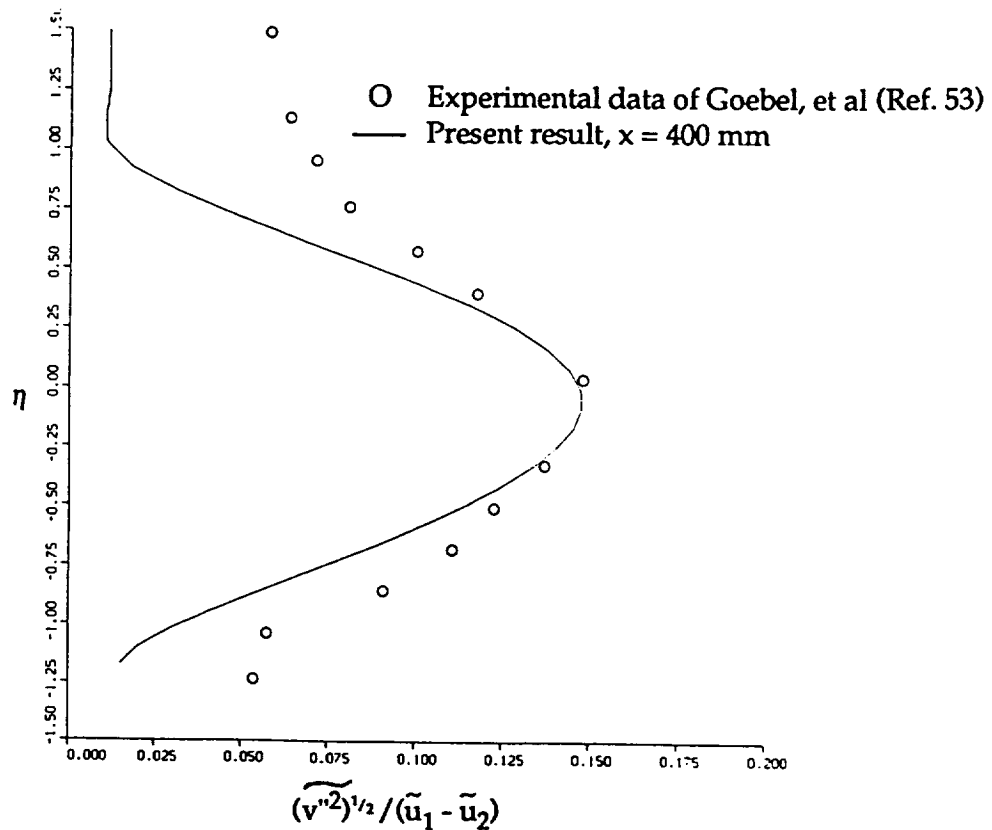


Figure 2.11d - Lateral turbulent intensity profile at $x = 400$ mm
 ($s = 1.0$, $r = 0.785$, $M_c = 0.2$, $k-\epsilon$ turbulence model used).

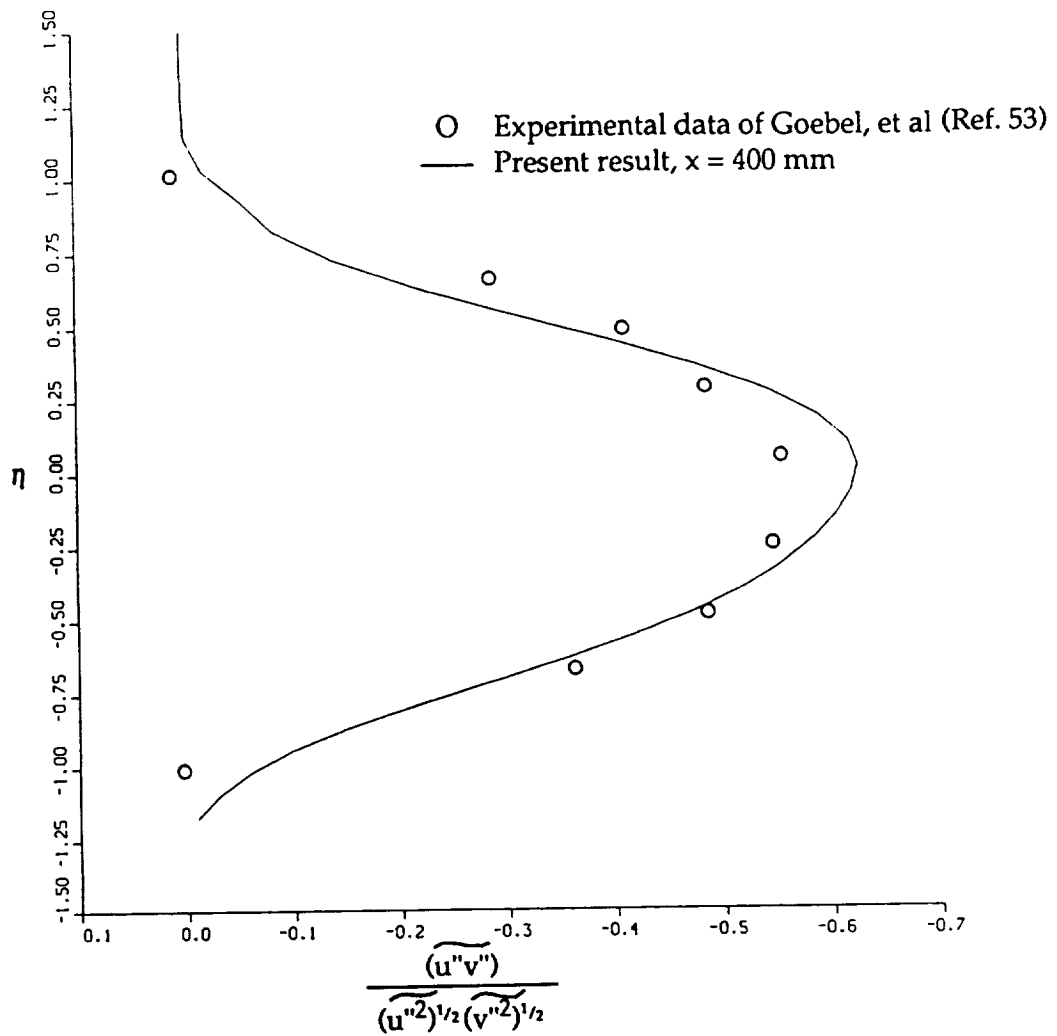


Figure 2.12 - Turbulent correlation coefficient at $x = 400$ mm
 ($s = 1.0$, $r = 0.785$, $M_c = 0.2$, $k-\epsilon$ turbulence model used).

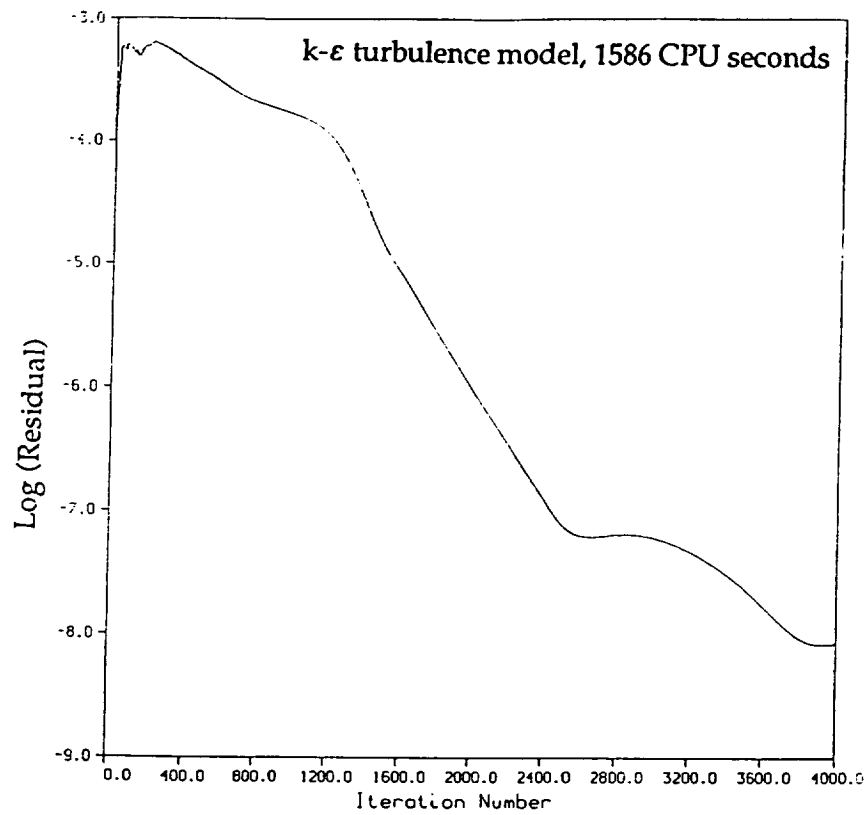


Figure 2.13 - Convergence history of nondimensionalized L_2 density residual ($s = 2.44$, $r = 0.51$, and $M_{cl} = 0.55$).

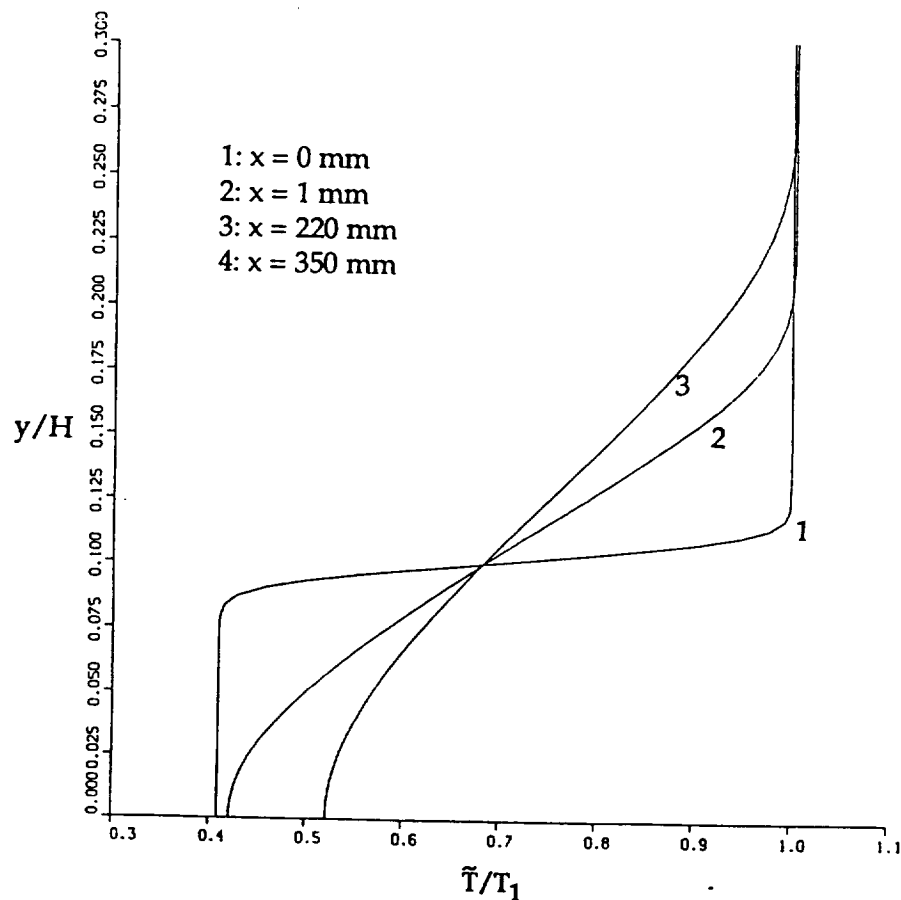


Figure 2.14a - Nondimensionalized temperature profiles at several downstream locations ($s = 2.44$, $r = 0.51$, and $M_{cl} = 0.55$, $k-\epsilon$ turbulence model used).

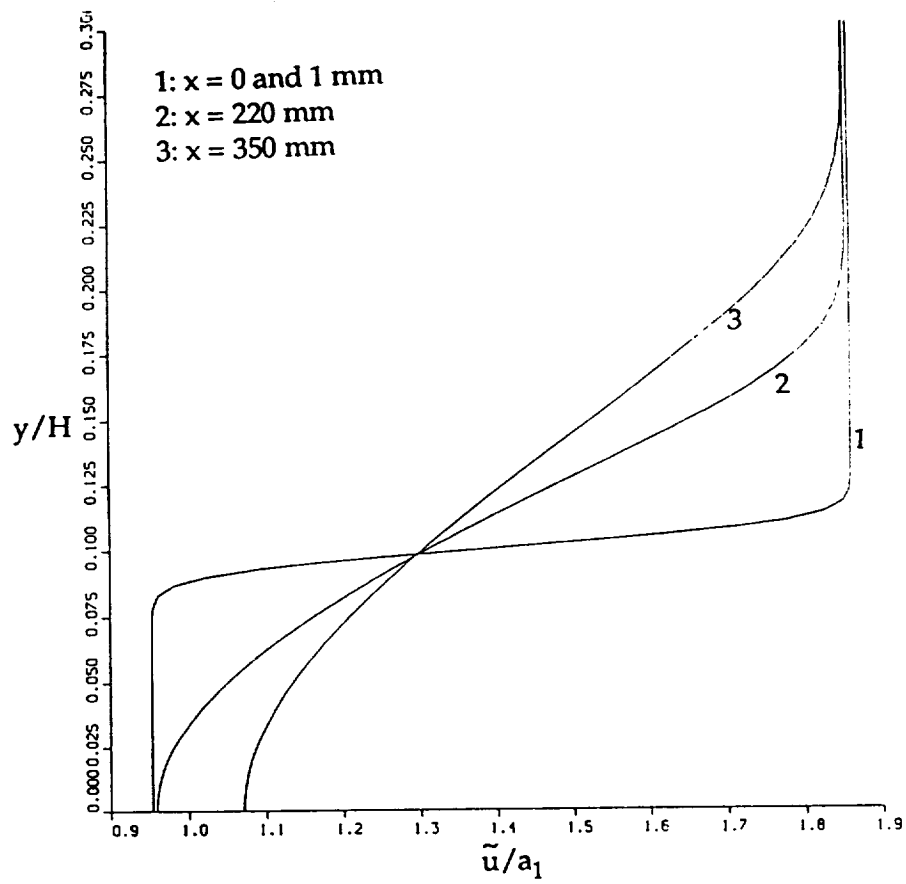


Figure 2.14b - Streamwise velocity profiles at several downstream locations ($s = 2.44$, $r = 0.51$, and $M_{c1} = 0.55$, $k-\epsilon$ turbulence model used).

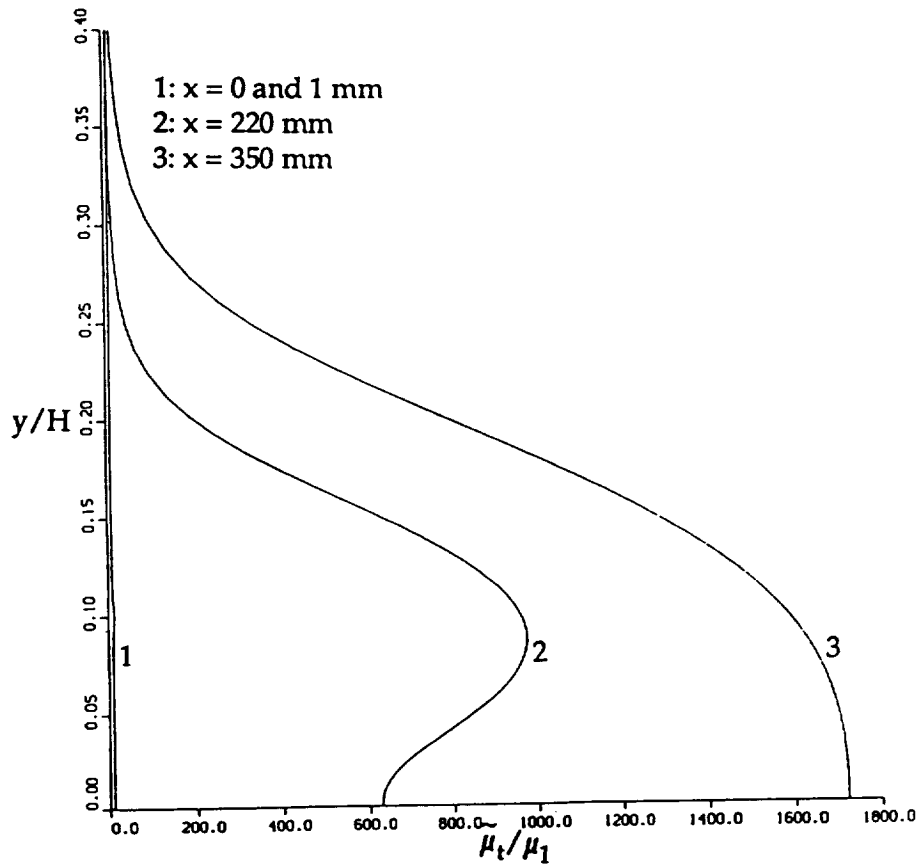


Figure 2.14c - Nondimensionalized turbulent viscosity profiles at several downstream locations ($s = 2.44$, $r = 0.51$, and $M_{c1} = 0.55$, $k-\epsilon$ turbulence model used).

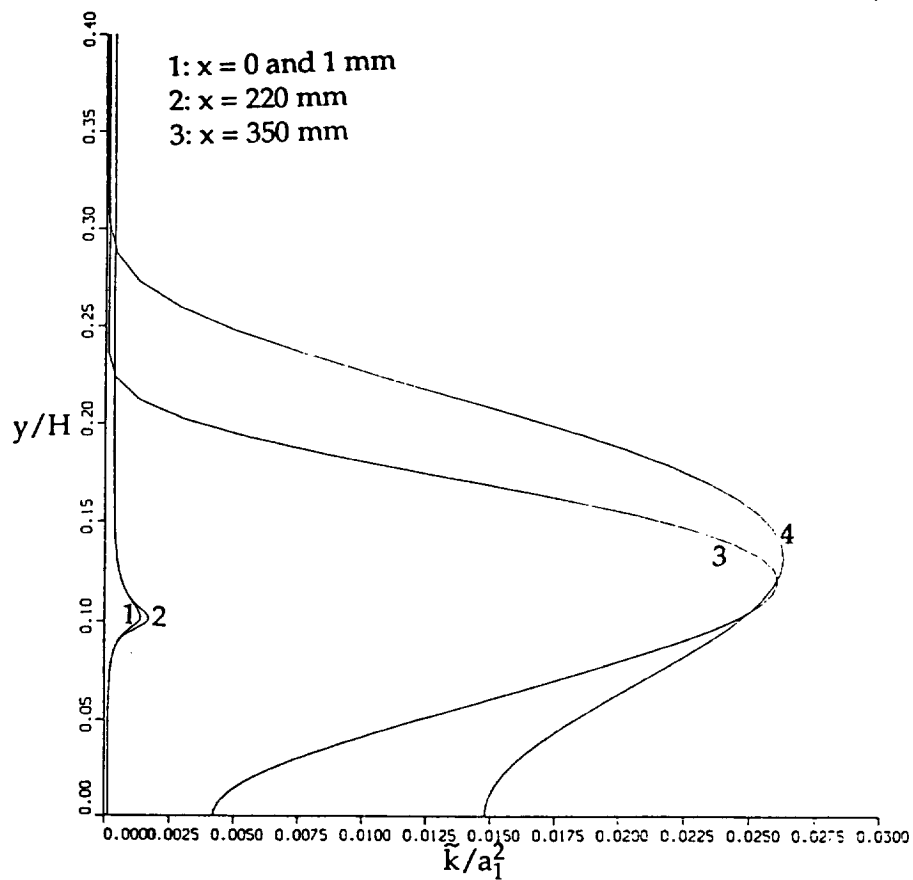


Figure 2.14d - Nondimensionalized turbulent kinetic energy profiles ($s = 2.44$, $r = 0.51$, and $M_{c1} = 0.55$, $k-\epsilon$ turbulence model used).

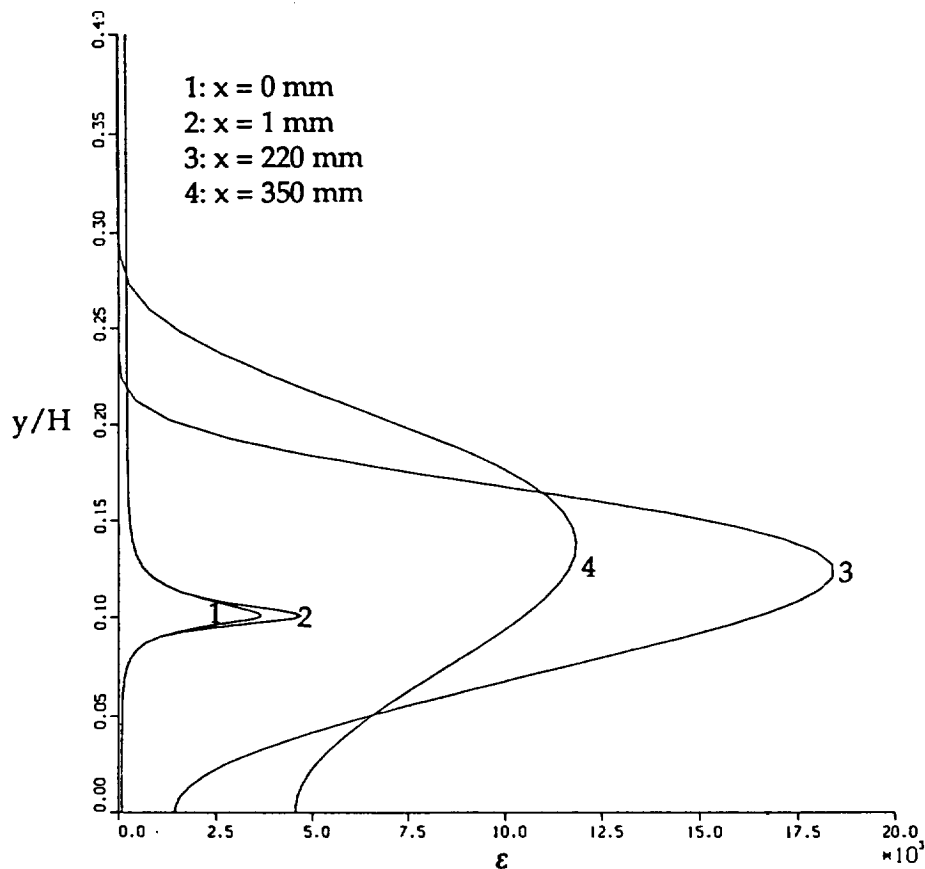


Figure 2.14e - Nondimensionalized turbulent kinetic energy dissipation rate ($s = 2.44$, $r = 0.51$, and $M_{c1} = 0.55$, $k-\epsilon$ turbulence model used).

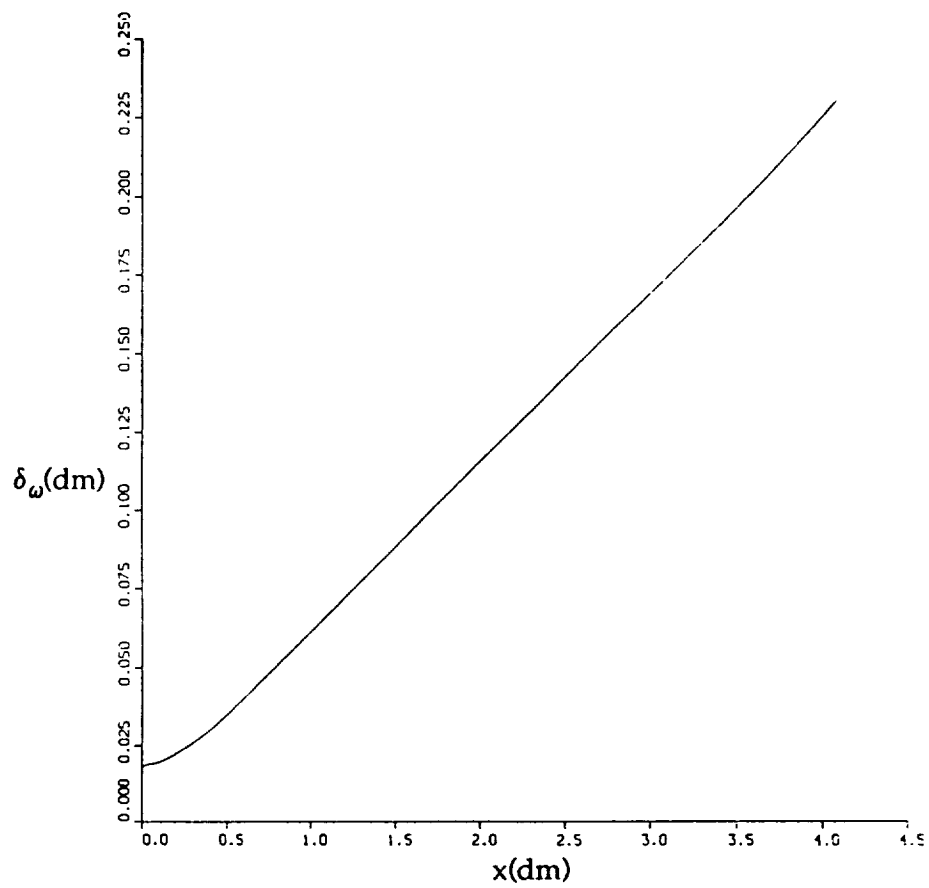


Figure 2.15 - Vorticity thickness growth
($s = 2.44$, $r = 0.51$, and $M_{c1} = 0.55$, $k-\epsilon$ turbulence model used).

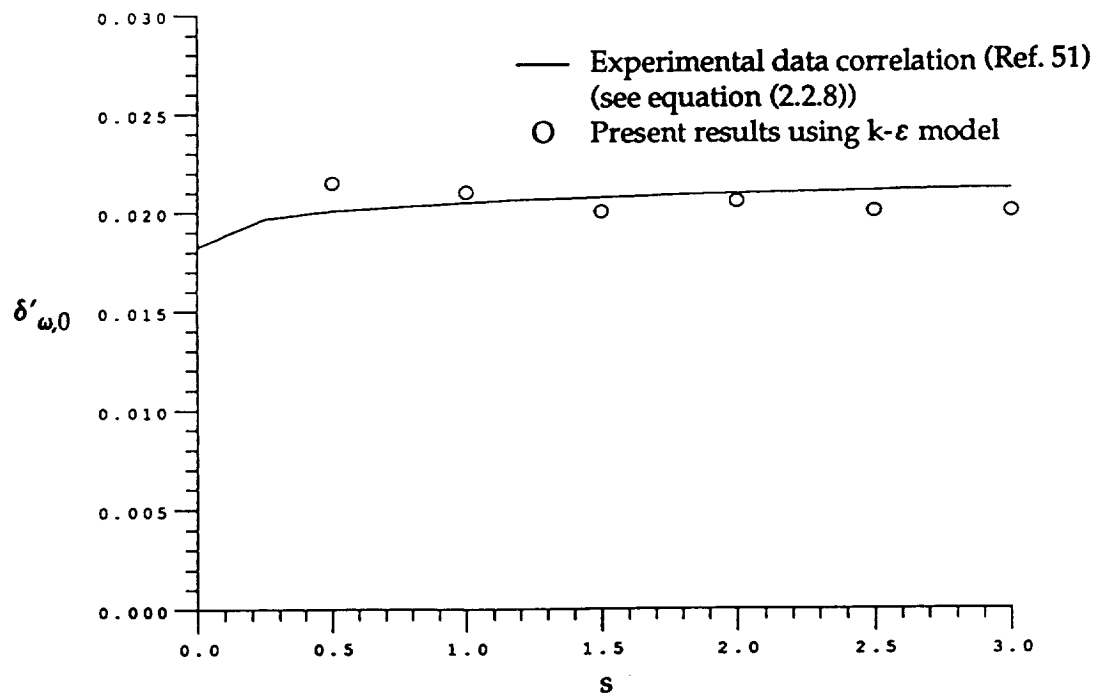


Figure 2.16 - Mixing layer spreading rate vs. density ratio at $r = 0.785$.

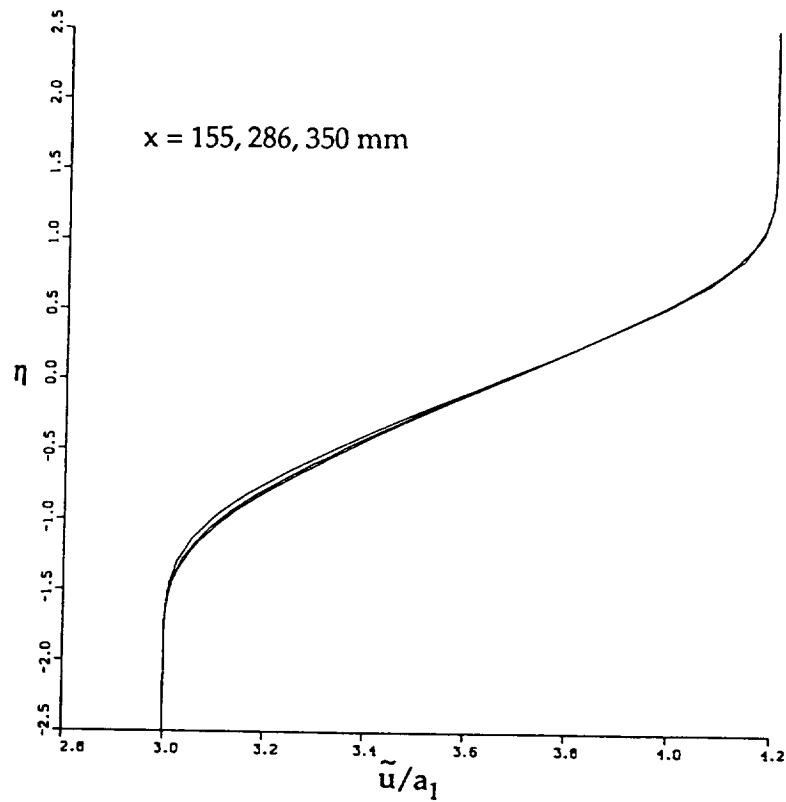


Figure 2.17 - Streamwise velocity profiles at several downstream locations ($s = 1$, $r = 0.714$, $M_c = 0.6$, $k-\epsilon$ turbulence model used).

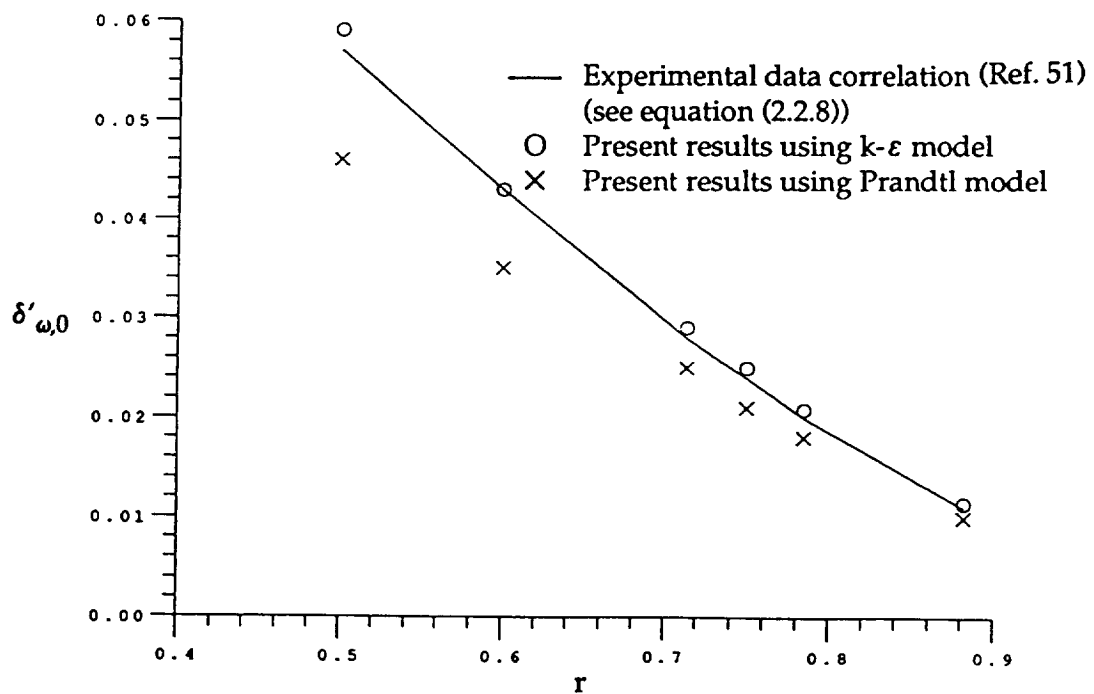


Figure 2.18 - Mixing layer spreading rate vs. velocity ratio at $s = 1$.

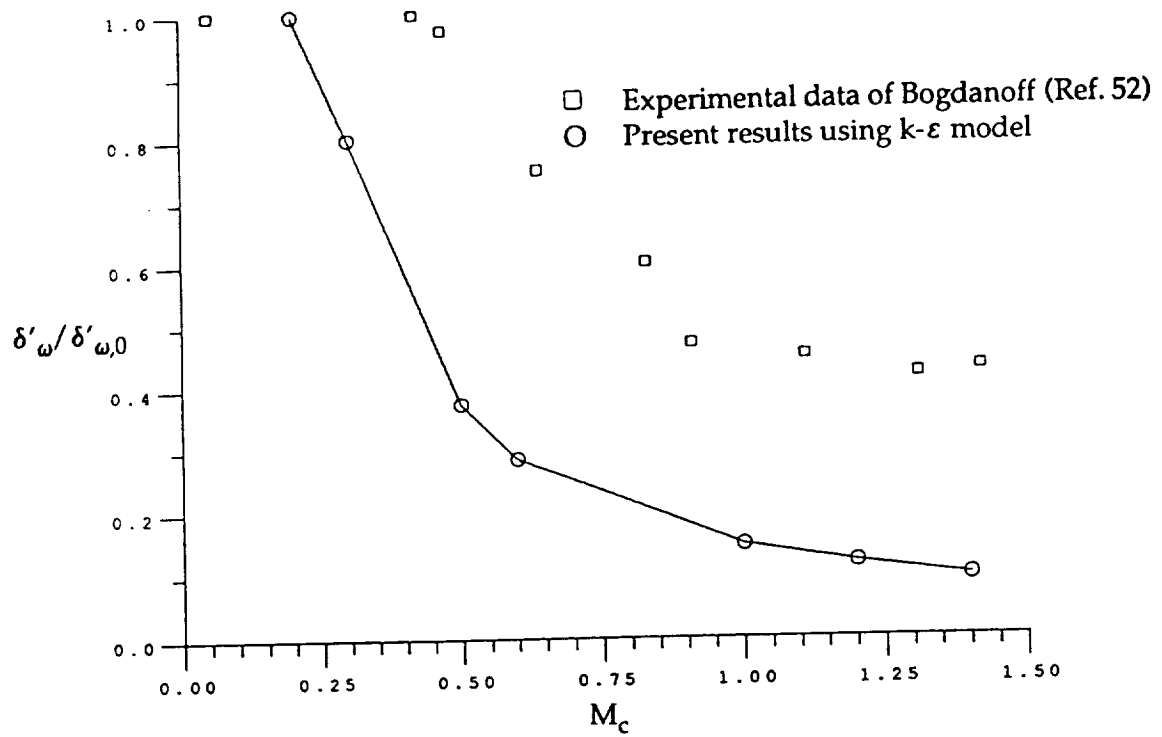


Figure 2.19 - Normalized vorticity growth rate vs. convective Mach number.

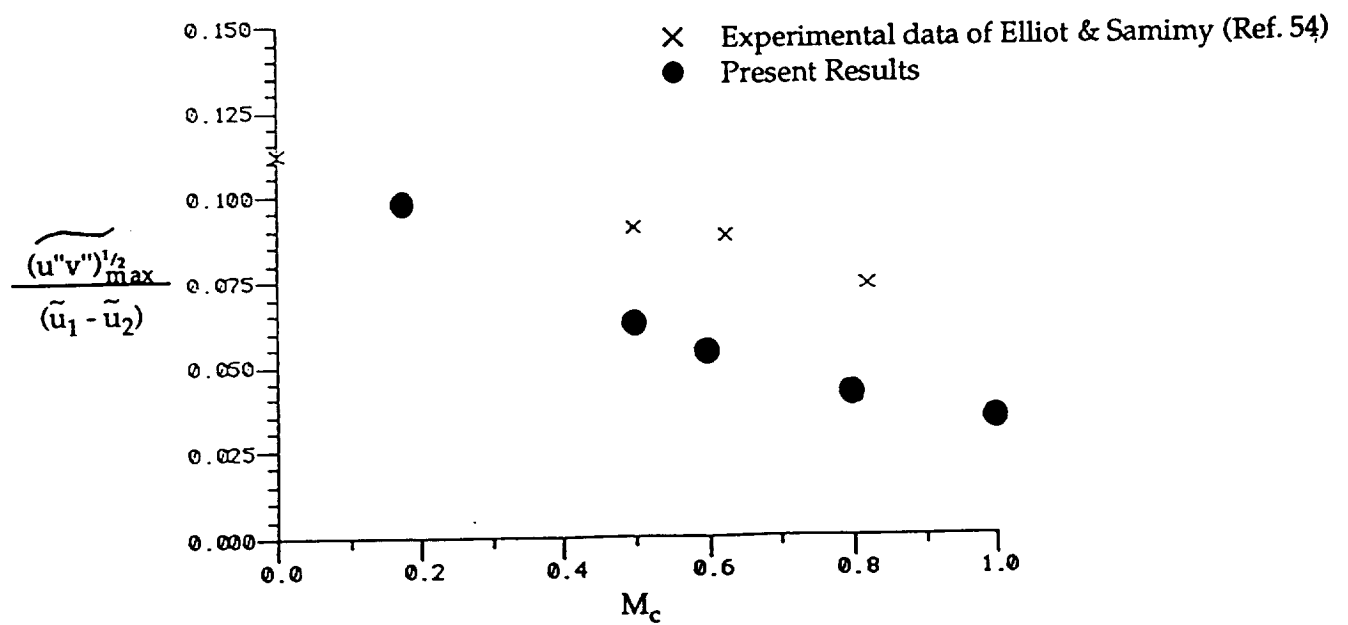


Figure 2.20 - Maximum turbulent shear stress intensity as a function of convective Mach number.

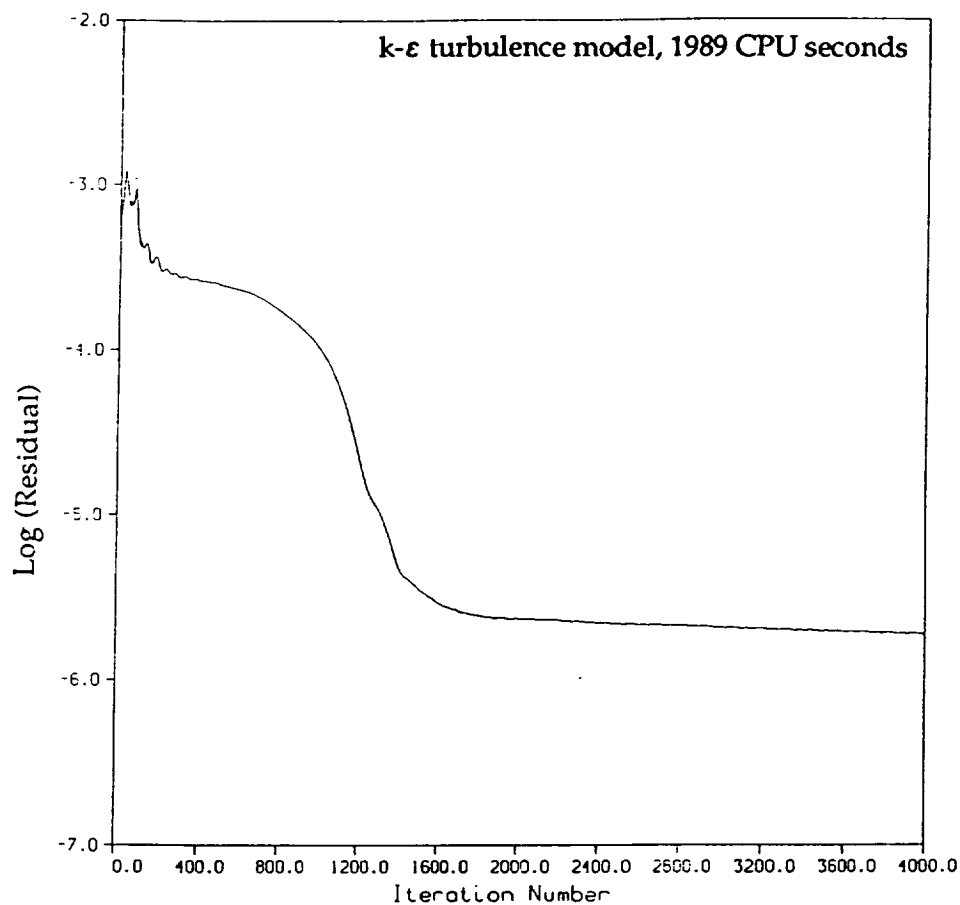


Figure 2.21 - Convergence history of nondimensionalized L_2 density residual (air/hydrogen, $s = 5.86$, $r = 0.51$, $M_{c1} = 0.517$).

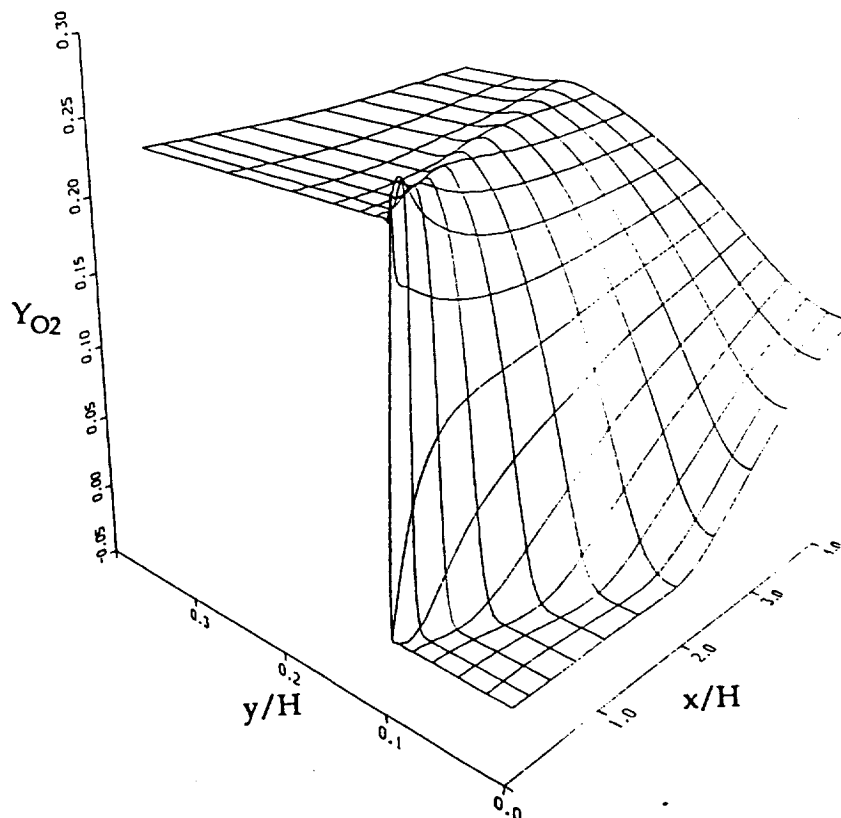


Figure 2.22a - Oxygen mass fraction variation in the solution domain (air/hydrogen, $s = 5.86$, $r = 0.51$, $M_{c1} = 0.517$, k- ϵ turbulence model used).

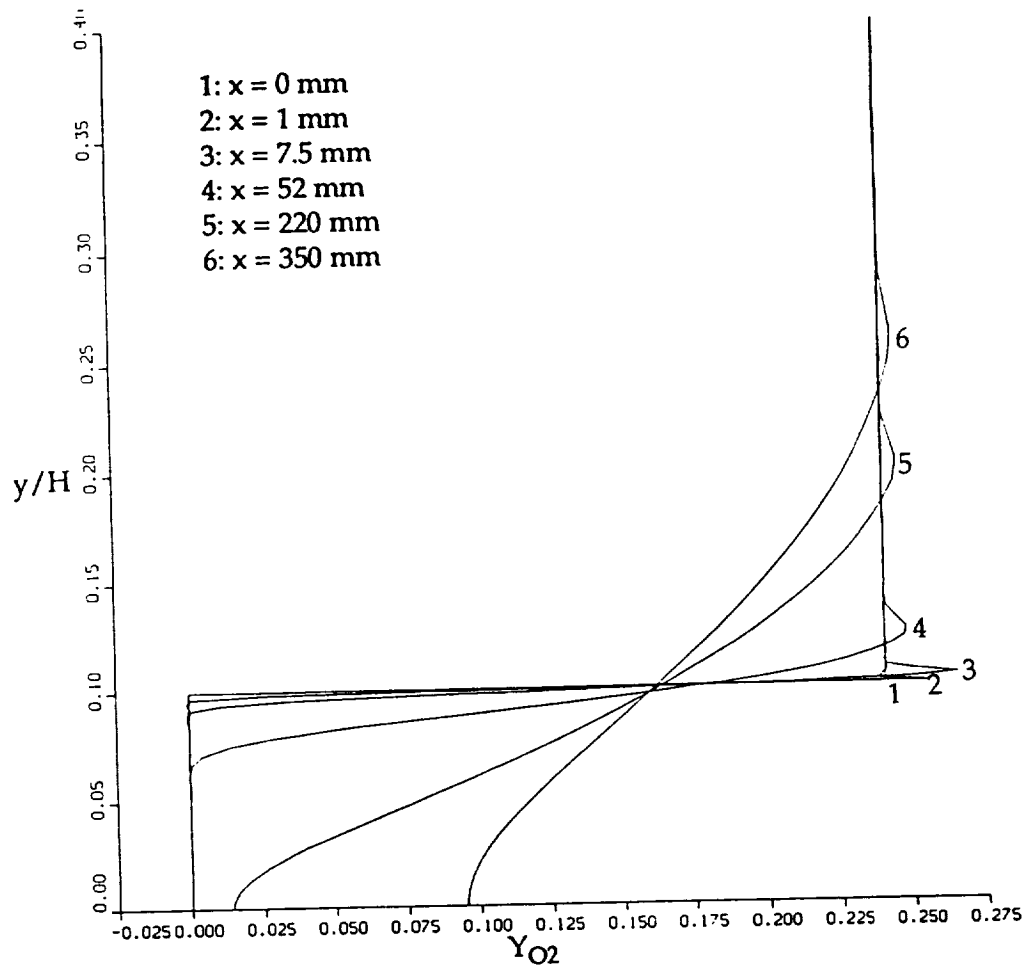


Figure 2.22b - Oxygen mass fraction profiles at several downstream locations (air/hydrogen, $s = 5.86$, $r = 0.51$, $M_{cl} = 0.517$, $k-\epsilon$ turbulence model used).

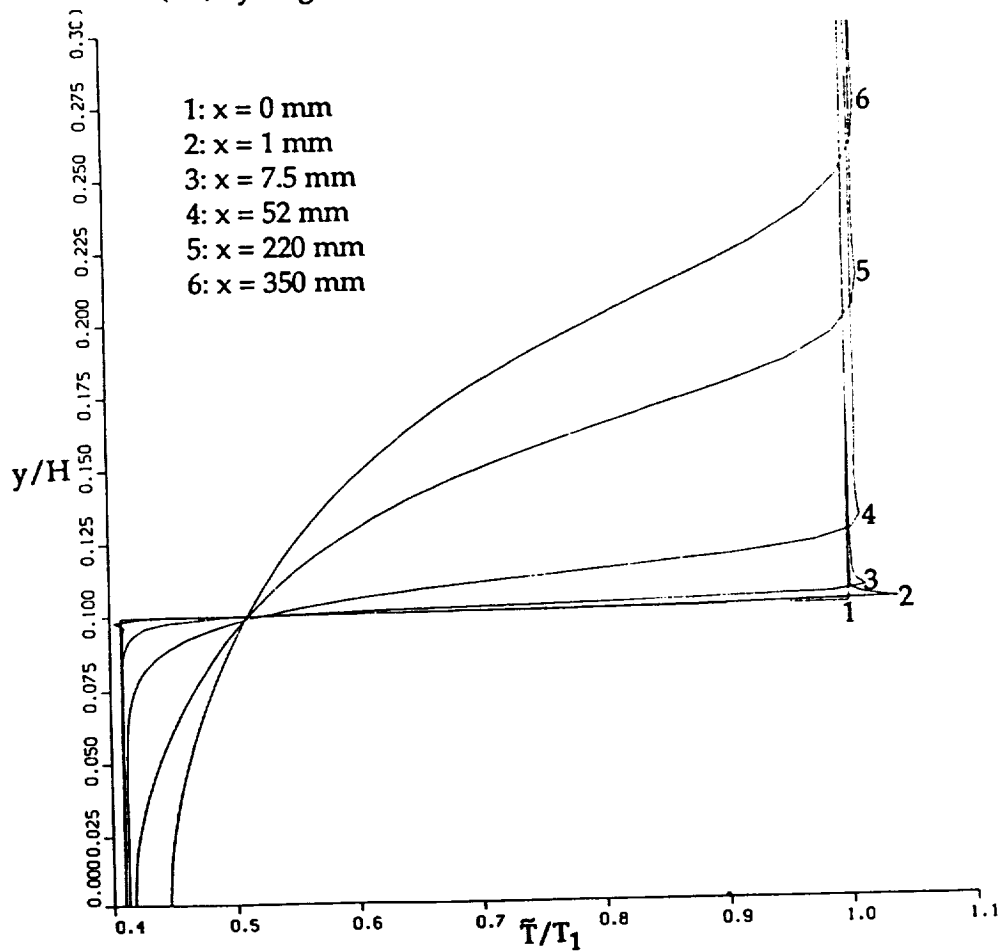


Figure 2.22c - Nondimensionalized temperature profiles at several downstream locations (air/hydrogen, $s = 5.86$, $r = 0.51$, $M_{cl} = 0.517$, $k-\epsilon$ turbulence model used).

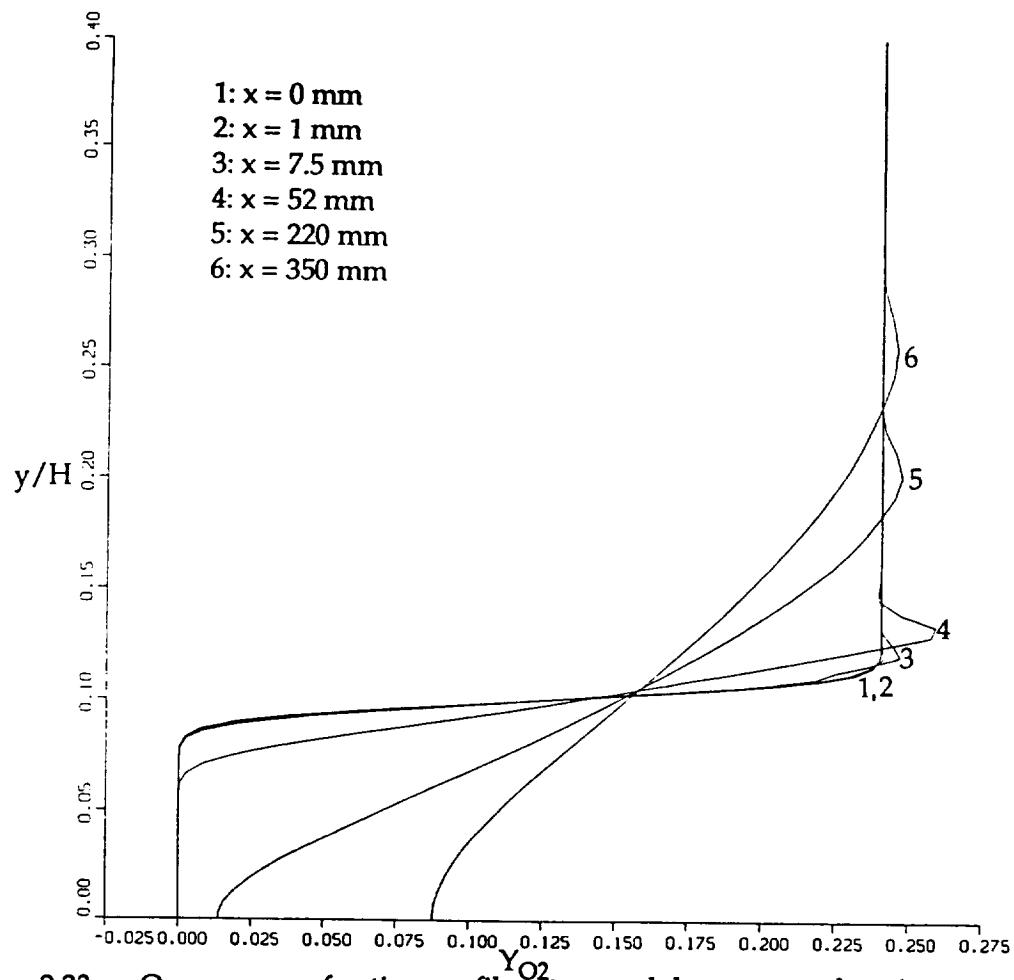


Figure 2.23a - Oxygen mass fraction profiles at several downstream locations. (smoothed inflow air/hydrogen, $s = 5.86$, $r = 0.51$, $M_{c1} = 0.517$, $k-\epsilon$ turbulence model used).

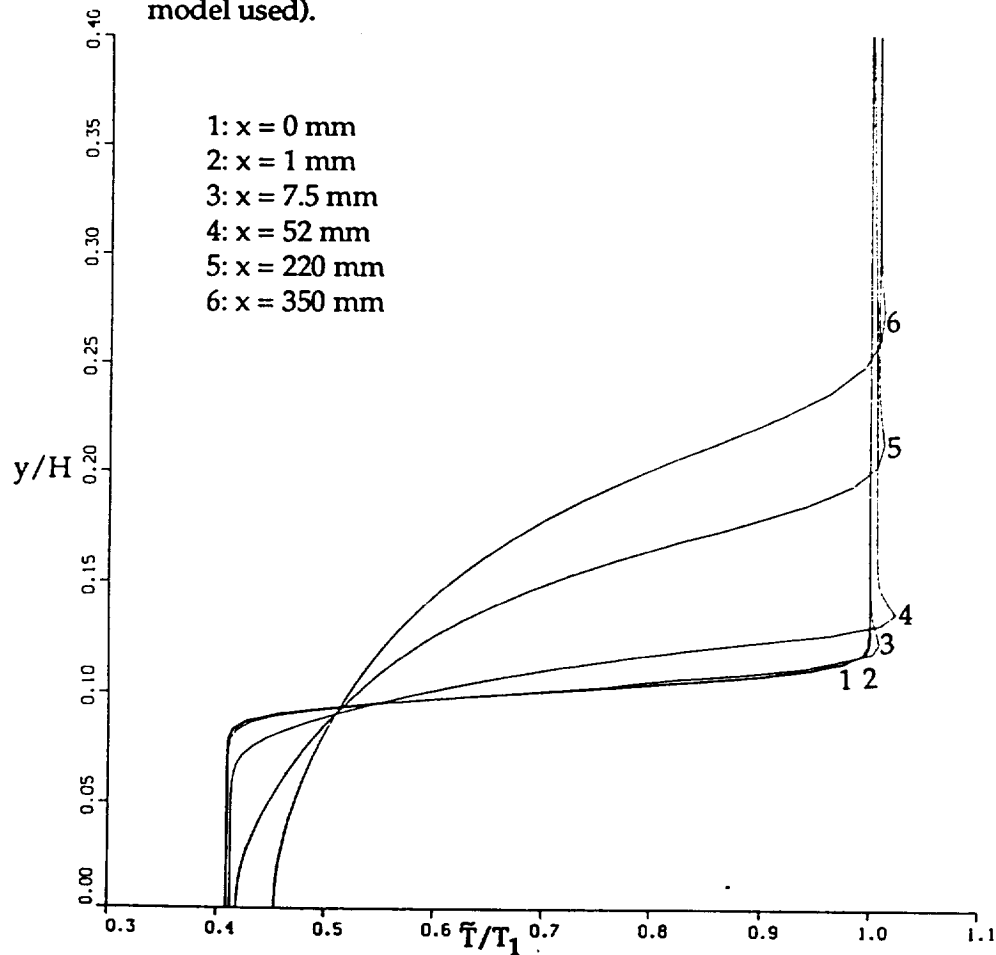


Figure 2.23b - Nondimensionalized temperature profiles at several downstream locations. (smoothed inflow air/hydrogen, $s = 5.86$, $r = 0.51$, $M_{c1} = 0.517$, $k-\epsilon$ turbulence model used).

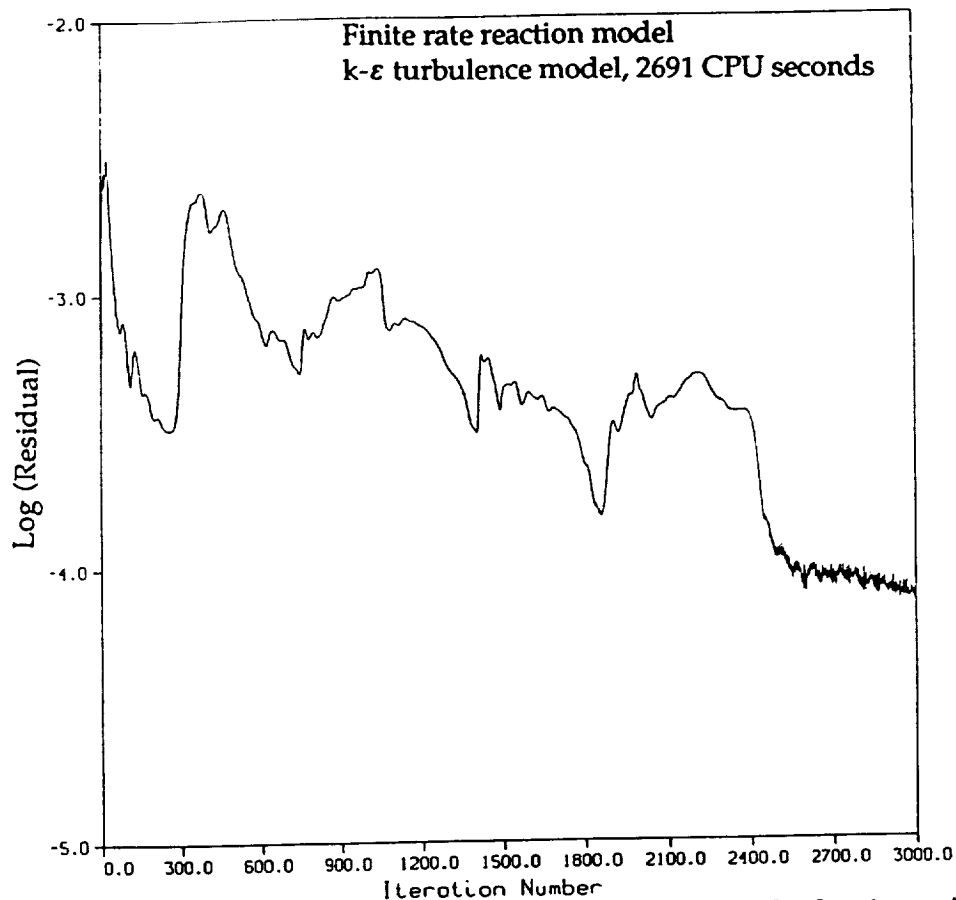


Figure 2.24a - Convergence history of nondimensionalized L_2 density residual (air/hydrogen reaction, $s = 3.0$, $r = 0.71$, $M_c = 0.27$).

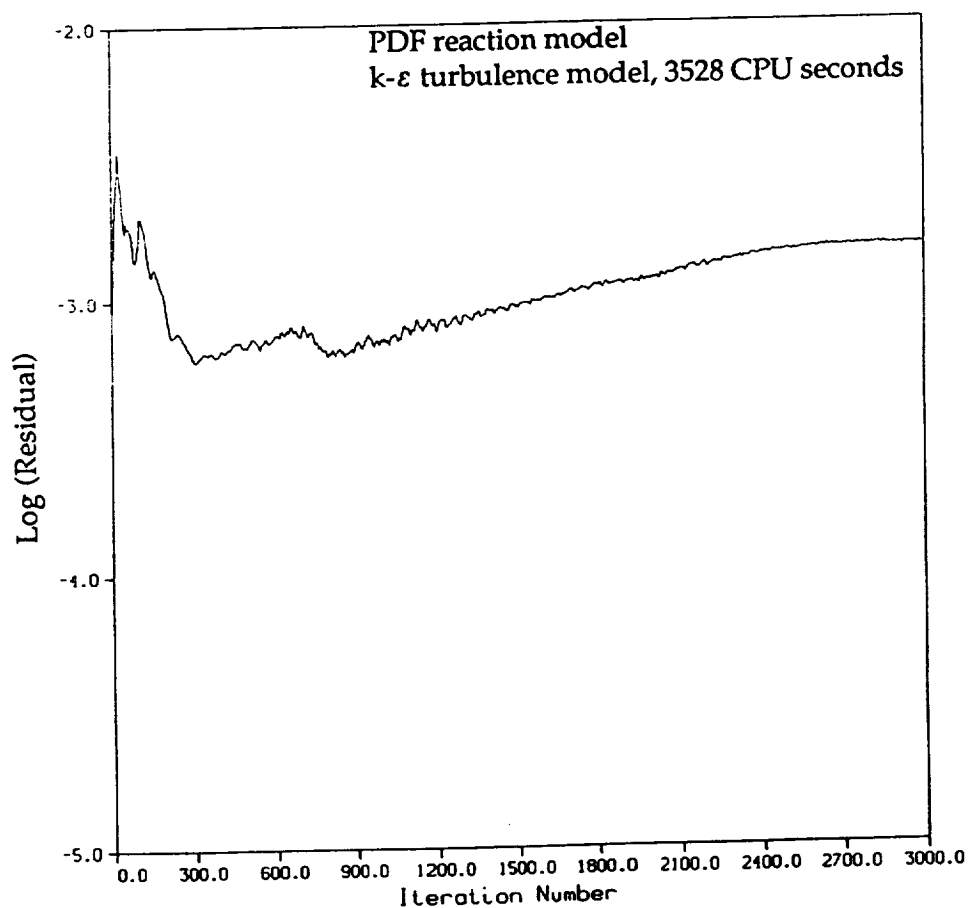


Figure 2.24b - Convergence history of nondimensionalized L_2 density residual (air/hydrogen reaction, $s = 3.0$, $r = 0.71$, $M_c = 0.27$).

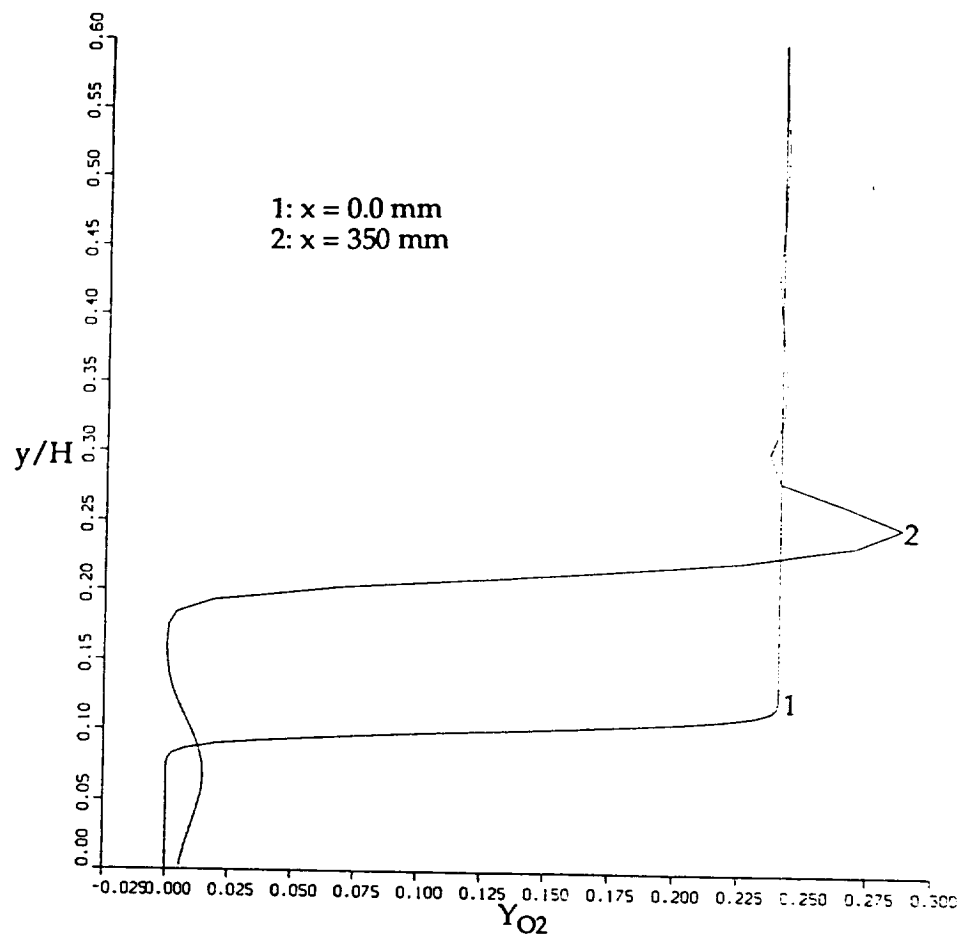


Figure 2.25a - Oxygen mass fraction profiles
(air/hydrogen reaction, $s = 3.0$, $r = 0.71$, $M_c = 0.27$, finite rate reaction model).

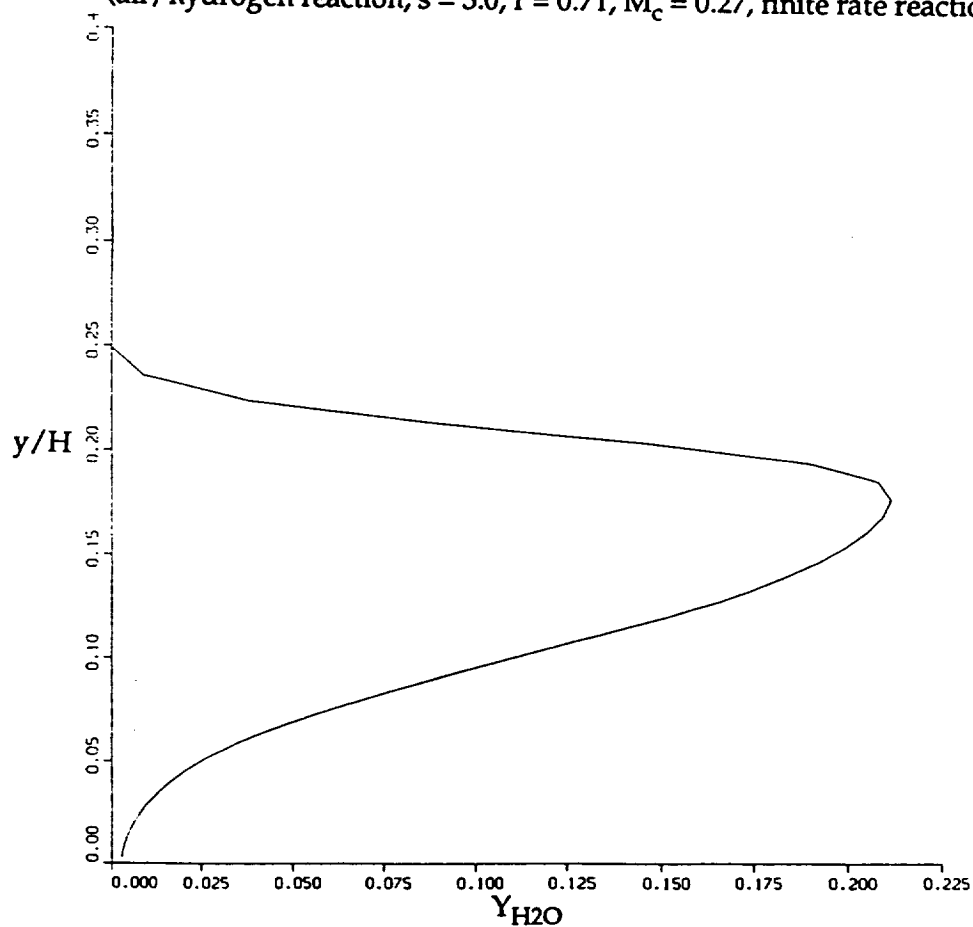


Figure 2.25b - Water mass fraction profile at $x = 350$ mm downstream
(air/hydrogen reaction, $s = 3.0$, $r = 0.71$, $M_c = 0.27$, finite rate reaction model).

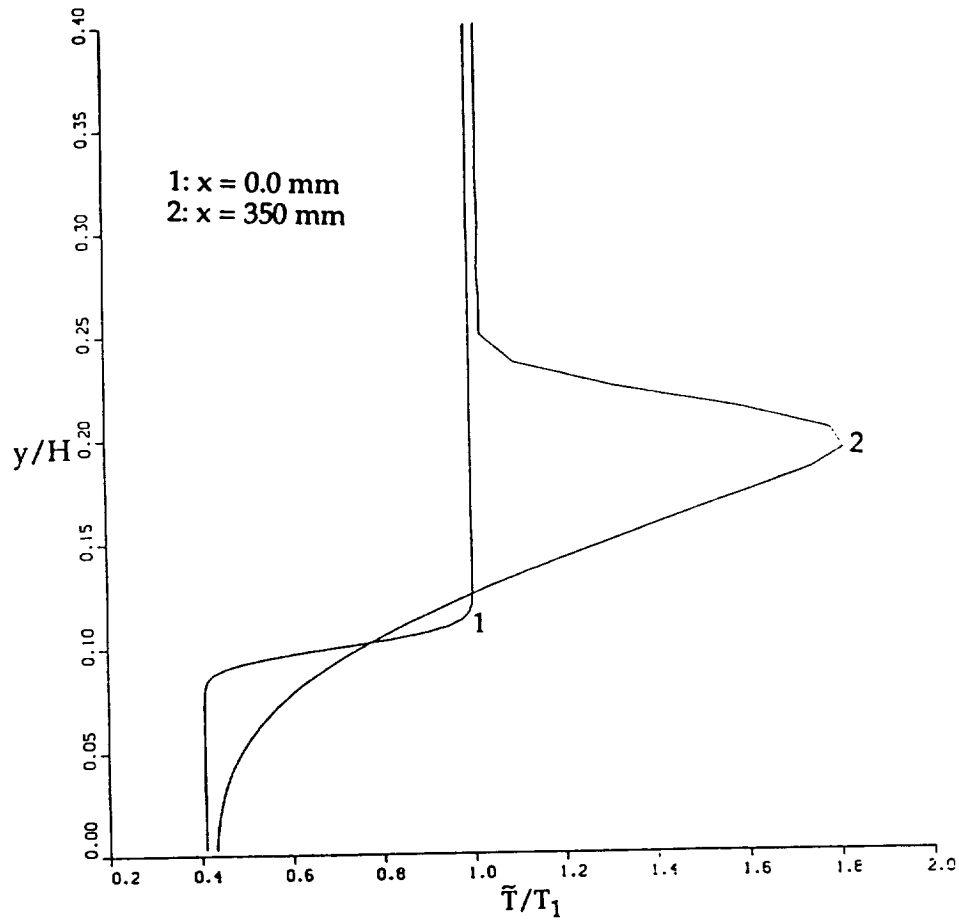


Figure 2.25c - Nondimensionalized mean temperature profiles
(air/hydrogen reaction, $s = 3.0$, $r = 0.71$, $M_c = 0.27$, finite reaction model).

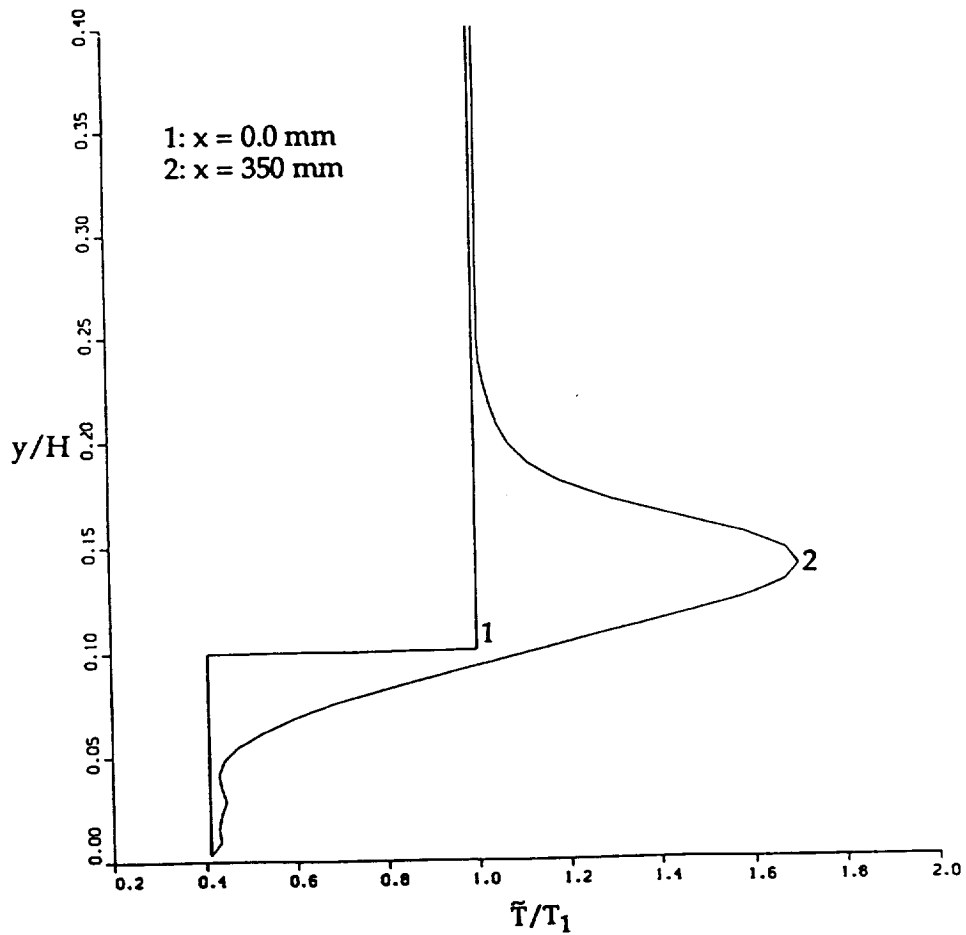


Figure 2.26a - Nondimensionalized mean temperature profiles
(air/hydrogen reaction, $s = 3.0$, $r = 0.71$, $M_c = 0.27$, PDF reaction model).

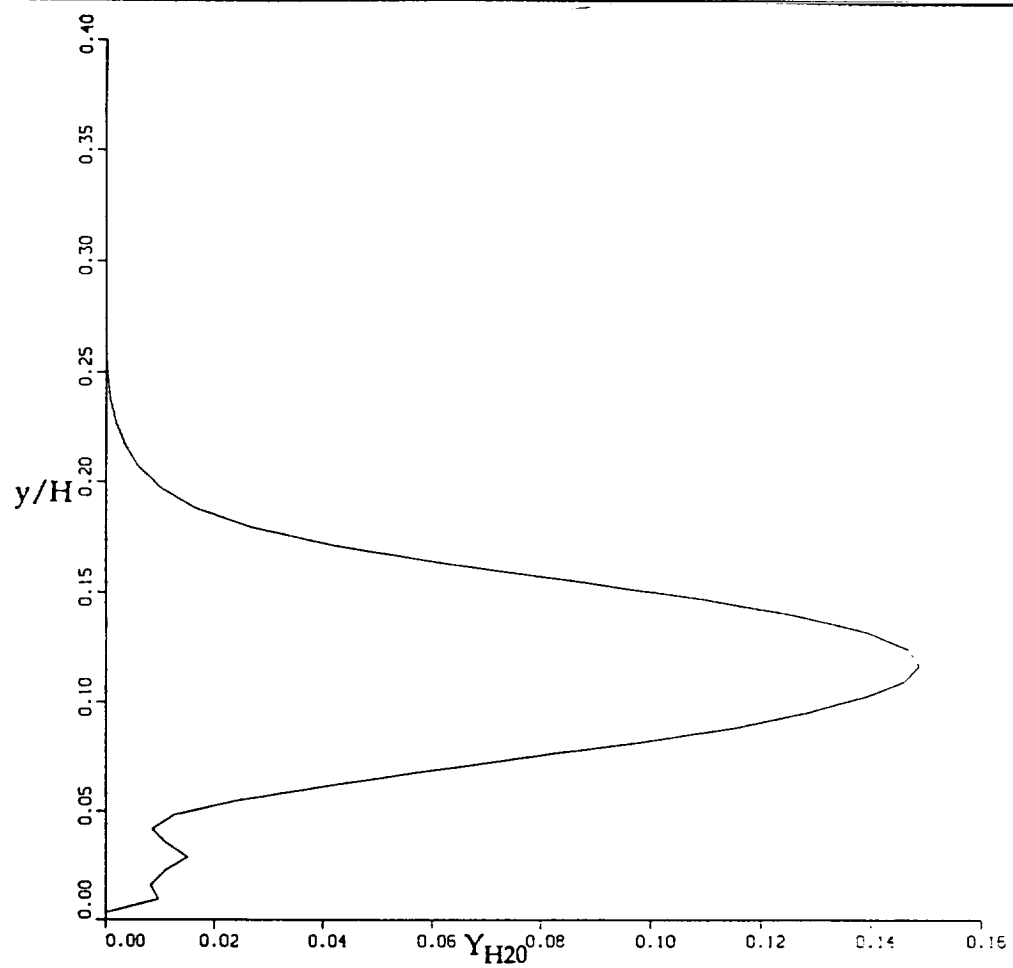


Figure 2.26b - Water mass fraction profile at $x = 350$ mm downstream.
(air/hydrogen reaction, $s = 3.0$, $r = 0.71$, $M_c = 0.27$, PDF reaction model).

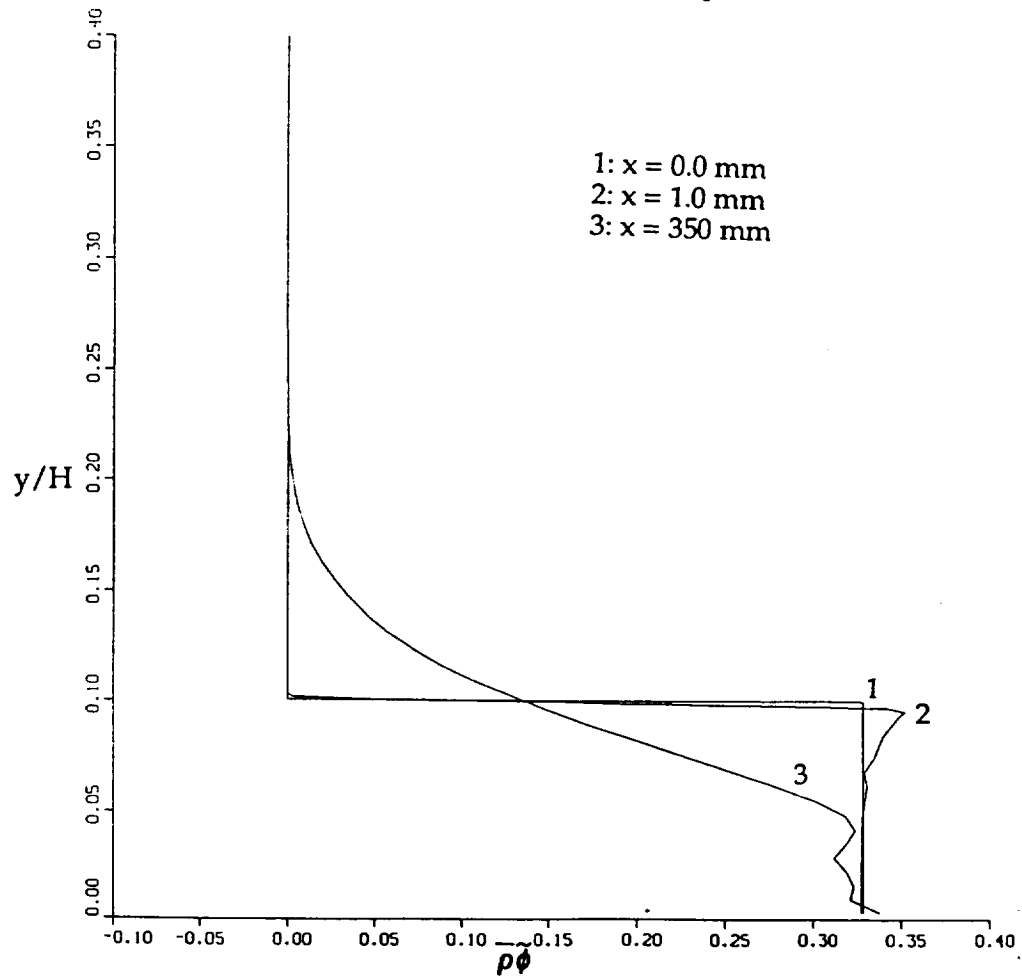


Figure 2.26c - Density-mixture fraction profiles
(air/hydrogen reaction, $s = 3.0$, $r = 0.71$, $M_c = 0.27$, PDF reaction model).

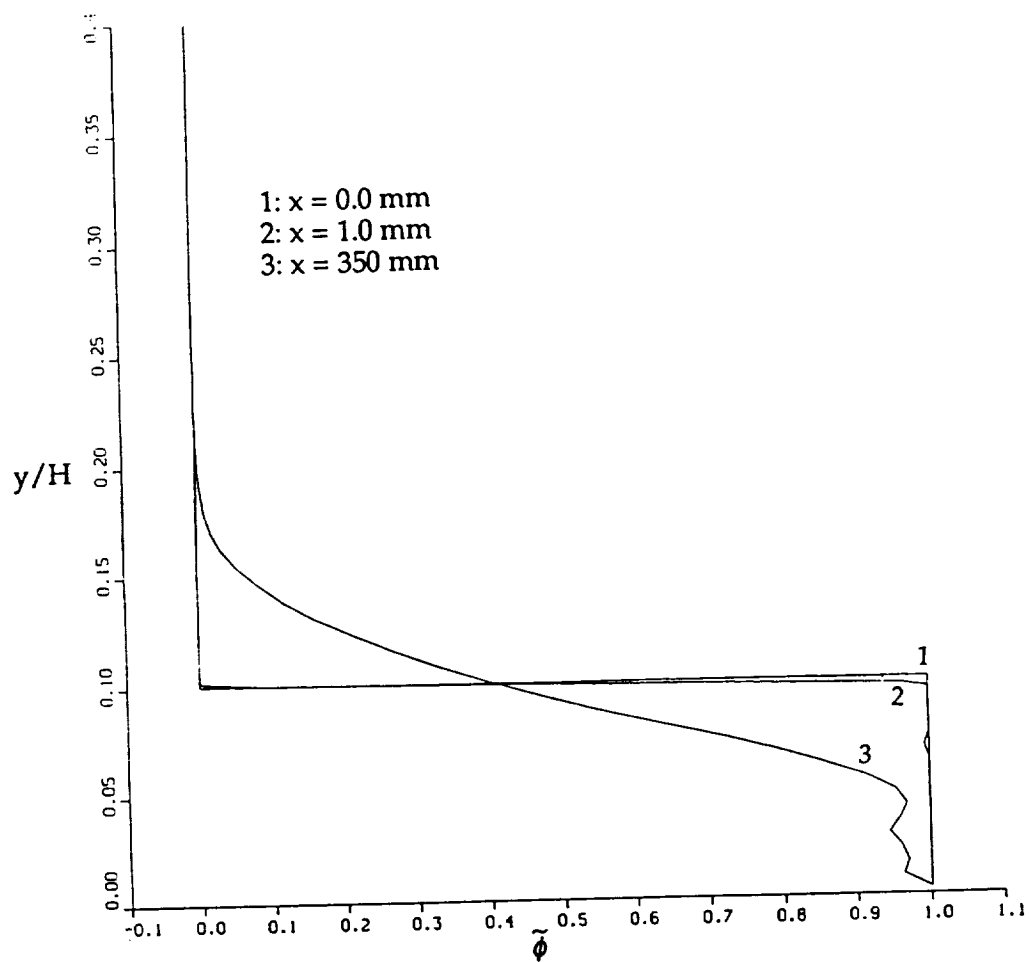


Figure 2.26d - Mixture fraction profiles
 (air/hydrogen reaction, $s = 3.0$, $r = 0.71$, $M_c = 0.27$, PDF reaction model).

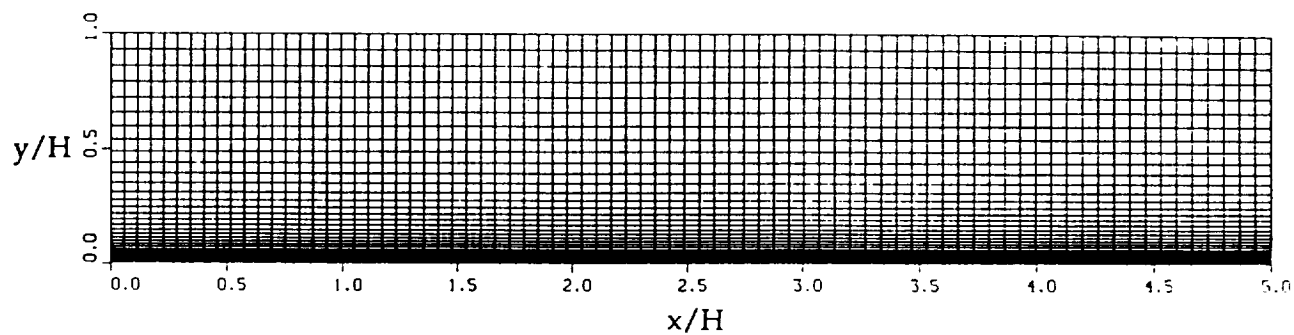


Figure 2.27a - 80 x 55 stretched grid
(Flatplate with $M_\infty = 3.0$ and $Re_\infty = 2.5 \times 10^6$).

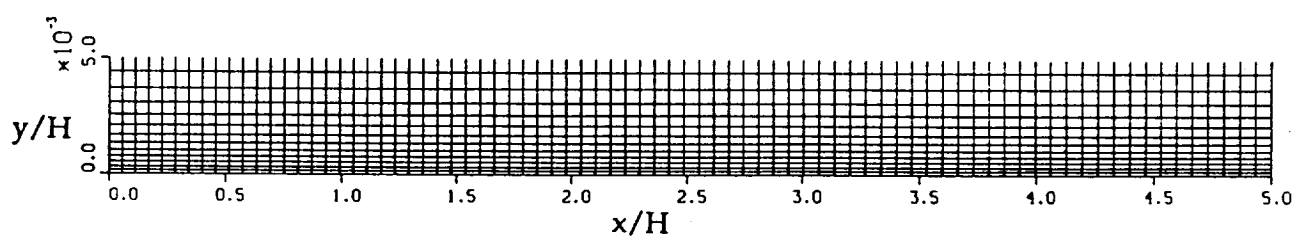


Figure 2.27b - Near wall magnification of the 80 x 55 stretched grid
(Flatplate with $M_\infty = 3.0$ and $Re_\infty = 2.5 \times 10^6$).

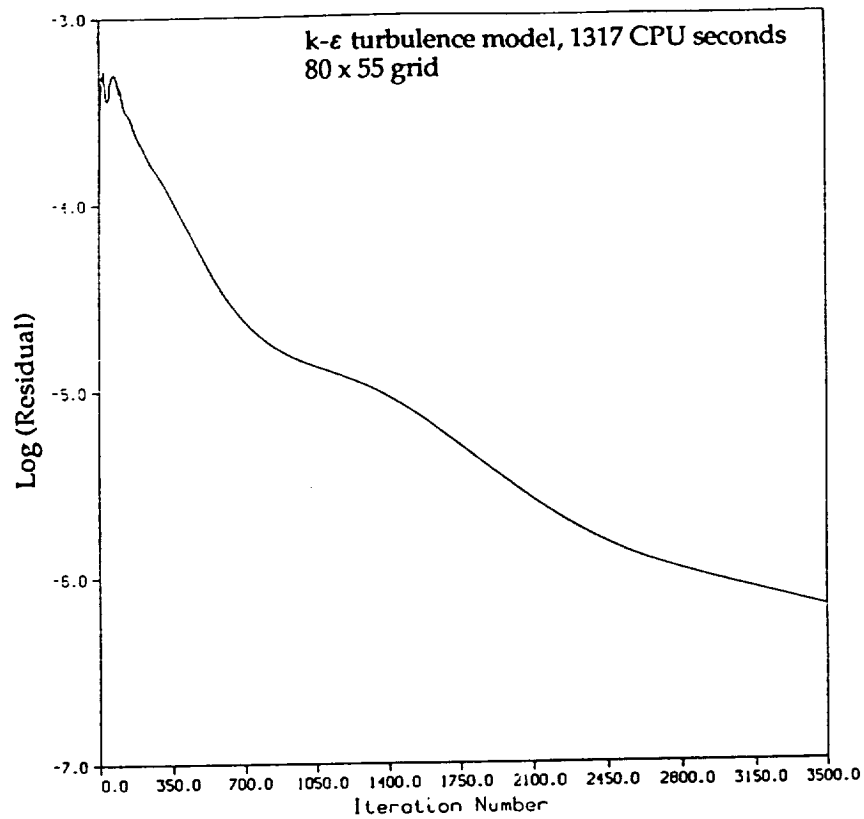


Figure 2.28 - Convergence history of nondimensional L_2 density residual (Flatplate with $M_\infty = 3.0$ and $Re_\infty = 2.5 \times 10^6$).

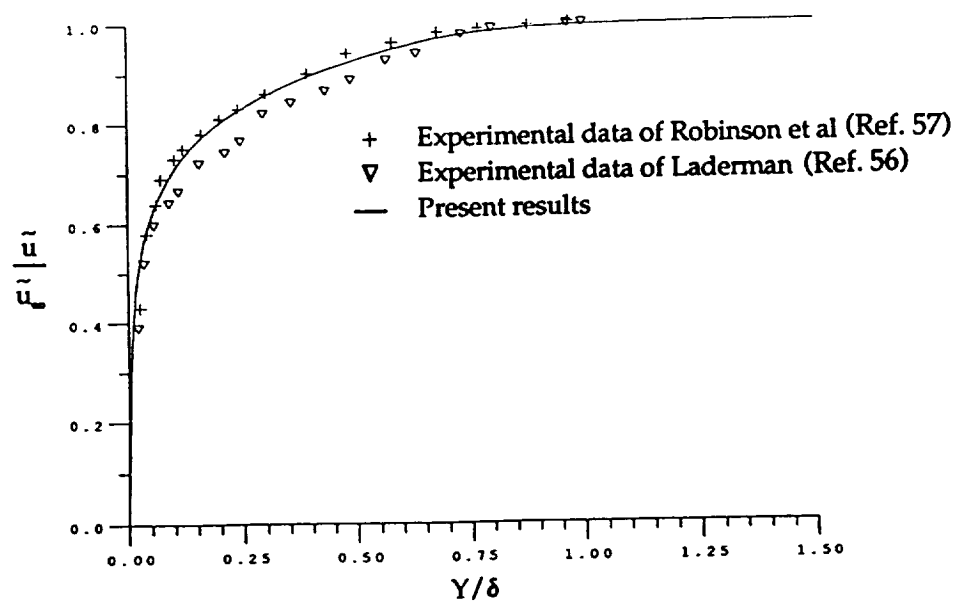


Figure 2.29 - Flat plate mean streamwise velocity profile at $M_\infty = 3$.

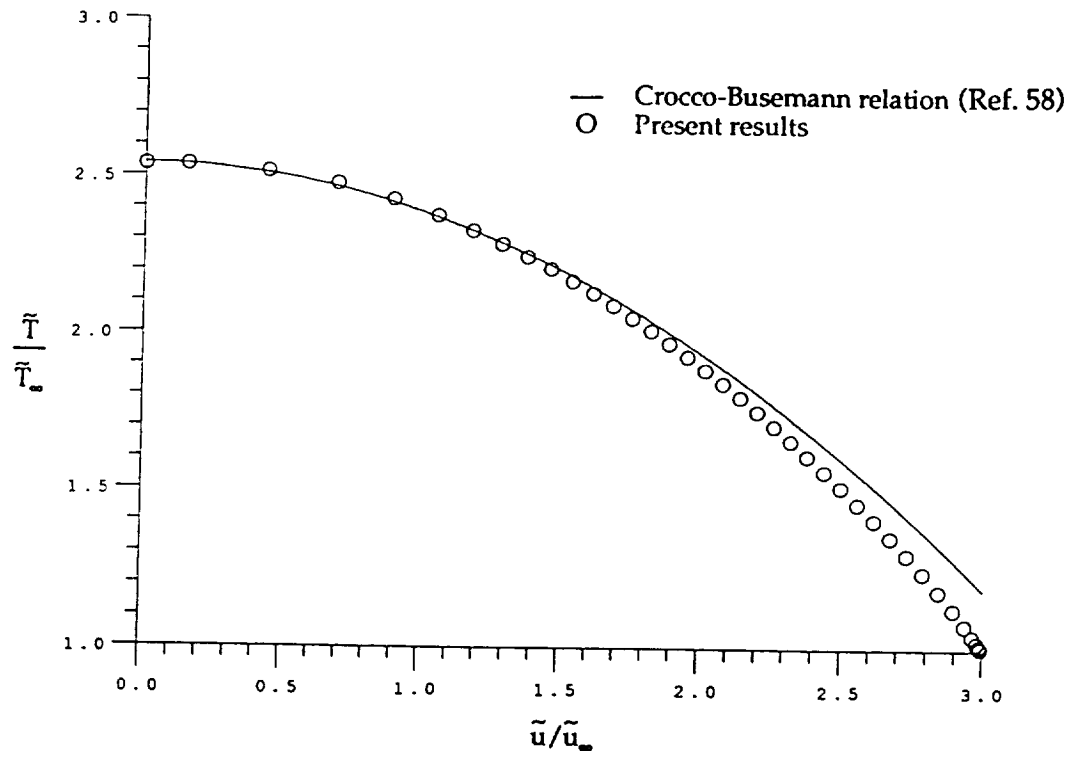


Figure 2.30 - Mean temperature-velocity relation in a Mach 3 boundary layer.

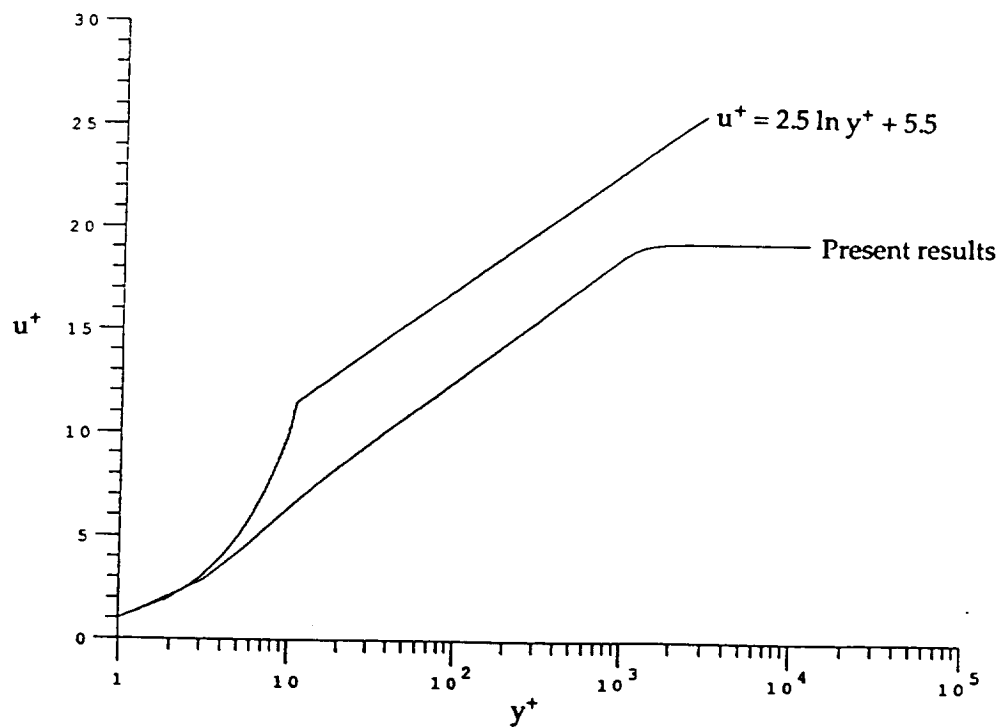


Figure 2.31 - Streamwise velocity profile for Mach 3 boundary layer

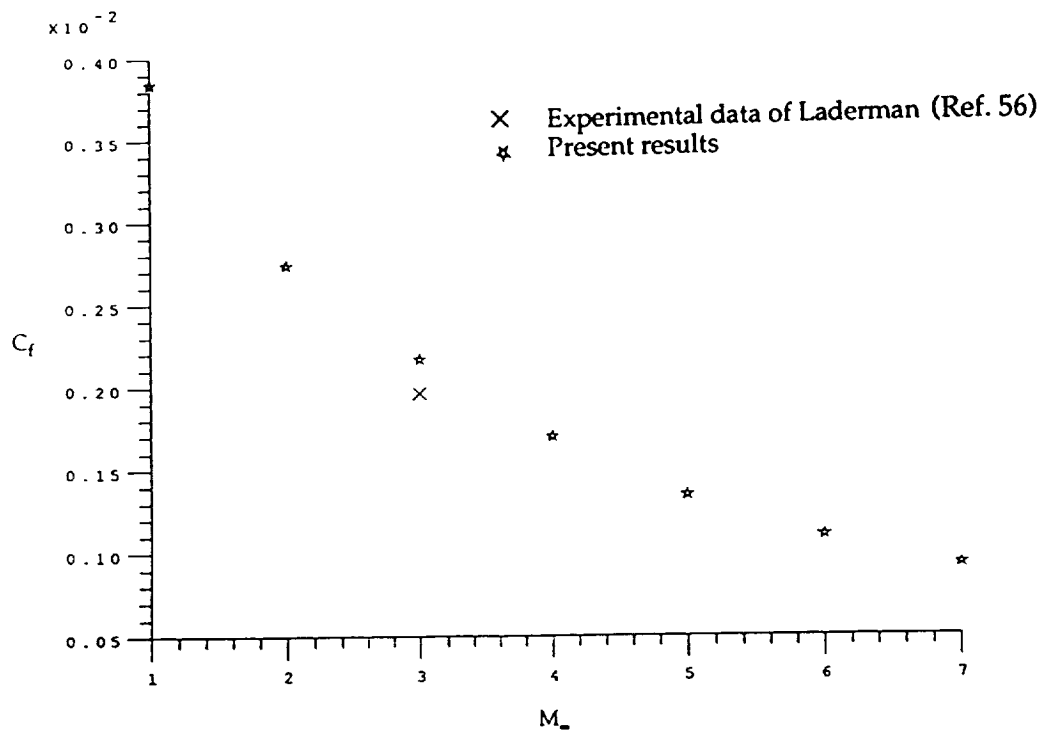


Figure 2.32a- Wall skin friction as a function of Mach number at $R_{ex} \sim 10^7$.

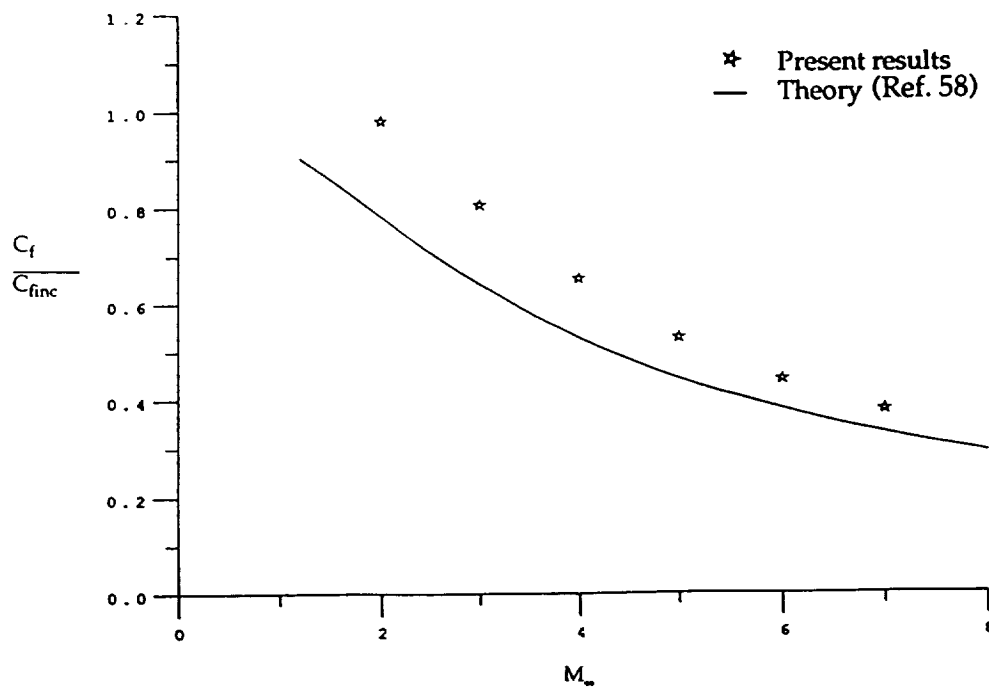


Figure 2.32b - Normalized skin friction as a function of Mach number at $R_{ex} \sim 10^7$.

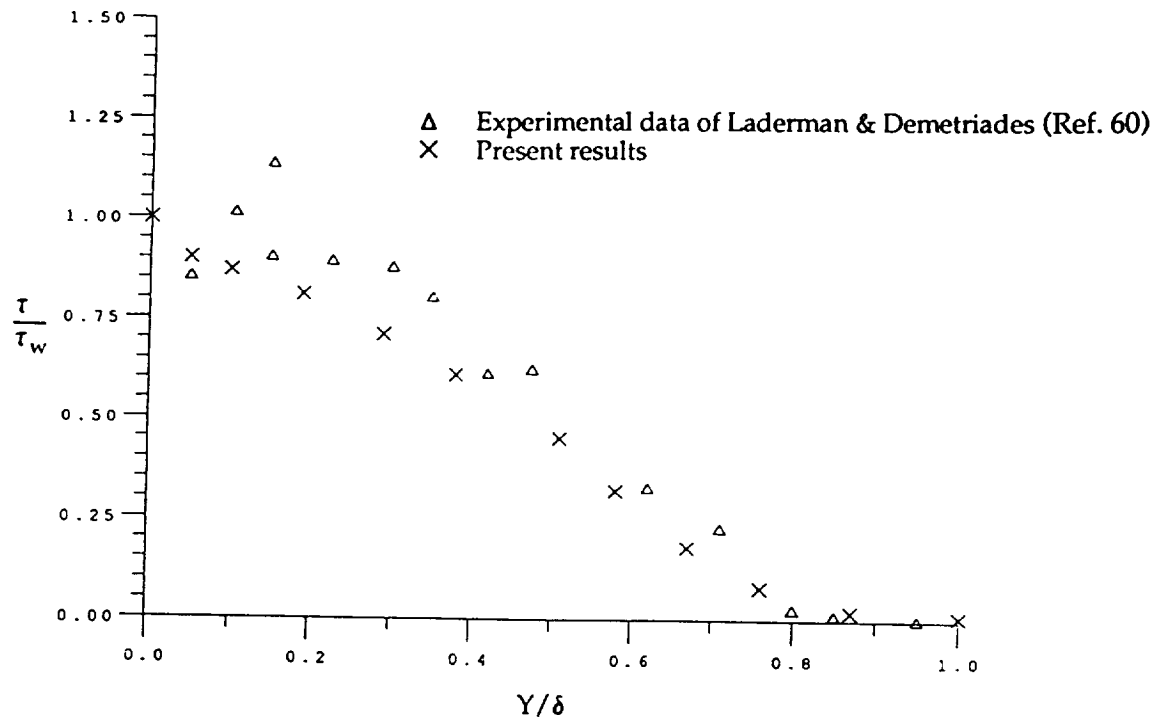


Figure 2.33a - Turbulent shear stress distributions
(Flat plate, $M_\infty = 3$, $R_{ex} = 10^7$).

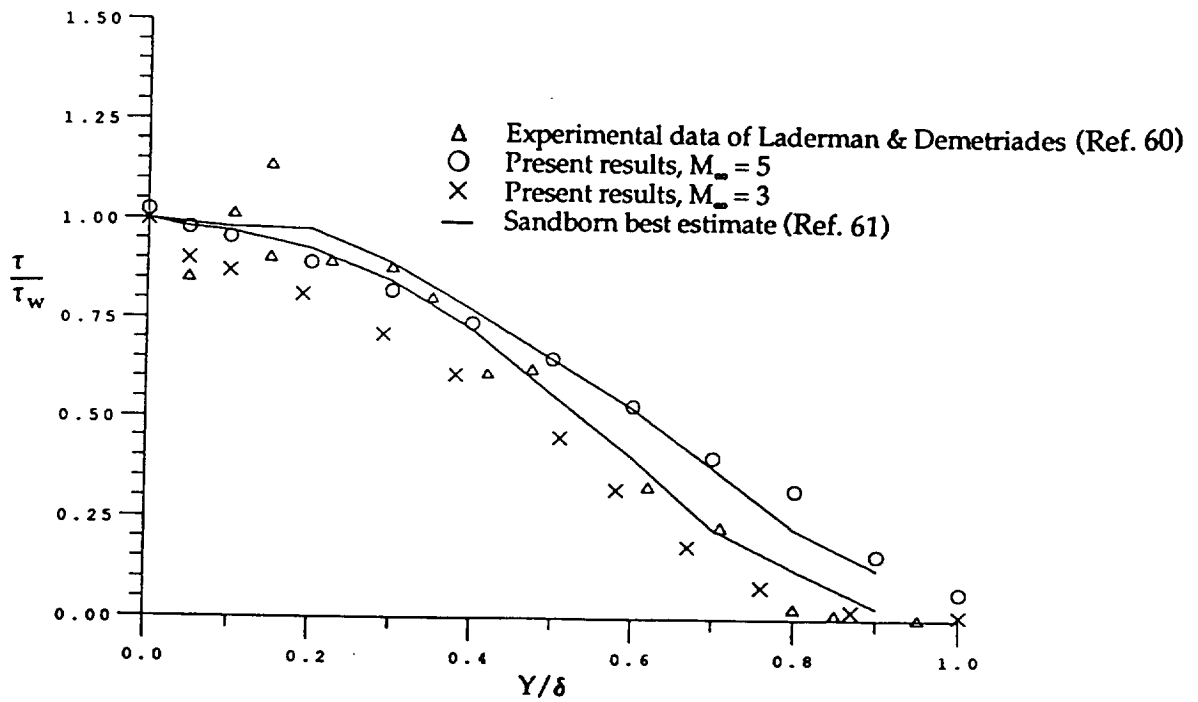


Figure 2.33b - Turbulent shear stress distributions

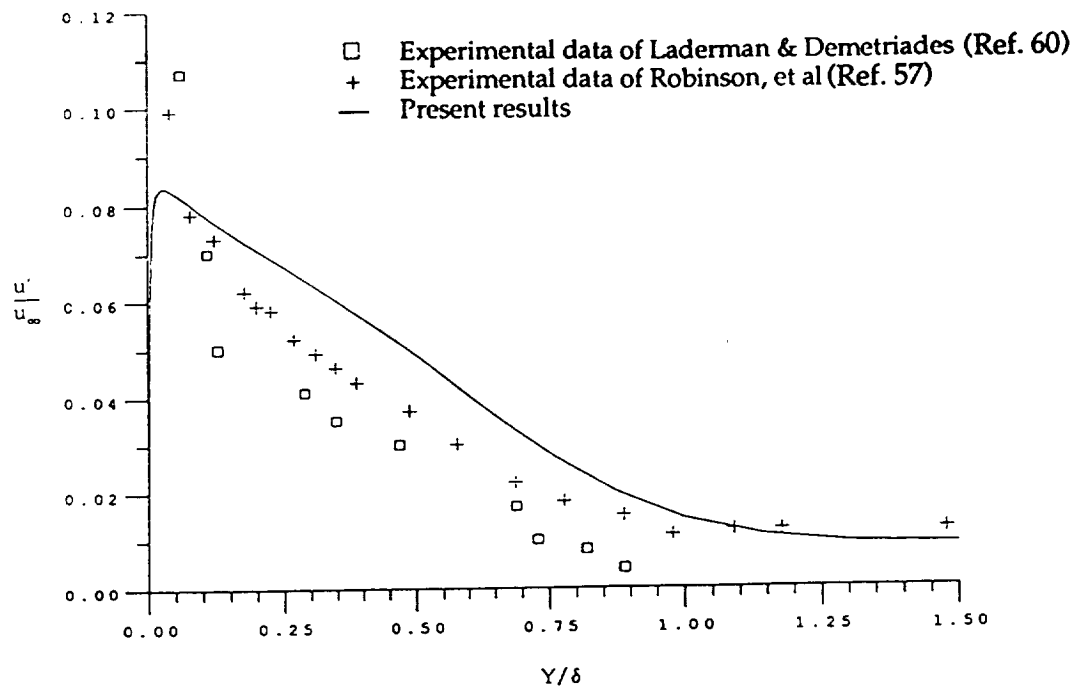


Figure 2.34a - Streamwise velocity fluctuations in a Mach 3 boundary layer.

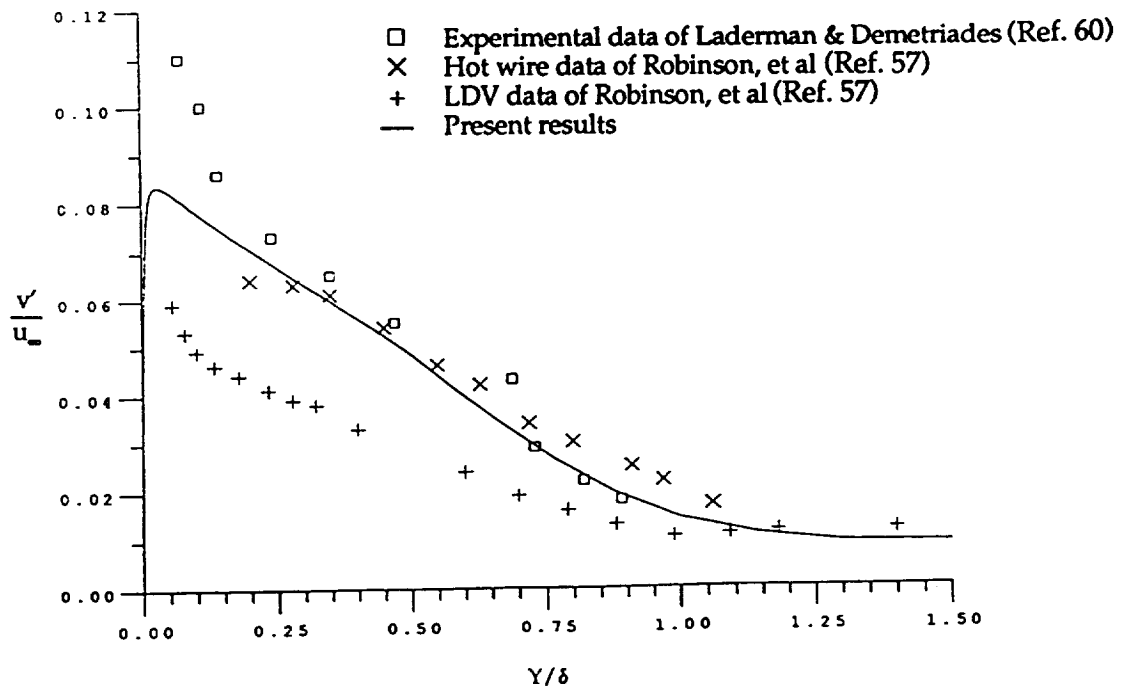


Figure 2.34b - Transverse velocity fluctuations in a Mach 3 boundary layer.

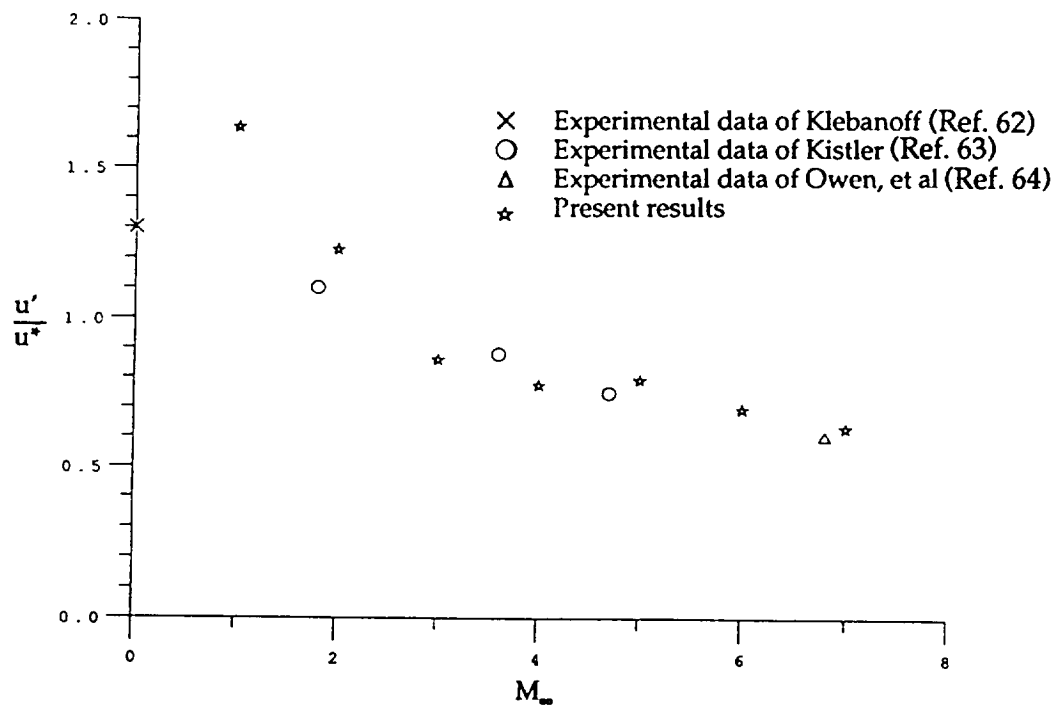


Figure 2.35a - Normalized streamwise velocity fluctuations at $Y/\delta = 0.5$ as a function of Mach number.

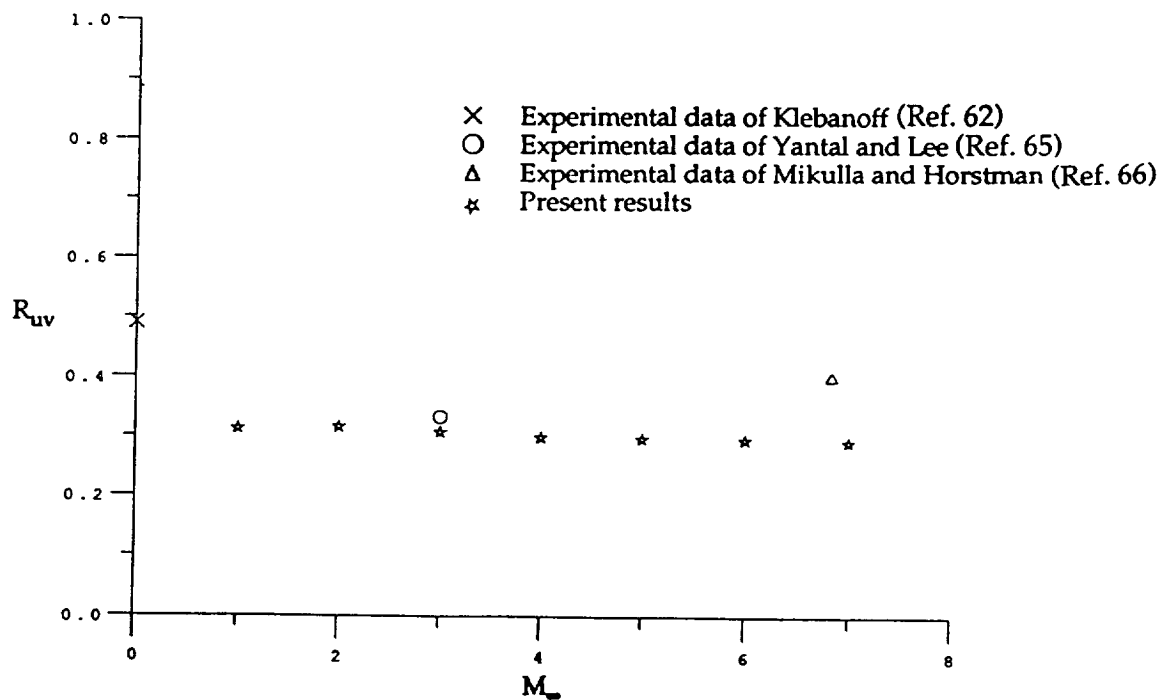


Figure 2.35b - Reynolds stress correlation coefficients at $y/\delta = 0.5$ as a function of Mach number.

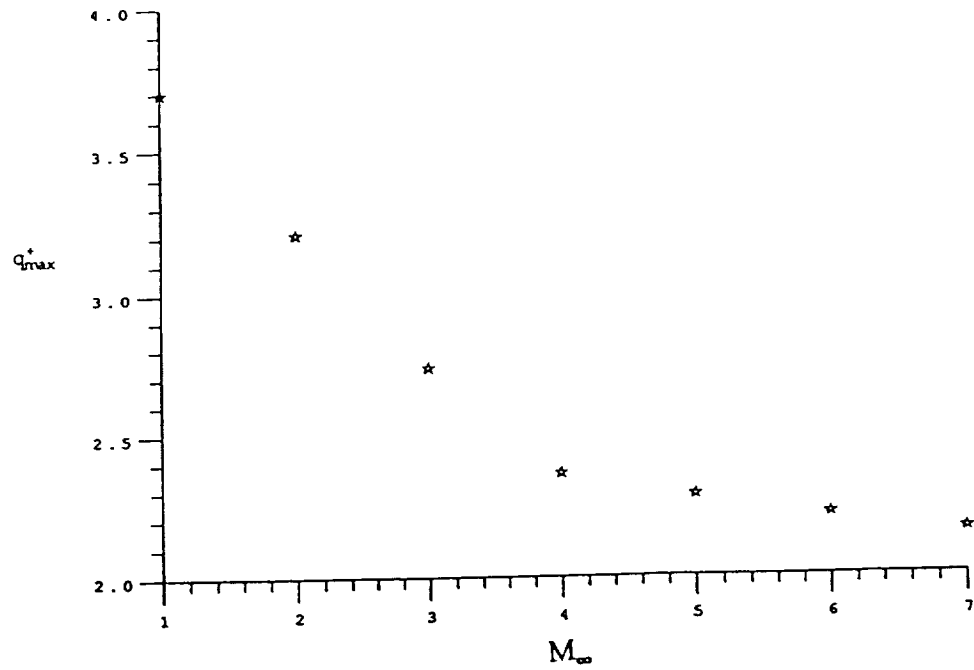


Figure 2.36a - Peak value of normalized turbulent kinetic energy as a function of Mach number.

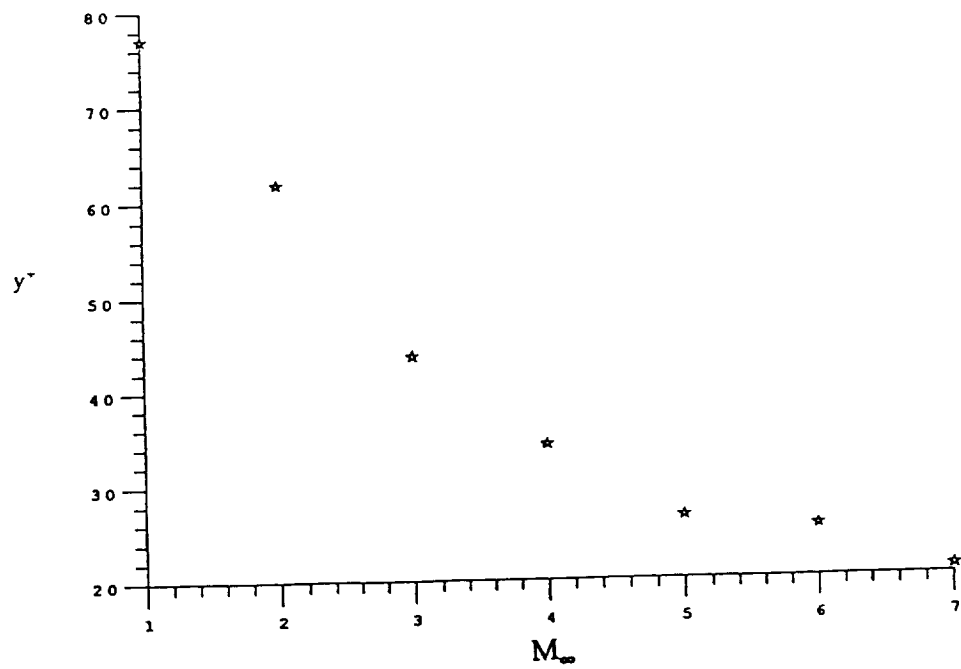


Figure 2.36b - y^+ at q_{\max}^+ as a function of Mach number.

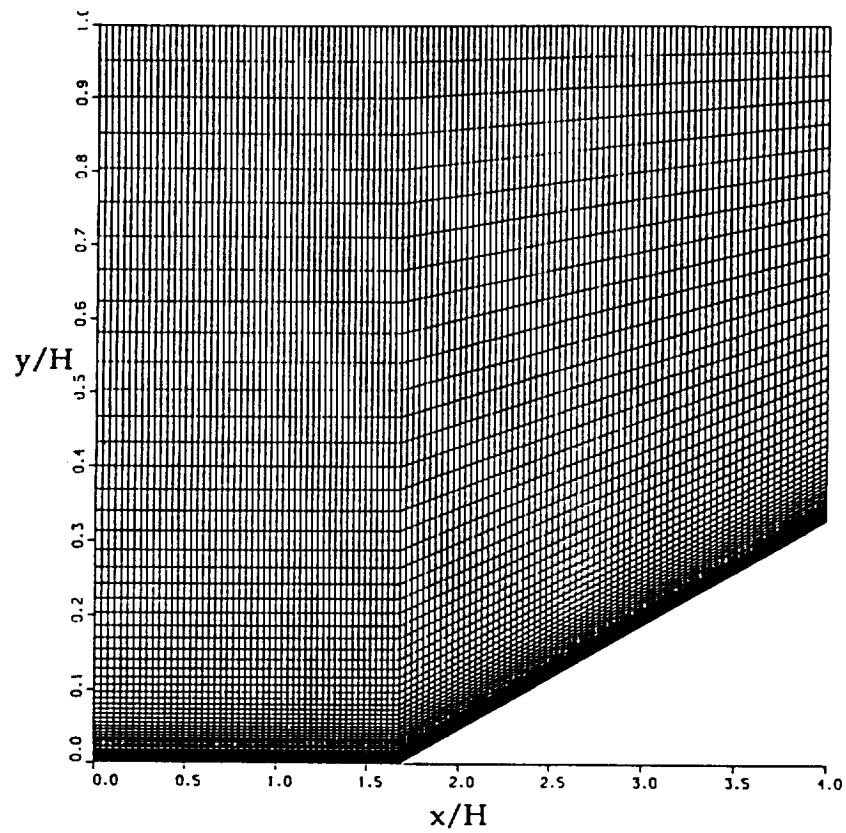


Figure 2.37 - 121 x 101 stretched grid for 8° ramp.

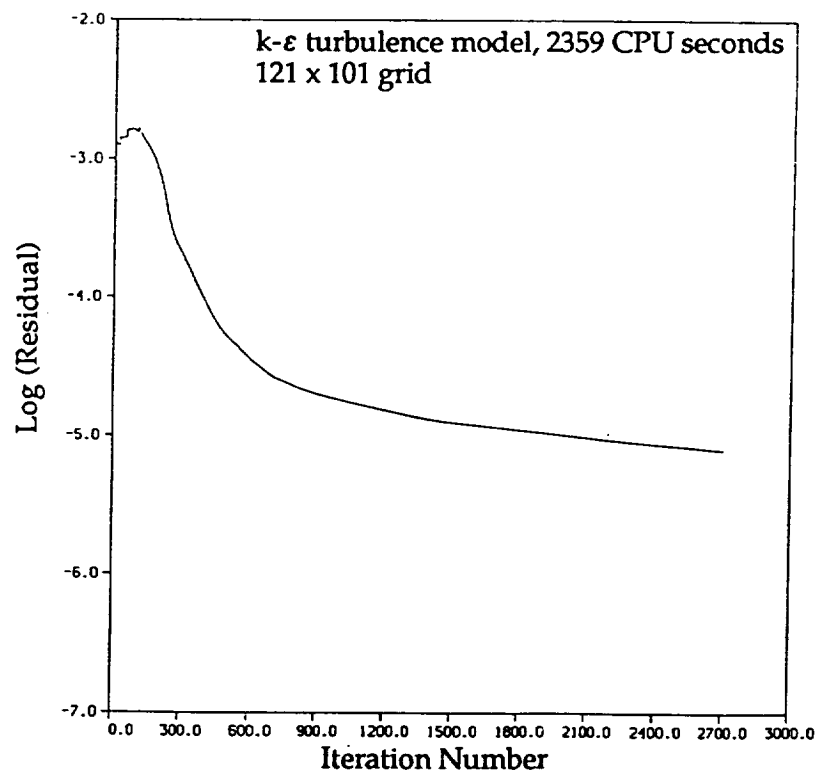


Figure 2.38 - Convergence history of nondimensionalized L_2 density residual (8° ramp, $M_\infty = 2.87$, $Re_\infty = 1.06 \times 10^8$).

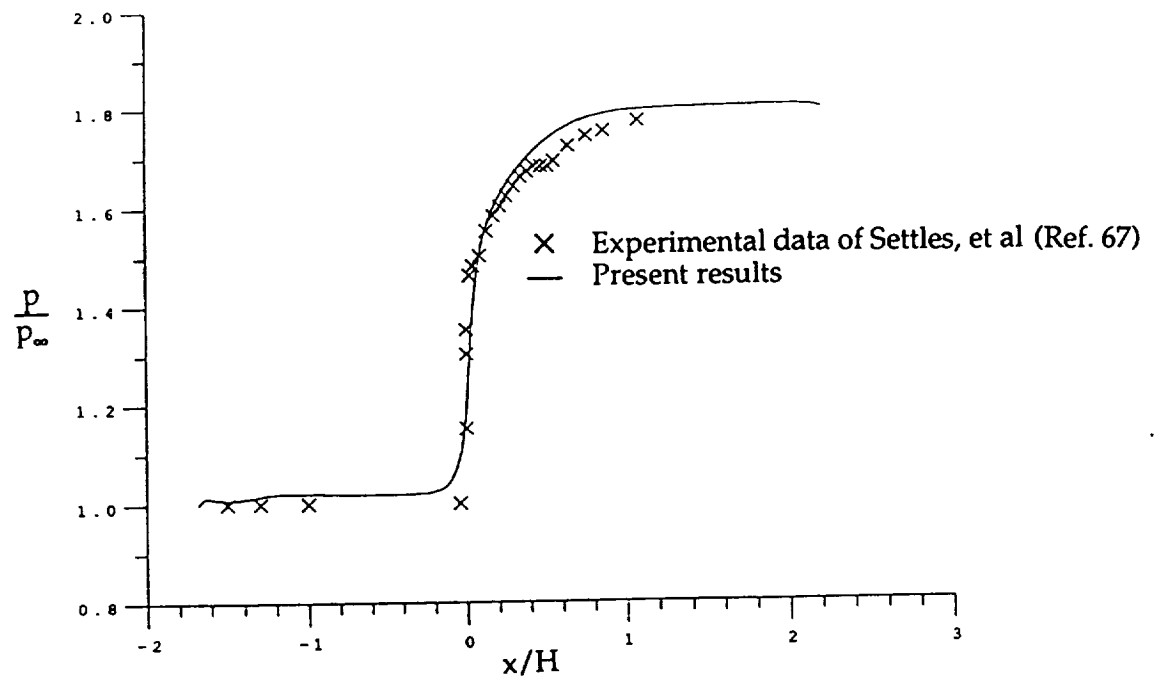


Figure 2.39 - Surface static pressure for 8° ramp, $M_\infty = 2.87$, $Re_\infty = 1.06 \times 10^8$.

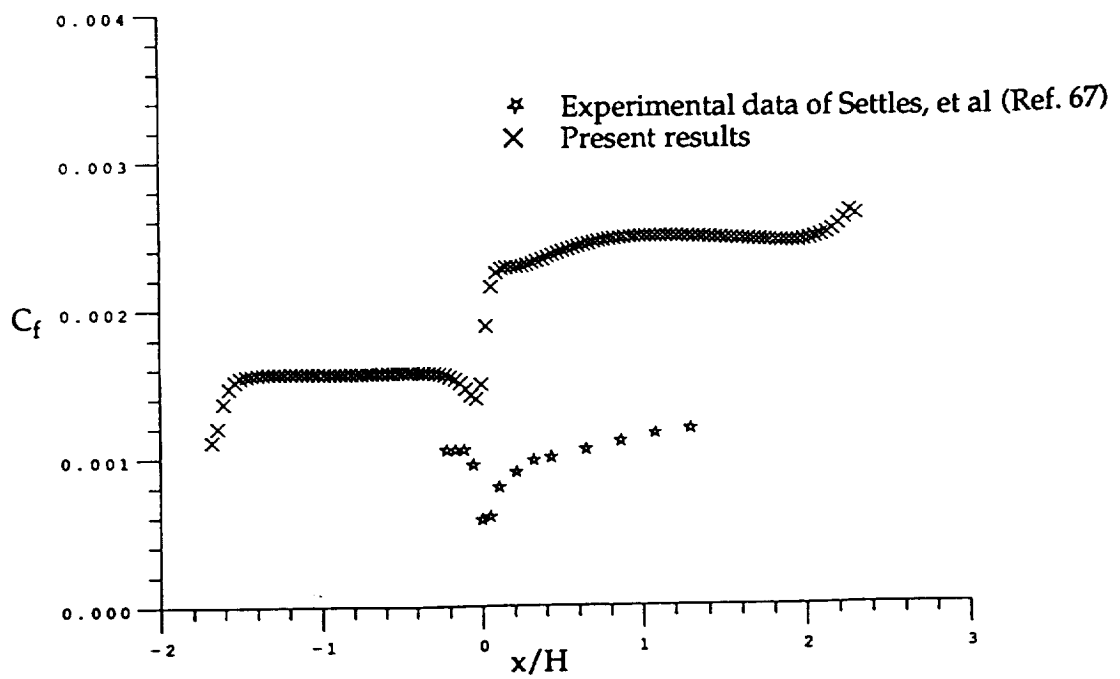


Figure 2.40 - Skin friction for 8° ramp, $M_\infty = 2.87$, $Re_\infty = 1.06 \times 10^8$.

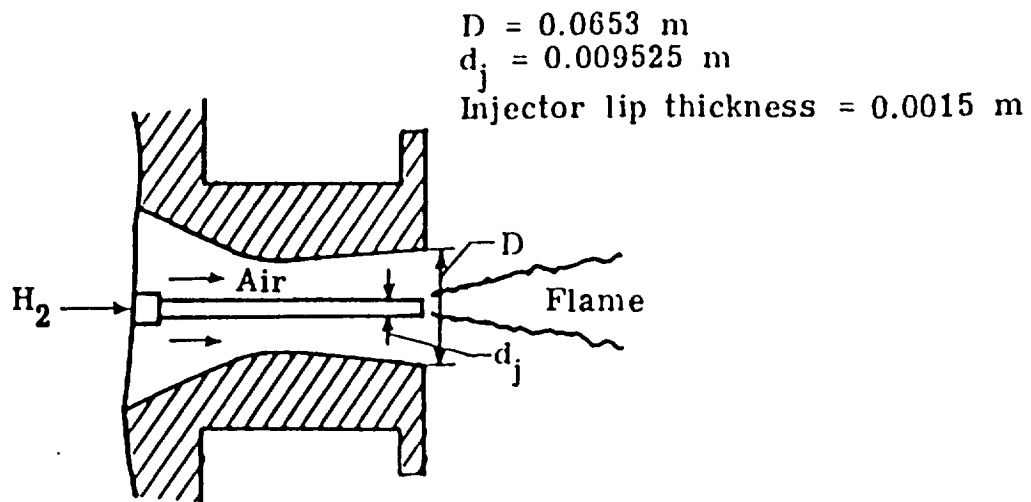


Fig.4.1 Geometrical properties of the test case 1 according to Evans et al. (1978).

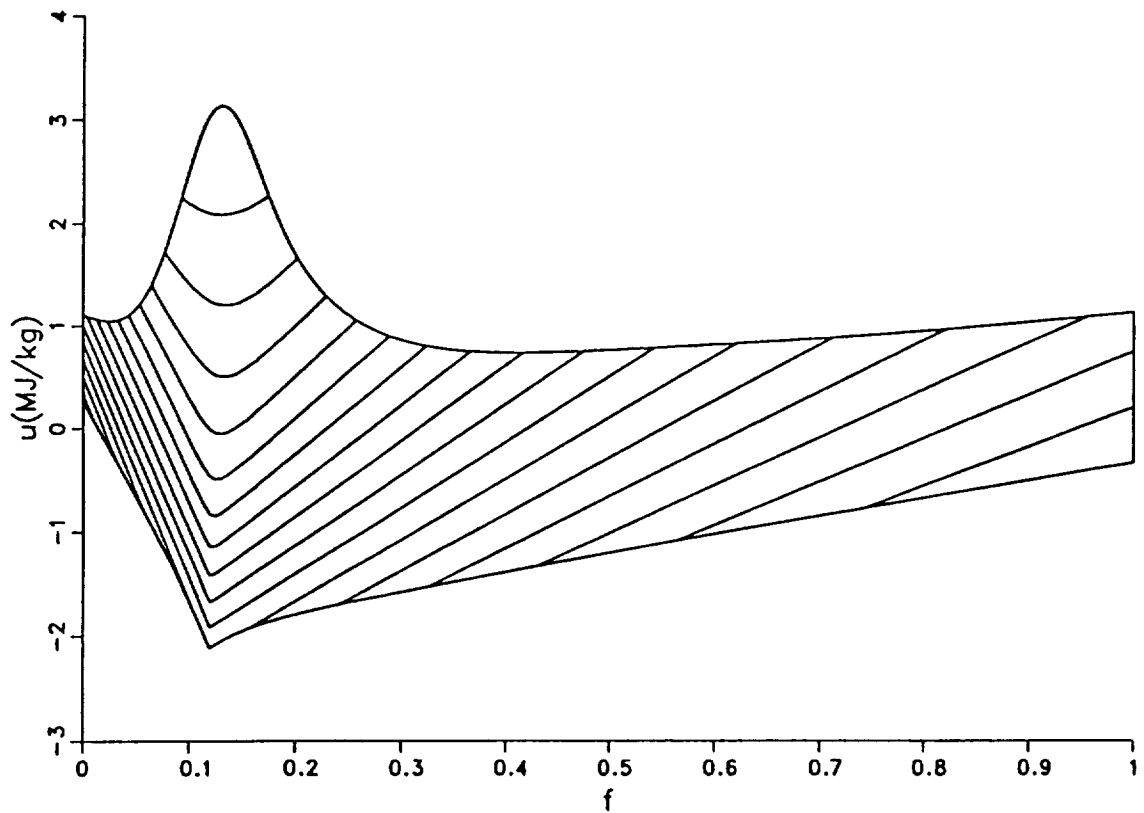


Fig.4.2 Temperature T as function of mixture fraction and internal energy for constrained equilibrium at the upper limit of density $\rho_{max}(\zeta)$.

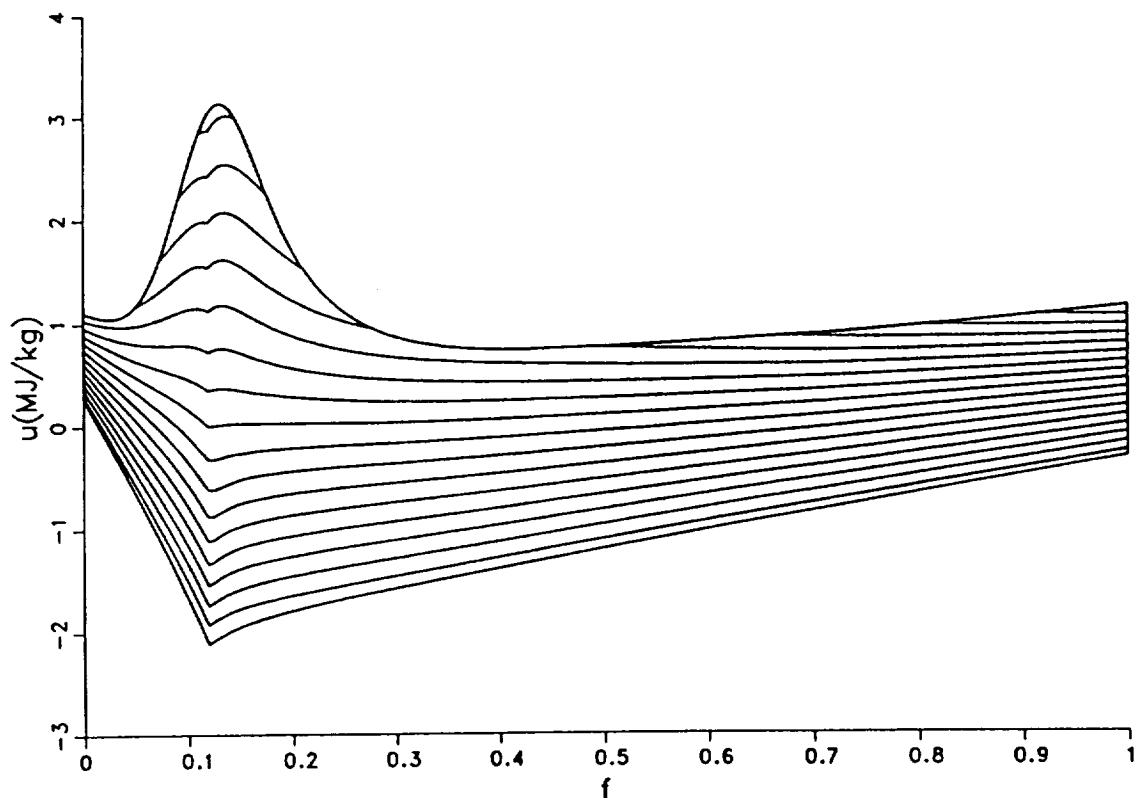


Fig.4.3 Pressure p as function of mixture fraction and internal energy for constrained equilibrium at the upper limit of density $\rho_{max}(\zeta)$.

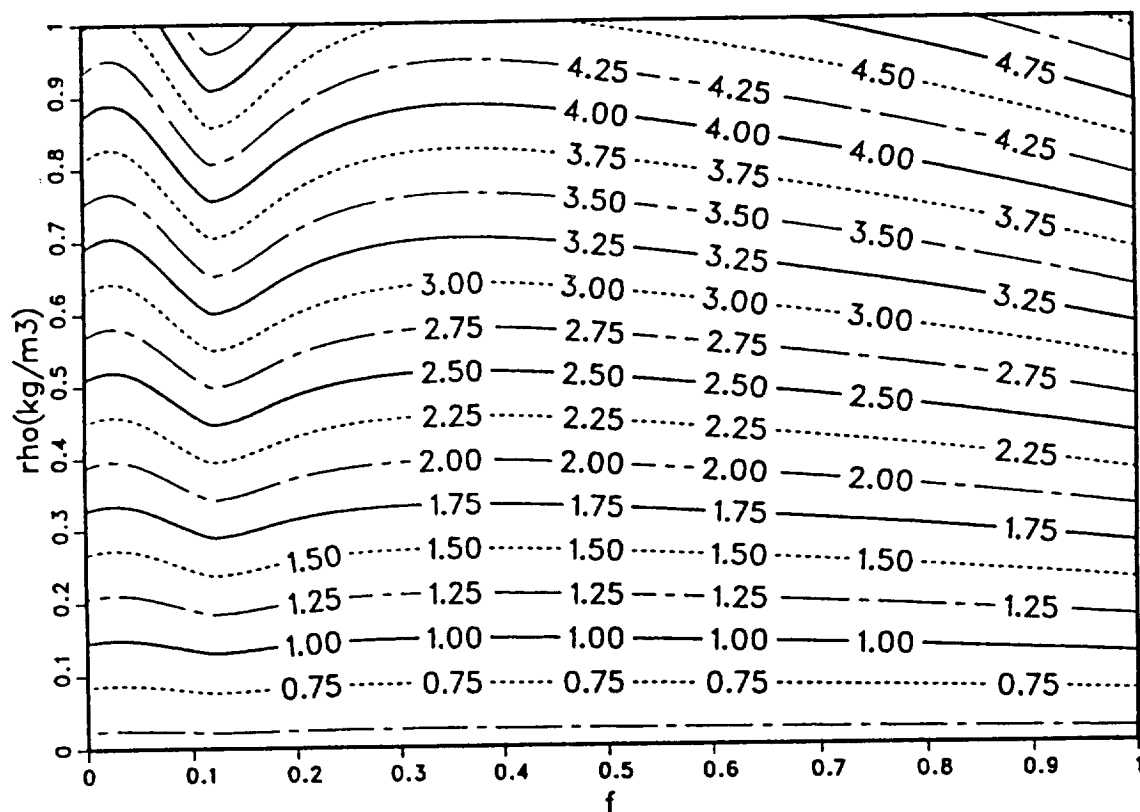


Fig.4.4 Pressure p as function of mixture fraction and normalized density for constrained equilibrium at the upper limit of internal energy $u_{max}(\zeta)$.

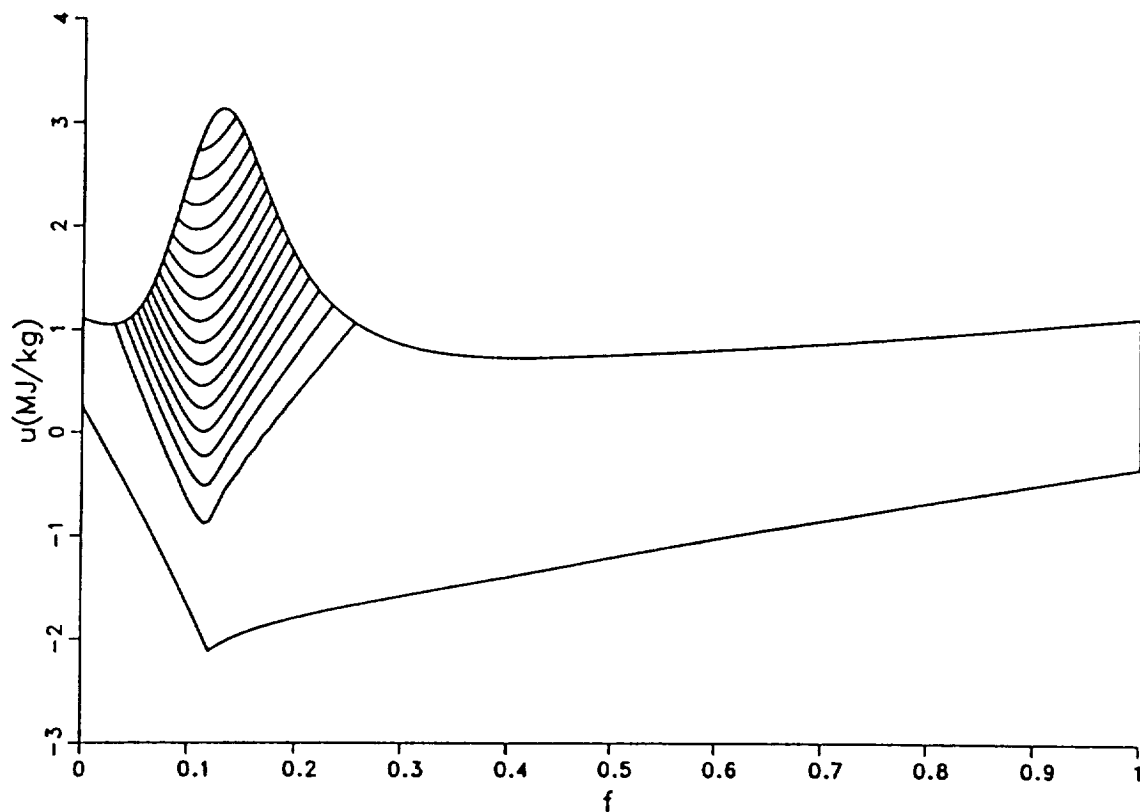


Fig.4.5 Mass fraction of OH as function of mixture fraction and internal energy for constrained equilibrium at the upper limit of density $\rho_{max}(\zeta)$.

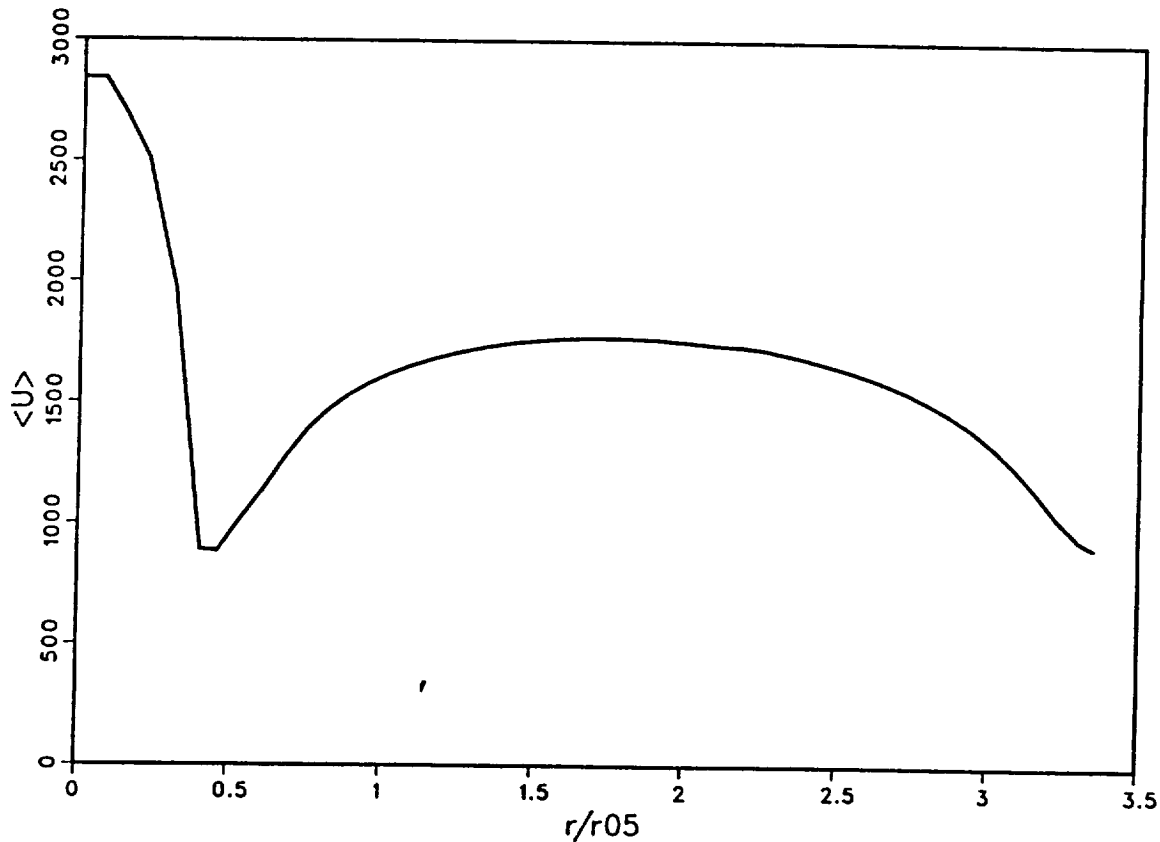


Fig.4.6 Mean velocity \bar{u} at $x/D = 6.56$ for a supersonic turbulent round jet flame burning H_2 with a coflowing air stream ($M_a^o = 2.0$ at jet pipe exit).

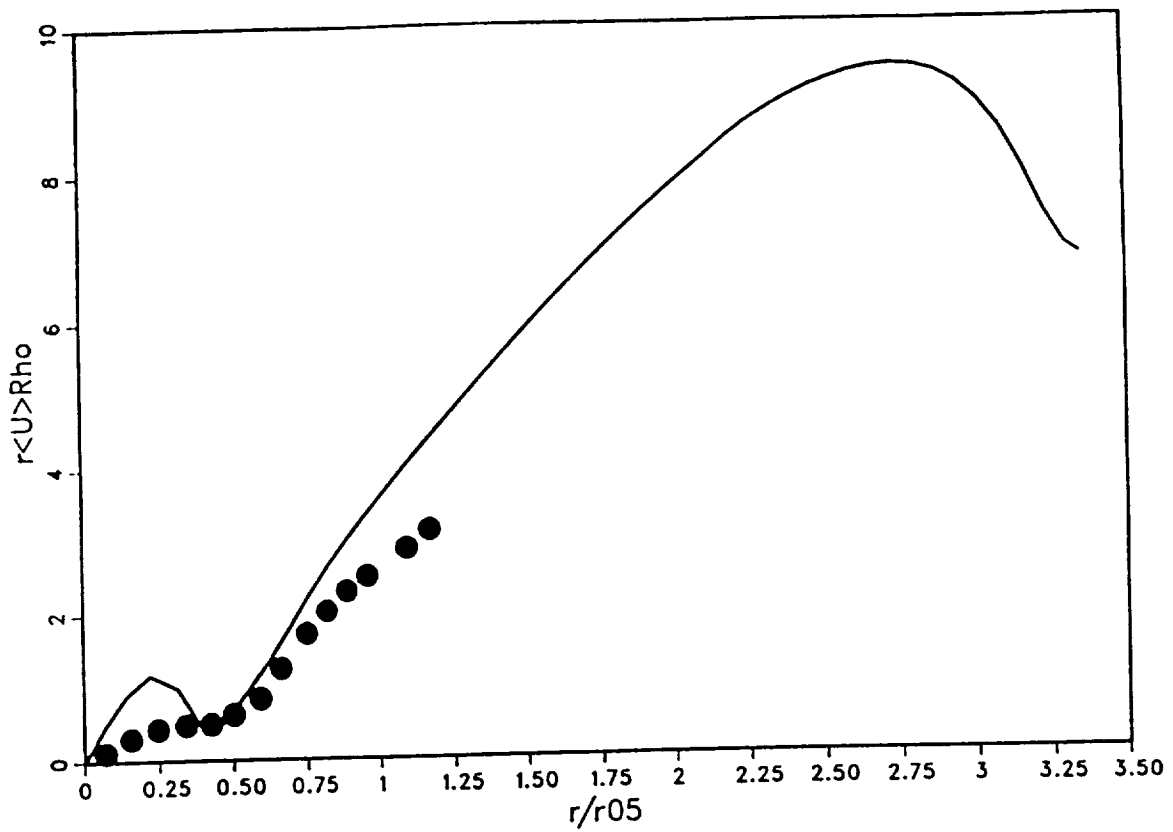


Fig.4.7 Comparison of calculated (line) and measured (symbols: Evans et al., 1978) product $r\bar{u}\langle\rho\rangle$ at $x/D = 6.56$ for a supersonic turbulent round jet flame burning H_2 with a coflowing air stream ($M_a^\circ = 2.0$ at jet pipe exit).

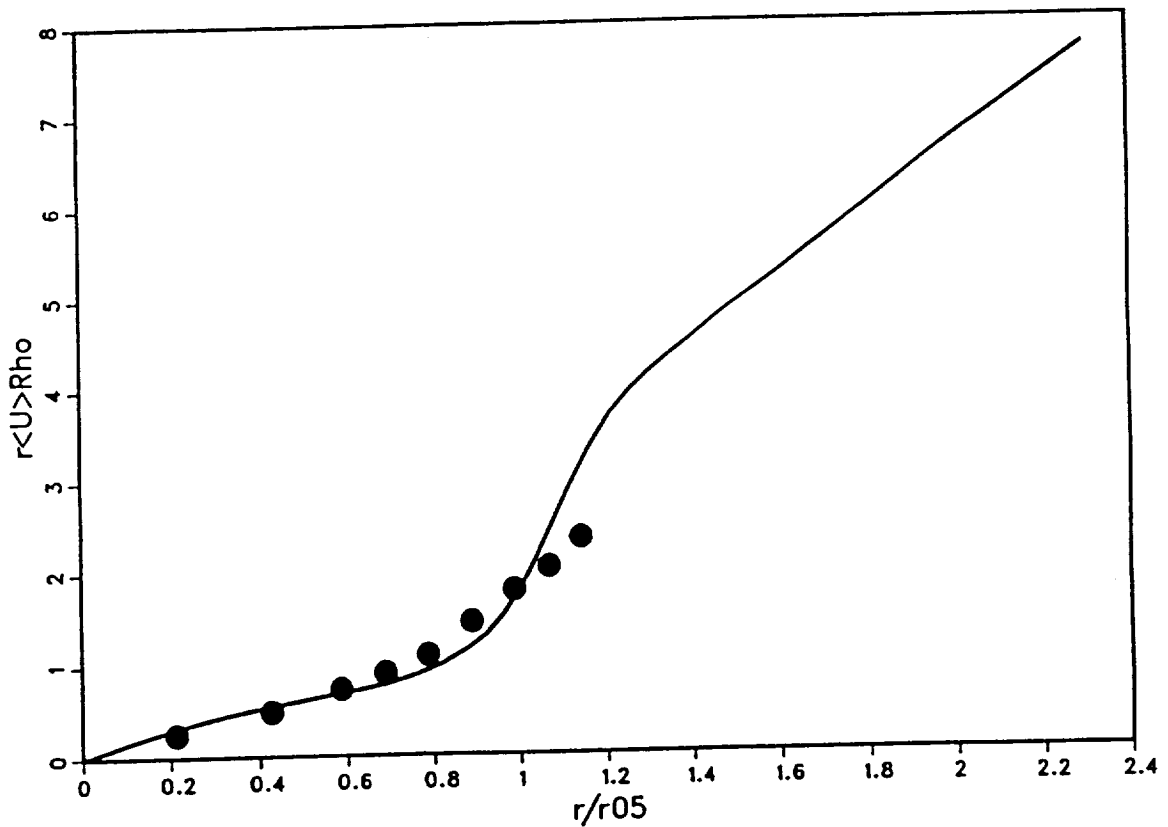


Fig.4.8 Comparison of calculated (line) and measured (symbols: Evans et al., 1978) product $r\bar{u}\langle\rho\rangle$ at $x/D = 26.2$ for a supersonic turbulent round jet flame burning H_2 with a coflowing air stream ($M_a^\circ = 2.0$ at jet pipe exit).

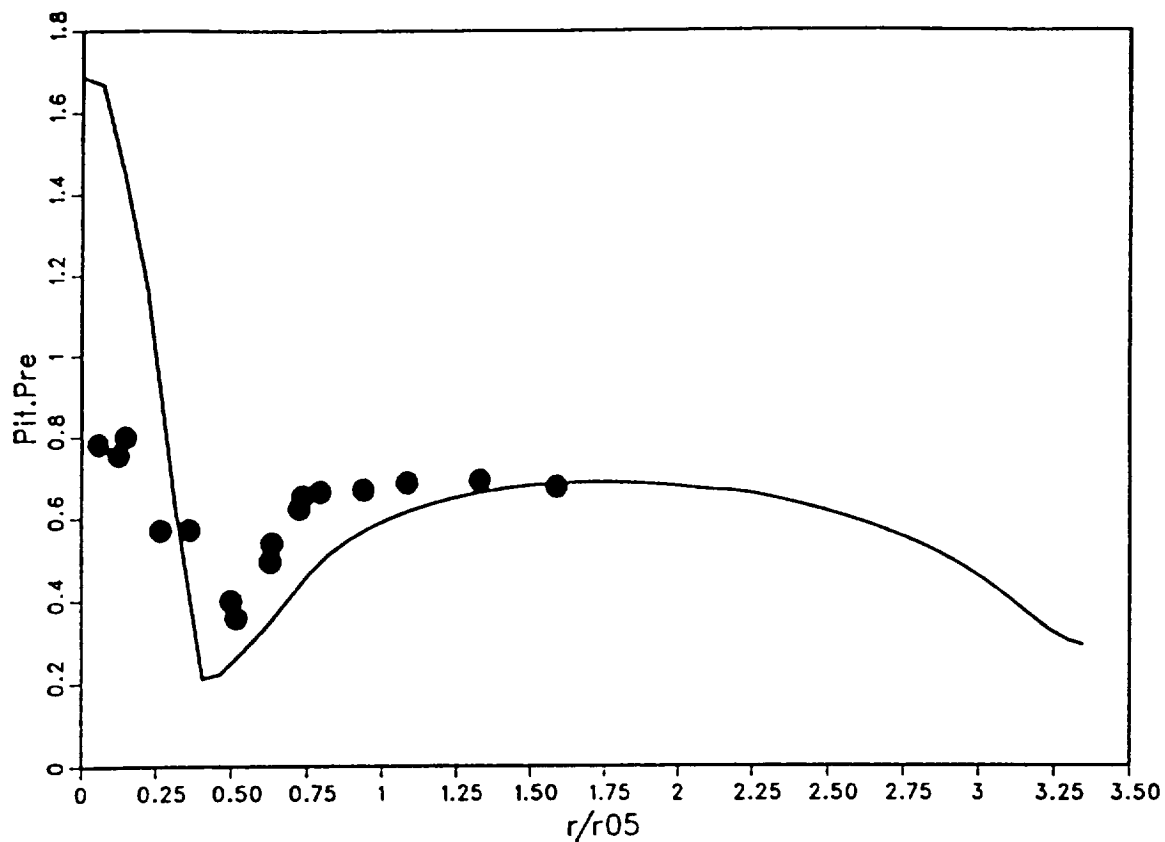


Fig.4.9 Comparison of calculated (line) and measured (symbols: Evans et al., 1978) Pitot pressure at $x/D = 6.56$ for a supersonic turbulent round jet flame burning H_2 with a coflowing air stream ($M_a^o = 2.0$ at jet pipe exit).

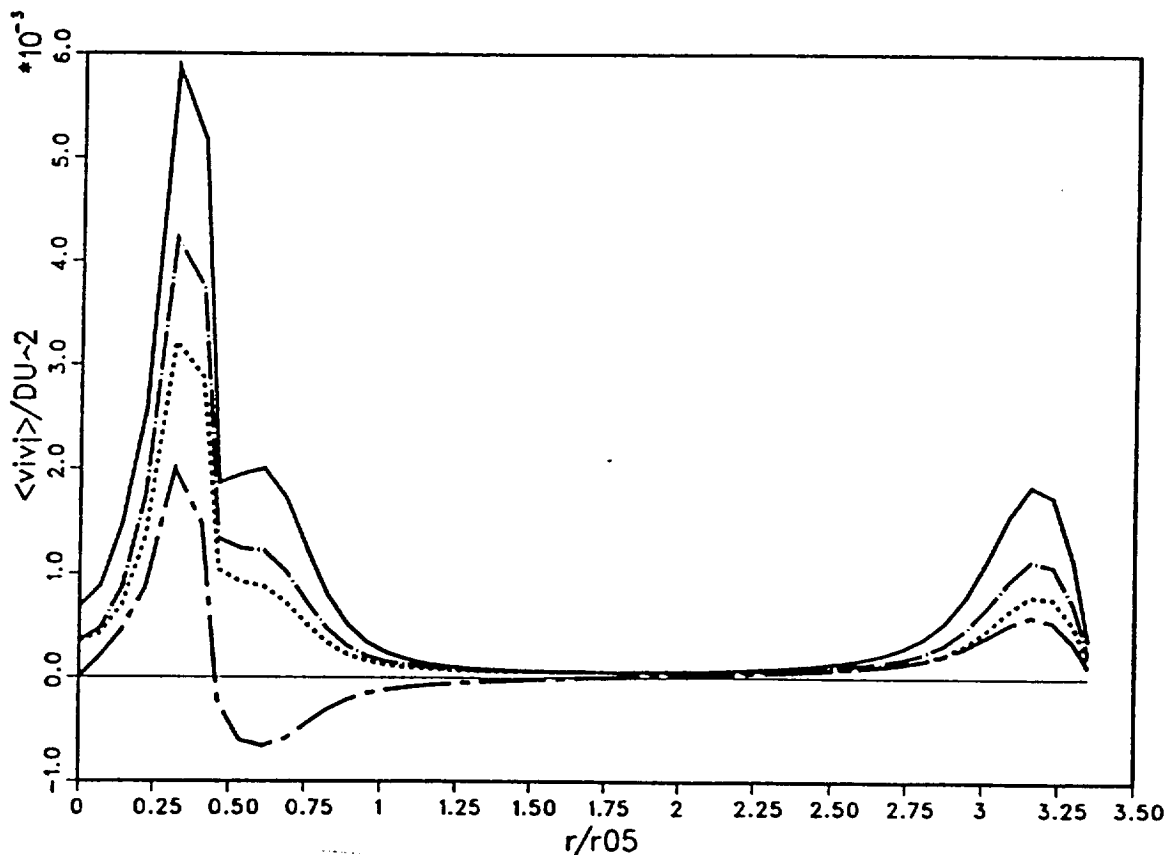


Fig.4.10 Reynolds stress components $\widetilde{u''^2}$: (full line), $\widetilde{v''^2}$: (broken line), $\widetilde{w''^2}$: (dashpot line), $\widetilde{u''v''}$: (long dashpot line) at $x/D = 6.56$ for a supersonic turbulent round jet flame burning H_2 with a coflowing air stream ($M_a^o = 2.0$ at jet pipe exit).

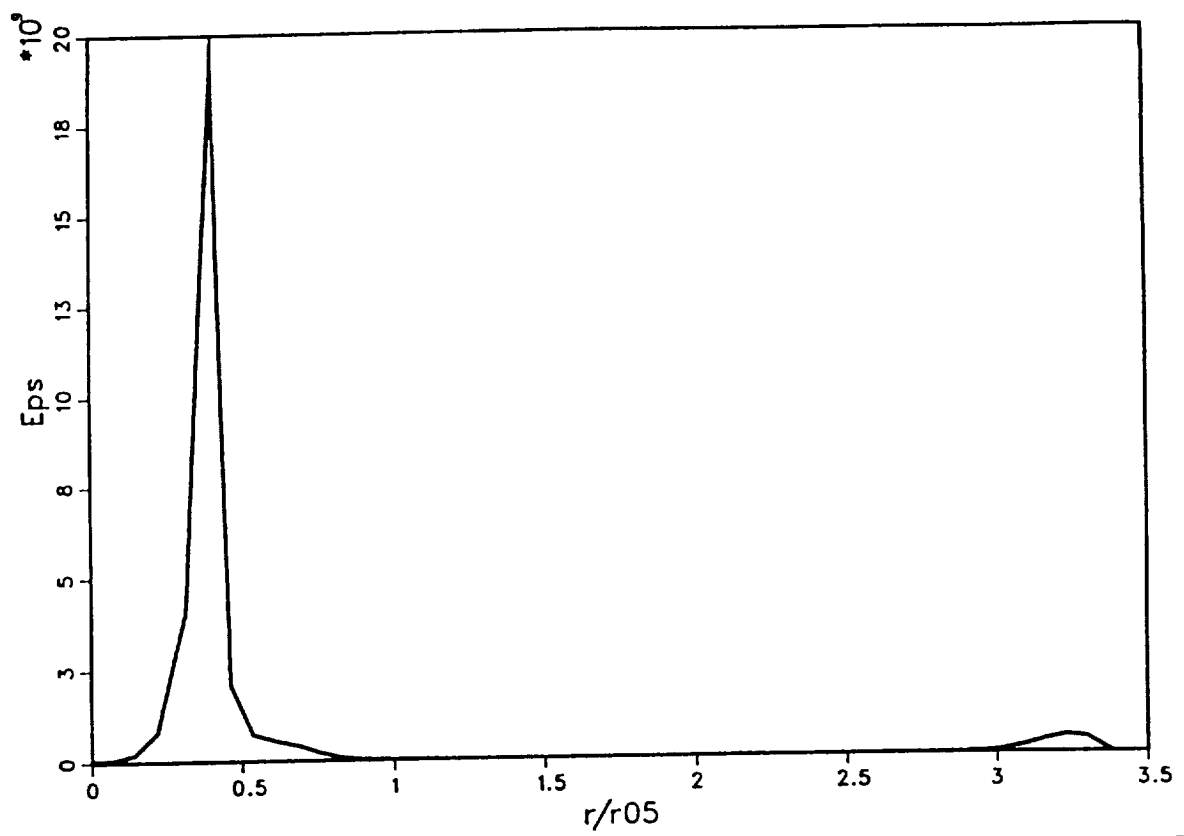


Fig.4.11 Dissipation rate at $x/D = 6.56$ for a supersonic turbulent round jet flame burning H_2 with a coflowing air stream ($M_a^o = 2.0$ at jet pipe exit).

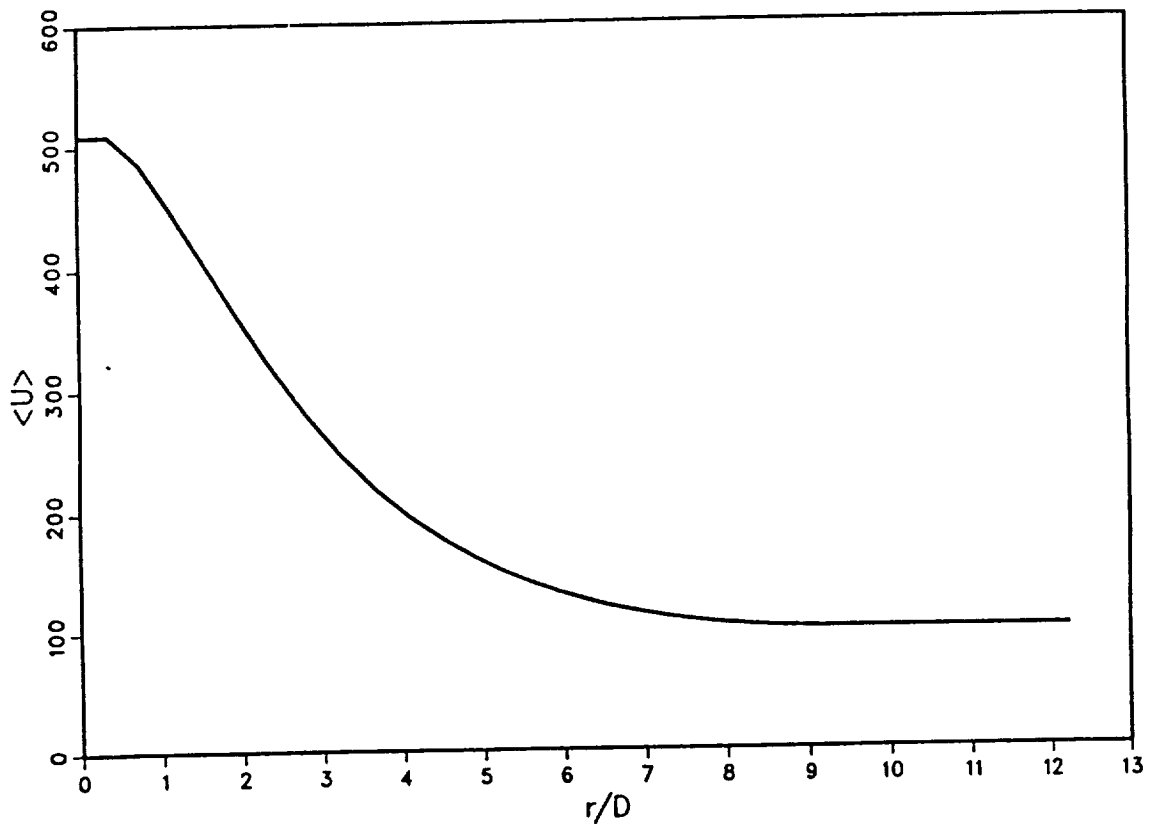


Fig.4.12 Mean velocity \tilde{u} at $x/D = 30.14$ for a supersonic turbulent round jet flame burning H_2 with a coflowing air stream ($M_a^o = 2.0$ at jet pipe exit).

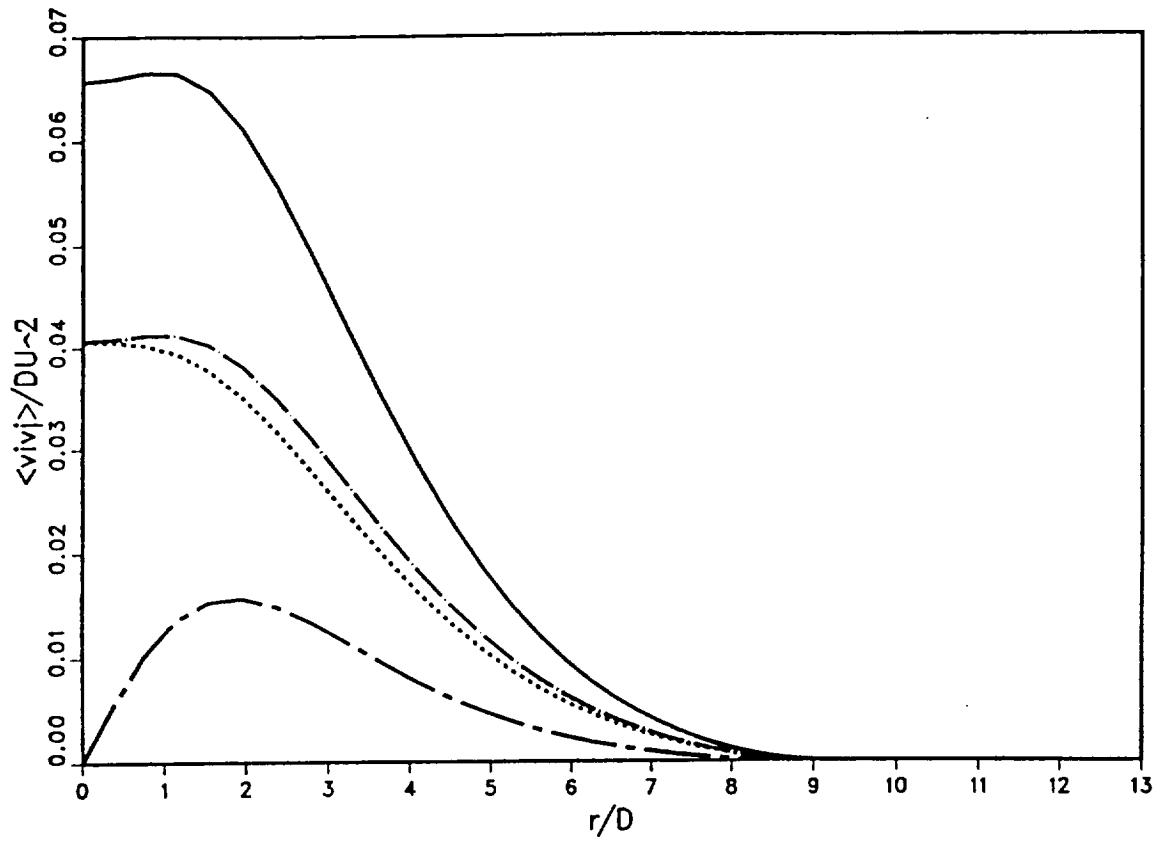


Fig.4.13 Reynolds stress components $\widetilde{u''^2}$: (full line), $\widetilde{v''^2}$: (broken line), $\widetilde{w''^2}$: (dashpot line), $\widetilde{u''v''}$: (long dashpot line) at $x/D = 30.14$ for a supersonic turbulent round jet flame burning H_2 with a coflowing air stream ($M_a^o = 2.0$ at jet pipe exit).

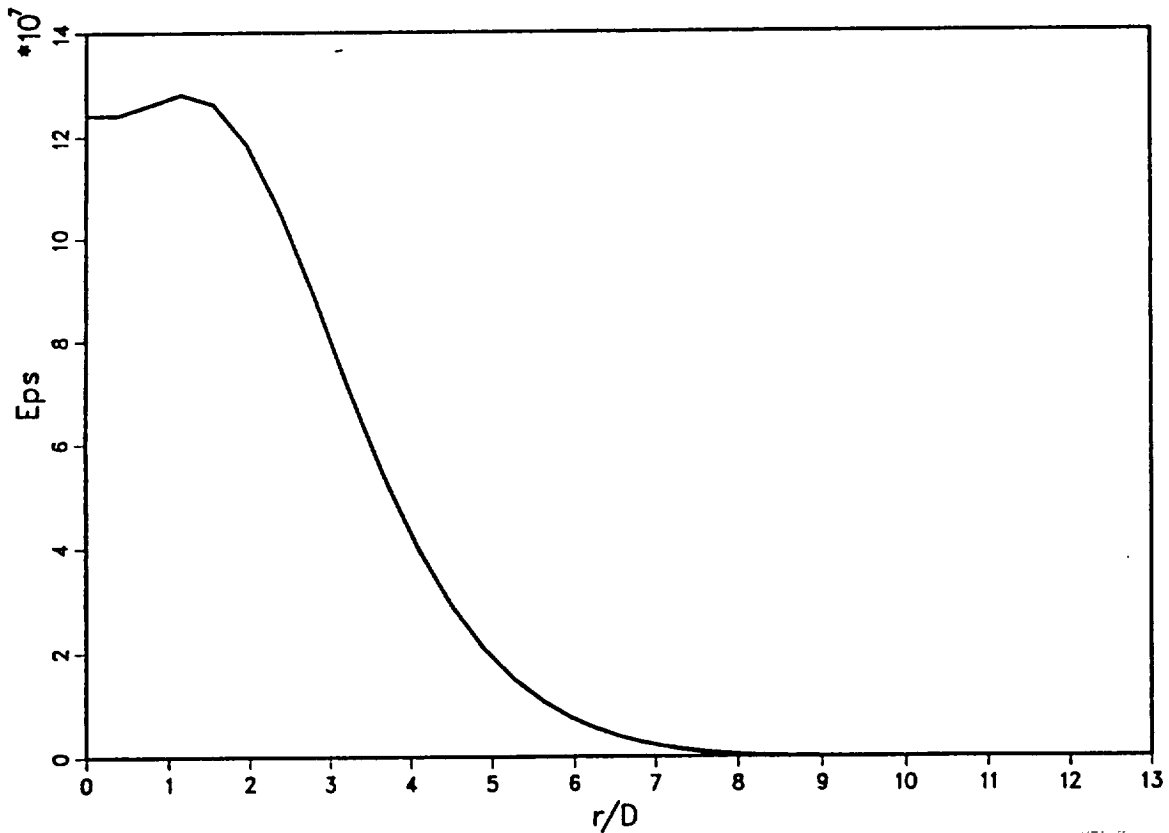


Fig.4.14 Dissipation rate at $x/D = 30.14$ for a supersonic turbulent round jet flame burning H_2 with a coflowing air stream ($M_a^o = 2.0$ at jet pipe exit).

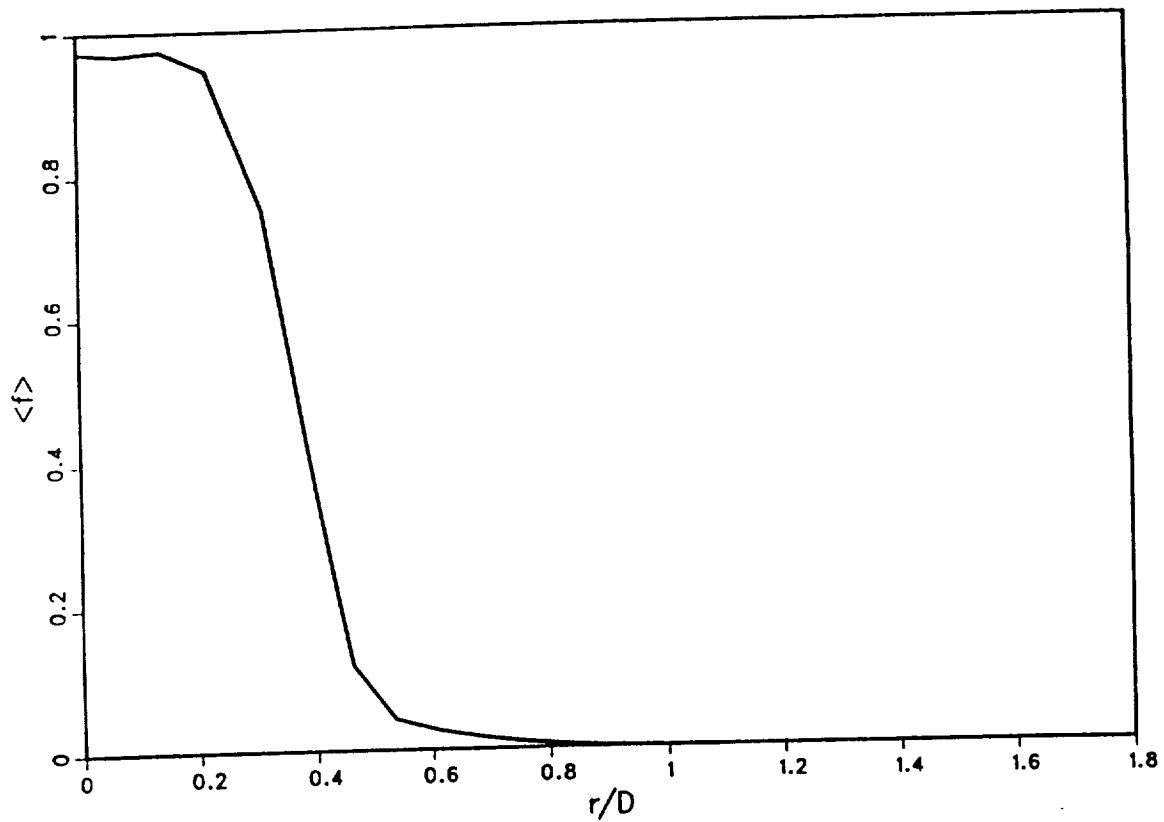


Fig.4.15 Mean mixture fraction at $x/D = 6.56$ for a supersonic turbulent round jet flame burning H_2 with a coflowing air stream ($M_a^o = 2.0$ at jet pipe exit).

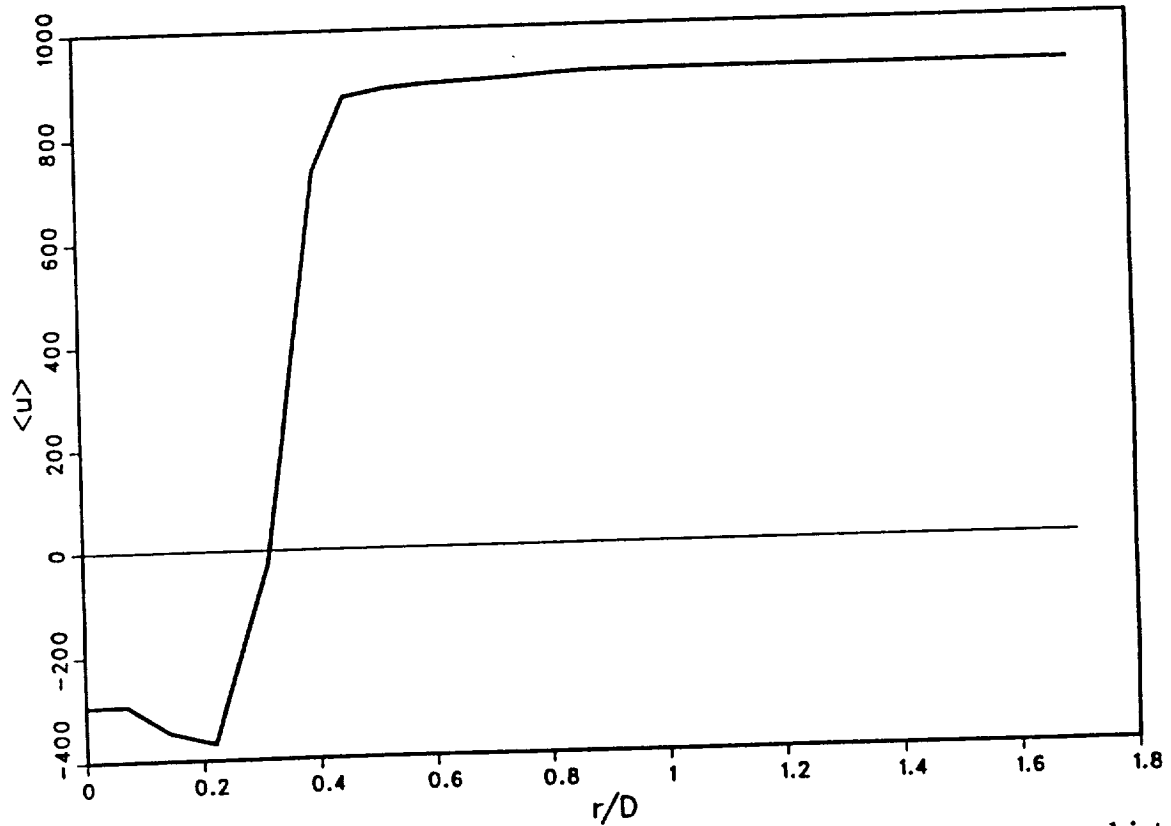


Fig.4.16 Mean internal energy at $x/D = 6.56$ for a supersonic turbulent round jet flame burning H_2 with a coflowing air stream ($M_a^o = 2.0$ at jet pipe exit).

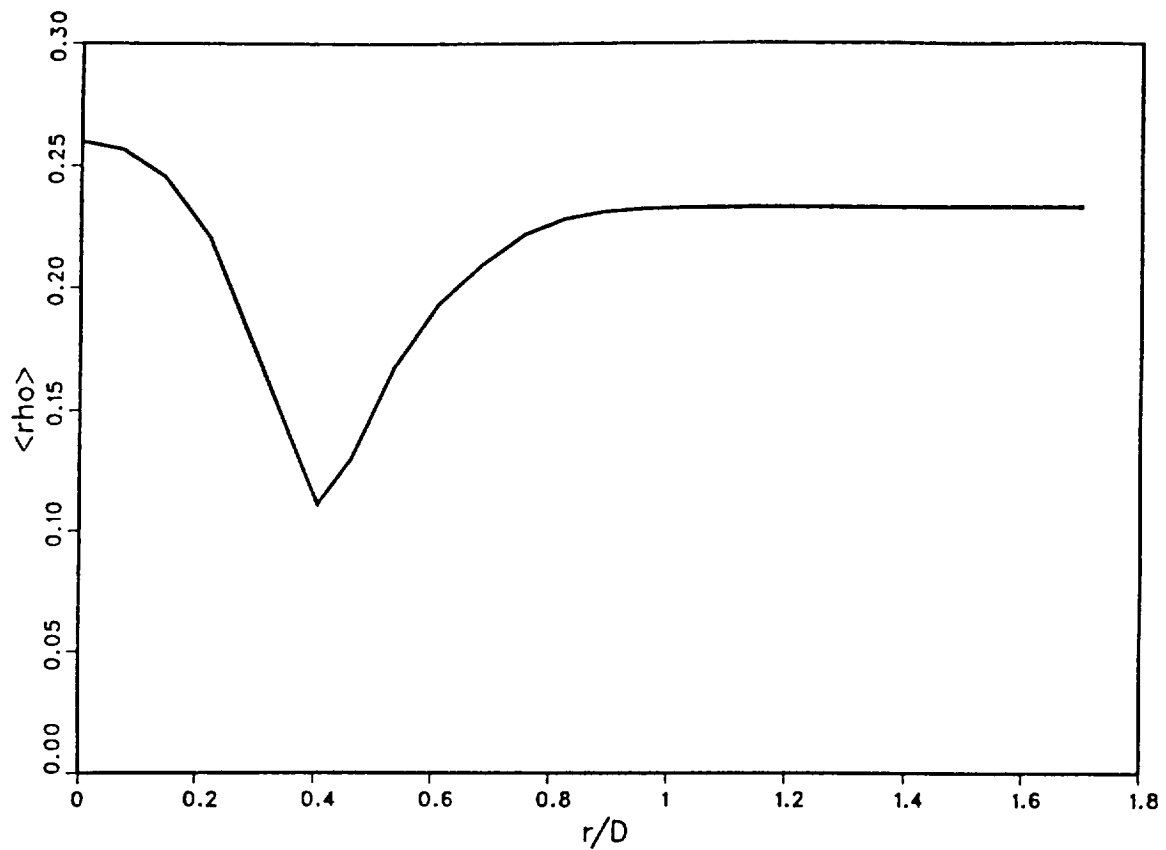


Fig.4.17 Mean density at $x/D = 6.56$ for a supersonic turbulent round jet flame burning H_2 with a coflowing air stream ($M_a^o = 2.0$ at jet pipe exit).

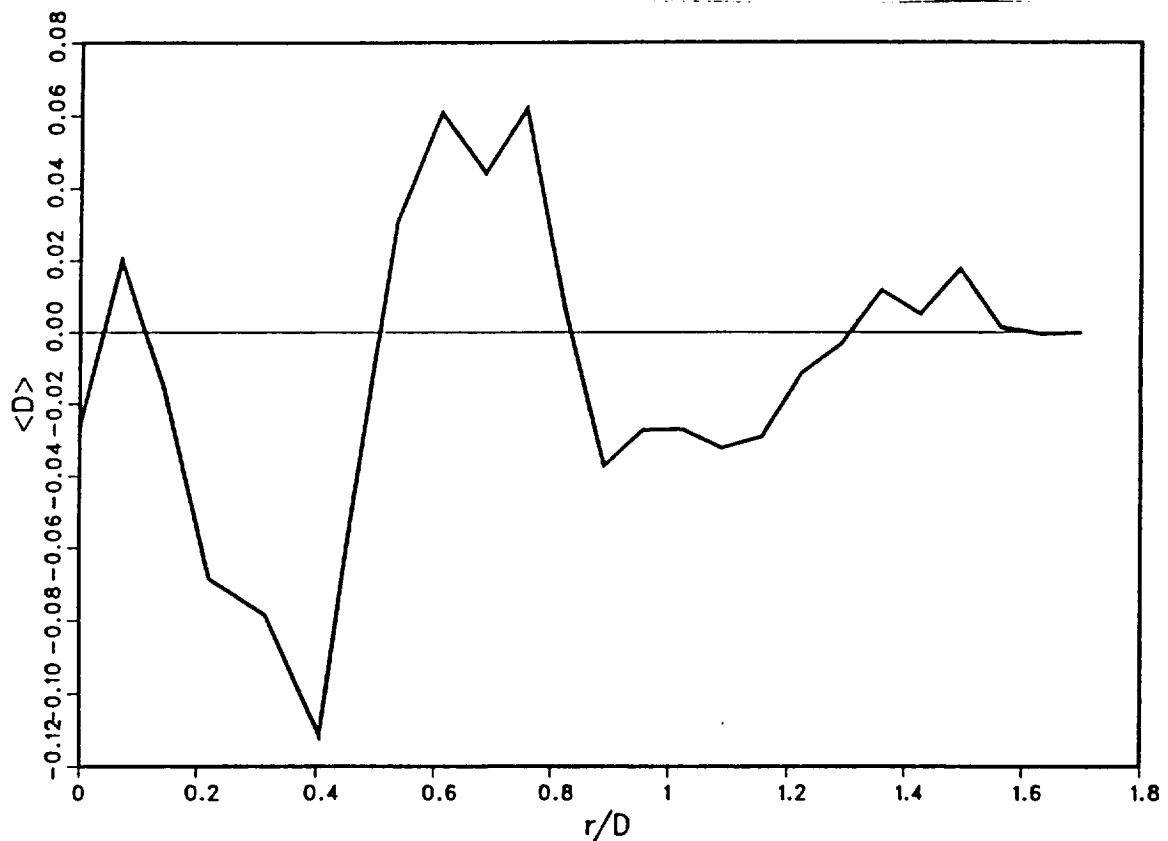


Fig.4.18 Mean value of the relative rate of volume expansion at $x/D = 6.56$ for a supersonic turbulent round jet flame burning H_2 with a coflowing air stream ($M_a^o = 2.0$ at jet pipe exit).

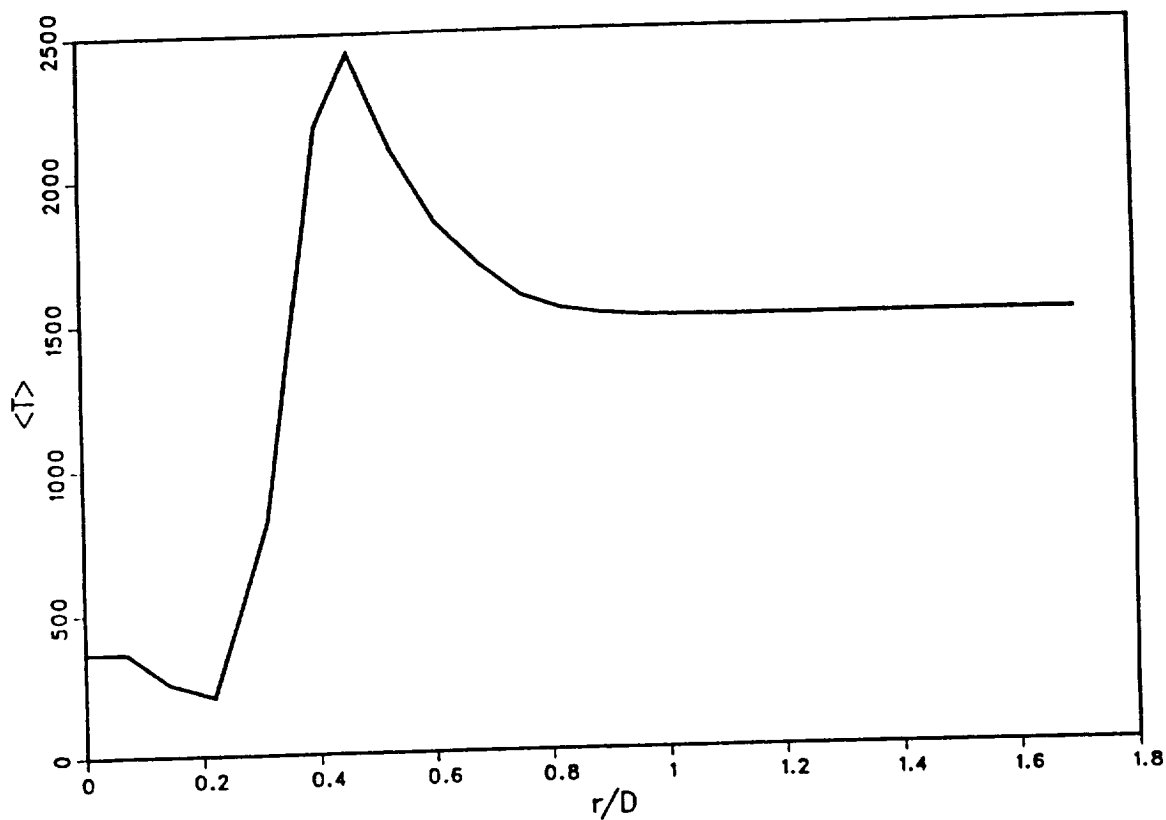


Fig.4.19 Mean temperature at $x/D = 6.56$ for a supersonic turbulent round jet flame burning H_2 with a coflowing air stream ($M_a^o = 2.0$ at jet pipe exit).

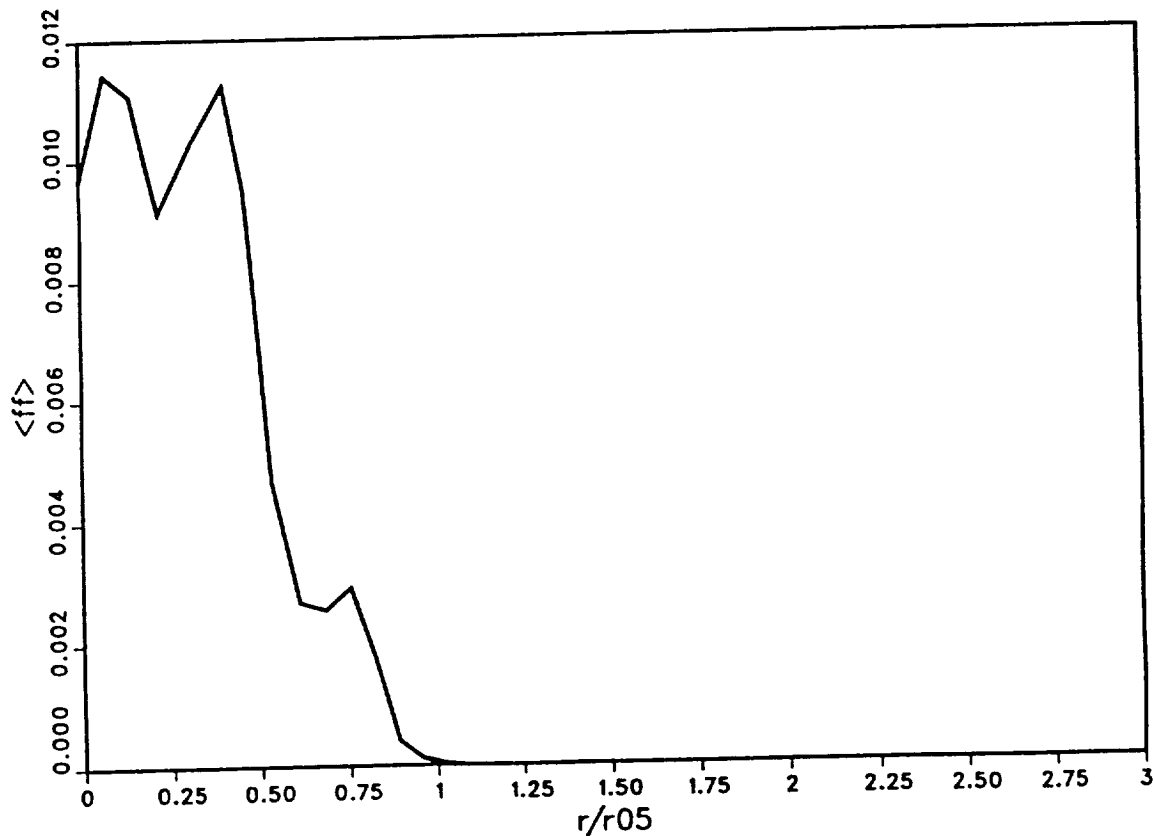


Fig.4.20 Variance of mixture fraction at $x/D = 6.56$ for a supersonic turbulent round jet flame burning H_2 with a coflowing air stream ($M_a^o = 2.0$ at jet pipe exit).

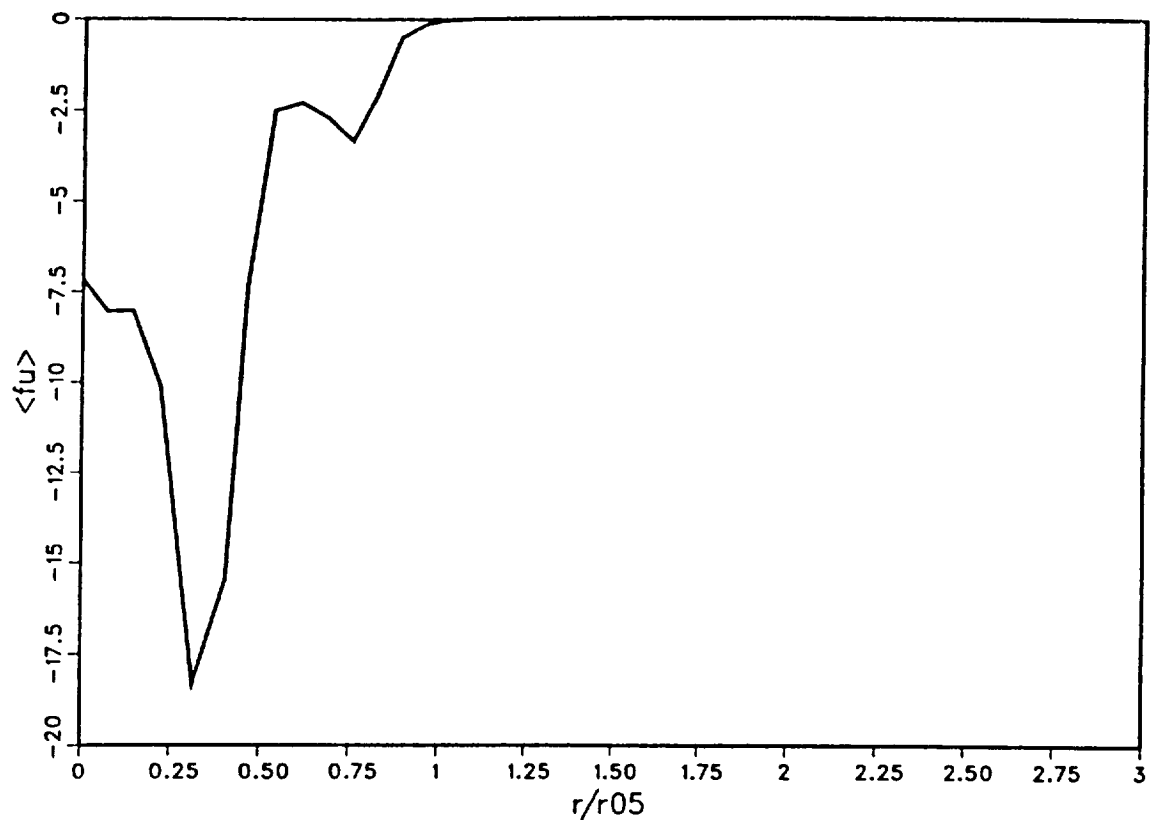


Fig.4.21 Covariance of mixture fraction and internal energy at $x/D = 6.56$ for a supersonic turbulent round jet flame burning H_2 with a coflowing air stream ($M_a^o = 2.0$ at jet pipe exit).

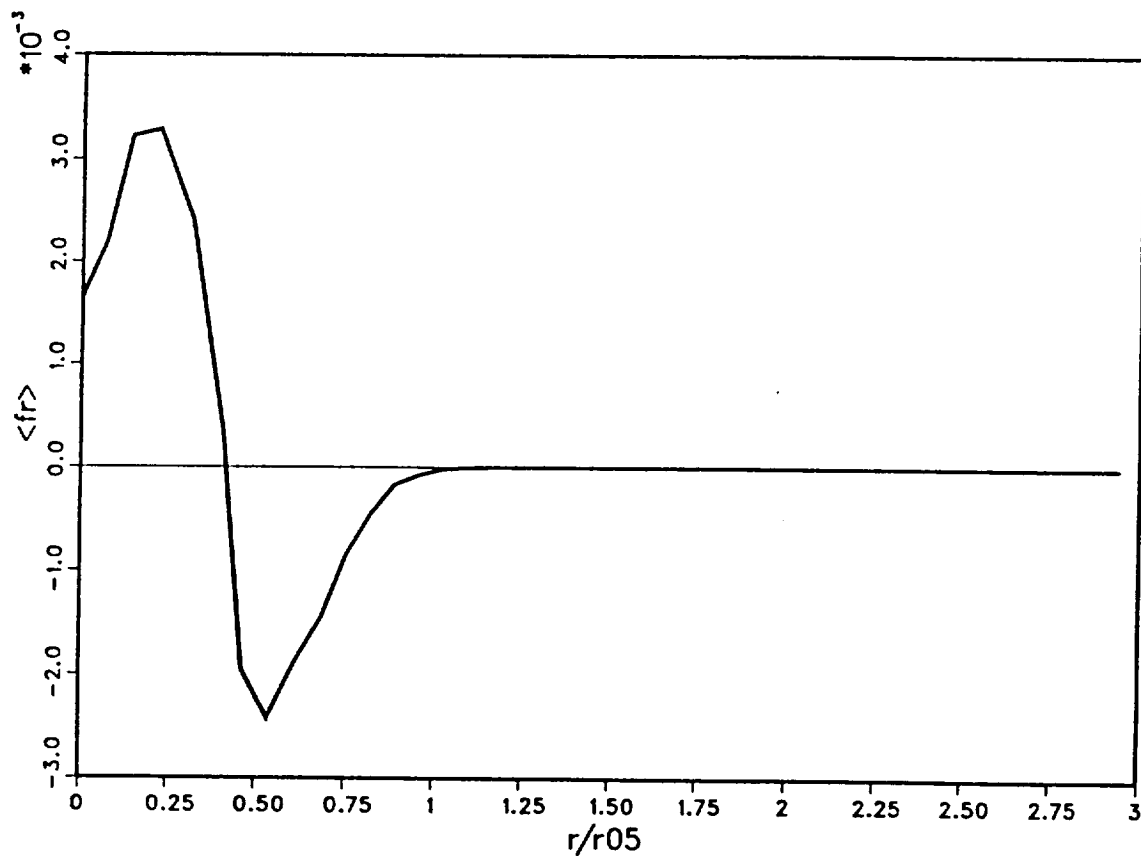


Fig.4.22 Covariance of mixture fraction and density at $x/D = 6.56$ for a supersonic turbulent round jet flame burning H_2 with a coflowing air stream ($M_a^o = 2.0$ at jet pipe exit).

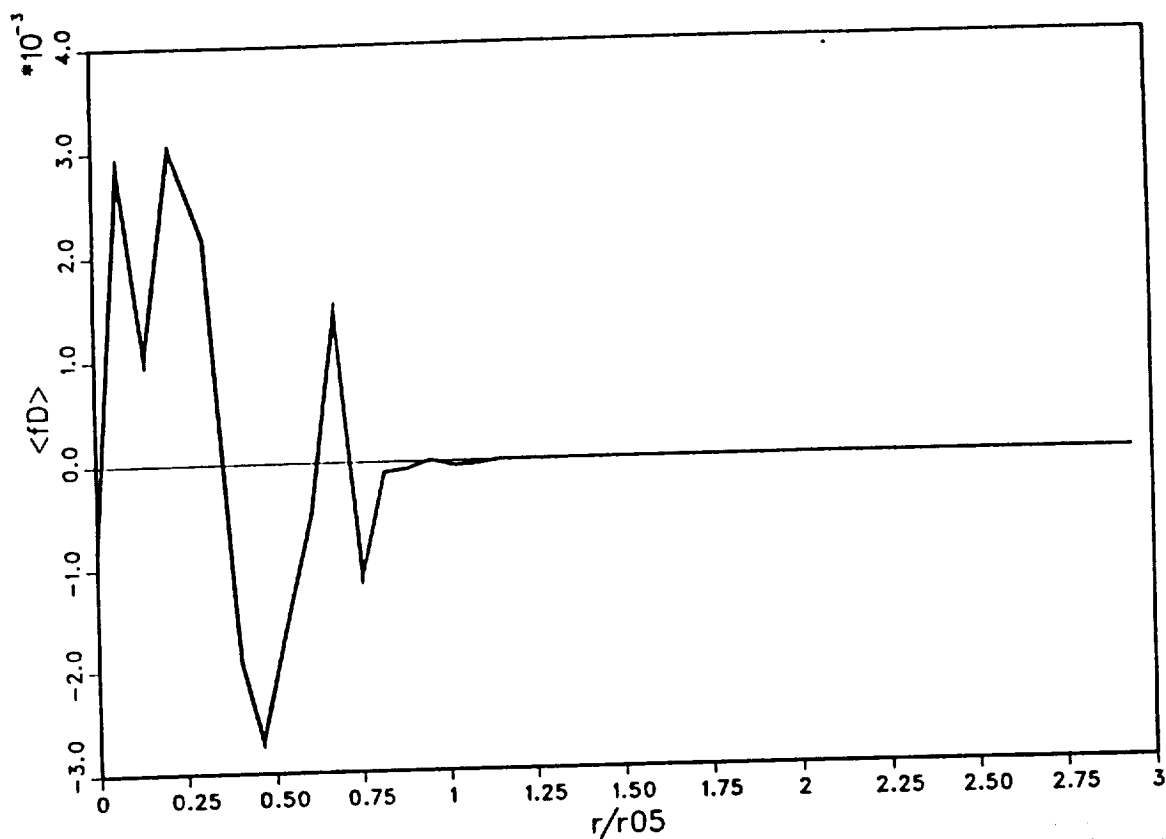


Fig.4.23 Covariance of mixture fraction and relative rate of volume expansion at $x/D = 6.56$ for a supersonic turbulent round jet flame burning H_2 with a coflowing air stream ($M_a^o = 2.0$ at jet pipe exit).

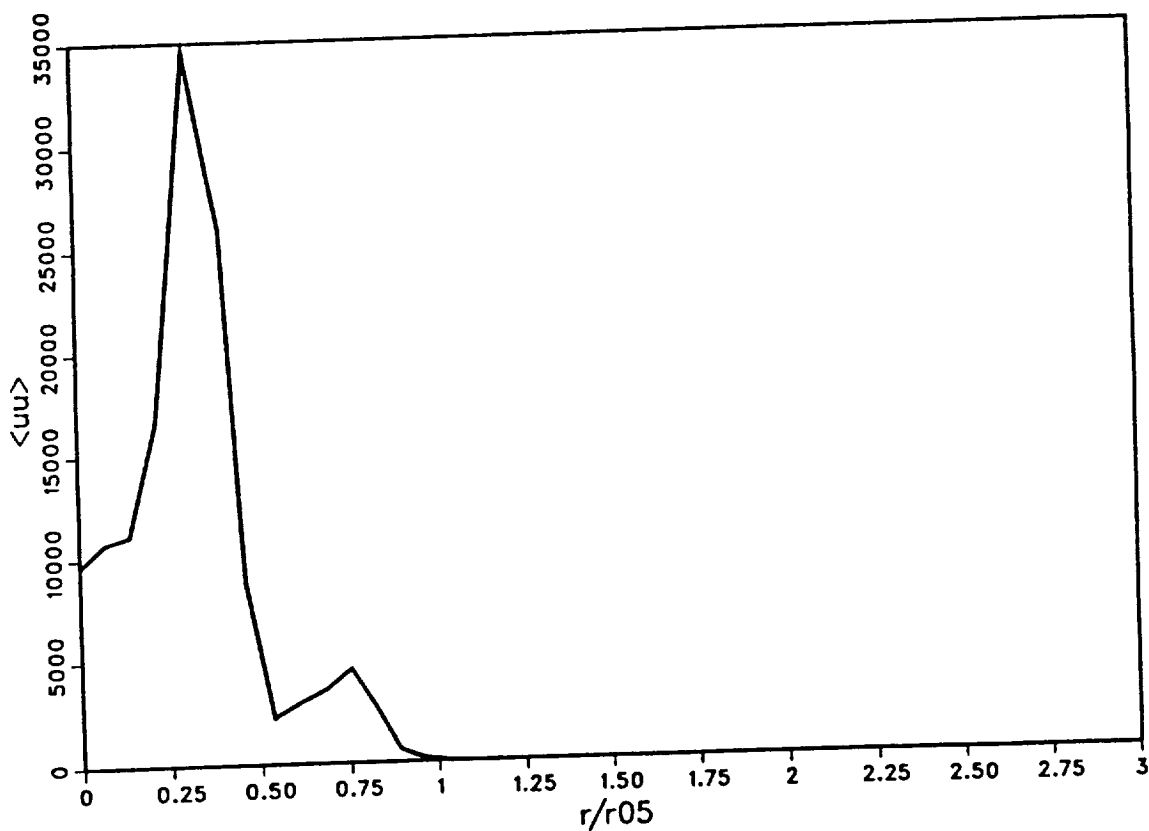


Fig.4.24 Variance of internal energy at $x/D = 6.56$ for a supersonic turbulent round jet flame burning H_2 with a coflowing air stream ($M_a^o = 2.0$ at jet pipe exit).

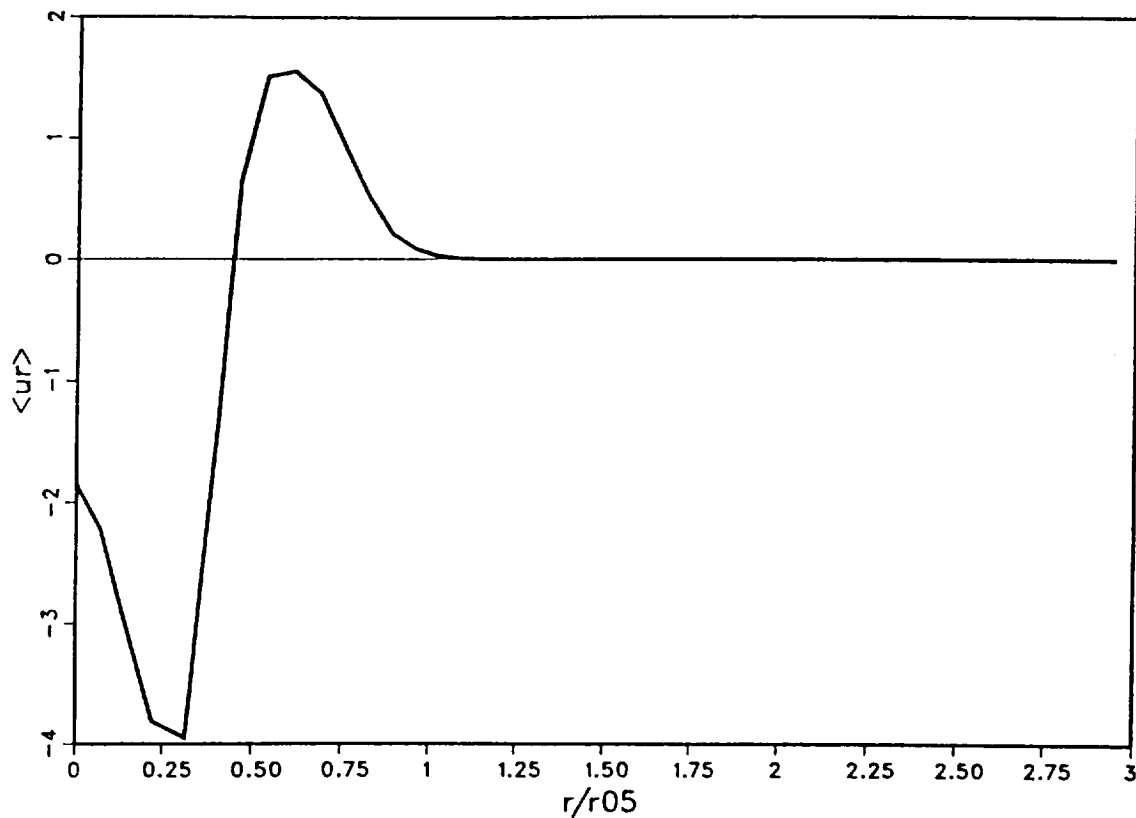


Fig.4.25 Covariance of density and internal energy at $x/D = 6.56$ for a supersonic turbulent round jet flame burning H_2 with a coflowing air stream ($M_a^o = 2.0$ at jet pipe exit).

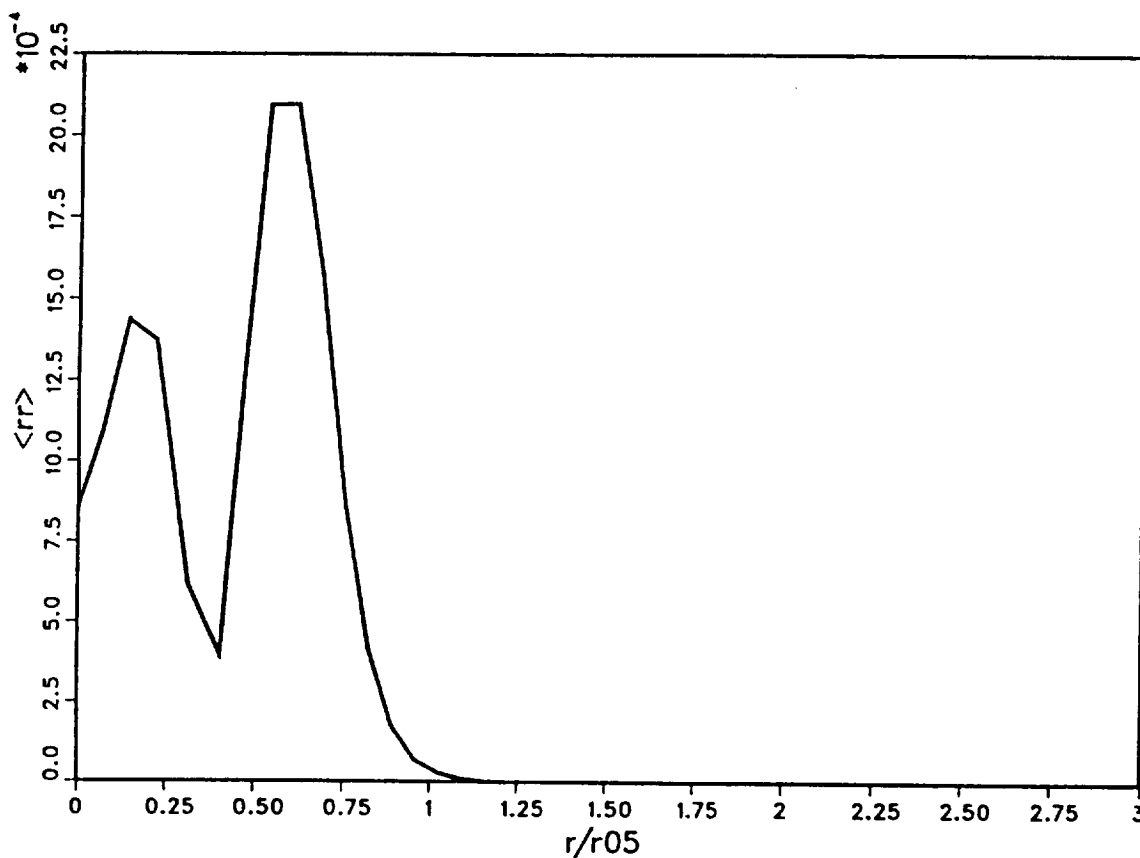


Fig.4.26 Variance of density at $x/D = 6.56$ for a supersonic turbulent round jet flame burning H_2 with a coflowing air stream ($M_a^o = 2.0$ at jet pipe exit).

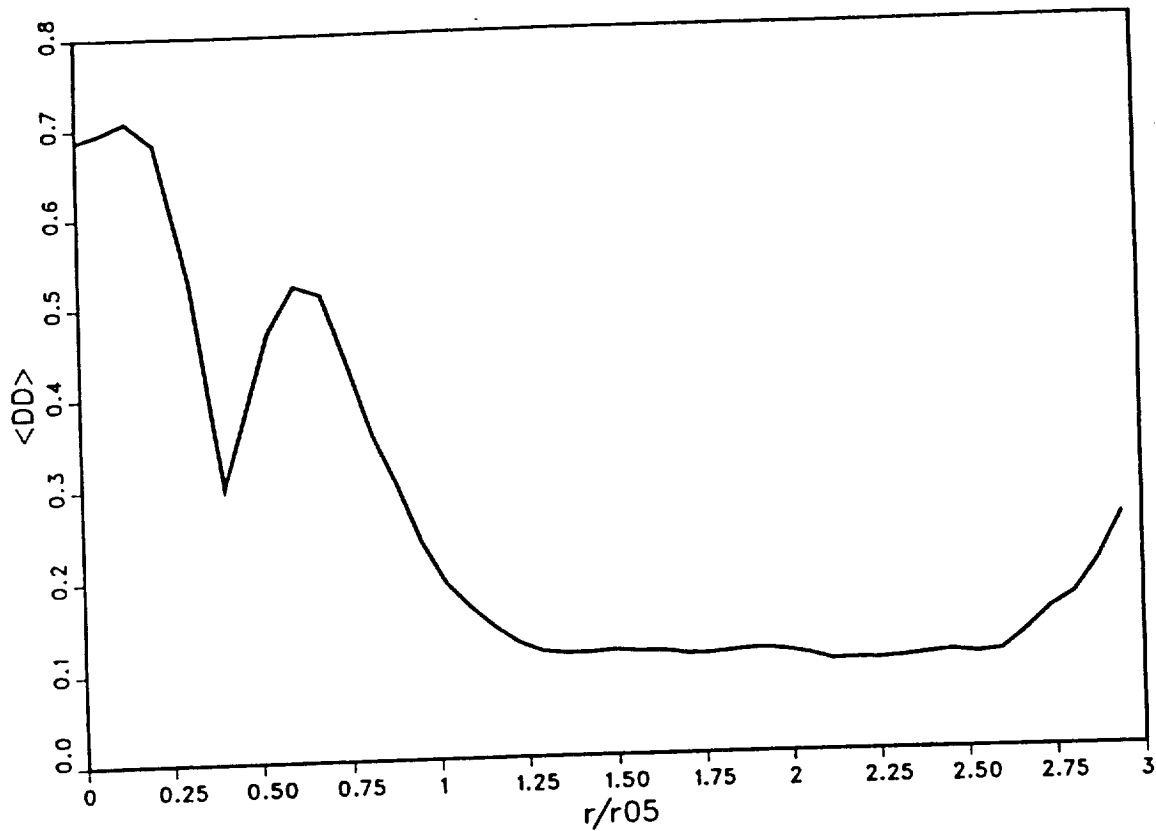


Fig.4.27 Variance of relative rate of volume expansion at $x/D = 6.56$ for a supersonic turbulent round jet flame burning H_2 with a coflowing air stream ($M_a^o = 2.0$ at jet pipe exit).

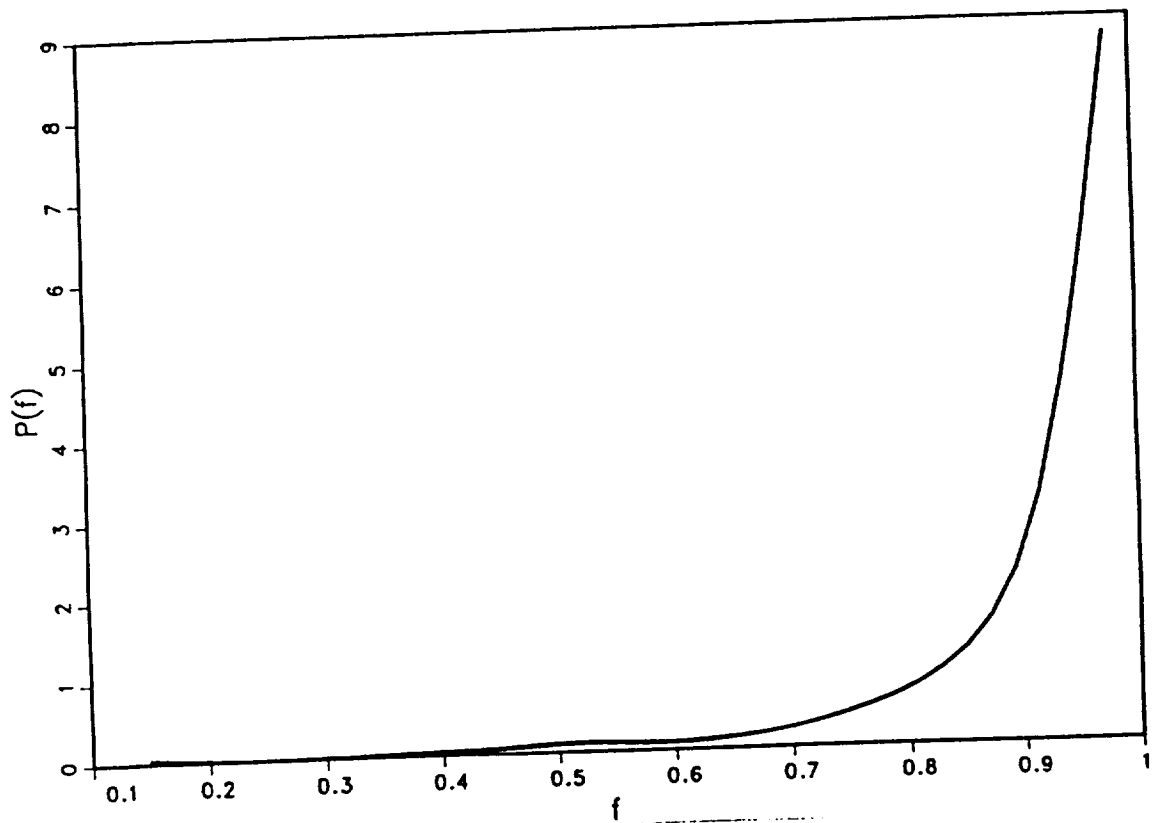


Fig.4.28 Pdf (smoothed) of mixture fraction at $x/D = 6.56$ and $r/D = 0.14$ for a supersonic turbulent round jet flame burning H_2 with a coflowing air stream ($M_a^o = 2.0$ at jet pipe exit).

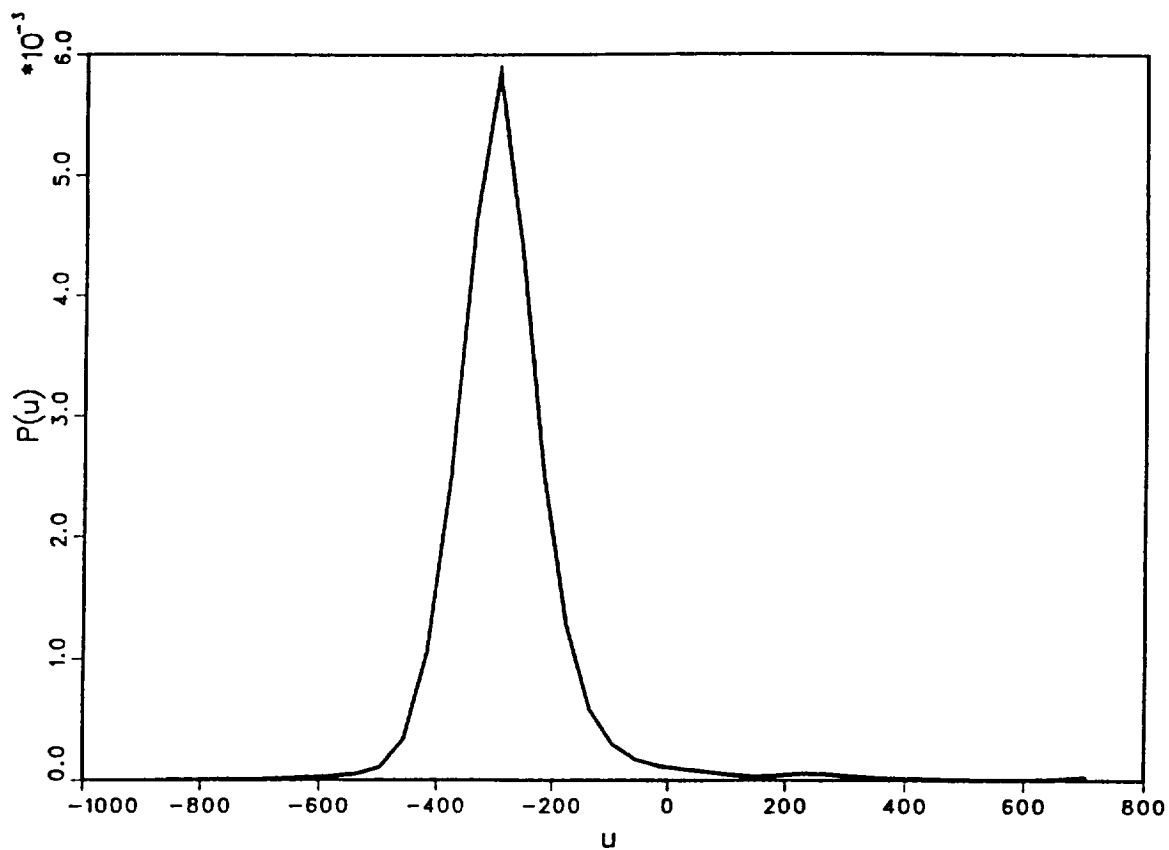


Fig.4.29 Pdf (smoothed) of internal energy at $x/D = 6.56$ and $r/D = 0.14$ for a supersonic turbulent round jet flame burning H_2 with a coflowing air stream ($M_a^\circ = 2.0$ at jet pipe exit).

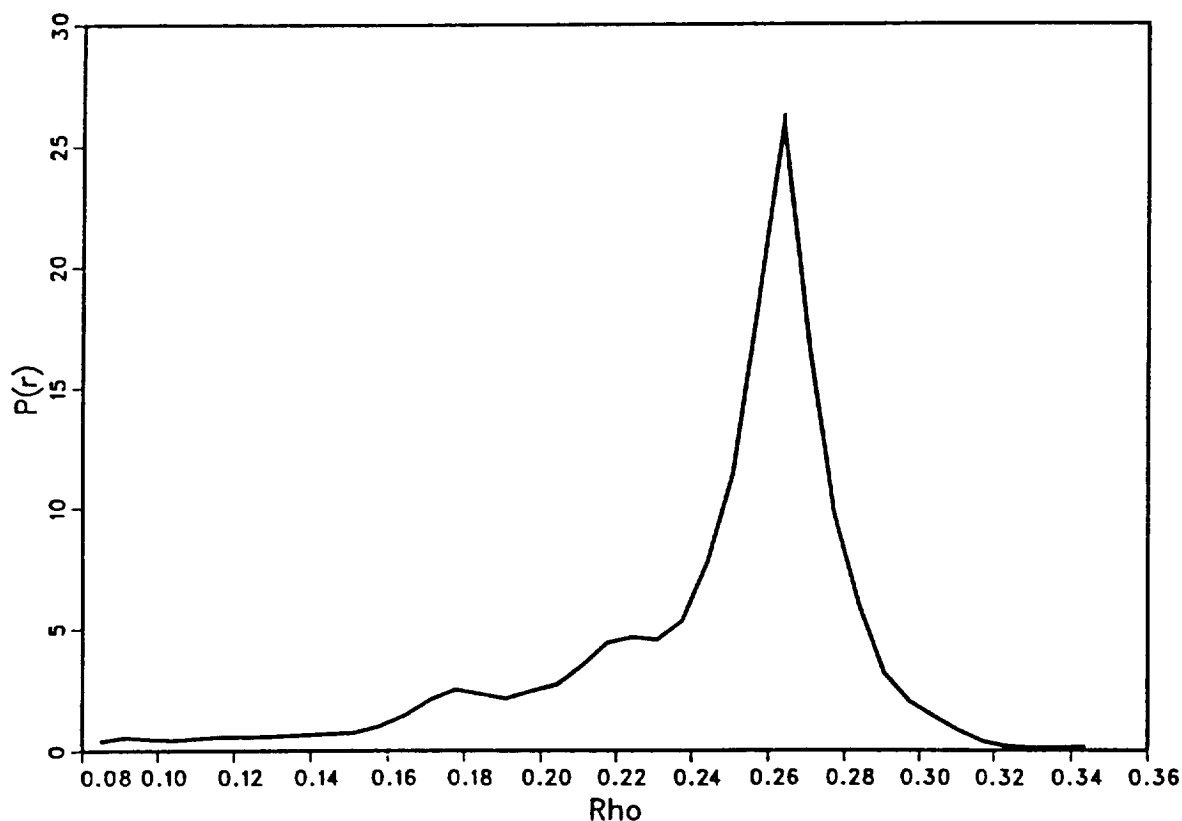


Fig.4.30 Pdf (smoothed) of density at $x/D = 6.56$ and $r/D = 0.14$ for a supersonic turbulent round jet flame burning H_2 with a coflowing air stream ($M_a^\circ = 2.0$ at jet pipe exit).

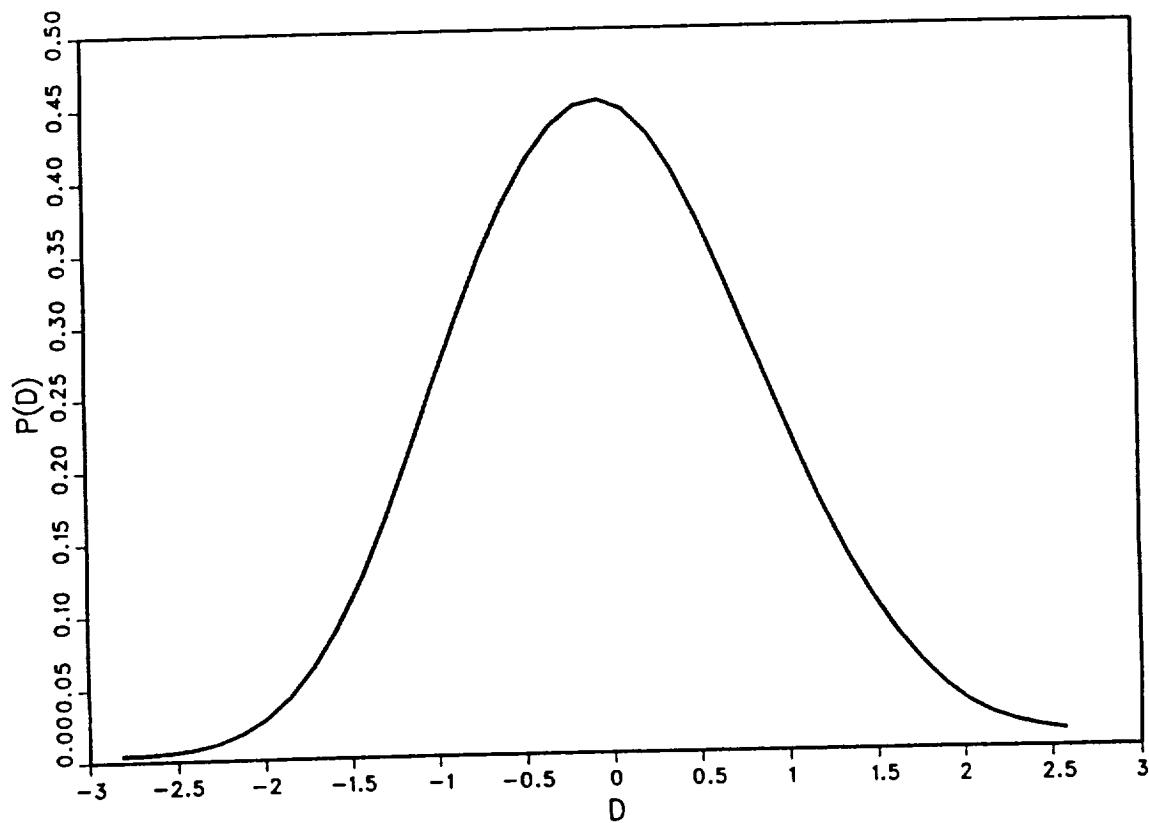


Fig.4.31 Pdf (smoothed) of relative rate of volume expansion at $x/D = 6.56$ and $r/D = 0.14$ for a supersonic turbulent round jet flame burning H_2 with a coflowing air stream ($M_a^\circ = 2.0$ at jet pipe exit).

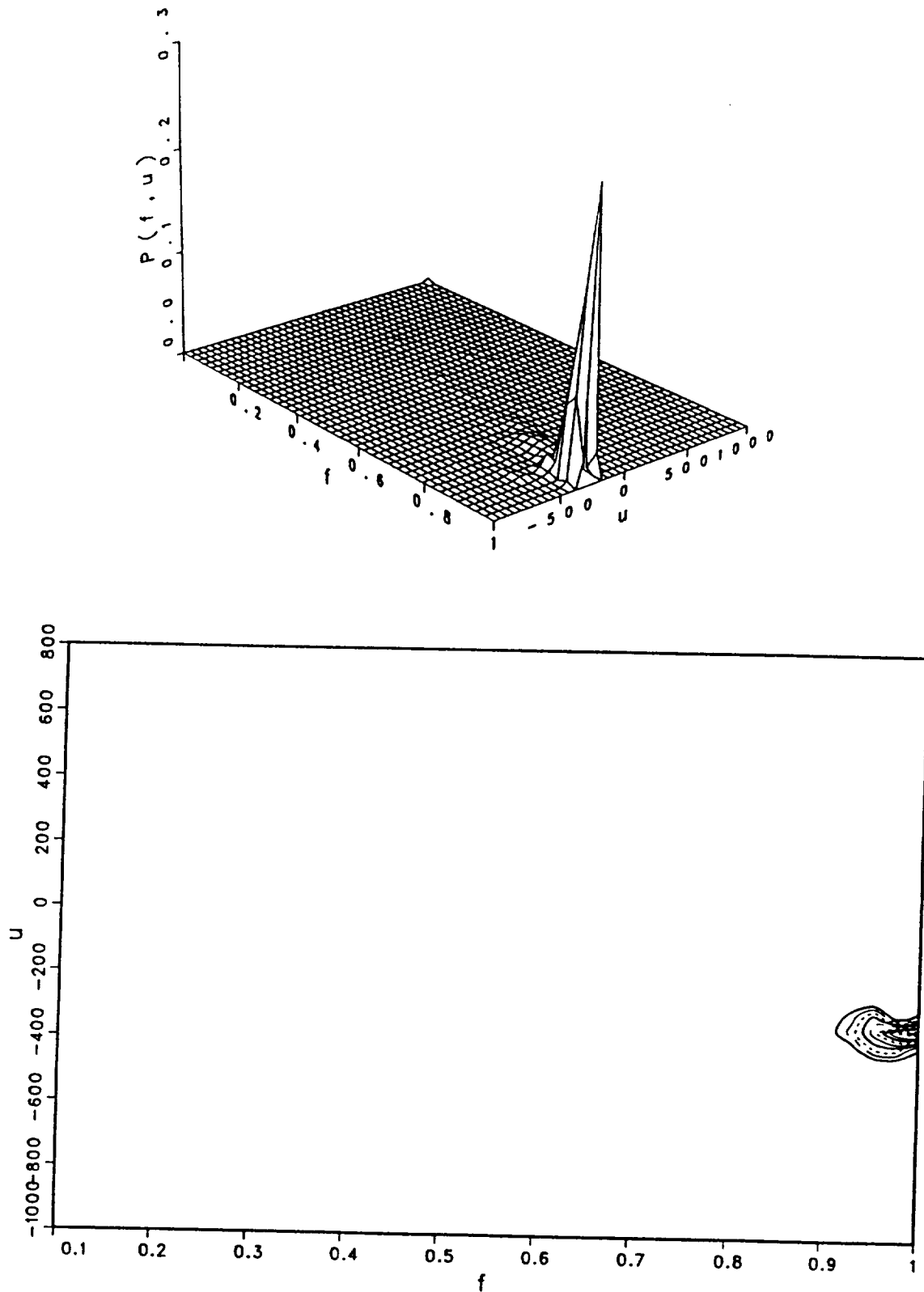


Fig.4.32 Pdf of mixture fraction and internal energy at $x/D = 6.56$ and $r/D = 0.14$ for a supersonic turbulent round jet flame burning H_2 with a coflowing air stream ($M_a^o = 2.0$ at jet pipe exit). Lower plot contains the same pdf in the form of iso-probability lines.

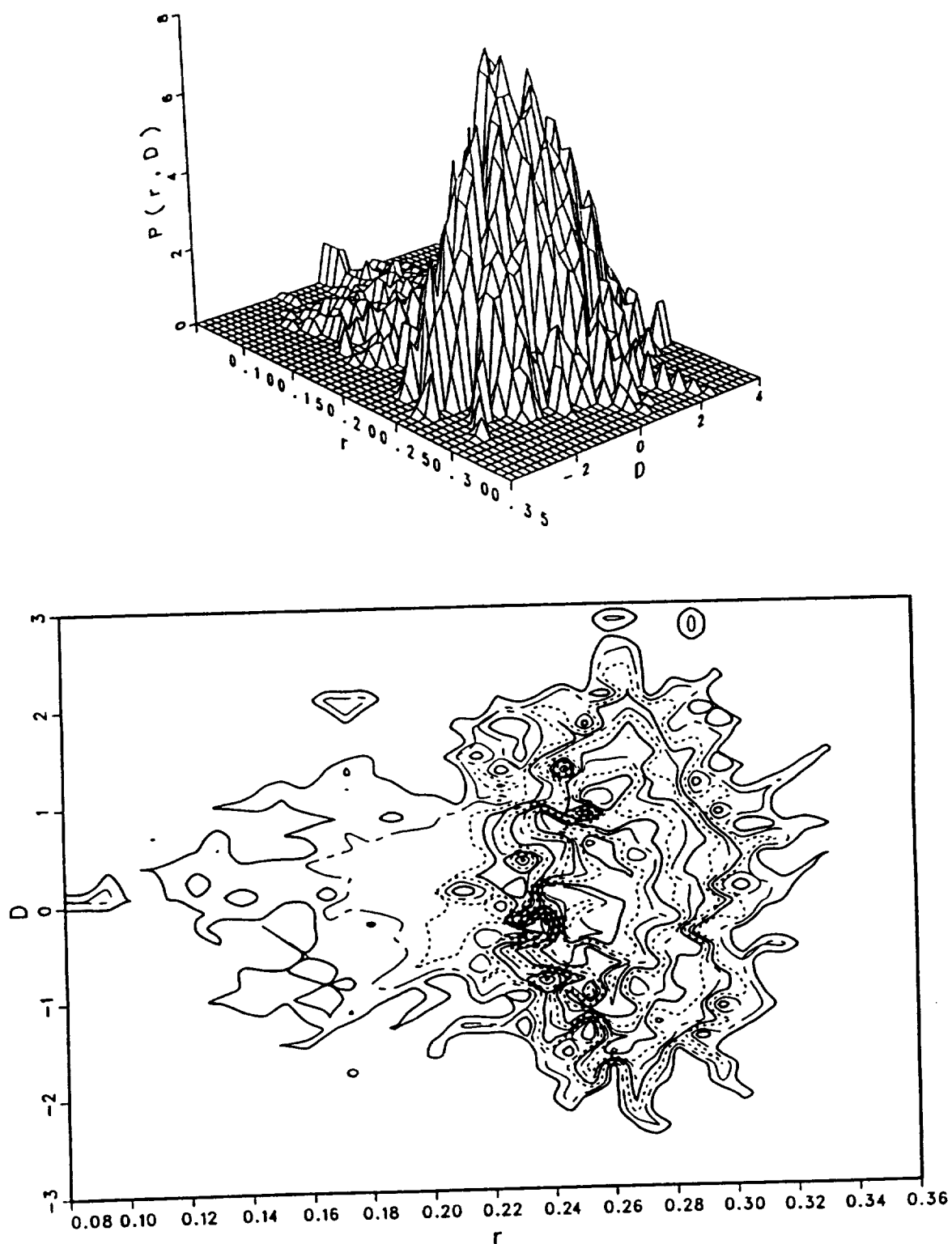


Fig.4.33 Pdf of density and relative rate of volume expansion at $x/D = 6.56$ and $r/D = 0.14$ for a supersonic turbulent round jet flame burning H_2 with a coflowing air stream ($M_a^o = 2.0$ at jet pipe exit). Lower plot contains the same pdf in the form of iso-probability lines.

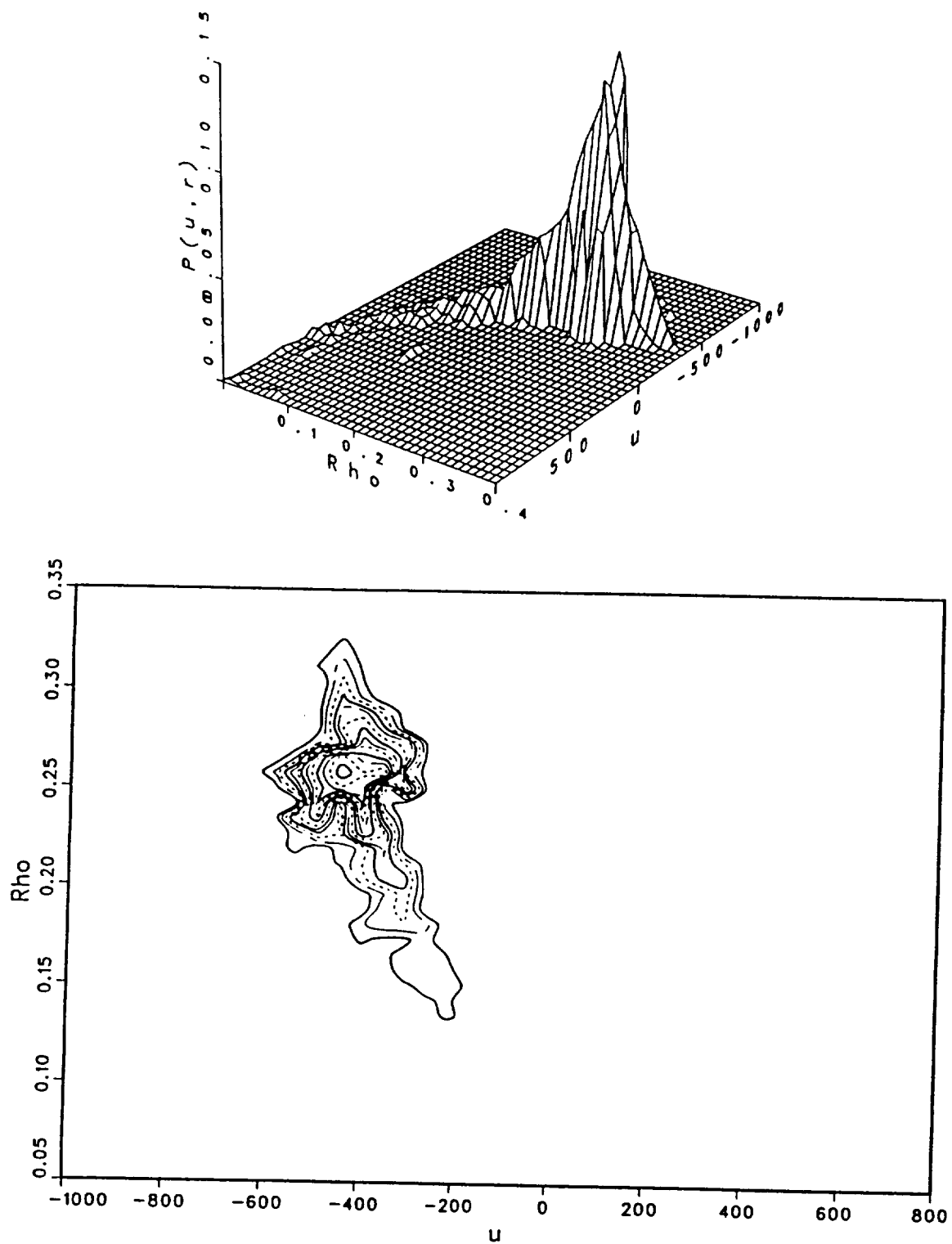


Fig.4.34 Pdf of density and internal energy at $x/D = 6.56$ and $r/D = 0.14$ for a supersonic turbulent round jet flame burning H_2 with a coflowing air stream ($M_a^o = 2.0$ at jet pipe exit). Lower plot contains the same pdf in the form of iso-probability lines.

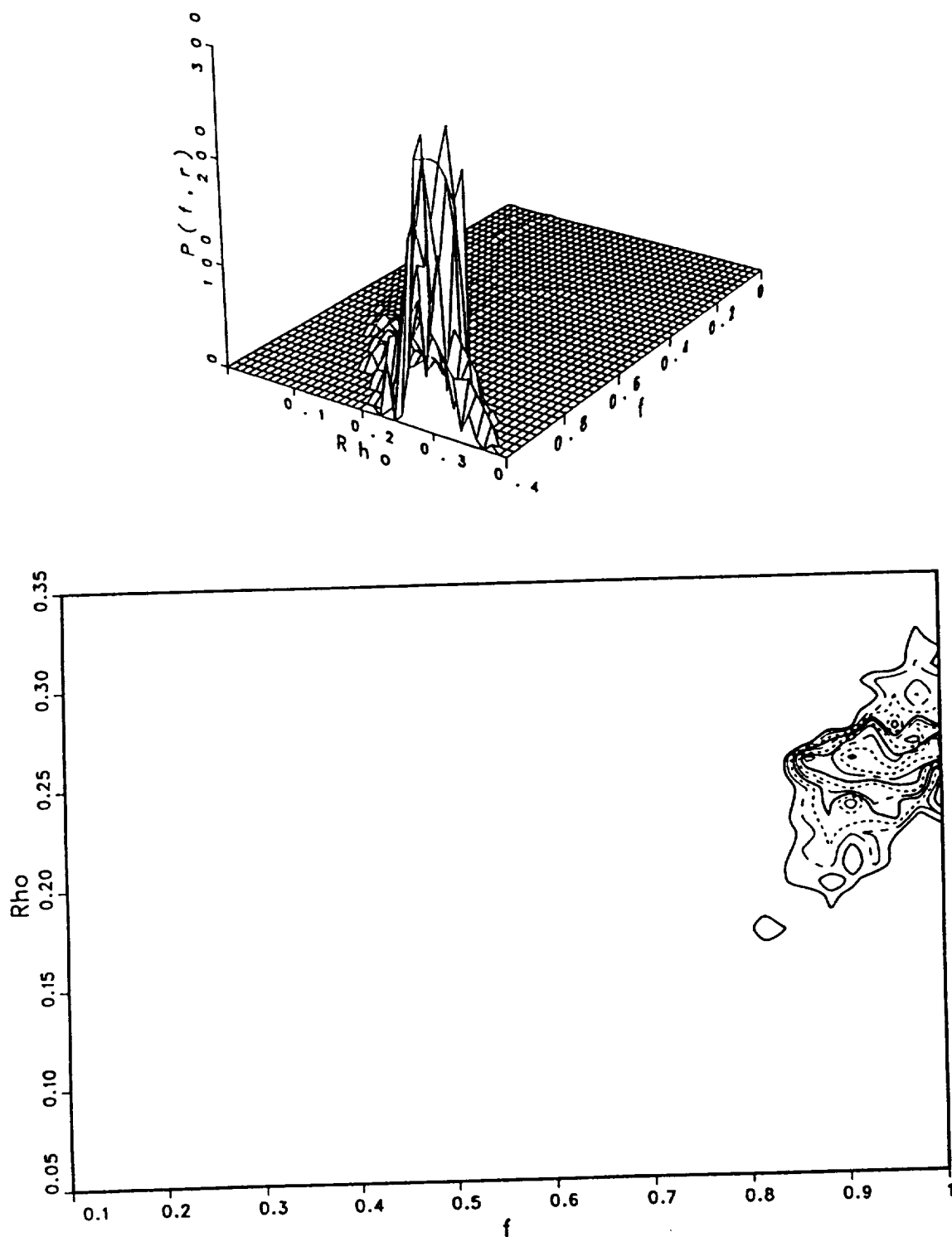


Fig.4.35 Pdf of mixture fraction and density at $x/D = 6.56$ and $r/D = 0.14$ for a supersonic turbulent round jet flame burning H_2 with a coflowing air stream ($M_a^o = 2.0$ at jet pipe exit). Lower plot contains the same pdf in the form of iso-probability lines.

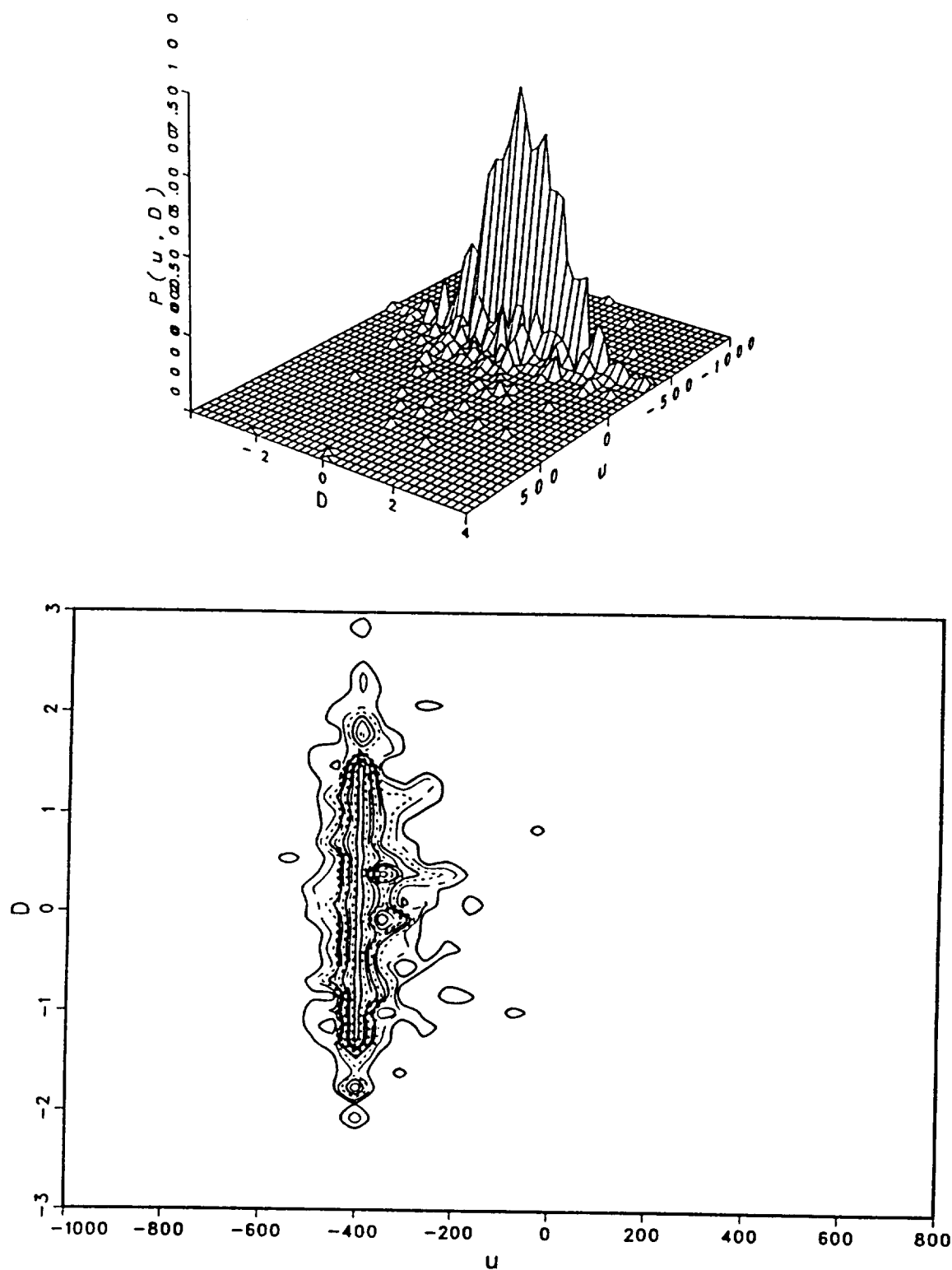


Fig.4.36 Pdf of internal energy and relative rate of volume expansion at $x/D = 6.56$ and $r/D = 0.14$ for a supersonic turbulent round jet flame burning H_2 with a coflowing air stream ($M_a^o = 2.0$ at jet pipe exit). Lower plot contains the same pdf in the form of iso-probability lines.

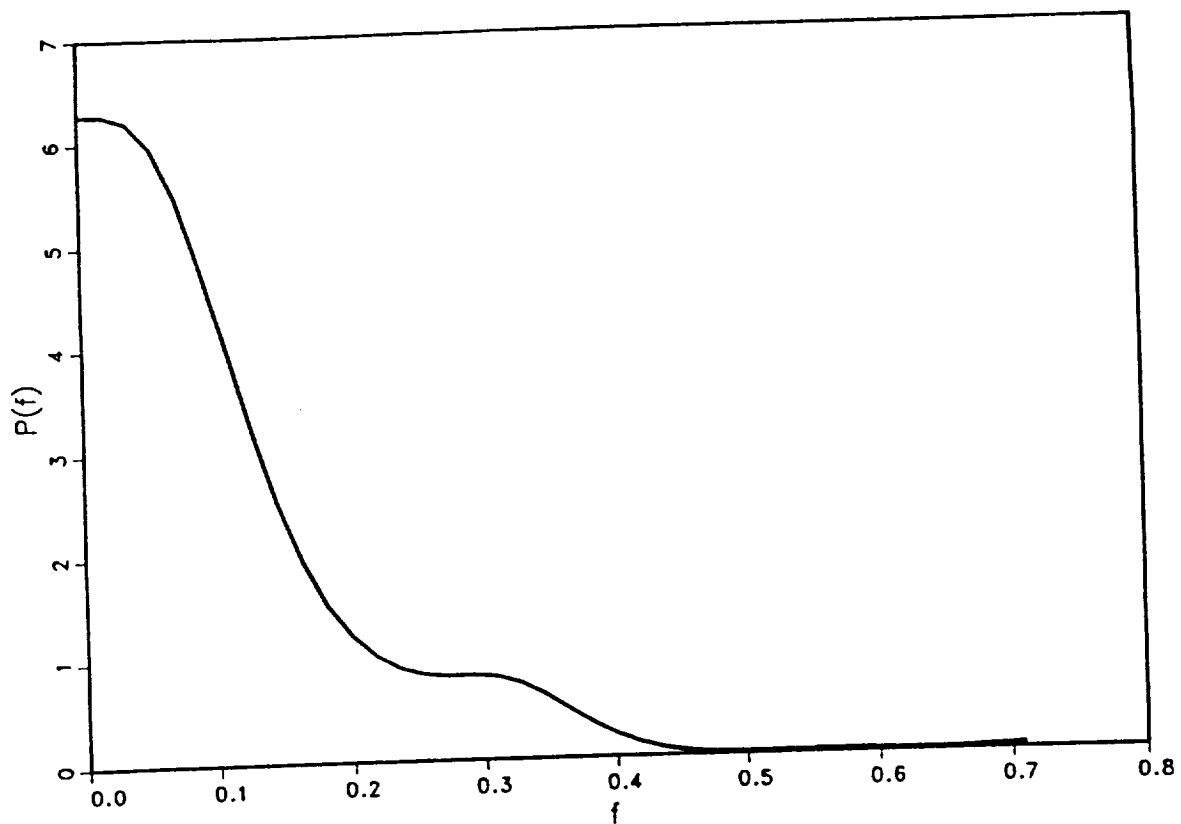


Fig.4.37 Pdf (smoothed) of mixture fraction at $x/D = 6.56$ and $r/D = 0.46$ for a supersonic turbulent round jet flame burning H_2 with a coflowing air stream ($M_a^o = 2.0$ at jet pipe exit).

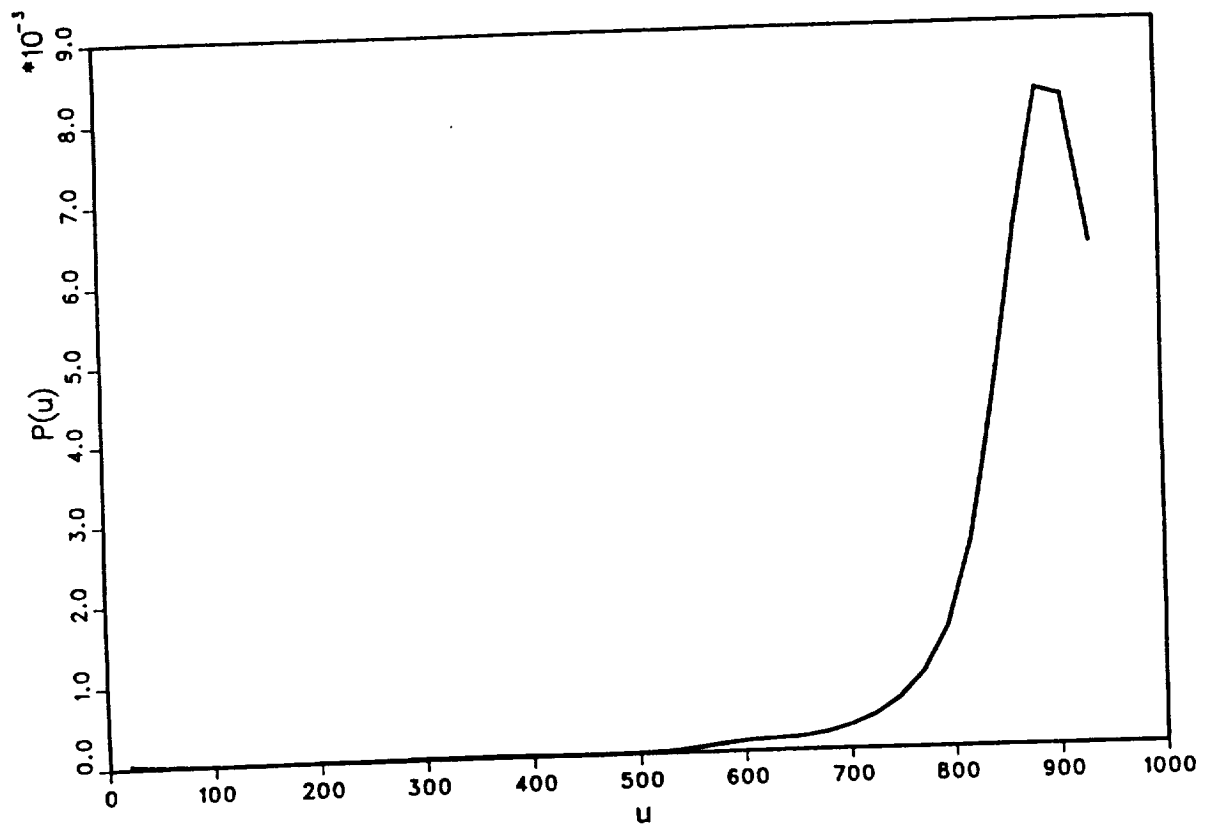


Fig.4.38 Pdf (smoothed) of internal energy at $x/D = 6.56$ and $r/D = 0.46$ for a supersonic turbulent round jet flame burning H_2 with a coflowing air stream ($M_a^o = 2.0$ at jet pipe exit).

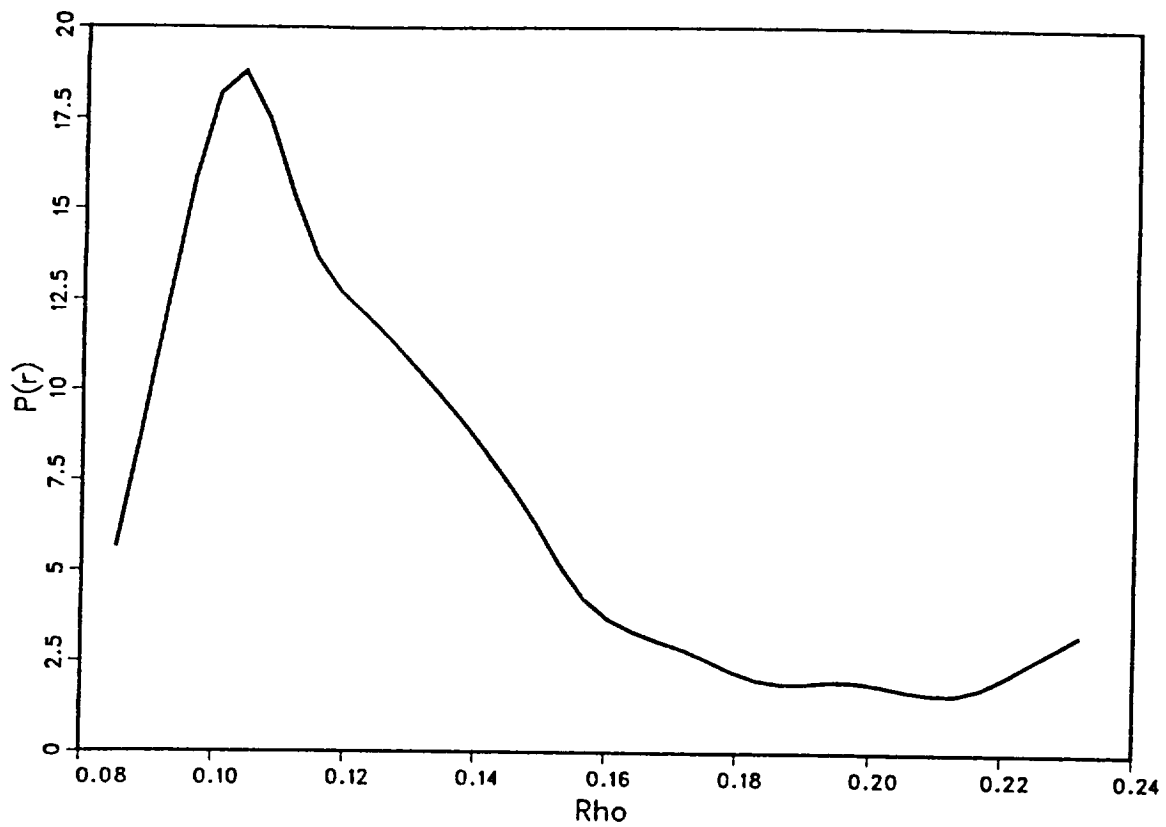


Fig.4.39 Pdf (smoothed) of density at $x/D = 6.56$ and $r/D = 0.46$ for a supersonic turbulent round jet flame burning H_2 with a coflowing air stream ($M_a^o = 2.0$ at jet pipe exit).

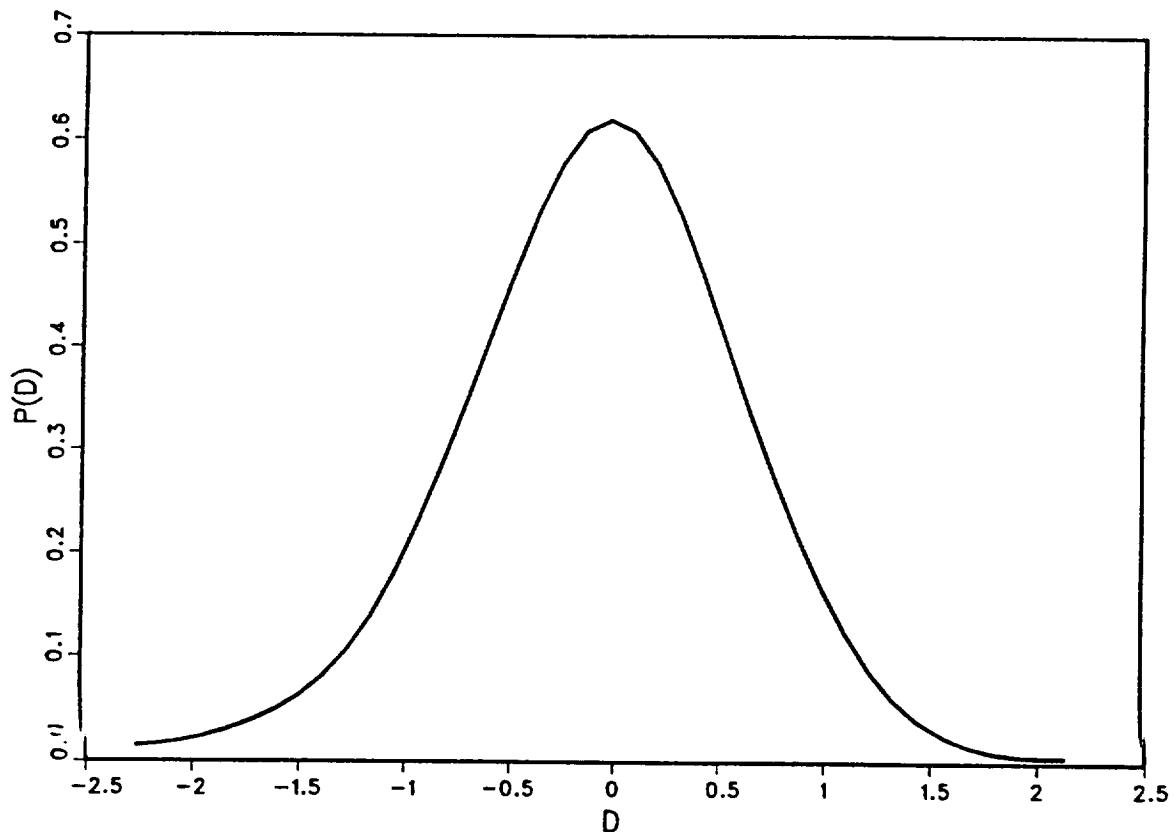


Fig.4.40 Pdf (smoothed) of relative rate of volume expansion at $x/D = 6.56$ and $r/D = 0.46$ for a supersonic turbulent round jet flame burning H_2 with a coflowing air stream ($M_a^o = 2.0$ at jet pipe exit).

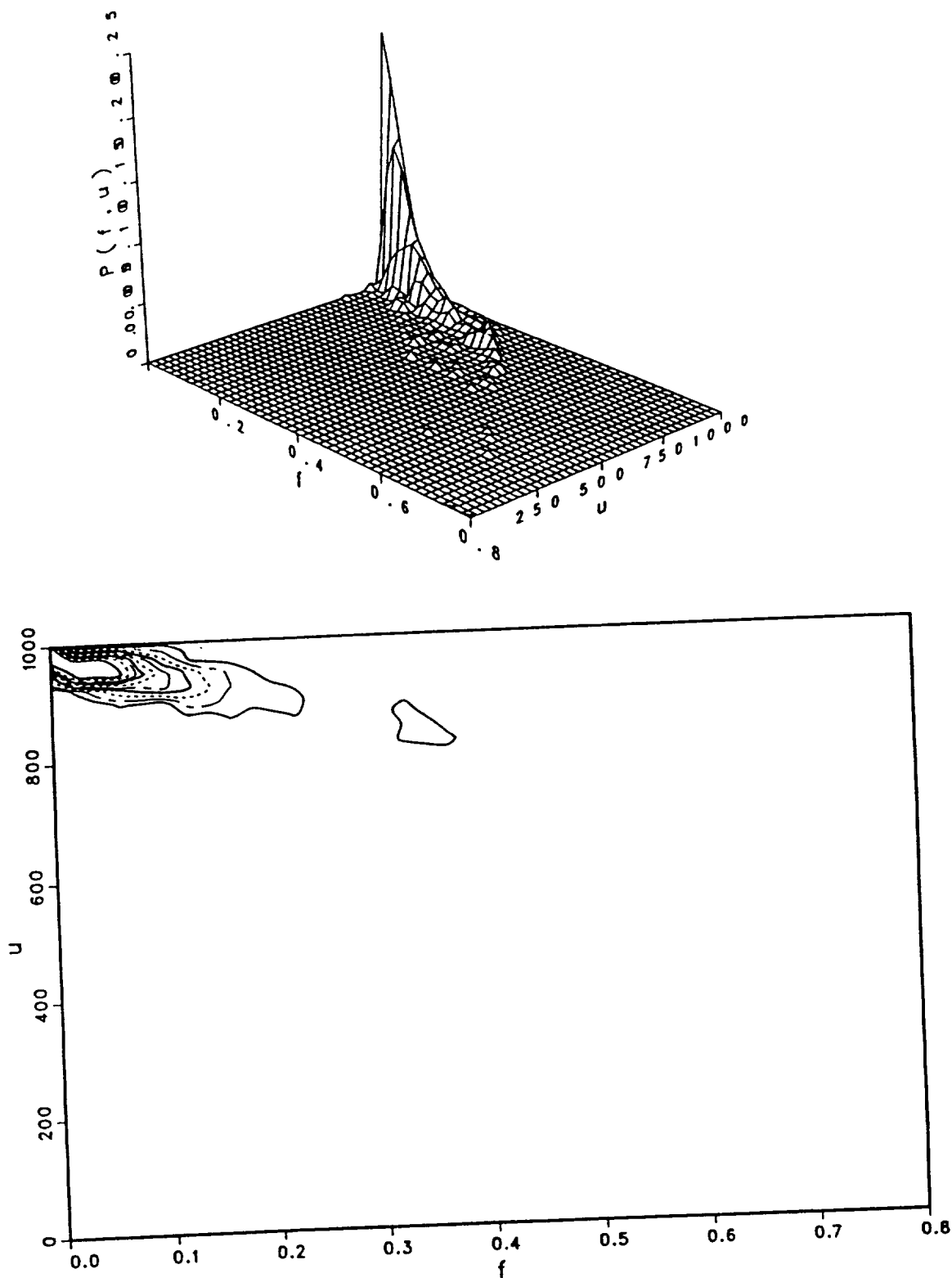


Fig.4.41 Pdf of mixture fraction and internal energy at $x/D = 6.56$ and $r/D = 0.46$ for a supersonic turbulent round jet flame burning H_2 with a coflowing air stream ($M_a^o = 2.0$ at jet pipe exit). Lower plot contains the same pdf in the form of iso-probability lines.

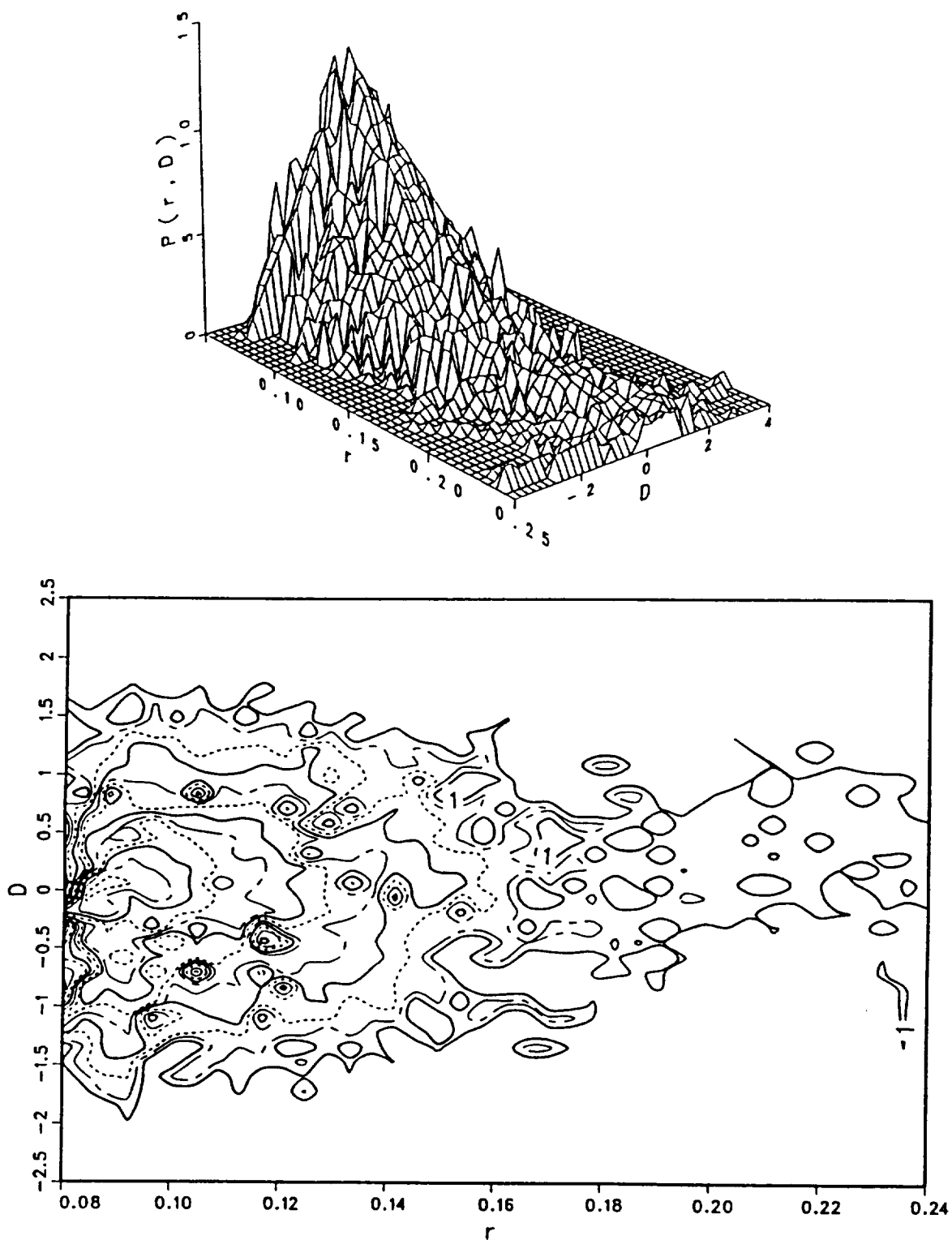


Fig.4.42 Pdf of density and relative rate of volume expansion at $x/D = 6.56$ and $r/D = 0.46$ for a supersonic turbulent round jet flame burning H_2 with a coflowing air stream ($M_a^o = 2.0$ at jet pipe exit). Lower plot contains the same pdf in the form of iso-probability lines.

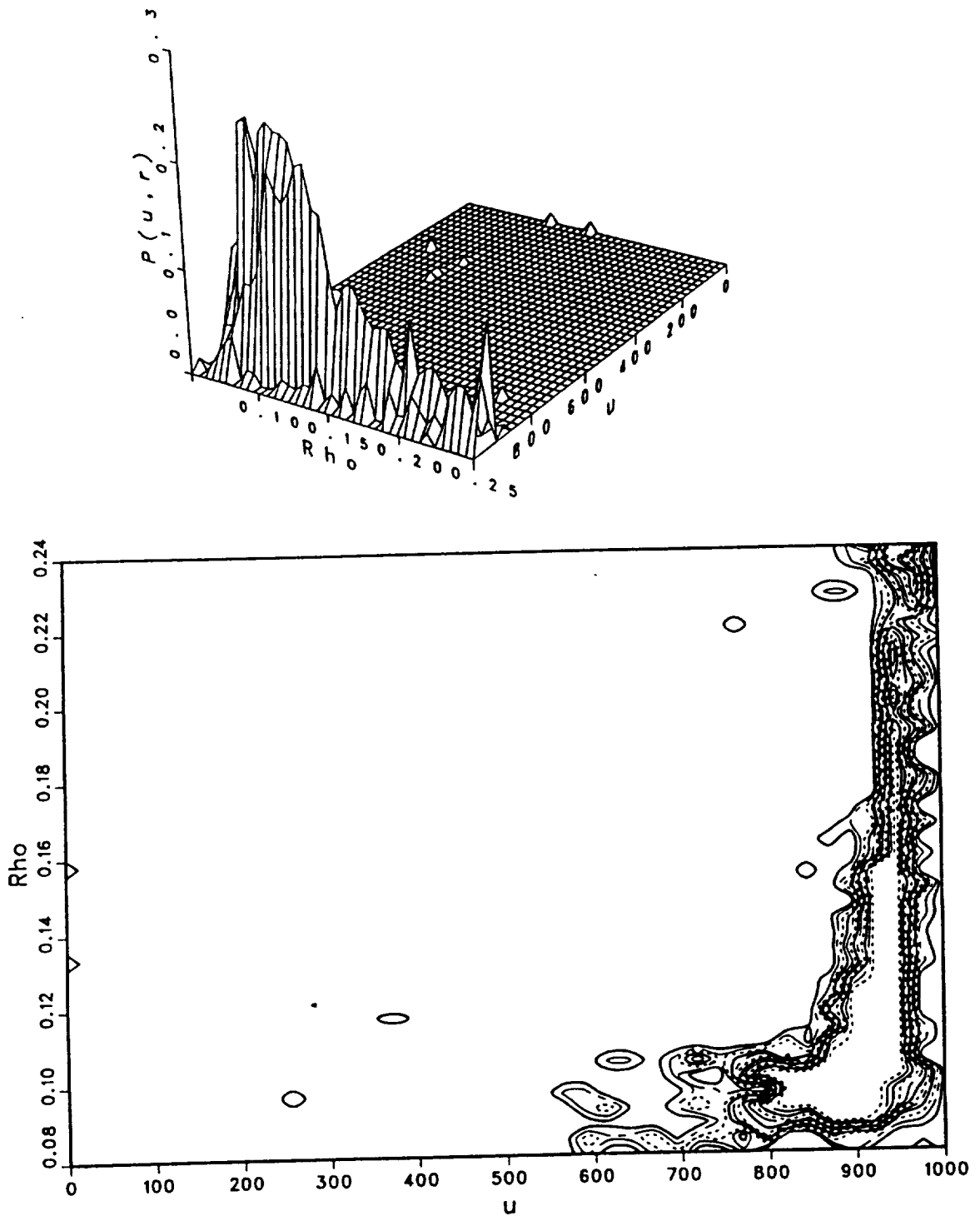


Fig.4.43 Pdf of density and internal energy at $x/D = 6.56$ and $r/D = 0.46$ for a supersonic turbulent round jet flame burning H_2 with a coflowing air stream ($M_a^o = 2.0$ at jet pipe exit). Lower plot contains the same pdf in the form of iso-probability lines.

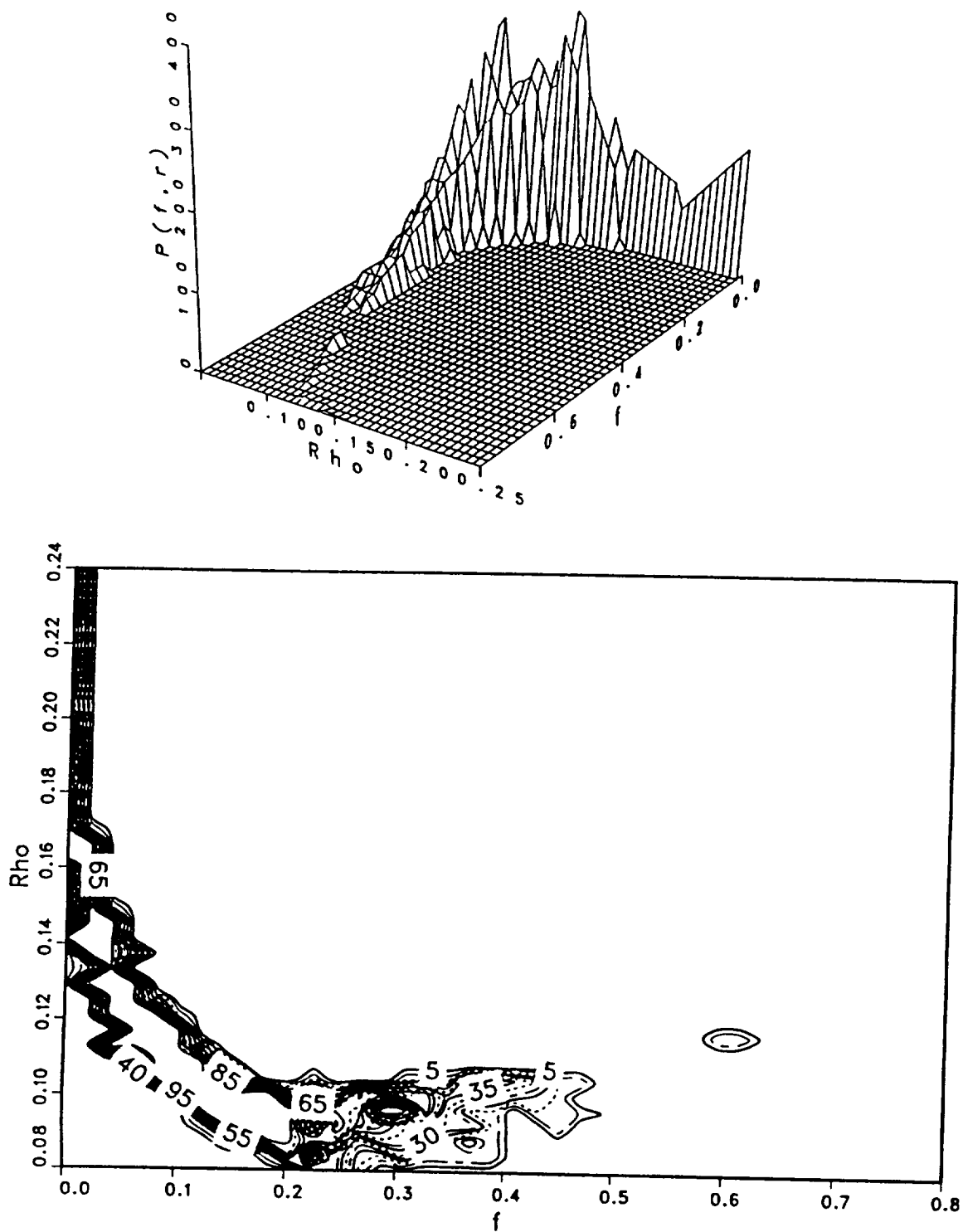


Fig.4.44 Pdf of mixture fraction and density at $x/D = 6.56$ and $r/D = 0.46$ for a supersonic turbulent round jet flame burning H_2 with a coflowing air stream ($M_a^o = 2.0$ at jet pipe exit). Lower plot contains the same pdf in the form of iso-probability lines.

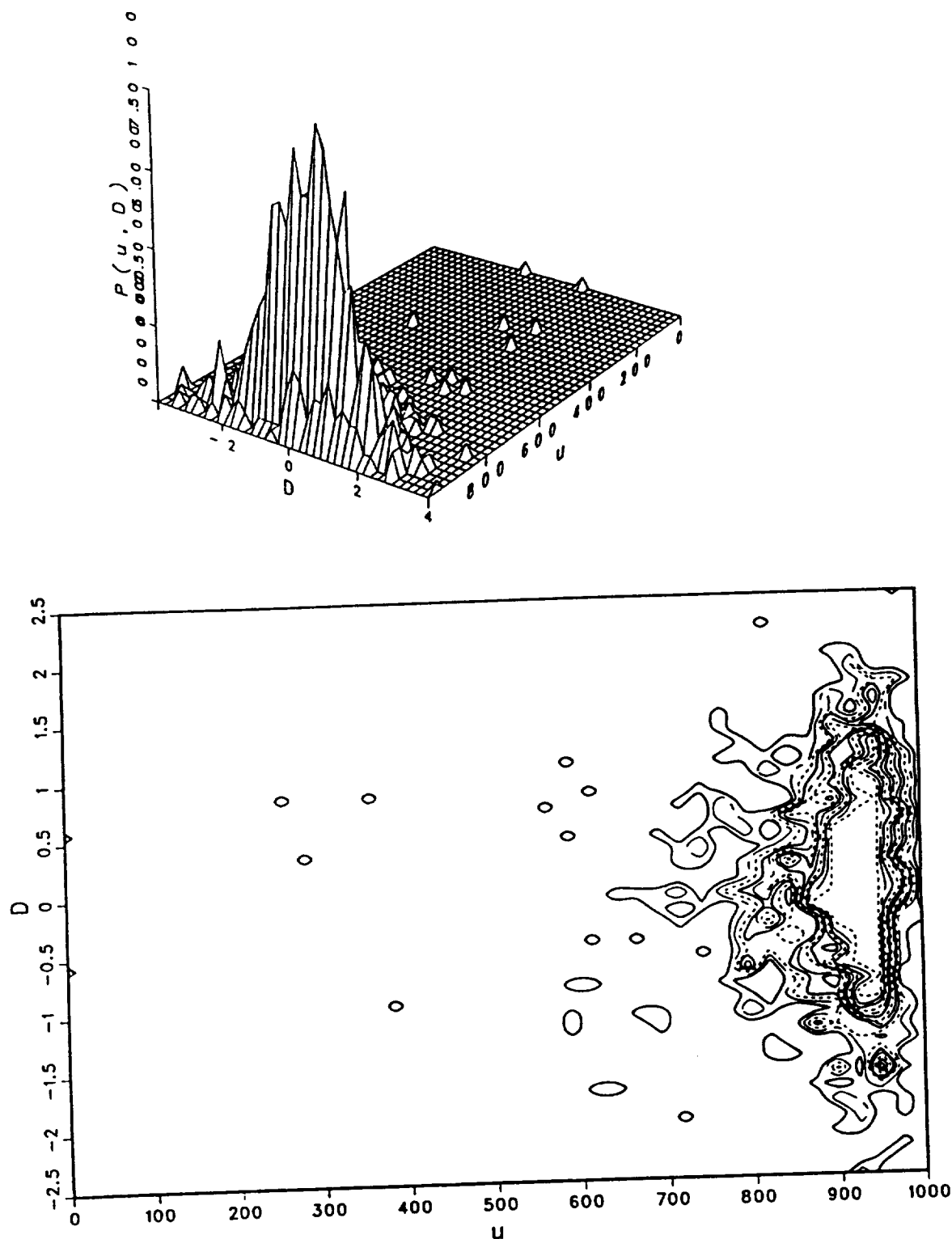


Fig.4.45 Pdf of internal energy and relative rate of volume expansion at $x/D = 6.56$ and $r/D = 0.46$ for a supersonic turbulent round jet flame burning H_2 with a coflowing air stream ($M_a^o = 2.0$ at jet pipe exit). Lower plot contains the same pdf in the form of iso-probability lines.

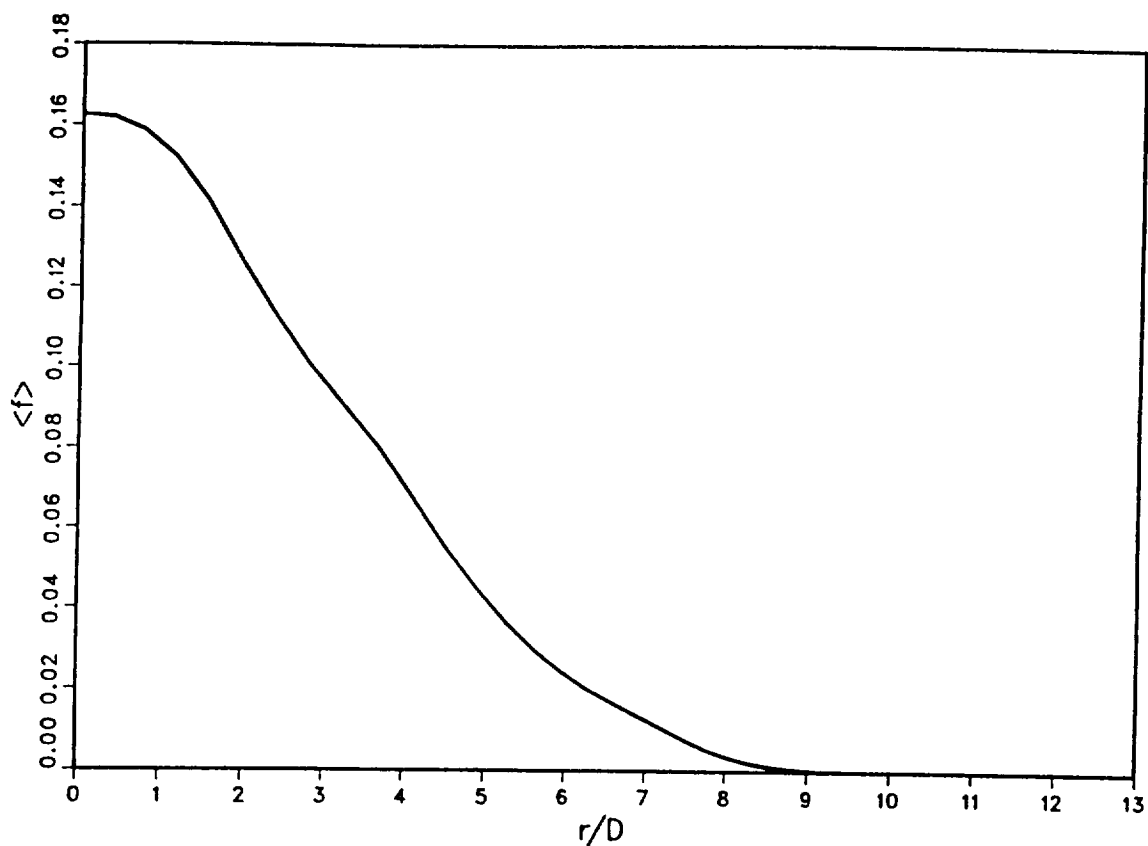


Fig.4.46 Mean mixture fraction at $x/D = 30.14$ for a supersonic turbulent round jet flame burning H_2 with a coflowing air stream ($M_a^o = 2.0$ at jet pipe exit).

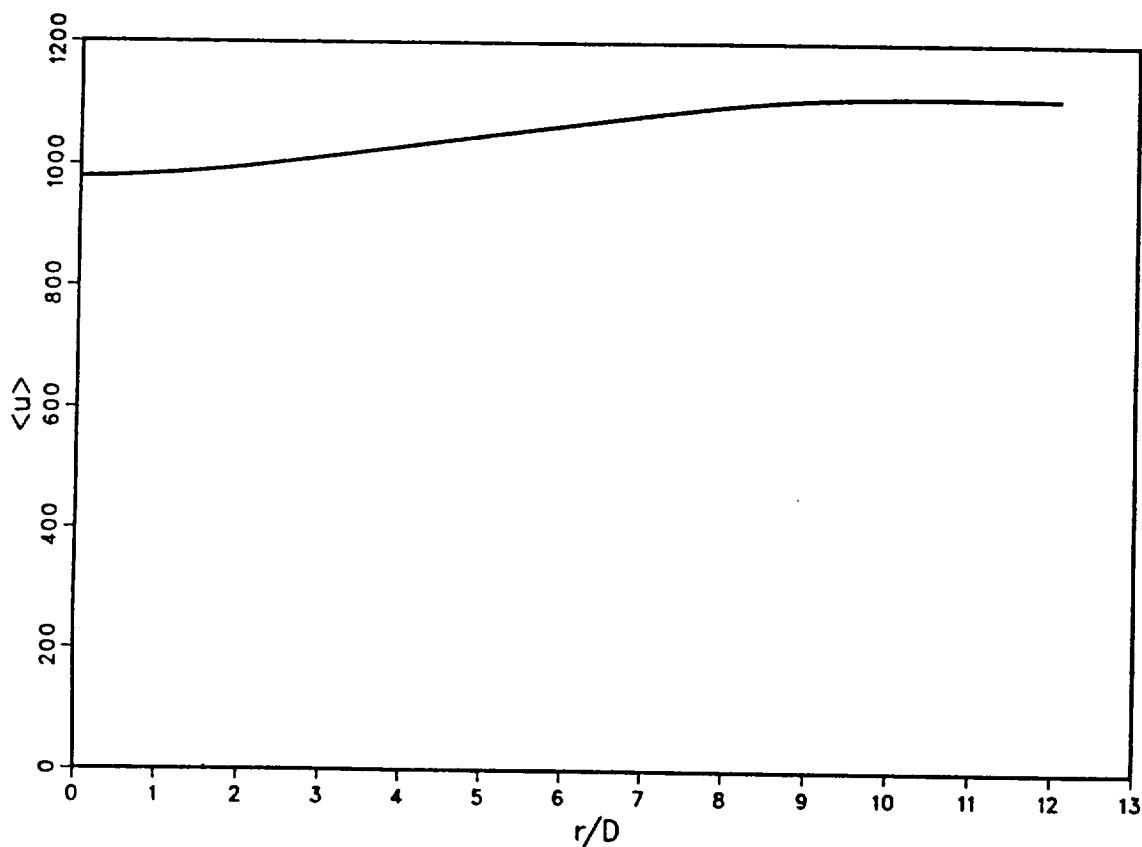


Fig.4.47 Mean internal energy at $x/D = 30.14$ for a supersonic turbulent round jet flame burning H_2 with a coflowing air stream ($M_a^o = 2.0$ at jet pipe exit).

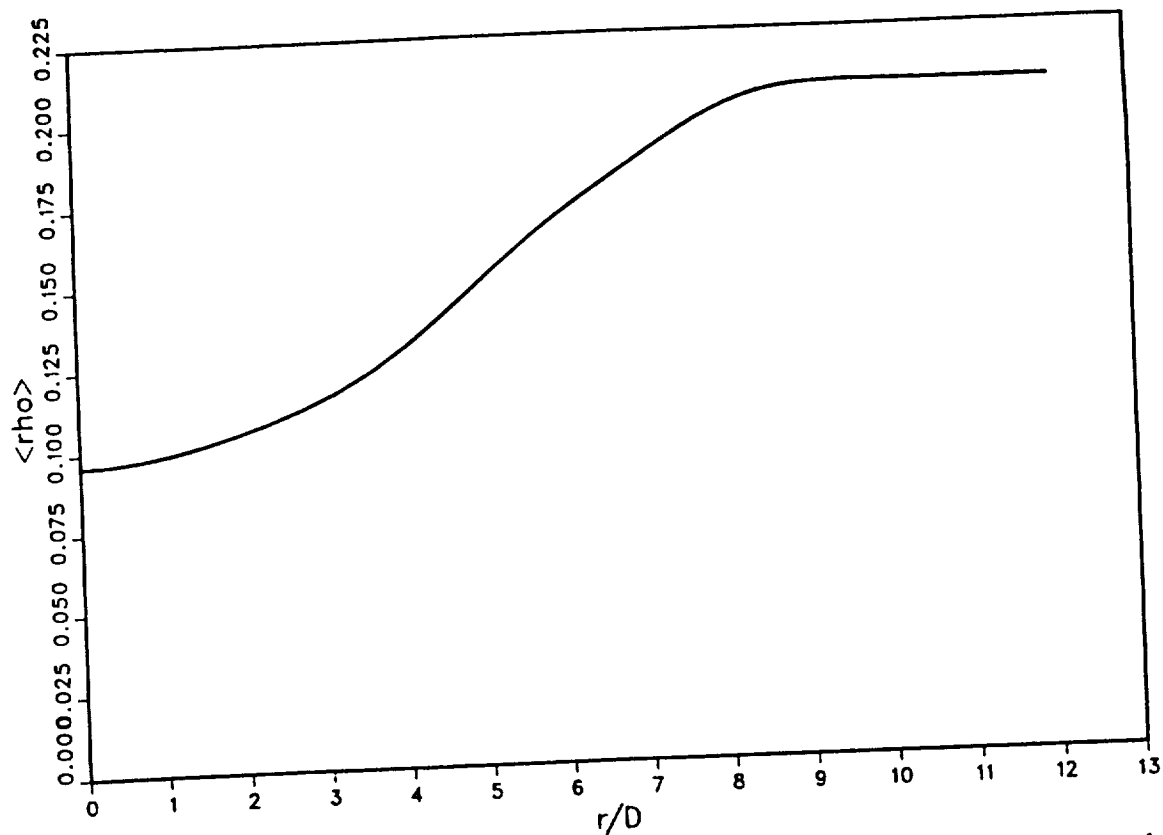


Fig.4.48 Mean density at $x/D = 30.14$ for a supersonic turbulent round jet flame burning H_2 with a coflowing air stream ($M_a^o = 2.0$ at jet pipe exit).

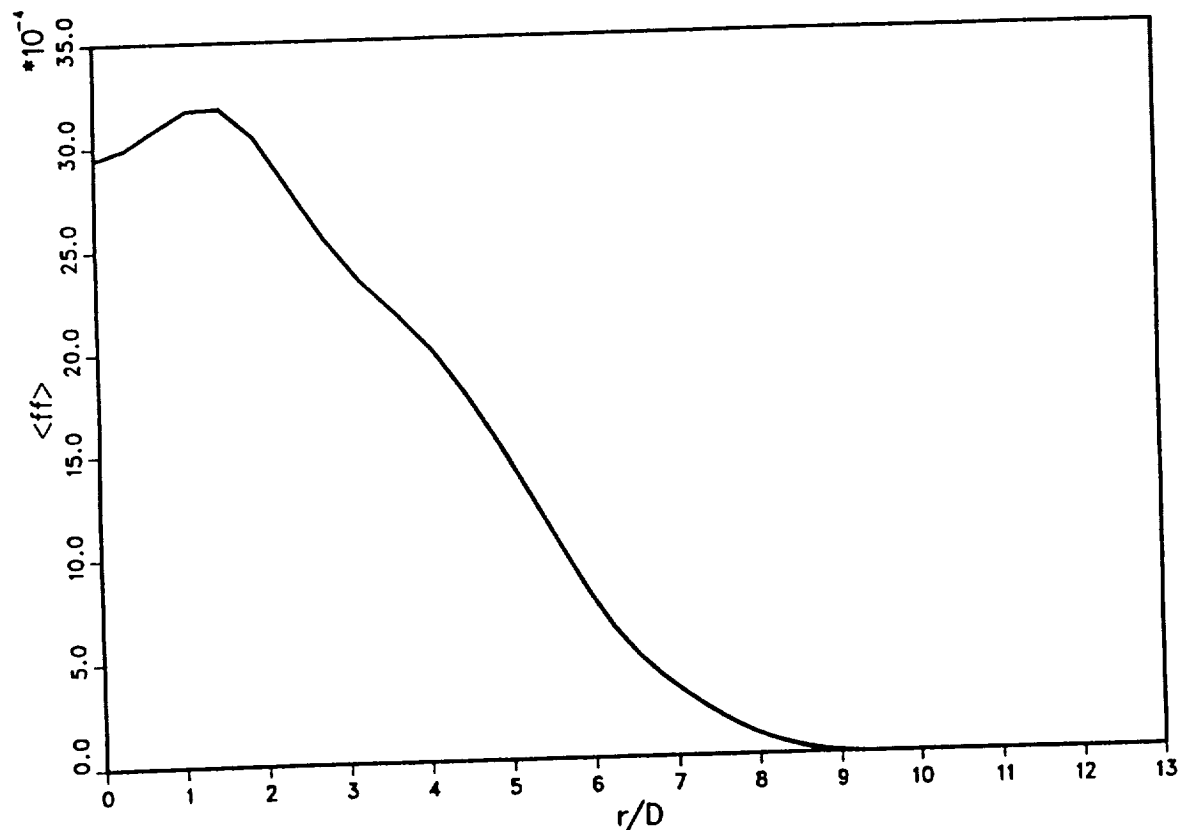


Fig.4.49 Variance of mixture fraction at $x/D = 30.14$ for a supersonic turbulent round jet flame burning H_2 with a coflowing air stream ($M_a^o = 2.0$ at jet pipe exit).

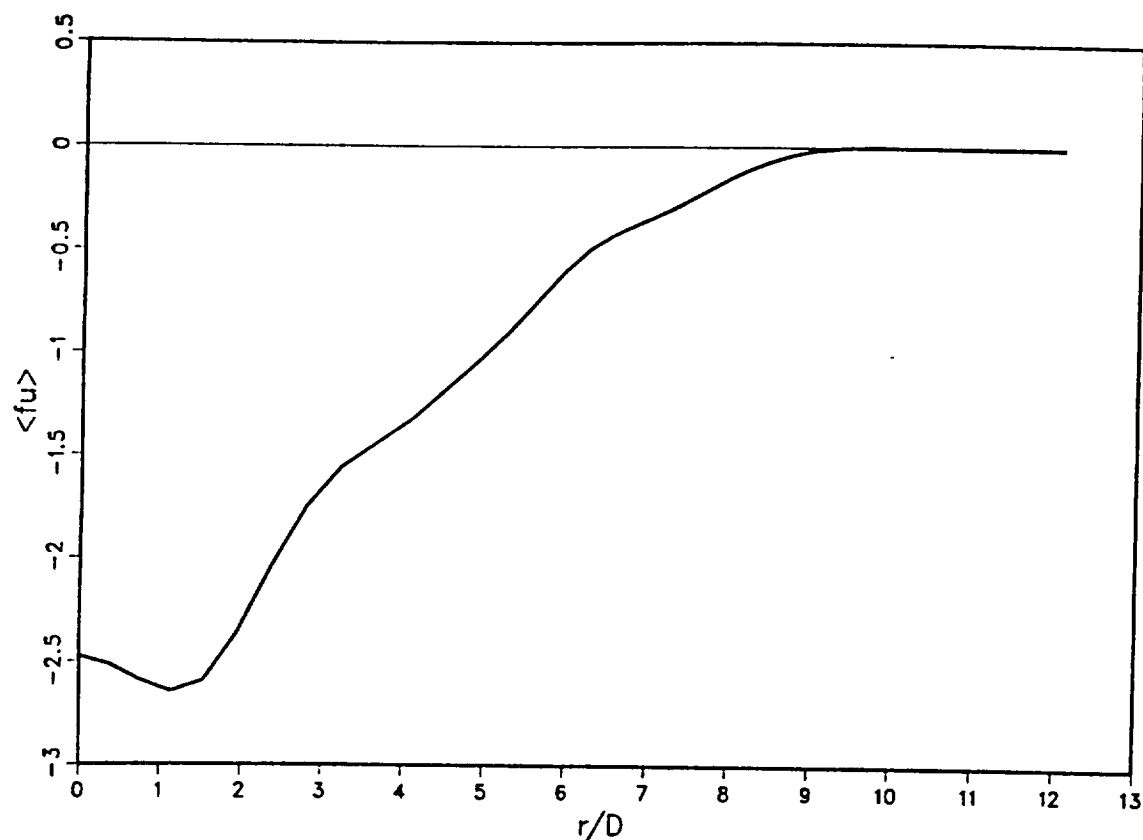


Fig.4.50 Covariance of mixture fraction and internal energy at $x/D = 30.14$ for a supersonic turbulent round jet flame burning H_2 with a coflowing air stream ($M_a^\circ = 2.0$ at jet pipe exit).

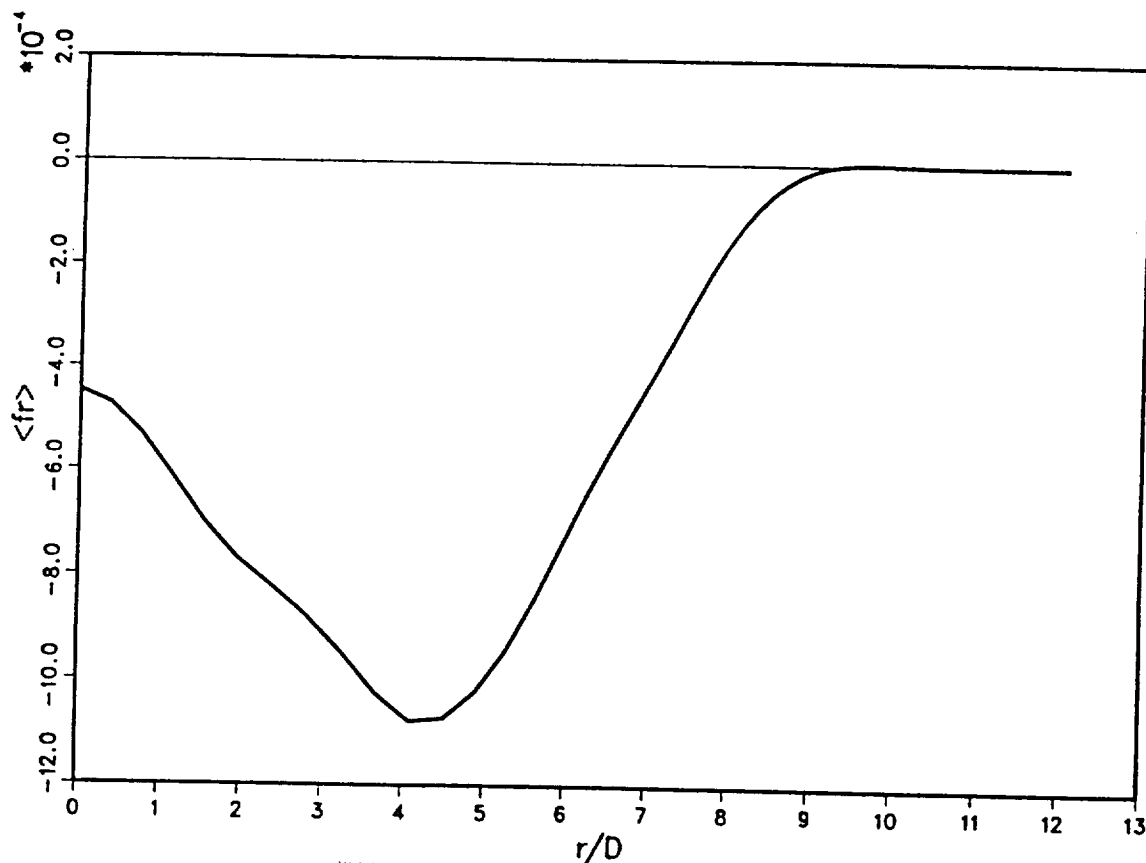


Fig.4.51 Covariance of mixture fraction and density at $x/D = 30.14$ for a supersonic turbulent round jet flame burning H_2 with a coflowing air stream ($M_a^\circ = 2.0$ at jet pipe exit).

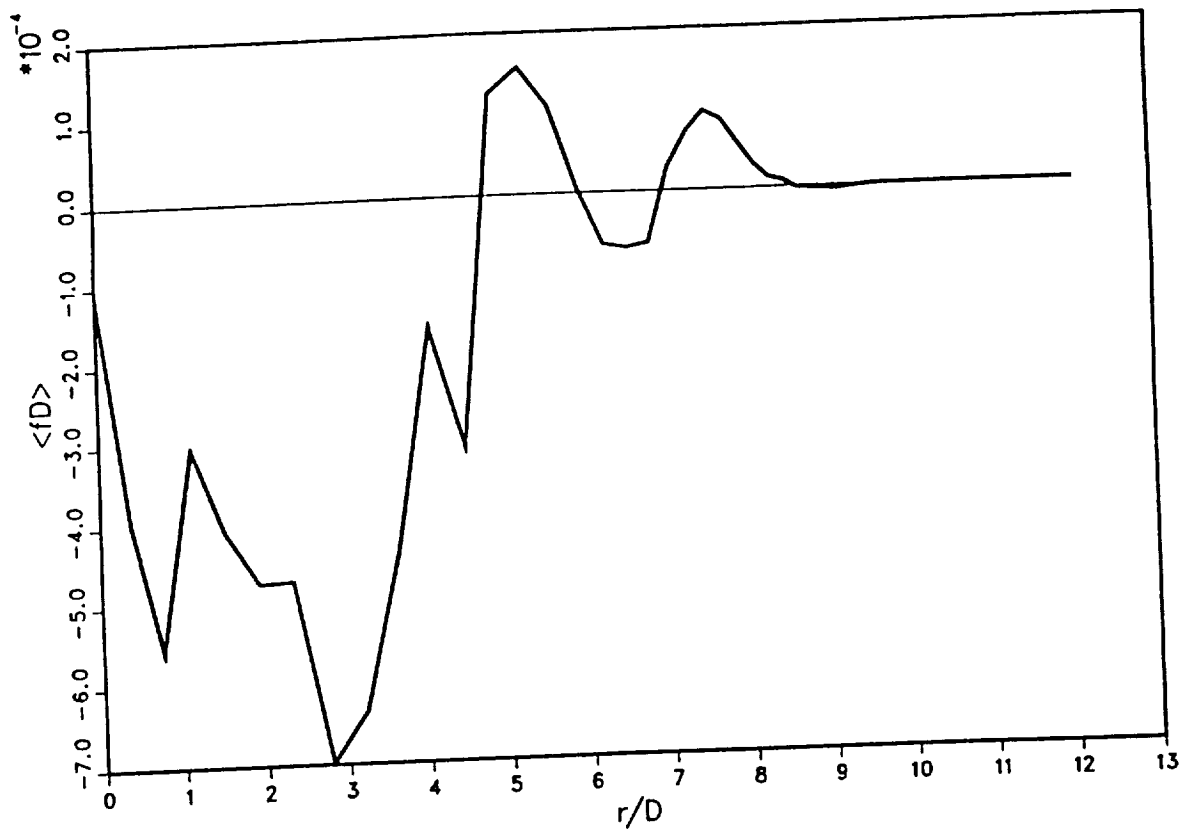


Fig.4.52 Covariance of mixture fraction and relative rate of volume expansion at $x/D = 30.14$ for a supersonic turbulent round jet flame burning H_2 with a coflowing air stream ($M_a^o = 2.0$ at jet pipe exit).

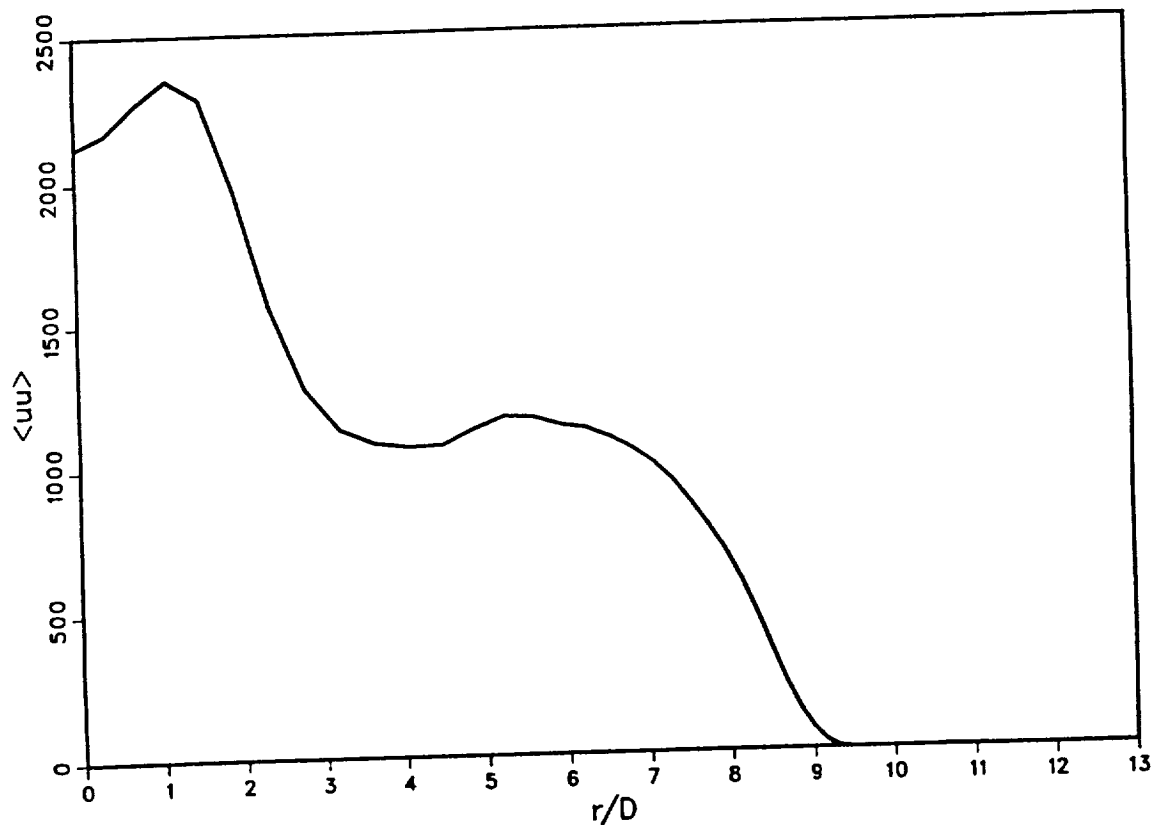


Fig.4.53 Variance of internal energy at $x/D = 30.14$ for a supersonic turbulent round jet flame burning H_2 with a coflowing air stream ($M_a^o = 2.0$ at jet pipe exit).

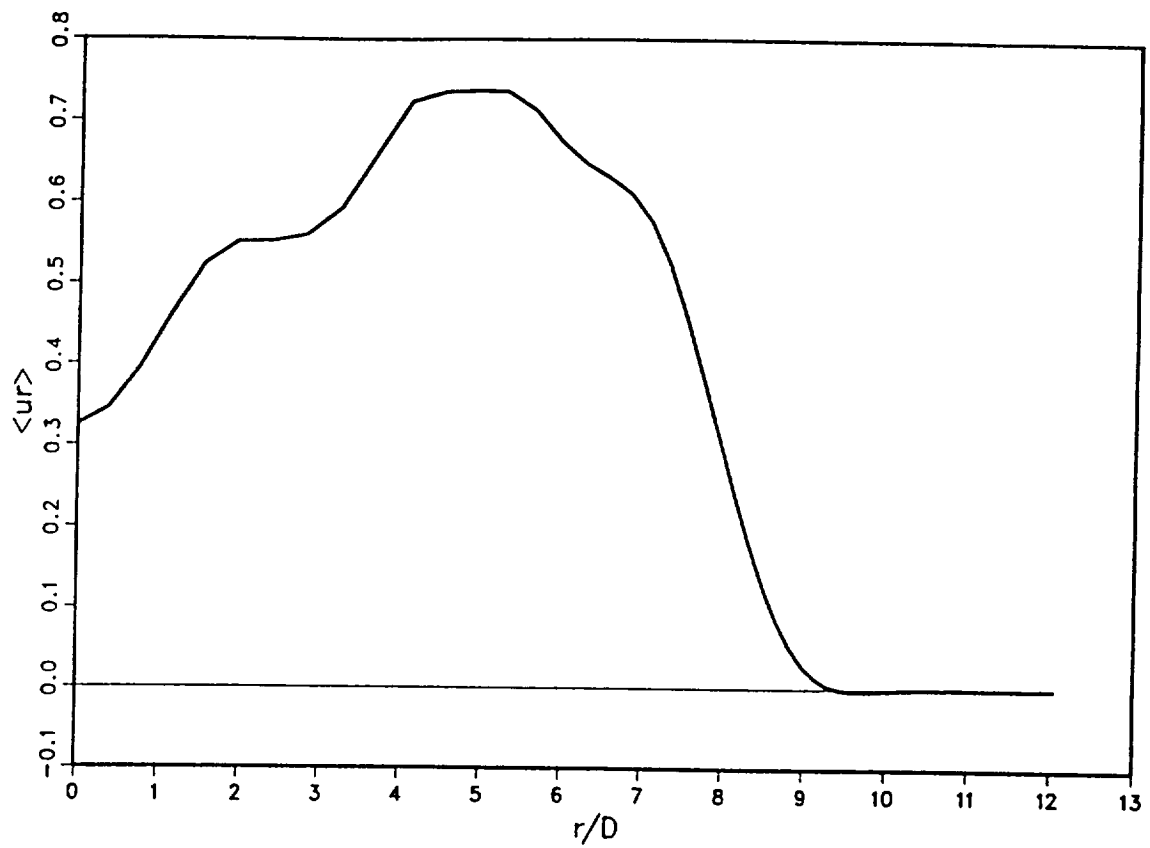


Fig.4.54 Covariance of density and internal energy at $x/D = 30.14$ for a supersonic turbulent round jet flame burning H_2 with a coflowing air stream ($M_a^o = 2.0$ at jet pipe exit).

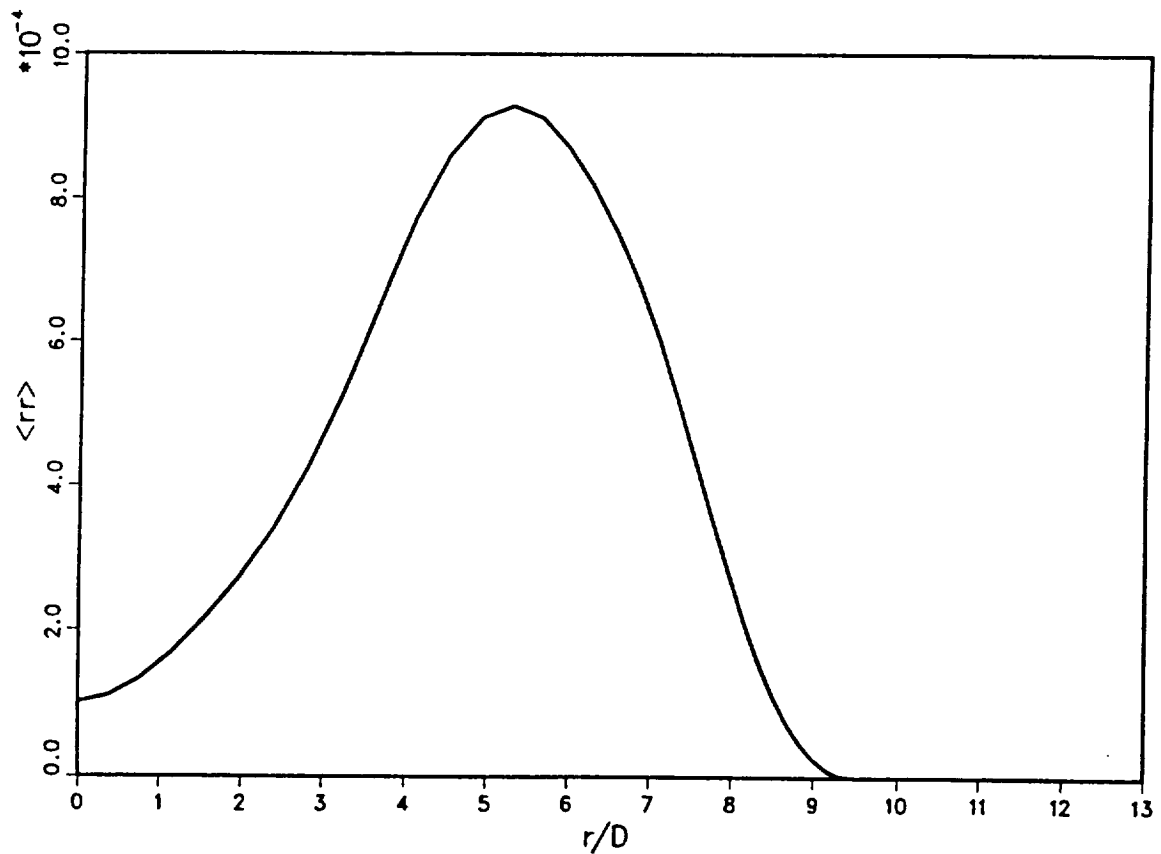


Fig.4.55 Variance of density at $x/D = 30.14$ for a supersonic turbulent round jet flame burning H_2 with a coflowing air stream ($M_a^o = 2.0$ at jet pipe exit).

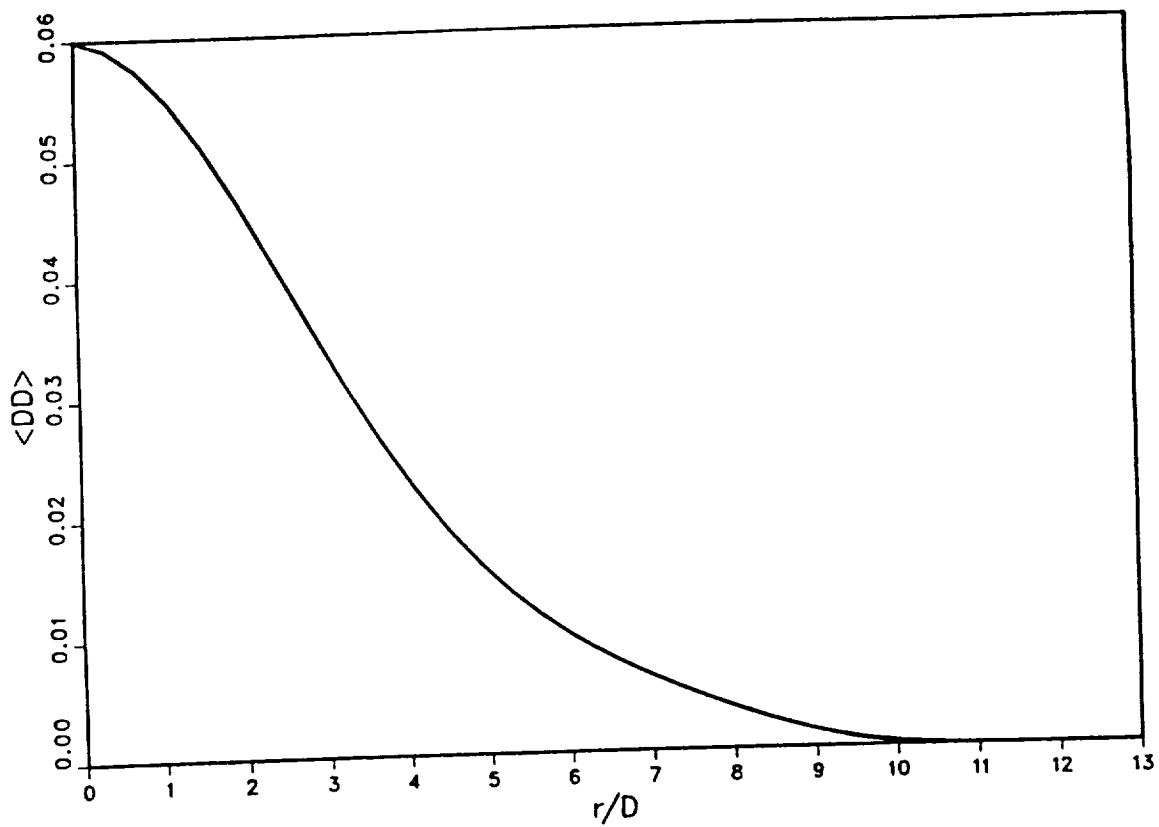


Fig.4.56 Variance of relative rate of volume expansion at $x/D = 30.14$ for a supersonic turbulent round jet flame burning H_2 with a coflowing air stream ($M_a^o = 2.0$ at jet pipe exit).

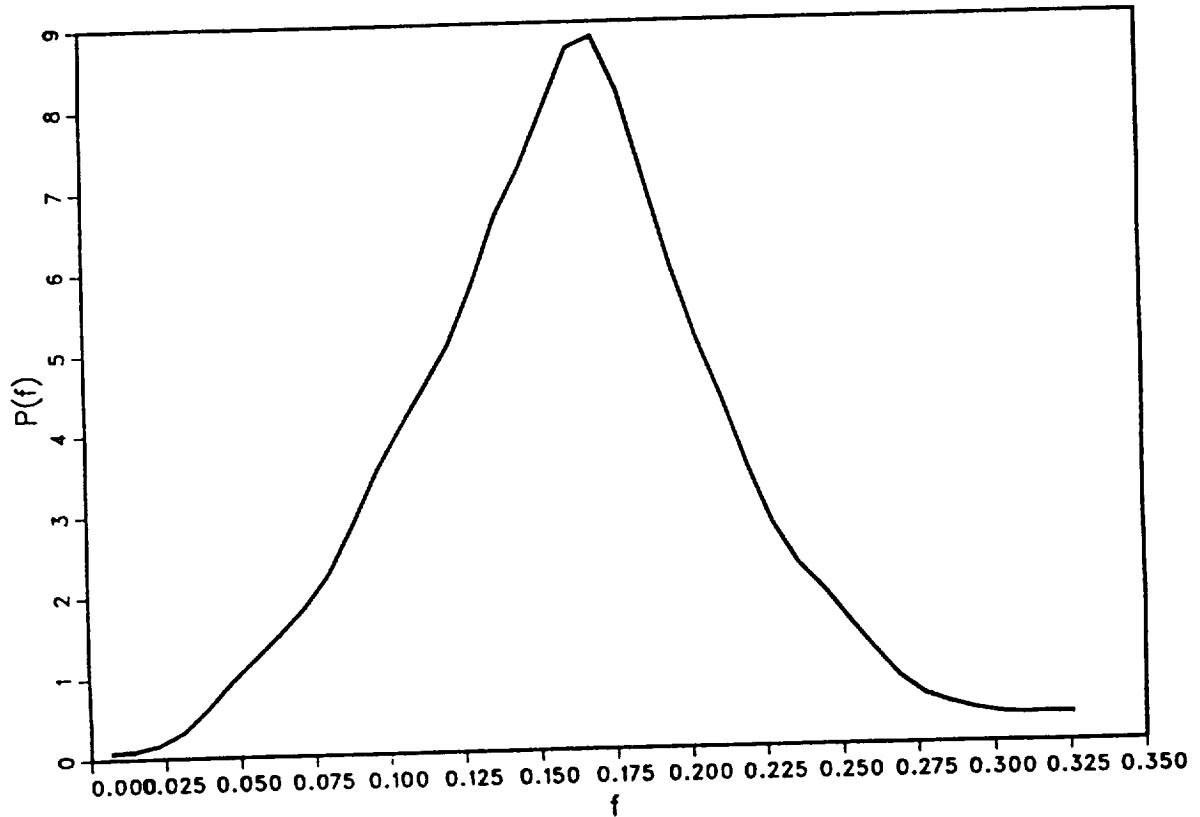


Fig.4.57 Pdf (smoothed) of mixture fraction at $x/D = 30.14$ and $r/D = 0.38$ for a supersonic turbulent round jet flame burning H_2 with a coflowing air stream ($M_a^o = 2.0$ at jet pipe exit).

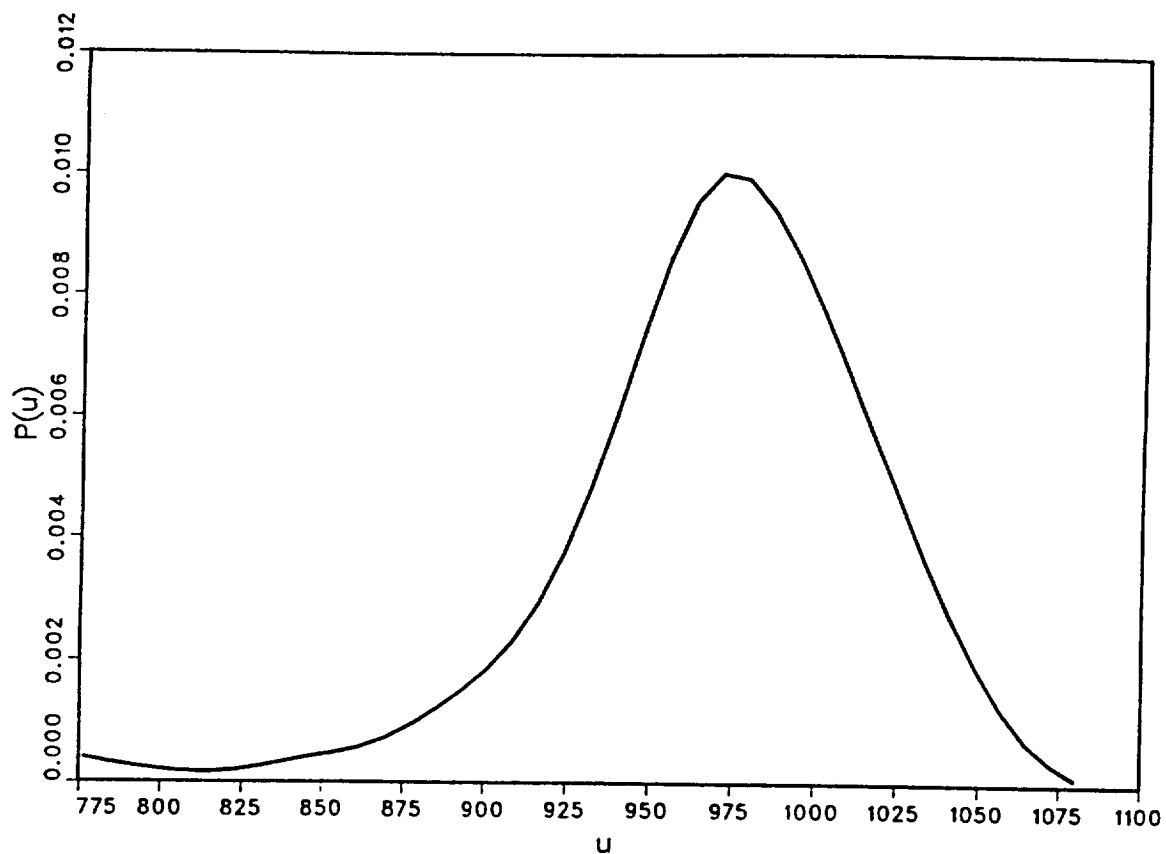


Fig.4.58 Pdf (smoothed) of internal energy at $x/D = 30.14$ and $r/D = 0.38$ for a supersonic turbulent round jet flame burning H_2 with a coflowing air stream ($M_a^o = 2.0$ at jet pipe exit).

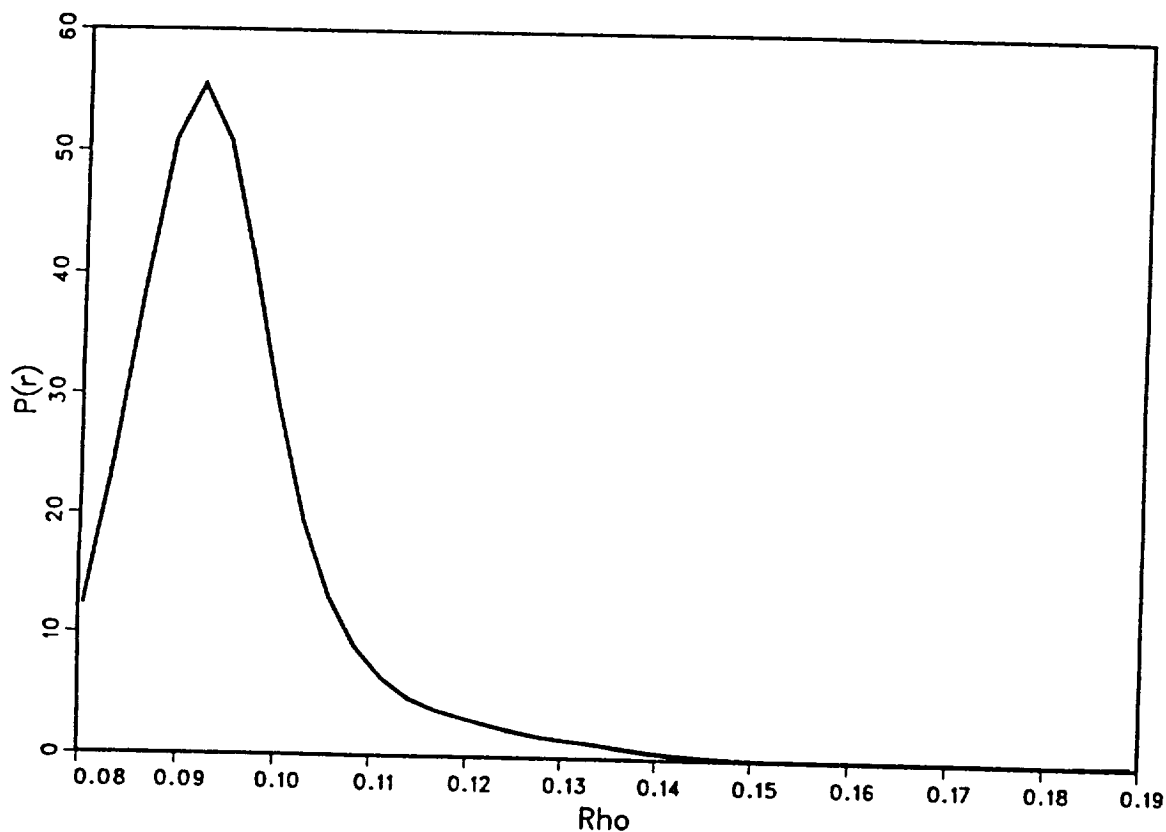


Fig.4.59 Pdf (smoothed) of density at $x/D = 30.14$ and $r/D = 0.38$ for a supersonic turbulent round jet flame burning H_2 with a coflowing air stream ($M_a^o = 2.0$ at jet pipe exit).

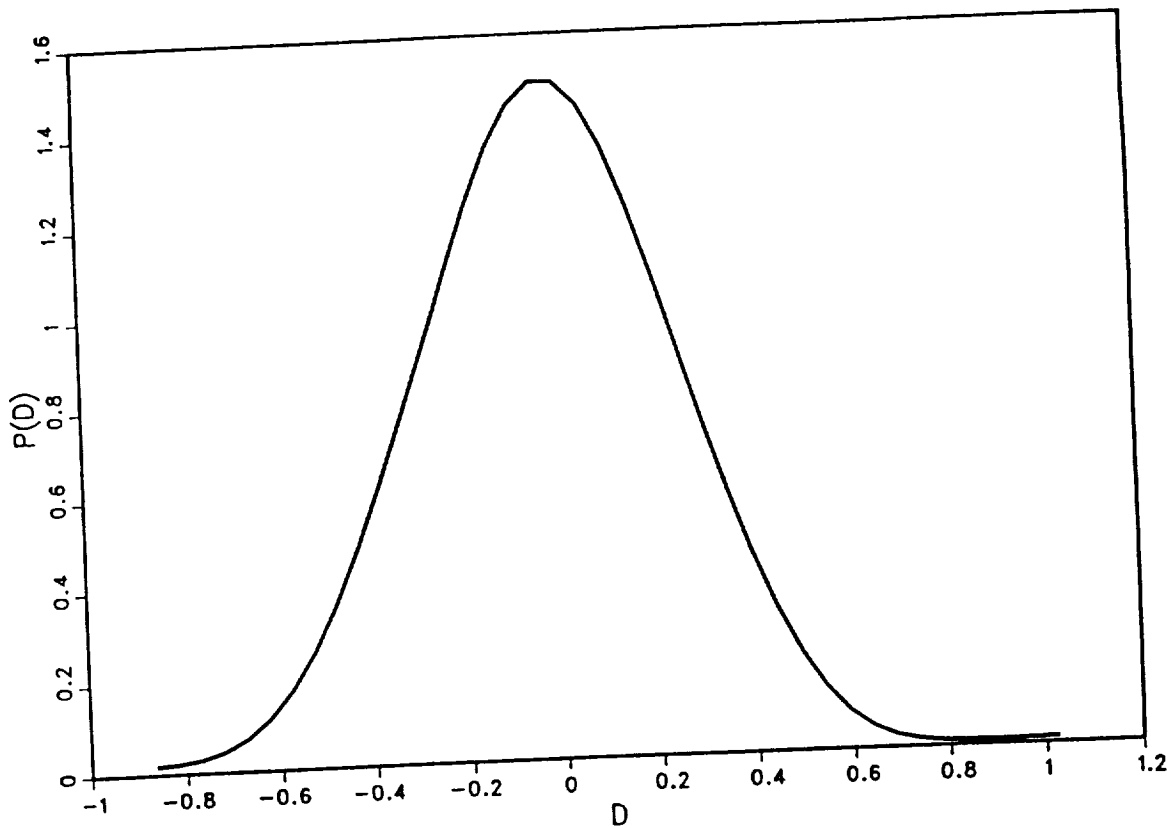


Fig.4.60 Pdf (smoothed) of relative rate of volume expansion at $x/D = 30.14$ and $r/D = 0.38$ for a supersonic turbulent round jet flame burning H_2 with a coflowing air stream ($M_a^o = 2.0$ at jet pipe exit).

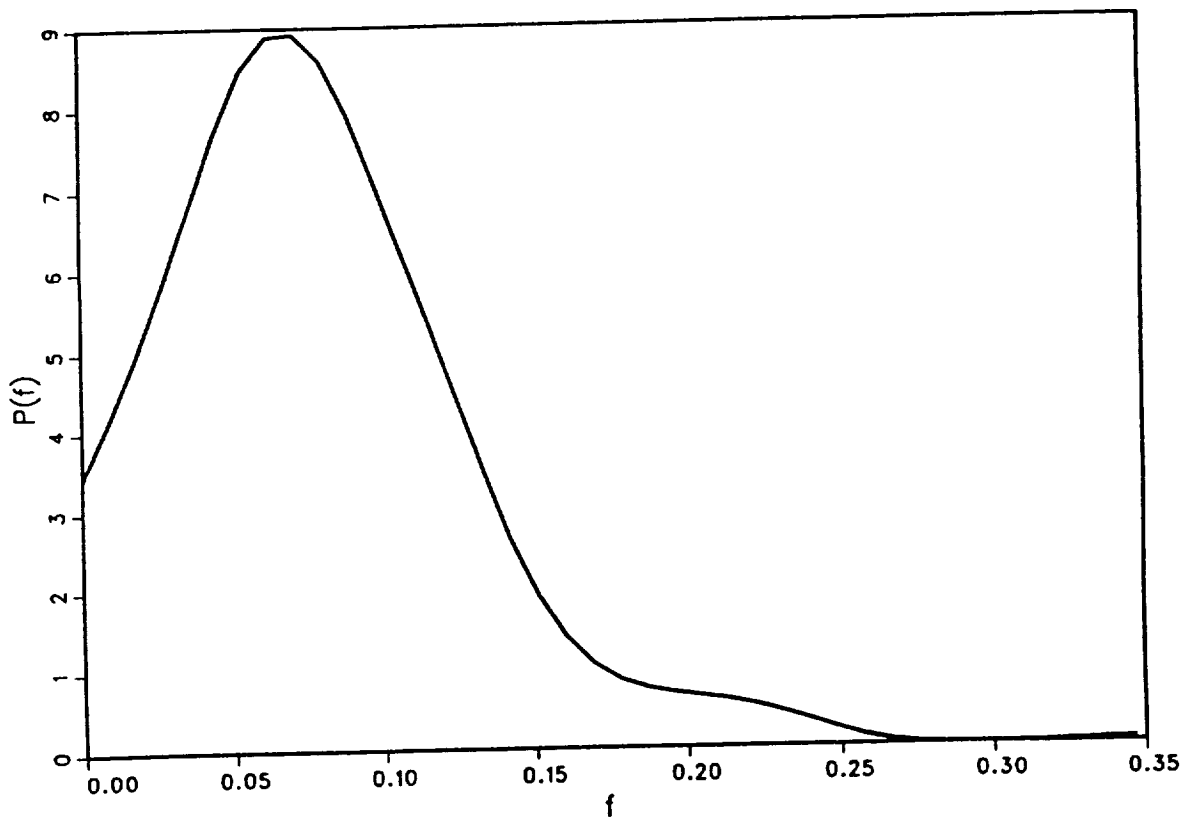


Fig.4.61 Pdf (smoothed) of mixture fraction at $x/D = 30.14$ and $r/D = 3.66$ for a supersonic turbulent round jet flame burning H_2 with a coflowing air stream ($M_a^o = 2.0$ at jet pipe exit).

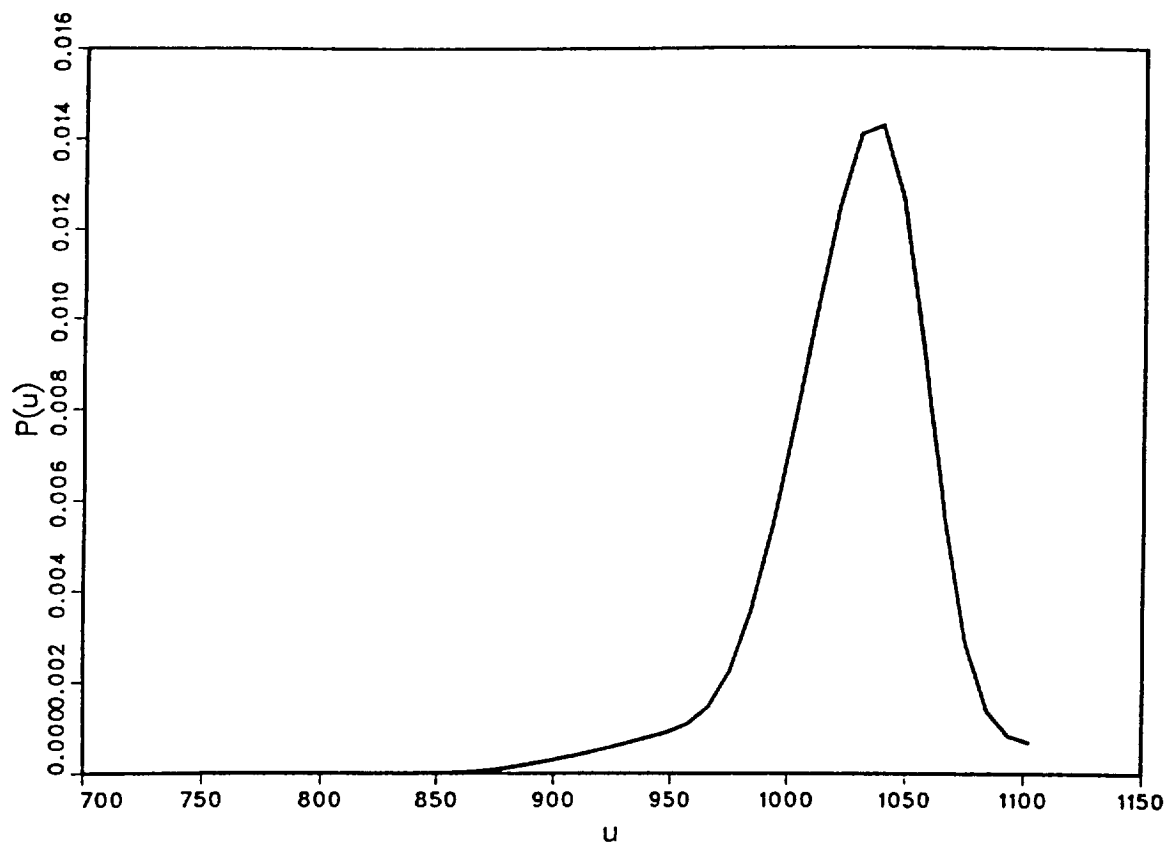


Fig.4.62 Pdf (smoothed) of internal energy at $x/D = 30.14$ and $r/D = 3.66$ for a supersonic turbulent round jet flame burning H_2 with a coflowing air stream ($M_a^o = 2.0$ at jet pipe exit).

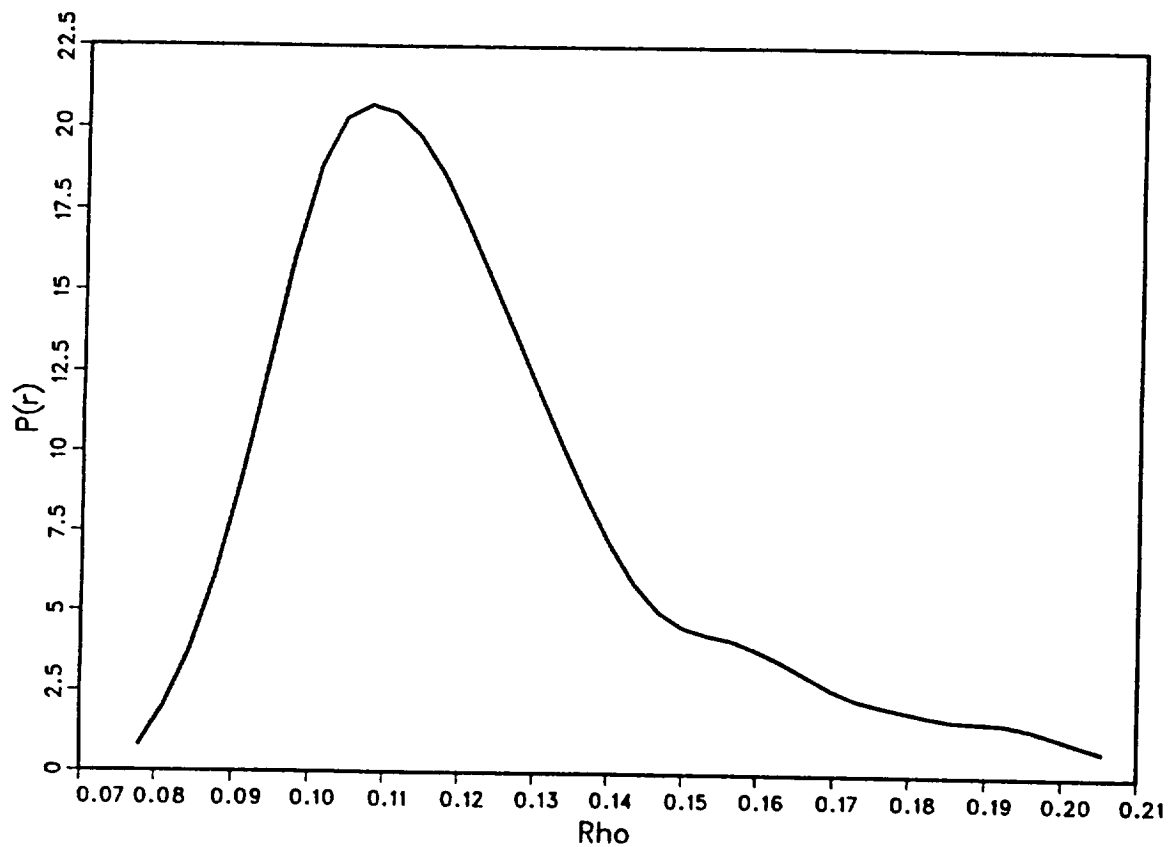


Fig.4.63 Pdf (smoothed) of density at $x/D = 30.14$ and $r/D = 3.66$ for a supersonic turbulent round jet flame burning H_2 with a coflowing air stream ($M_a^o = 2.0$ at jet pipe exit).

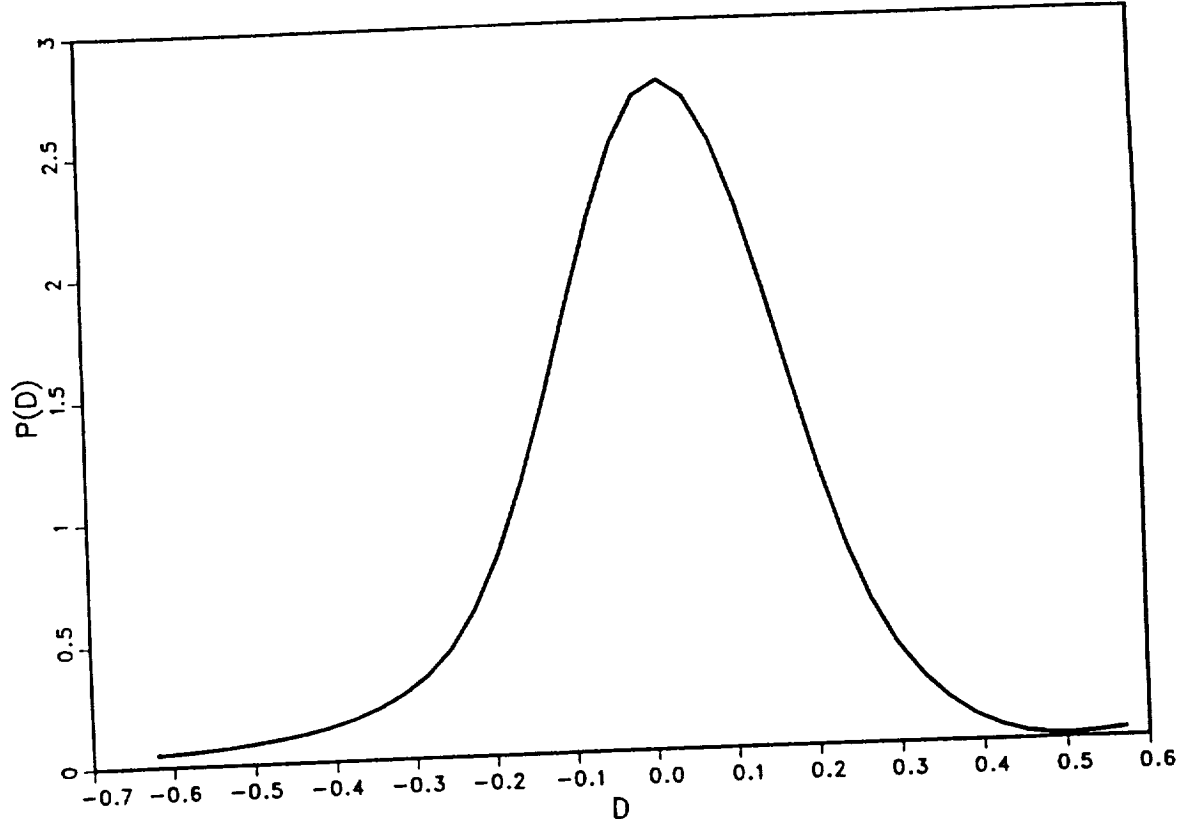


Fig.4.64 Pdf (smoothed) of relative rate of volume expansion at $x/D = 30.14$ and $r/D = 3.66$ for a supersonic turbulent round jet flame burning H_2 with a coflowing air stream ($M_a^o = 2.0$ at jet pipe exit).

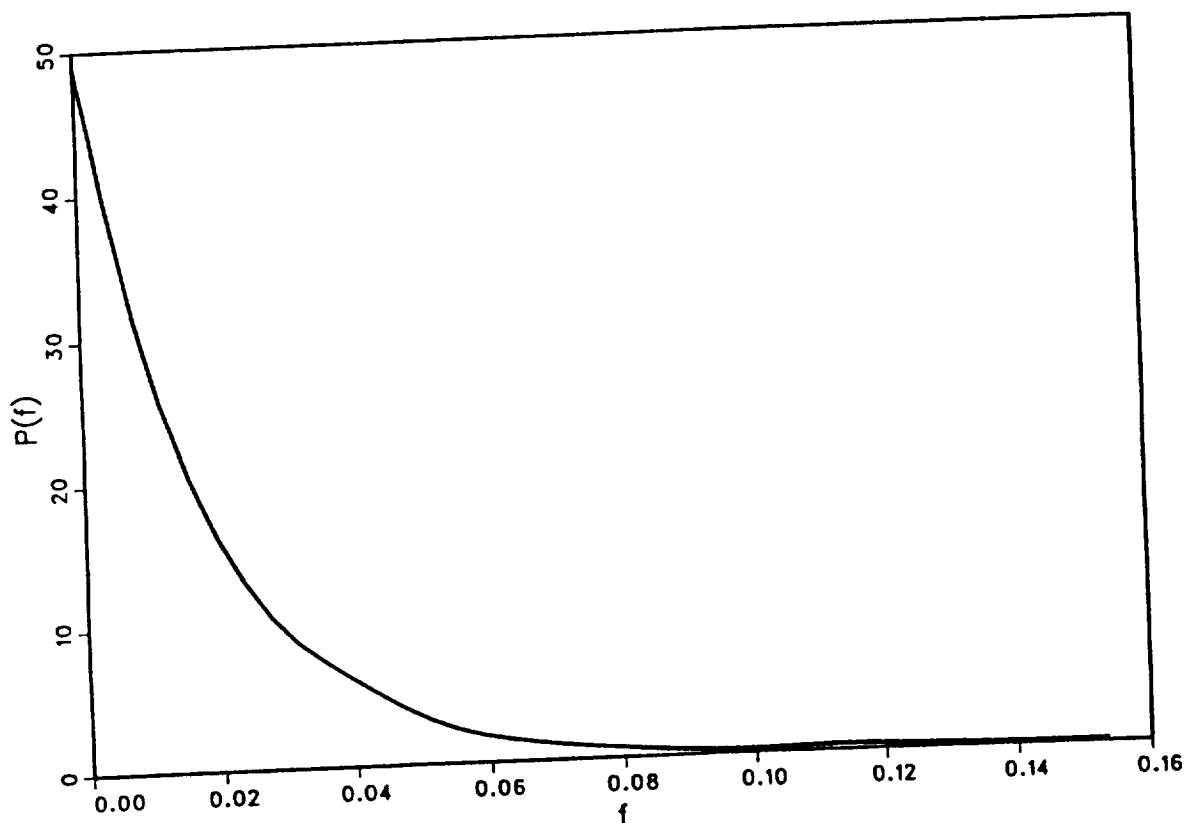


Fig.4.65 Pdf (smoothed) of mixture fraction at $x/D = 30.14$ and $r/D = 6.55$ for a supersonic turbulent round jet flame burning H_2 with a coflowing air stream ($M_a^o = 2.0$ at jet pipe exit).

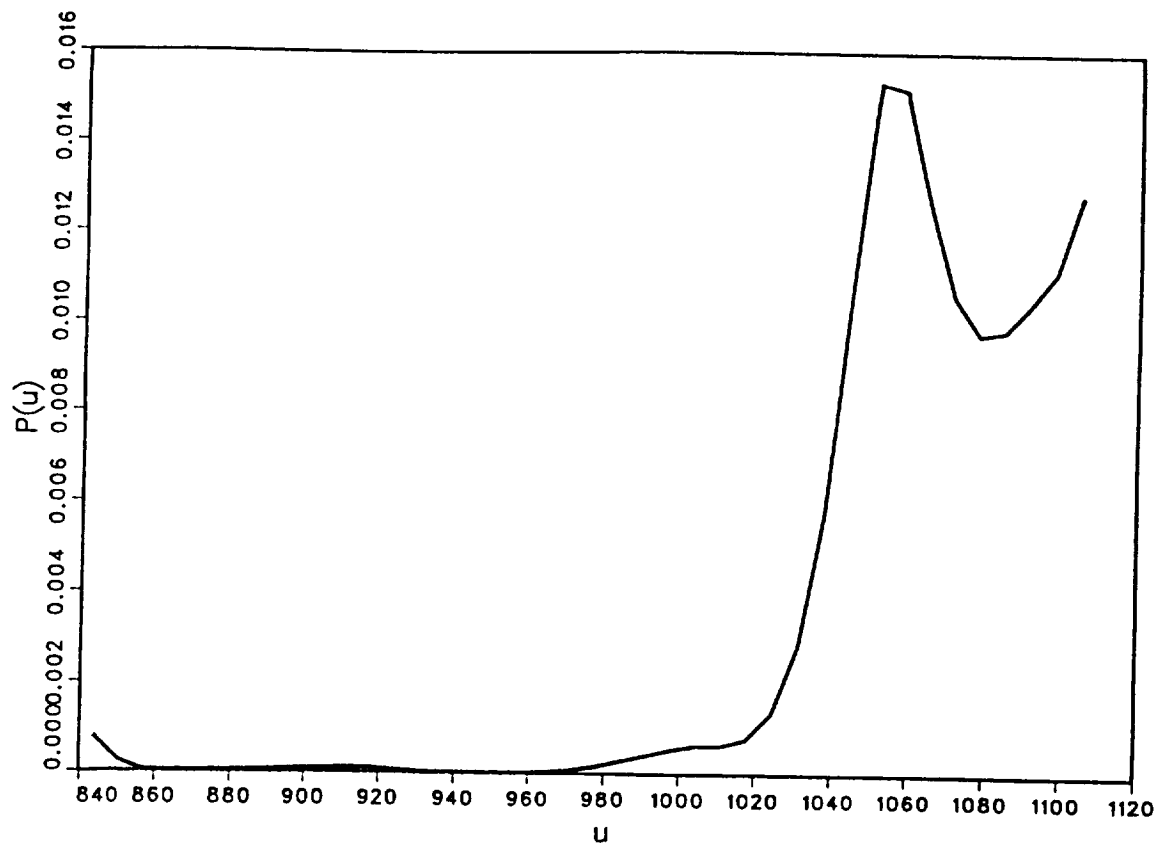


Fig.4.66 Pdf (smoothed) of internal energy at $x/D = 30.14$ and $r/D = 6.55$ for a supersonic turbulent round jet flame burning H_2 with a coflowing air stream ($M_a^o = 2.0$ at jet pipe exit).

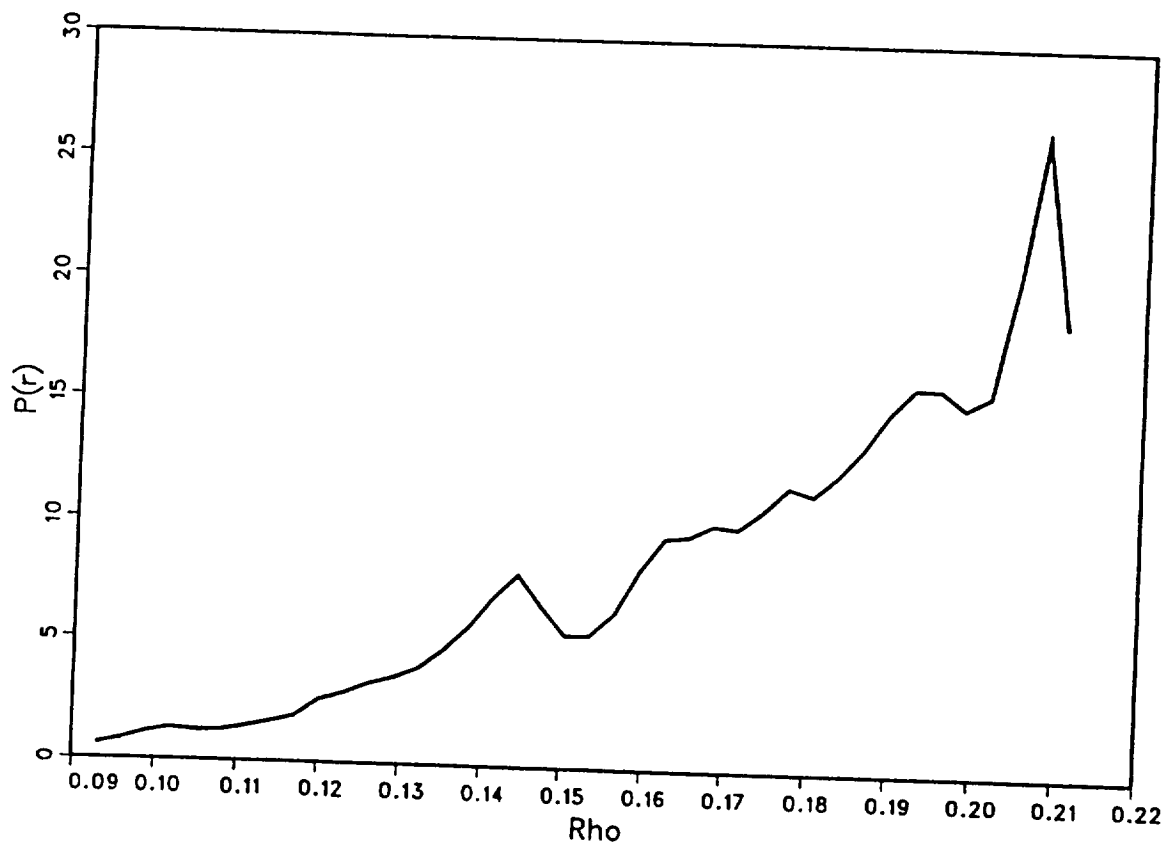


Fig.4.67 Pdf (smoothed) of density at $x/D = 30.14$ and $r/D = 6.55$ for a supersonic turbulent round jet flame burning H_2 with a coflowing air stream ($M_a^o = 2.0$ at jet pipe exit).

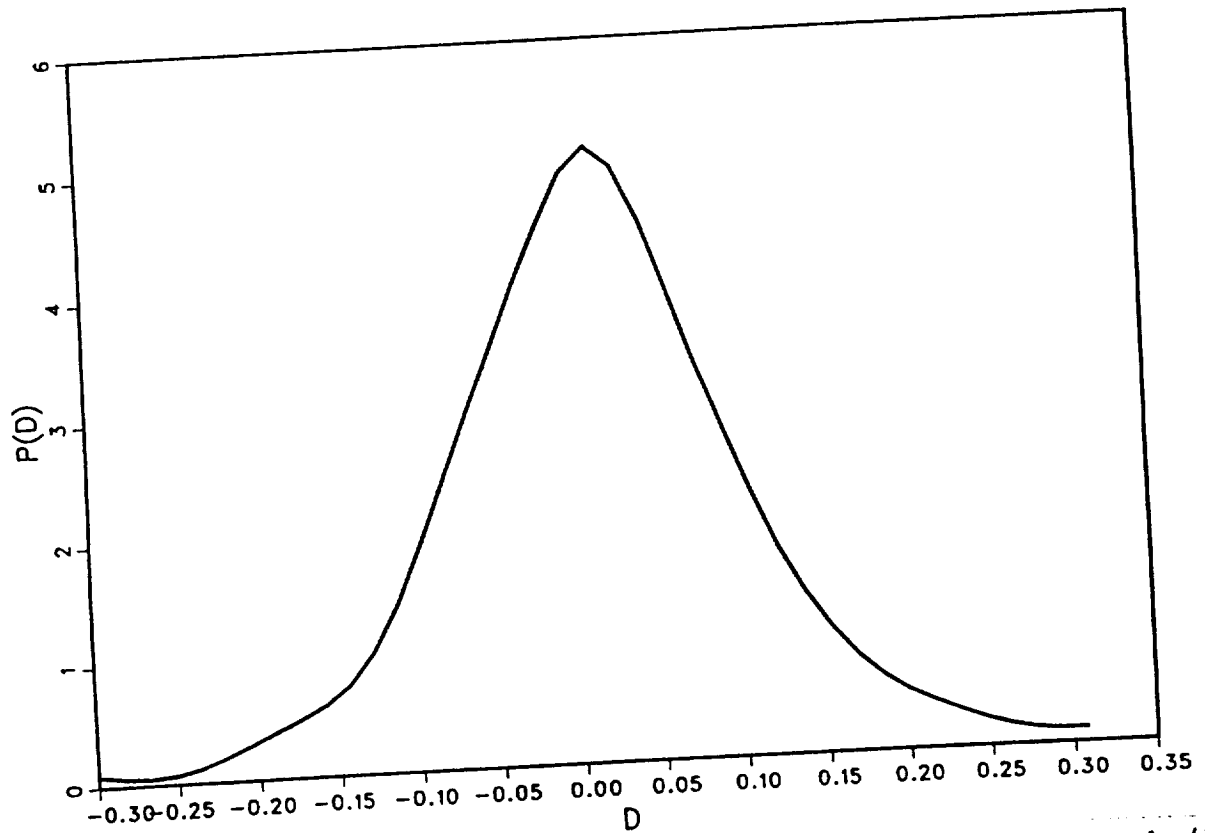


Fig.4.68 Pdf (smoothed) of relative rate of volume expansion at $x/D = 30.14$ and $r/D = 6.55$ for a supersonic turbulent round jet flame burning H_2 with a coflowing air stream ($M_a^o = 2.0$ at jet pipe exit).

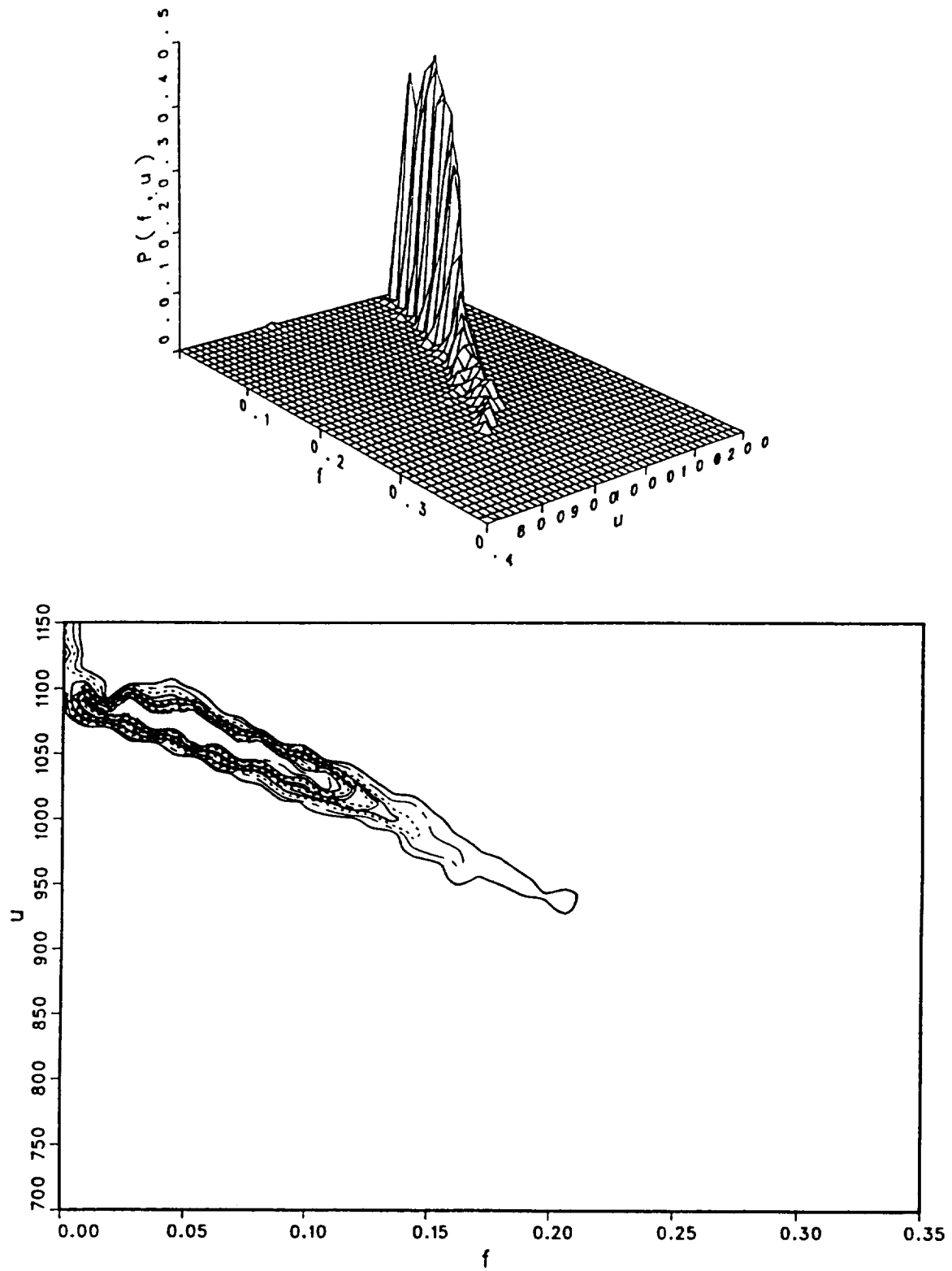


Fig.4.69 Pdf of mixture fraction and internal energy at $x/D = 30.14$ and $r/D = 3.66$ for a supersonic turbulent round jet flame burning H_2 with a coflowing air stream ($M_a^o = 2.0$ at jet pipe exit). Lower plot contains the same pdf in the form of iso-probability lines.

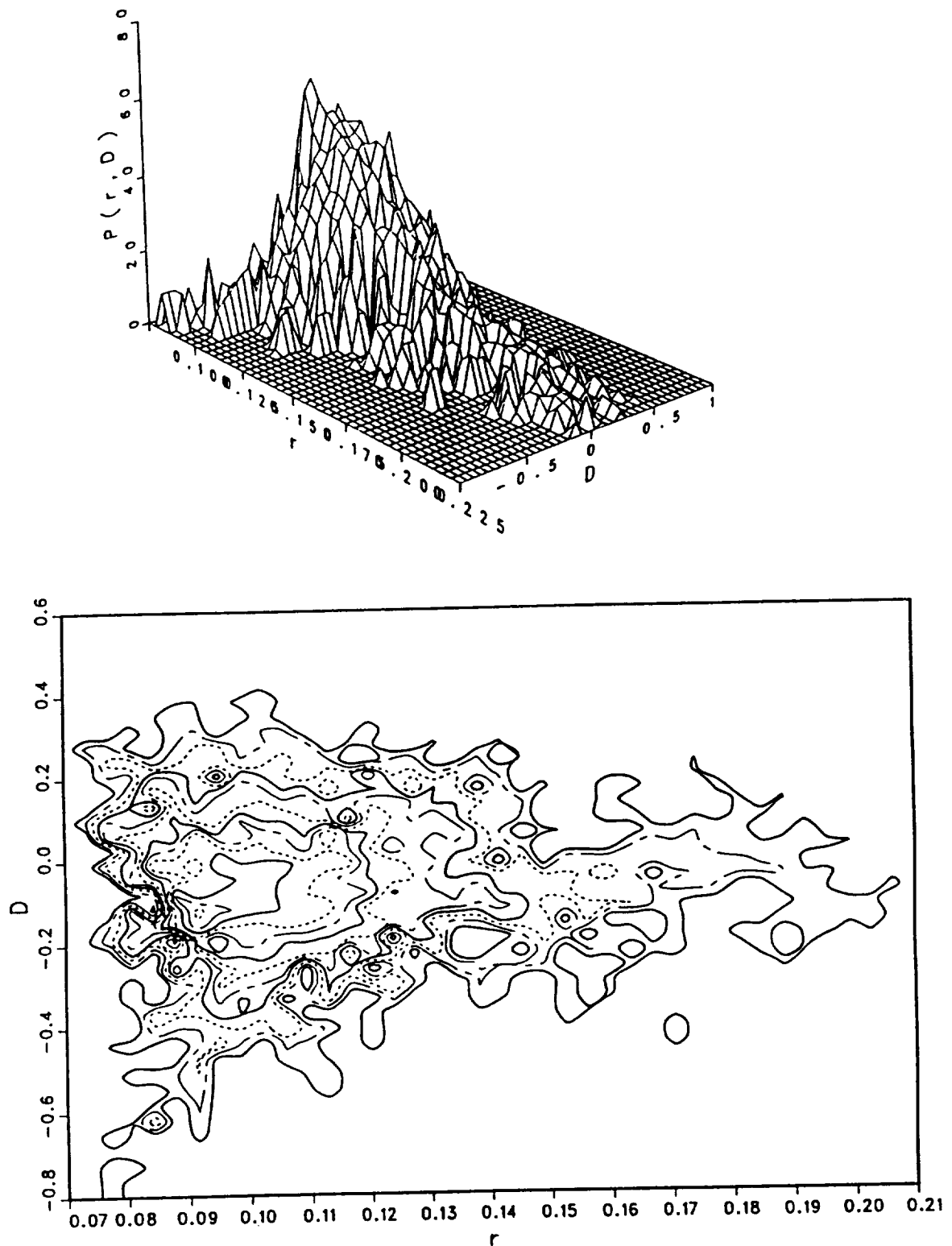


Fig.4.70 Pdf of density and relative rate of volume expansion at $x/D = 30.14$ and $r/D = 3.66$ for a supersonic turbulent round jet flame burning H_2 with a coflowing air stream ($M_a^o = 2.0$ at jet pipe exit). Lower plot contains the same pdf in the form of iso-probability lines.

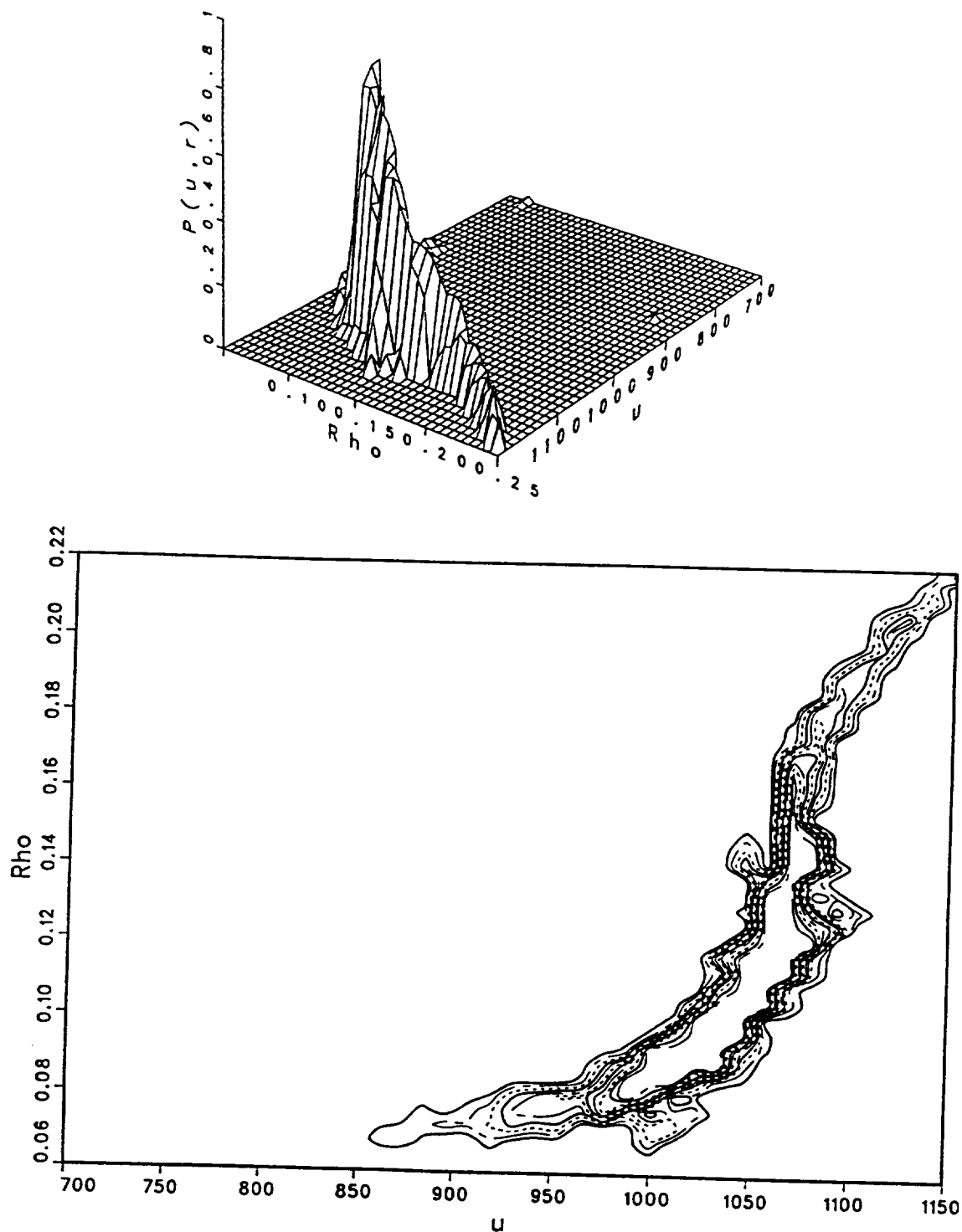


Fig.4.71 Pdf of density and internal energy at $x/D = 30.14$ and $r/D = 3.66$ for a supersonic turbulent round jet flame burning H_2 with a coflowing air stream ($M_a^o = 2.0$ at jet pipe exit). Lower plot contains the same pdf in the form of iso-probability lines.

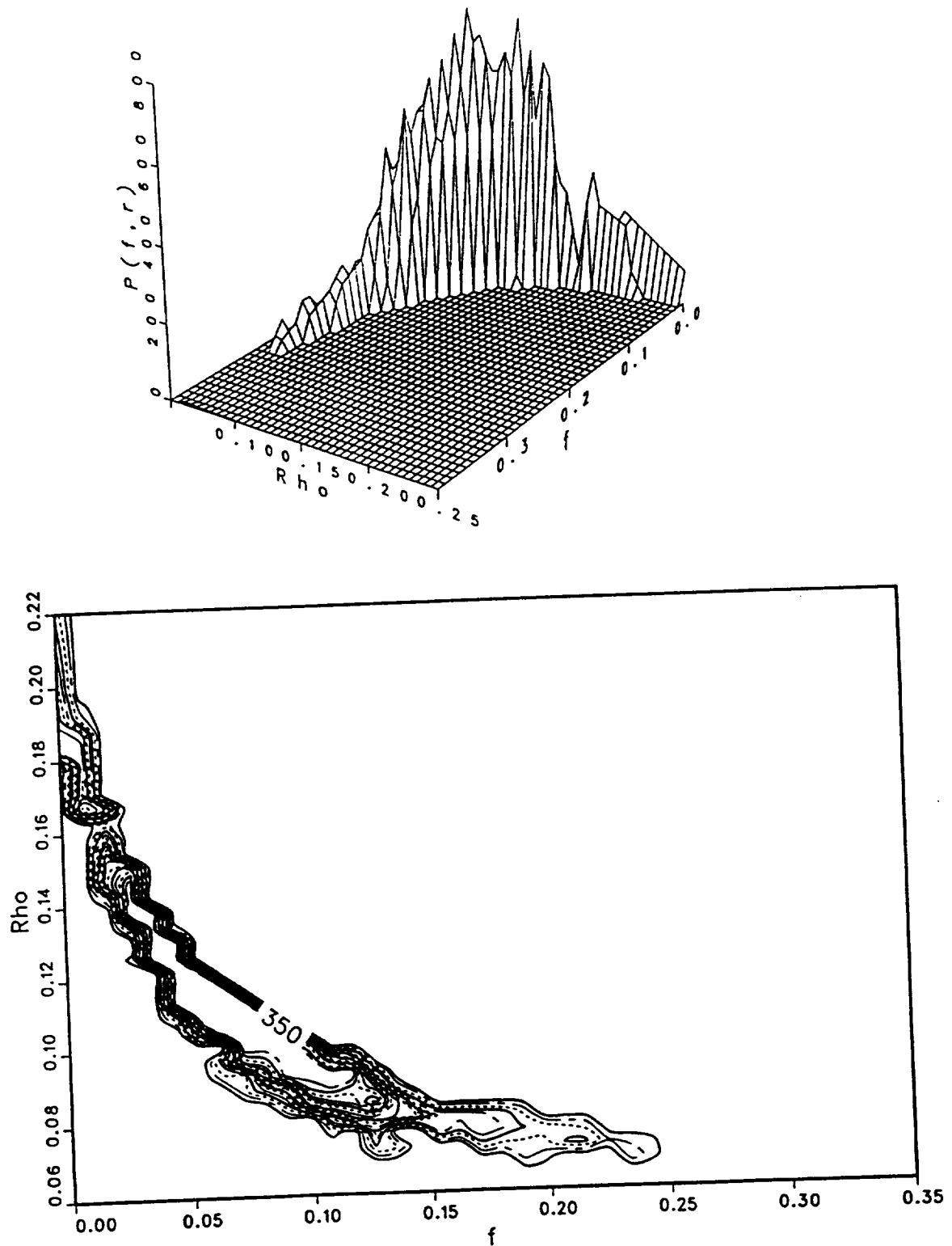


Fig.4.72 Pdf of mixture fraction and density at $x/D = 30.14$ and $r/D = 3.66$ for a supersonic turbulent round jet flame burning H_2 with a coflowing air stream ($M_a^o = 2.0$ at jet pipe exit). Lower plot contains the same pdf in the form of iso-probability lines.

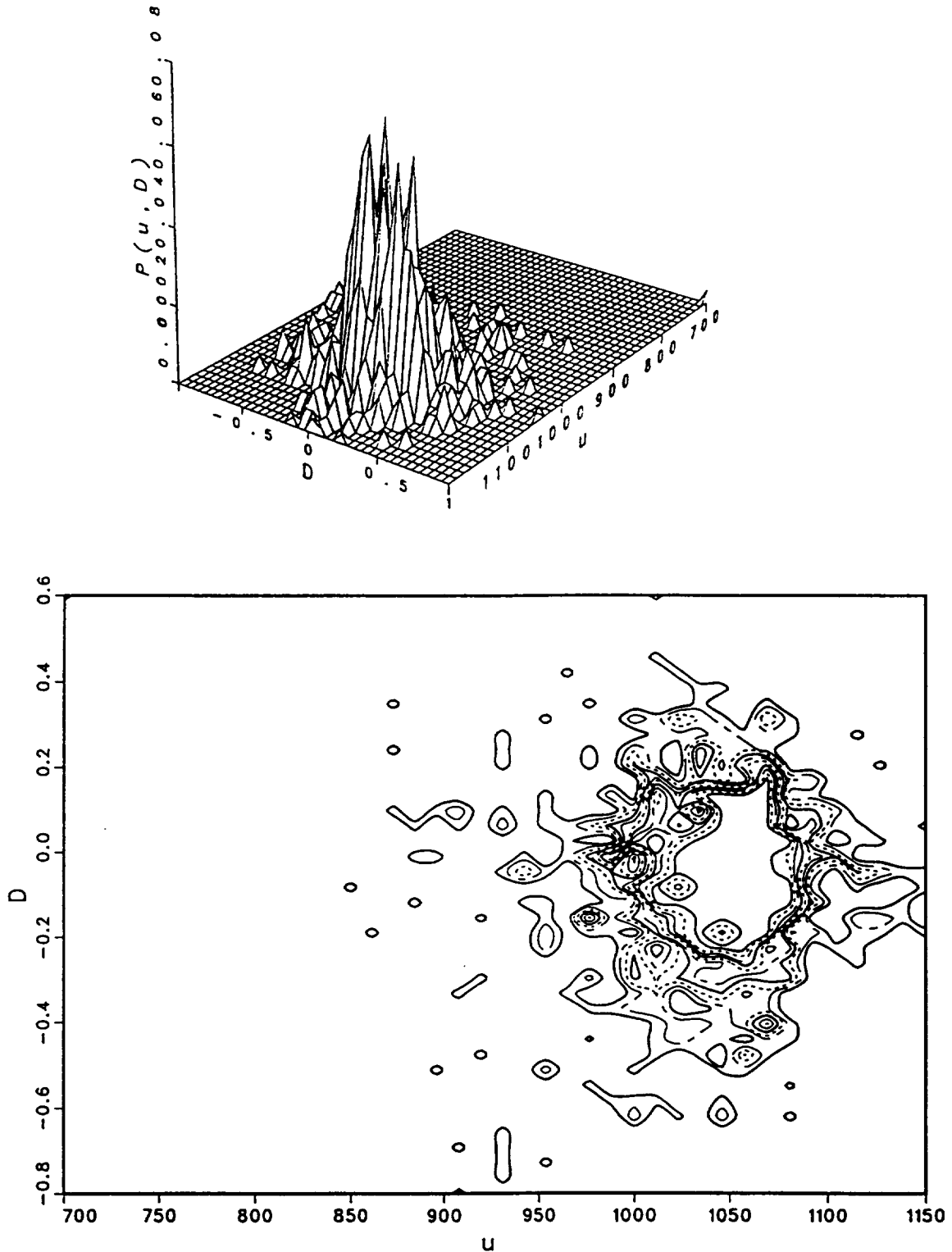


Fig.4.73 Pdf of internal energy and relative rate of volume expansion at $x/D = 30.14$ and $r/D = 3.66$ for a supersonic turbulent round jet flame burning H_2 with a coflowing air stream ($M_a^o = 2.0$ at jet pipe exit). Lower plot contains the same pdf in the form of iso-probability lines.

